A Tale of Two Spins: Electron Spin Centre Assemblies with $N@C_{60}$ for use in QIP



Benjamin J Farrington

Trinity College

A thesis submitted for the Degree of Doctor of Philosophy

University Of Oxford

Trinity Term 2013

A Tale of Two Spins:
Electron Spin Centre Assemblies with N@C_{60} for use in QIP

Benjamin J Farrington,Trinity College
Submitted for the Degree of Doctor of Philosophy
University Of Oxford, Trinity Term 2013

Abstract

Quantum information processing (QIP) has the potential to reduce the complexity of many classically 'hard' computational problems. To implement quantum information algorithms, a suitable physical quantum computer architecture must be identified. One approach is to store quantum information in the electron spins of an array of paramagnetic N@C_{60} endohedral fullerene molecules, using the electron-electron dipolar interaction to permit the formation of the entangled quantum states needed to implement QIP. This thesis explores two different chemical methods to create two-spin centre arrays that contain N@C_{60}. The first method uses a double 2,3 dipolar cycloaddition reaction to a dibenzaldehyde-terminated oligo-*p*-phenylene polyethynylene (OPE) unit , to create an ($S_{3/2}$, $S_{3/2}$) N@C_{60}-N@C_{60} dimer with a fixed spin centre separation of 2.7 nm. The second approach is via a self-assembly scheme in which a Lewis base functionalised N@C_{60} molecule coordinates to an antiferromagnetic metallic ring magnet to form a ($S_{3/2}$, $S_{1/2}$) two-spin centre N@C_{60}-Cr_7Ni system with an inter-spin separation of 1.4 nm. In both systems, a significant perturbation of the electron spin transition energies is observed using CW ESR, this perturbation is shown to be well accounted for by the inclusion of an electron-electron dipolar coupling term in the electron spin Hamiltonians.

To create entanglement in an ensemble of two-spin centre molecules, the dipolar coupling interaction must lie within a narrow distribution. To achieve this not only the separation but also the orientation of the inter-spin axis with respect to the applied magnetic field must be controlled for which a method of macroscopic alignment is required. The potential of using a uniaxially drawn liquid crystal elastomer to exert uniaxial order on fullerene dimers is tested, finding that the degree of alignment is insufficient, possibly a result of the propensity for the fullerene molecules to phase separate from the elastomer. This phase separation is shown to restrict N@C_{60} phase coherence lifetime to 1.4 μs at 40 K due to instantaneous spin diffusion. The electron spin environment of both N@C_{60} and an N@C_{60}-C_{60} dimer in a polymer matrix is examined using polystyrene as the host matrix. By deuteration of the polystyrene matrix, a maximum phase coherence lifetimes of 48 μs and 21 μs are measured for the N@C_{60} and N@C_{60}-C_{60} dimer, respectively.

The concept of reading out the electron spin state of N@C_{60} molecules by coupling it to a spin system that can be probed using optically detected magnetic resonance (ODMR) such as an NV^- centre has been previously suggested. To this end, the photostability of N@C_{60} under 637 nm laser illumination has been examined in solution. The effect of the presence of an atmospheric concentration of oxygen is striking, affording a 57-fold retardation in the photodecomposition of N@C_{60} compared to a degassed solution. When ambient oxygen is present, the average number of excitations that are required to cause decomposition is ≈ 60000. Finally, for future UV photophysics experiments involving N@C_{60}, the best solvent to use was found to be decalin, finding that it significantly slowed decomposition of N@C_{60} in both ambient and degassed solutions. The conclusions of this work make a significant contribution to the field of QIP with N@C_{60}, showing that there is a bright future for N@C_{60}.

Acknowledgements

Over the last four years I have had the pleasure of working with so many gifted and kind people, it is difficult to name them all....but I will try anyway.

First of all, I would like to thank my supervisors Dr Kyriakos Porfyrakis and Professor Andrew Briggs for their constant support, encouragement and belief in me. Kyriakos, thank you also for your relentless optimism and determination to always make time to discuss my project. I would also like to thank Andrew for the opportunity to Travel Air-Briggs, providing me with both a memorable experience and a story to tell for years to come.

My research has been very interdisciplinary in nature and required much collaboration; as such I have a lot of people to thank. Dr Martyn Jevric a.k.a. 'frank the tank' you taught me to be an organic research chemist and showed me just how much caffeine is humanly possible to consume in one day! Dr Simon Plant for the great 'dimer' chats which helped define my project. Dr Guoquan Lui for keeping me sane in the lab. Professor Arzhang Ardavan for acting like a surrogate supervisor by answering my many questions about ESR Spin dynamics and physics, and making sure I always had spectrometer time. Dr John Morton for giving up your time to teach me how to use the Elexsys and Pulse Spell. Danielle Kaminski and Dr Amy Webber for keeping me company on the many 24 hour Elexsys sessions and collecting those critical last few data points. Dr Jeff Harmer for always being available to troubleshot the spectrometer and demonstrating just how dry Australian humor can be. Dr Grigore Timco for providing beautiful antiferromagnetic ring compounds to complex with fullerenes. Dr Min Sang Park for teaching me about polarized Raman spectroscopy. Dr Ryan Kincer for showing me the bright lights of Atlanta and teaching me the importance of having a driving license. Alex Robertson, thank you for listening, or at least pretending to listen, to my many mumblings over the past four years in our office and at the R'Oak, and for helping me discover the joy of Lagavulin while in Amsterdam.

A doctorate is much like an endurance race, with many twists and turns and emotional highs and lows. Owing to this I would like to thank my family, Fiona, Joe, Sam and Athene for their constant support, helping iron out the highs and lows and getting me to the finish line. Lastly, and most importantly I would like to thank my fiancée Stephanie, for without her constant support, positivity, and fantastic ability at speed proof reading I genuinely don't know how I would have made it to this point.

Contributions

"*In the long history of humankind (and animal kind, too) those who learned to collaborate and improvise most effectively have prevailed."* —Charles Darwin.

Scientific discovery, often occurs via an evolutionary process, as such it greatly benefits from effective collaboration. I would therefore like to highlight the specific contributions from different collaborations that have been included in this thesis.

In chapter 3 the amino acid derivative N-(4-(hexyloxy)benzyl)glycine was synthesised by Dr Martyn Jevric and the precursor 1,4- didodecyl-2,5-diethynylbenzene was synthesised by Dr Graham Rance at the University of Nottingham.

In Chapter 4 the fitting of the ODF to the angularly dependent Raman bands was done in collaboration with Dr Min Sang Park at the Georgia Institute of Technology.

In Chapter 5 the two antiferromagnetic magnet ring complexes $Cr_7NiF_3(Etglu)(O_2CCMe_3)15(H_2O)$ and $Cr_7CoF_3(Etglu)(O_2CCMe_3)15(H_2O)$ were synthesised by Dr Grigore Timco at the University of Manchester. Dr Amy Webber and Danielle Kaminski also helped collect the low temperature T_2 and Echo detected field sweeps data sets recorded from the $N@C_{60}(py)$ and $N@C_{60}(py)$-Cr_7Ni samples at the CAESR facility in Oxford.

In Chapter 6 the flash photolysis experiments on the $N@C_{60}$ degassed and ambient samples were performed by Dr Kiminori Maeda at the CAESR facility in Oxford.

I can confirm that other work included in this thesis was performed by me.

Publications

A significant proportion of this thesis has either already been published or is in the process of being published in the following publications:

B.J. Farrington, A. L. Webber, G.A.D. Briggs, A. Ardavan, K. Porfyrakis, submitted. Title: *ESR environmental study of $N@C_{60}$ and its derivatives in polymer matrices.*

B.J. Farrington and K. Porfyrakis (2013) *Nitrogen atom-based endohedral fullerenes and potential applications*, in S Yang and C Wang (ed) Endohedral Fullerenes, World scientific, in press.

B. J. Farrington, M. Jevric, G. A. Rance, A. Ardavan, A. N. Khlobystov, G. A. D. Briggs, and K. Porfyrakis**,** *Angew. Chem. Int. Ed*., 51 (2012), 3587 –3590. Title: *Chemistry at the nanoscale: synthesis of an $N@C_{60}$-$N@C_{60}$ endohedral fullerene dimer.*

B.J. Farrington, T.J. Hingston, G.A.D Briggs, M.R. Sambrook, and K. Porfyrakis, ECS Transactions. 35(25) (2011), 113-117. Title: *Photostability of $N@C_{60}$ in common solvents.*

Table of content

Abbreviations v
Chapter 1 Introduction 1
1.1 Quantum Information Processing with N@C_{60} 1
1.2 An introduction to N@C_{60} 4
1.2.1 Synthesis 4
Commercial ion source method. 4
Glow discharge 5
R.F. plasma method 5
Electron cyclotron resonance method 6
1.2.2 Purification 7
1.2.3 Physical properties 8
Electron Spin Resonance 8
Stability 10
1.2.4 Chemical derivatives of N@C_{60} 11
Comparison of chemical reactivity with C_{60} 11
Exo ring-adducts 11
Cyclopropane exohedral adducts 11
Pyrrolidine exohedral adducts 12
ESR studies 13
Stability 15
1.3 C_{60} dimers 16
1.3.1 Directly bonded dimers 16
1.3.2 Dumbbell dimers 18
1.3.3 Methanofullerene attached dimers 23
1.3.4 Prato [2+3]cycloadditions 28
1.3.5 Other [3+2]cycloadditions 34
1.2.6 [4+2]cycloadditions 36
1.2.7 Metal-bridged dimers 40
1.3.8 Summary 42
1.4 N@C_{60} dimers 42
1.4.1 N@C_{60}-C_{60} dimers 42
1.4.2 N@C_{60}- hetero spin centre dimers 47
Current systems 47
Cr_7Ni rings - an ideal test hetero spin centre 48

1.5 Thesis Motivation and Aims 51
Chapter 2 Analytical and Preparative Techniques 52
2.1 Ion implantation of N@C_{60} 52
2.2 HPLC purification 53
2.2.1 Introduction 53
2.2.2 Purifying N@C_{60} 54
2.3 ESR spectroscopy 56
2.3.1 CW ESR 56
2.3.2 Static Spin Hamiltonian 56
2.3.3 Pulsed ESR 61
2.3.4 Relaxation 63
2.5 Polarised Raman spectroscopy 66
2.6 UV-Vis spectroscopy 70
2.7 FTIR Spectroscopy 71
2.8 Mass Spectrometry 71
2.9 NMR 71
2.9.1 1D ^{1}H NMR and ^{13}C NMR 72
2.9.2 2D COSY and me-HSQC NMR 72
Chapter 3 Synthesis of ^{14}N@C_{60} dimers with controlled separation 74
3.1 Introduction 74
3.2 Synthesis approach overview 76
3.3 Synthesis and characterisation of bridging units 77
3.2.2 Characterisation 79
^{1}H NMR 81
^{13}C NMR 82
IR 83
Mass Spectra 84
3.4 Synthesis and characterisation of C_{60}-C_{60} dimers 86
3.4.1 Characterisation 86
HPLC 87
^{1}H NMR 90
^{13}C NMR 91
UV-Vis 94
Mass Spectra 94
3.4.2 Reaction optimisation for small scale 95
3.5 Synthesis and ESR characterisation of ^{14}N@C_{60}-C_{60} dimers 98
3.5.1 N@C_{60} synthesis and enrichment 98

3.5.2 Characterisation 99
HPLC 99
CW ESR 100
3.6 Synthesis and ESR characterisation of an $^{14}N@C_{60}$-$^{14}N@C_{60}$ dimer 103
3.6.1 $N@C_{60}$ synthesis and enrichment 104
3.6.2 Characterisation 105
3.7 Discussion 111
3.8 Summary of Experimental Details 112
Chapter 4 Characterisation of C_{60} and $N@C_{60}$ dimers in polymer matrices 118
4.1 Introduction 118
4.2 Alignment of Dimer-3bzo and Ald-5bz in a silicone elastomer 119
4.2.1 Sample preparation 120
4.2.2 Creating orientation 121
4.2.3 Probing for orientation 121
Ald-5bz in Si-LCE 123
Dimer-3bzo in Si-LCE 127
4.2.4 $N@C_{60}$ Dimer-3bzo in Si-LCE 129
4.3 ESR characterisation of $N@C_{60}$ in a polystyrene matrix. 131
4.3.1 Sample preparation 131
4.3.2 CW ESR study 132
4.3.3 Pulsed ESR study 135
4.4 Discussion 137
Chapter 5 Synthesising a heterospin centre $N@C_{60}$-Cr_7Ni complex. 140
5.1 Introduction 140
5.2 C_{60}(py)-Cr_7Co 141
5.2.1 Characterisation of C_{60}(py) 142
5.2.2 Characterisation of C_{60}(py)-Cr_7Co 147
5.3 $N@C_{60}$(py)-Cr_7Ni 151
5.3.1 Characterisation of $N@C_{60}$(py) 151
5.3.2 ESR study of $N@C_{60}$(py)-Cr_7Ni 153
5.4 Discussion 159
Chapter 6 Photostability of $N@C_{60}$ 162
6.1 Introduction 162
6.2 254 nm UV stability of $N@C_{60}$ in common solvents 163
6.2.1 Experimental set-up 163
6.2.2 Solvent dependency 164
6.3 637 nm laser stability of $N@C_{60}$ 167

6.3.1 Experimental set-up 168
6.3.2 Results 171
6.4 Discussion 176
Chapter 7 Conclusions and future outlook 178
7.1 Conclusions 178
7.2 Future focus 181
References 183
Appendix A 191
Appendix B 197

Abbreviations

A	Hyperfine interaction tensor
A_{iso}	Isotropic Hyperfine coupling constant
A_{750nm}	Transient-absorbance measured at 750 nm
A	Ampere
A	First derivative ESR signal magnitude
Å	Angstrom
a_{iso}	Isotropic Hyperfine Fermi contact interaction
AFM	Atomic Force Microscopy
atm	Atmospheres of pressure
$\boldsymbol{\alpha}$	Symmetric polarisability tensor (Raman)
$\boldsymbol{\alpha}'$	First derivative of symmetric polarisability tensor (Raman)
$\boldsymbol{B}_0$	Static magnetic field vector
$\boldsymbol{B}_1$	Applied microwave field vector
COSY	Correlation spectroscopy
CNOT	Controlled NOT universal quantum gate
CW ESR	Continuous Wave Electron Spin Resonance
D	Zero-Field Splitting interaction tensor
D	Axial zero field splitting component
D_{strain}	Axial zero field splitting strain parameter
dB	Decibel
DBU	1,8-Diazabicyclo[5.4.0]undec-7-ene
DFT	Density Functional Theory
D-ps	Deuterated Polystyrene
DSC	Differential Scanning Calorimetry
$\boldsymbol{E}$	Incident electromagnetic radiation vector (Raman)
E	Rhombohedral zero field splitting component
ENDOR	Electron Nuclear Double Resonance
ESI	Electro-spray Ionisation
ESR	Electron Spin Resonance
eV	Electron Volt
FTIR	Fourier Transform Infra Red Spectroscopy
G	Gauss
g	g-value
$\boldsymbol{g}$	Electron g-vale tensor
g_e	g-value of free electron
g_{iso}	Isotropic g-value
g_n	Nuclear g-value
g_x	x component of electron g-value tensor
g_y	y component of electron g-value tensor
g_z	z component of electron g-value tensor
$\widehat{\boldsymbol{H}}$	Static Electron Spin Hamiltonian operator

$\widehat{H}_{EZ}$	Electron Zeeman interaction term
$\widehat{H}_{ZF}$	Zero Field interaction term
$\widehat{H}_{HF}$	Hyperfine interaction term
$\widehat{H}_{NZ}$	Nuclear Zeeam interaction term
$\widehat{H}_{NQ}$	Nuclear Quadrupole interaction term
$\widehat{H}_{NN}$	Nuclear-Nuclear dipole exchange interaction term
$\widehat{H}_{EX}$	Electron spin exchange interaction term
$\widehat{H}_{EE}$	Electron spin dipole-dipole interaction term
h	Planks constant
$\hbar$	h-bar ($\frac{h}{2\pi}$)
HOMO	Highest Occupied Molecular Orbital
HPLC	High Pressure Liquid Chromatography
H-ps	Protonated Polystyrene
HSVM	High Speed Vibrational Milling
I	Intensity of scattered light (Raman)
I	Primary nuclear spin quantum number
IR	Infra Red
$\boldsymbol{J}$	Electron-electron dipolar interaction tensor
$\boldsymbol{J}^{diag}$	Diagonalised traceless form for electron-electron dipolar tensor
j_{dip}	Electron-electron dipolar coupling term
K	Kelvin
k_{CS}	Rate constant for charge separation
k_{CR}	Rate constant for charge recombination
k_{IC}	Rate constant for Internal Conversion
k_{ISC}	Rate constant for Intersystem Crossing
k_{NR}	Rate constant for non-radiative relaxation
k_p	Rate constant for phosphorescence
k_q	Rate constant for triplet quenching by $^3O_2$
K_{iso}	Scalar isotropic Heisenberg exchange interaction term
LCE	Liquid Crystalline Elastomer
LUMO	Lowest Unoccupied Molecular Orbital
$lwpp$	Peak to peak line width
$\boldsymbol{M}$	Macroscopic magnetisation vector
M_I	Secondary nuclear spin quantum number
M_n	Number average molar mass
M_S	Secondary electron spin quantum number
M_w	Mass average molar mass
MALDI	Matrix Assisted Laser Desorption/Ionisation
me-HSQC	Multiplicity-edited Hetero-nuclear Single Quantum Correlation
ODCB	*ortho*-dichlorobenzene
ODF	Orientation Distribution Function
ODMR	Optically Detected Magnetic Resonance
OPE	Oligo(*p*-phenylene polyethynylene)
OPV	Oligo(phenylenevinylene)

N	Average number of excitations required to cause N@C_{60} to decay
NIR	Near Infra Red
NMR	Nuclear magnetic Resonance
NV^-	Nitrogen-Vacancy
ppb	Parts per billion
ppm	Parts per million
P	Nuclei-nuclei coupling tensor
P_2	2nd order ODF order parameter (Hermans orientation factor)
P_4	4th order ODF order parameter
Q	Nuclear quadrupole interaction tensor
Q	Magnitude of atoms spatial displacement (Raman)
Q factor	Quality factor of resonator
R	Depolarisation ratio (Raman)
RT	Room Temperature
$r_{1,2}$	Separation between two electron spin centres
S	Electron spin-vector
S	Primary electron spin quantum number
S_1	First excited singlet state of fullerene
Si-LCE	Siloxane Liquid Crystalline Elastomer
$t_{1/2}$	Decay half life
$T_1^{triplet}$	First exited triplet state of fullerene
T_1	Spin-lattice relaxation lifetime
T_2	Spin-spin relaxation lifetime
T_m	Phase memory time
t_d	Microwave pulse delay length for inversion recovery pulse sequence
t_p	Microwave pulse length
T	Traceless diagonal tensor component of Hyperfine interaction tensor
T	Tesla
T_g	Glass transition temperature
TLC	Thin Layer Chromatography
TTF	Tetrathiafulvalene
$\boldsymbol{\mu}_i$	Induced dipole moment vector (Raman)
μ	Magnetic moment of free electron
μ_B	Bohr magneton
μ_N	Nuclear magneton
μ_k^{vib}	Induced dipole moment associated with a vibrational frequency
V	Volt
v_{ex}	Photon frequency of excitation (Raman)
v_r	Photon frequency of Rayleigh scattering
v_s	Photon frequency of Stokes scattering
v_{as}	Photon frequency of Antistokes scattering
W	Watt
ω_{EE}	Dipolar interaction energy
ω_s	Stationary state angular frequency

ω_{mw}	Angular frequency of a linearly polarised microwave pulse
ω_1	Precession angular frequency due to B_1
ZFS	Zero Field Splitting
1D	1-dimentional
3D	3-dimentional
5PBB	5 µm silica beads functionalised with PBB stationary phase
15PBB	15 µm silica beads functionalised with PBB stationary phase
$\sim$	Transpose of a matrix or vector
$\mathbb{I}$	Identity opperator
β	Polar angle describing orientational distribution of molecules (fig. 2.7)
θ	Angle between incident polarisation and stretch direction (fig. 2.7)
θ_{dip}	Dipolar interaction polar angle
τ	Wait time in pulsed microwave experiment
τ_d	Mean lifetime of an N@C_{60} molecule
λ	Extension ratio
γ	Gyro-magnetic ratio
ϕ	Quantum yield

Chapter 1 Introduction

Quantum information processing (QIP) has the potential to reduce the complexity of many classically 'hard' computational problems. To implement quantum information algorithms, a suitable physical quantum computer architecture must be identified. One approach is to store quantum information in the electron spins of an array of paramagnetic N@C_{60} endohedral fullerene molecules, using the electron-electron interaction to permit the formation of the entangled quantum states needed to implement QIP.

This thesis aims to address a number of important questions concerning the construction of an N@C_{60} based quantum computer. Is it possible to control the electron-electron interaction between two N@C_{60} molecules by chemically linking them together to form a platform for a two qubit array? If so, what effect does this interaction have on the Electron Spin Hamiltonian of the system and does this agree with the theoretical assumptions used in current proposed N@C_{60} QIP architectures? An optimal electron spin based QIP architecture might well comprise of a number of different types of molecular based qubits that each have different ideal properties. As such, the question of how the unusually long phase memory time (T_m) of N@C_{60} is altered when linked to a different type of molecular qubit is also investigated.

1.1 Quantum Information Processing with N@C_{60}

Since Alan Turing fathered the concept of the modern day computer, also known as a 'Turing Machine', around the time of the Second World War,[1] governments, academic institutions and corporations alike have been fascinated by making computers faster and more efficient (in both a coding and, more recently, energy sense). As society has become more connected and digital information plays an ever greater role in our lives,[2] the potential social and commercial reward from more efficient and faster computing is only set to increase.

In 1985, David Deutsch published a paper, which showed that a 'universal quantum computer' based on the principles of quantum mechanics had the potential to fundamentally outperform a classical Turing Machine in a subset of computational tasks.[3] Later, Peter Shor went on to show that it was possible to implement a factoring algorithm using a quantum computer that would require exponentially fewer computational steps than an equivalent classical computer,[4] providing the first real impetus to construct a physical quantum computer. Physical implementation of this algorithm to factorise the number 15 has since been achieved by a number of groups using nuclear spins qubits[5], photonic qubits[6] and solid state Josephson qubits.[7] To date, the larger numbers 21 and 143 have also been factorised using photonic qubits [8] and nuclear spin qubits[9], respectively. A number of other tasks that have also been theoretically shown to be more efficient on a quantum computer[10] including searching unsorted databases[11-12] and simulating quantum processes.[13-14]

To assess the suitability of a particular physical implementation of a quantum computer the 5 DiVincenzo criteria are often used.[15] These criteria state that a potential quantum information processing architecture must comprise the following:

1. A scalable physical system with well characterized qubits.
2. The ability to initialise the state of the qubits.
3. Long relevant decoherence times, much longer than the gate operation time.
4. A "universal" set of quantum gates.
5. A qubit-specific measurement capability.

The long electron spin coherence time (T_2) achievable in N@C_{60} was the founding reason it was identified as an potential qubit in an electron spin based quantum computer architecture.[16] This is because information can be stored and read from an ensemble of electron spins using short microwave pulses of the order of a few tens of ns long for each operation.[17] Consequently, the 250 μs phase coherence time achievable in N@C_{60} would permit over 10,000 sequential operations to be performed before electron spin needs to be re-initialised, in pursuit of criterion 3. It has been shown using N@C_{60}

that, by employing composite microwave pulses, large systematic errors in single qubit operations can be corrected for[18] to retain a fidelity of between 0.999 and 0.9999, a prerequisite to satisfy criterion 4. The nuclear spin of N@C_{60} has also been used to store quantum information, enhancing the storage time that is achievable when purely using the electron spin to over 100 ms.[19] The ability to create and read out the density matrix of a pseudo-pure entangled state between the electron and nitrogen nuclear spin of an ensemble of ^{15}N@C_{60} molecules shows that using ESR and ENDOR (Electron Nuclear Double Resonance) a single N@C_{60} can act as a well characterised qubit that can be measured,[20] partly satisfies criteria 1, 2 and 5. To satisfy criteria 1 there are a number of routes being investigated to construct scalable arrays of N@C_{60} qubits. By applying a low temperature method based on refluxing n-hexane it has been shown possible to encapsulate N@C_{60} within SWCNTs to create a 1D array of qubits.[21] Higher dimensional arrays based 3D single crystal structures that incorporate N@C_{60} and N@C_{70} have also been pursued. To date, the co-crystal systems that have been reported are N@C_{60}-:2,4,6-tris-(4-bromophenoxy)-1,3,5-triazine[22] and N@C_{60}:Buckyclutcher.[23] These have both been found to have angularly dependent ESR spectra, proving the ability to create alignment between isolated N@C_{60} molecules. A suitably scalable method to address individual N@C_{60} qubits is required to satisfy criteria 5, for which a number of approaches have been suggested. [16, 24-25] These include using local magnetic field gates beneath each fullerene to control the magnetic environment of N@C_{60} element in a two dimensional solid state array. The first significant step towards fabricating a working device based on this approach has been made by electrical read out of magnetic spin excitations in a single N@C_{60} molecule.[26] Possibly the simplest multi qubit readout/measurement approach, especially for small array sizes, is based on utilising the difference in transitional frequencies found in different similar molecular qubits such as ^{14}N@C_{60}, ^{15}N@C_{60} and ^{31}P@C_{60} to create an hetero-endohedral fullerene array of individually addressable qubits.[27-29]

1.2 An introduction to N@C_{60}

Nitrogen atom-based endohedral fullerenes are structurally similar to the noble gas endohedral fullerenes,[30-31] in that the endohedral atom is located at the centre of the fullerene cage. What makes the nitrogen analogue remarkable is the ability of the fullerene cage to contain an extremely reactive atom such as nitrogen without forming any chemical bonds to it, behaving as a chemical analogue of an ion trap. This results in paramagnetic molecules with very unusual electron spin properties that are ideal candidates for use in applications such as electron spin based QIP.

1.2.1 Synthesis

A number of different techniques have been utilised for the synthesis of N@C_{60}. A common requirement for all methods is the acceleration of N^+ ions towards a fullerene cage to achieve nitrogen implantation, with the optimum acceleration of the N^+ ions consistently found to be around 40 eV. All systems also use an effusion cell to sublime the empty fullerene starting materials either onto a target or into the path of the N^+ ions.

Commercial ion source method.

The first report of the synthesis of N@C_{60} was made by Murphy and co-workers in 1996.[32] Their production method used a commercial ion source to bombard a thin film of deposited C_{60} with nitrogen ions. Using this method, both ^{14}N@C_{60} and ^{15}N@C_{60} were detected and selectively produced using a modified N_2 isotope ratio feed gas source. The above method for ion implantation was subsequently modified to allow continuous deposition of C_{60} on to the target by utilising an effusion cell to sublime C_{60} on to the target (see Figure 1.1). The optimised parameters of the ion beam energy and beam current were found to be 40 eV and 50 μA respectively, producing a yield of N@C_{60} in C_{60} of 10^{-4}-10^{-5} (10-100 ppm).[33] To date, this method remains the most widely used technique to synthesise nitrogen encapsulated fullerenes due the combination of good yields and large mass of implanted material that can be produced at a time (up to 500 mg of soluble fullerenes).

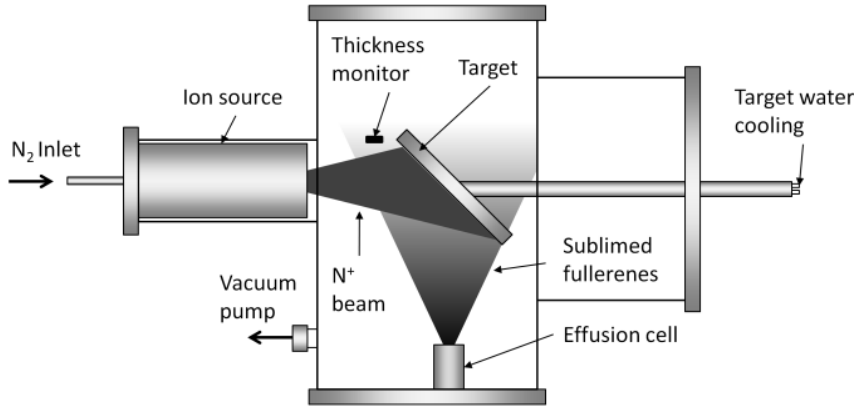


Figure 1.1 Schematic view of nitrogen implantation apparatus using a commercial ion source.

Glow discharge

Murphy and co-workers also demonstrated a second, lower cost method for the production of N@C_{60} using a glow discharge reactor (see Figure 1.2)[34]. The drawback to this technique is the low purity that N@C_{60} is produced in, about 5 ppm in C_{60}. Conditions for the production of N@C_{60} using the glow discharge technique were later optimised by Ito *et al.* to produce N@C_{60} in a 15 ppm yield.[35] However, while this represents a significant improvement on Murphy's work, the production yield still remains lower in comparison to the commercial ion source method.

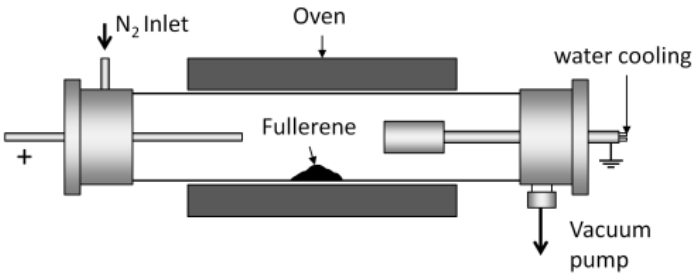


Figure 1.2 Schematic view of a glow discharge reactor

R.F. plasma method

In 2002, Huang and co-workers reported the formation of N@C_{60} from a radio frequency (rf) plasma. The set-up uses a capacitively coupled plasma system, incorporating a 13.56 MHz plasma generator.[36] The plasma is generated from within the evacuated chamber using the partial atmosphere of nitrogen as the source of N^+ while C_{60} is introduced by evaporation from an effusion cell (see Figure 1.3). This technique was optimised to produce a yield of N@C_{60} in C_{60} of between 200-500 ppm,[37] which remains the highest yield reported to date. Using this method, N@C_{60} was only reported to be recovered from

the outer casing of the chamber with all of the material deposited on the cathode completely insoluble in CS_2, suggesting that the cages were seriously deformed at the cathode surface.[38] To reduce the destruction of the fullerene species, an external ring electrode arrangement was trialled (see Figure 1.3). However, this method failed to yield any measurable amount of $N@C_{60}$. This was attributed to insufficient acceleration of the N^+ towards the fullerene in (b). While in (a) this acceleration is present from the natural negative self-bias of the cathode.

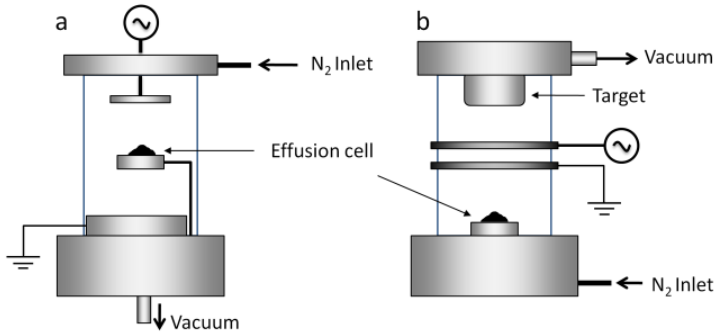


Figure 1.3 (a) Schematic of the internal parallel plate electrode arrangement of the capacitively coupled RF plasma implantation method. (b) External ring electrode arranged capacitively coupled plasma implantation system, equipped with two external ring electrodes.

Electron cyclotron resonance method

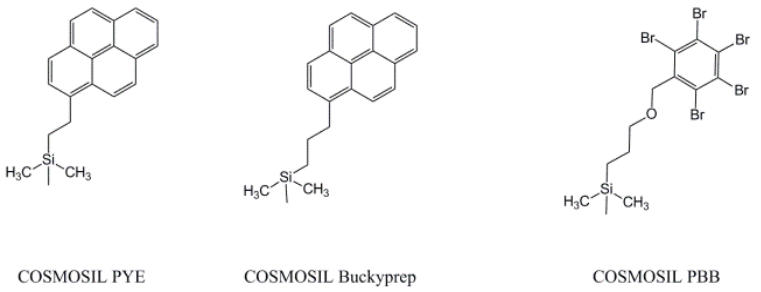
Electron cyclotron resonance has also been used to effectively create a nitrogen plasma. Similar to the commercial ion source method, the energy of the incident N^+ on the C_{60} target can be optimised using an electric field gradient between the plasma and the target. The optimal beam energy of 40 eV is in agreement with the value identified by Murphy *et al.*[39] It was then subsequently shown that by introducing radial as well as axial magnetic confinement to the plasma, the electron temperature can be increased by a factor of three to 30 eV.[40] Using the relative intensities of optical emission spectra for the excited nitrogen species, Kaneko and co-workers showed that increasing the electron temperature significantly raised the proportion of N^+ and N^* species compared to N_2^* exiting the plasma generation region, leading to a maximum yield of $N@C_{60}$ in C_{60} of 300 ppm.[40]

1.2.2 Purification

Purification remains one of the biggest challenges to the synthesis of endohedrally-doped nitrogen fullerenes due to the almost complete chemical and physical indistinguishability of $N@C_{60}$ with C_{60}. The most common method for purification uses HPLC (High Pressure Liquid Chromatography) to exploit the larger polarisability and slightly larger mass of nitrogen doped endohedral fullerenes compared to the empty fullerene analogue. This effect causes endohedral molecules to have a greater interaction with the HPLC column's stationary phase causing it to elute at a slightly later time compared to C_{60}.

The enrichment of $N@C_{60}$ using HPLC has been demonstrated using a range of HPLC columns such as Pyren[33], Buckyprep[41], PYE[41] and PBB,[42] (see Figure 1.4 for structure) with the separation of elution time between C_{60} and $N@C_{60,}$ calculated from the ESR signal intensity distribution recorded from consecutive aliquots sampled from within the $N@C_{60}/C_{60}$ peak.[33] The most efficient protocol for the enrichment of $N@C_{60}$ uses a 5PBB column (i.e. a column packed with 5 μm silica beads functionalised with PBB), for which the retention time of $N@C_{60}$ is 3% longer than of $C_{60,}$ and a two stage purification process.[42] The first stage consists of single pass injections in which the C_{60}/C_{70} peak is split into two at its apex. This process is repeated four further times, each time retaining and injecting the second fraction collected on the previous run. In the second stage, the enriched material is injected and recycled 12 times as shown in Figure 1.4 and the $N@C_{60}$ peak is collected. This recycling procedure is repeated a further two times on the $N@C_{60}$ peak to isolate pure endohedral fullerene material (see insert of Figure 1.4.b). It has also been shown that the separation of $N@C_{60}$ from the parent C_{60} peak increases proportionally with the ratio of hexane to toluene used as the eluent.[41] Purification using an iterative HPLC approach has been used successfully by a handful of groups to isolate $N@C_{60}$ with a purity of up to 99.5%. [42-44]

a



b

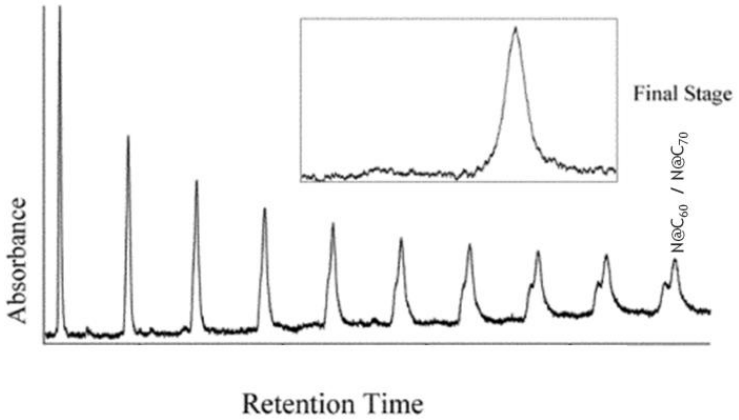


Figure 1.4 (a) Chemical structure of the HPLC column stationary phase commonly used to purify N@C_{60}. (b) The recycling HPLC profile for the 2nd stage of N@C_{60} purification using a 5PBB column, showing separation of C_{60} from N@C_{60}.[42] The inset shows the final cycle from the following stage containing pure N@C_{60}.

1.2.3 Physical properties

N@C_{60} is a black solid, identical to the empty fullerene. There is however still a debate over the exact UV-Vis absorption profiles as they have been reported as being both identical to the empty fullerene[43] or containing weaker absorption peaks in the 440-640 cm^{-1} region.[42] Either way, the absorption profile is very similar to that found for the empty fullerene, with no additional absorption peaks present.

Electron Spin Resonance

The most fascinating and unique feature of N@C_{60} is the combination of the highly symmetric central location of the nitrogen atom within the fullerene cage[45] together with negligible mixing between the nitrogen atom and carbon atom electronic wave functions. This environment imparts a degree of isolation to the nitrogen atom usually only attainable using an ion trap and permits the nitrogen centre to retain the same $^4S_{3/2}$ electron spin ground state[46] present in gas phase $N^{\cdot}$. The upshot of this is that the higher symmetry N@C_{60} molecules have an extraordinarily long electron transverse relaxation time (T_2) of up to 250 μs,[47] the longest coherence time reported for a molecular system.

The ESR spectrum of $N@C_{60}$ is dominated by an isotropic hyperfine interaction between the $^4S_{3/2}$ electron spin ground state and the ^{14}N or ^{15}N nuclear spin of I= 1 or $\frac{1}{2}$, respectively. By considering only the first-order hyperfine interaction, the allowed electron transitions are triply degenerate, as illustrated in Figure 1.5. This causes the observed continuous-wave (CW) EPR spectrum of $^{14}N@C_{60}$ and $^{15}N@C_{60}$ dissolved in toluene at room temperature to comprise of three or two sharp resonance peaks respectively (see Figure 1.6), corresponding to each of the allowed nuclear spin states. Each of the ESR resonances is extremely narrow. Their intrinsic linewidth has been measured to be less than 0.3 μT,[47] with the observed linewidth often limited by inhomogeneous broadening caused by the magnet stability and field homogeneity of the spectrometer.

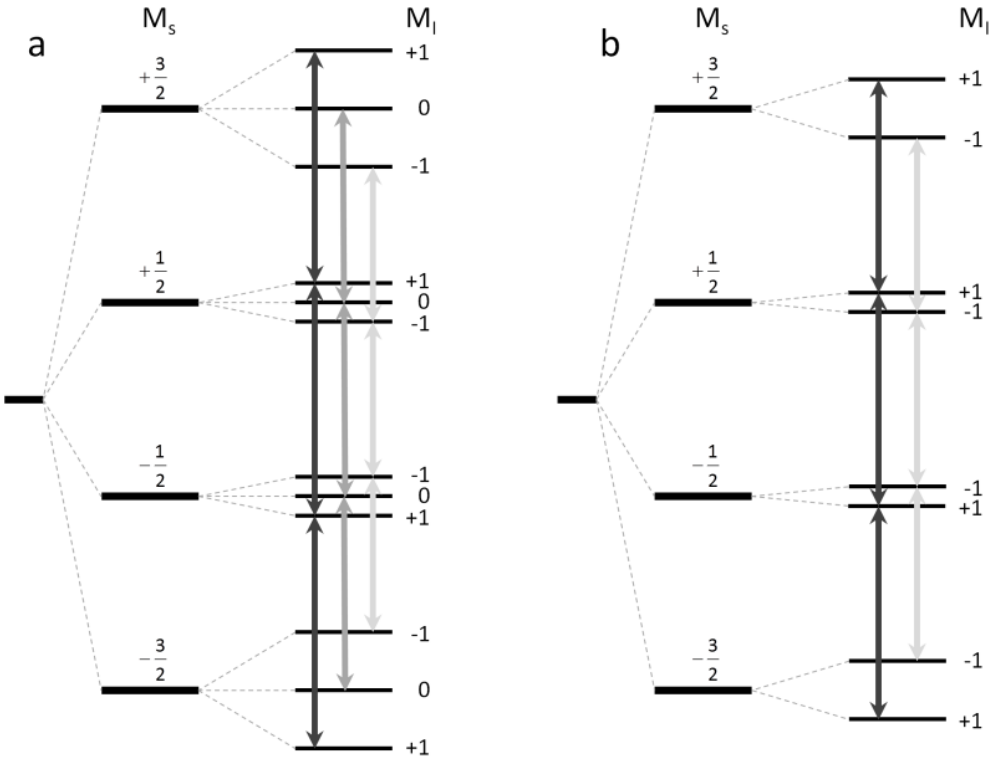


Figure 1.5 Energy level diagrams of (a) $^{14}N@C_{60}$ and (b) $^{15}N@C_{60}$ in a static magnetic field. $^{14}N@C_{60}$ and $^{15}N@C_{60}$ have a nuclear spin of I=1 and I=$\frac{1}{2}$ respectively. In a magnetic field, Zeeman splitting gives rise to a 12-level structure in $^{14}N@C_{60}$ and an 8-level structure in $^{15}N@C_{60}$. By considering only the first-order hyperfine interaction and the selection rules $\Delta M_S = 1$ and $\Delta M_I = 0$, the allowed transitions are triply degenerate (indicated as different shades of gray).

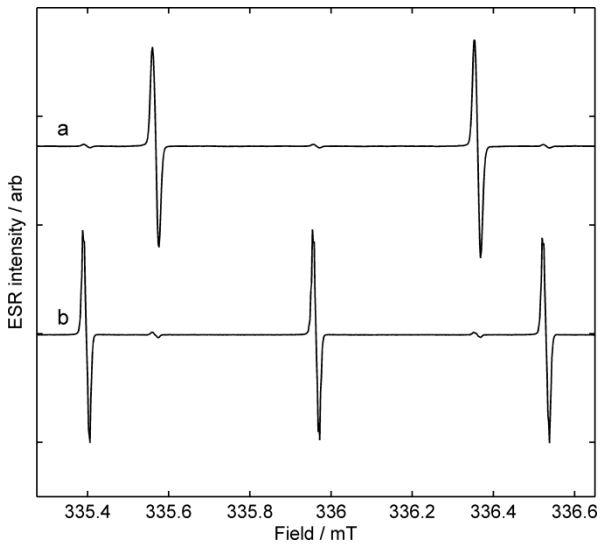


Figure 1.6 Comparison of room temperature solution based CW ESR spectra of (a) $^{15}N@C_{60}$ and (b) $^{14}N@C_{60}$. Spectra collected using toluene as the solvent and the following parameters: Modulation amplitude 200 mG microwave attenuation 30dB (50 μW microwave power).

Stability

The thermal stability of $N@C_{60}$ was the first decay parameter to be investigated. Weidinger *et al.* recorded the in-situ ESR spin signal dependence as a function of temperature of a low purity oxygen-free $N@C_{60}$ sample in both a solution of chloronaphthalene and in a powder.[48] The results indicated that in both solid and solution appreciable decomposition of $N@C_{60}$ only occurred at temperatures higher than 480 K with the decomposition rate increasing with temperature. This corresponds to a low escape energy of only 1.7 eV, far less than recorded for other endohedral fullerenes such as $He@C_{60}$. A proposed mechanism for the escape of the nitrogen via an internal azabridge is proposed and outlined in Figure 1.7. The positive correlation between external pressure and thermal stability[49] also supports the proposed nitrogen escape mechanism.

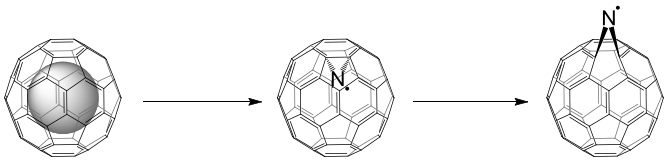


Figure 1.7 Weidinger and co-workers proposed mechanism for the escape of nitrogen from the fullerene cage. Initially, an internal azabridge is formed which then inverts and bonds exohedrally to the cage.[50]

The photostability of $N@C_{60}$ has also been investigated by a number of groups, however the exact decay mechanism(s) remain to be determined. It has been shown that pulsing a low purity $N@C_{60}$ and $N@C_{70}$ toluene solution with a 355 nm Nd:YAG laser results in the deterioration of the ESR signal.[51] Goedde *et al.* used the observed relative decay rates of $N@C_{60}$ and $N@C_{70}$ as evidence that the decay was caused by vibrational excitation initiated by non-radiative relaxation of the excited triplet molecular species to the electronic ground state. This mechanism would also explain the observation that when oxygen (known to efficiently quench the triplet excited state of fullerenes) is present in the solvent of the endohedral fullerene solution the photostability is significantly enhanced.[52]

1.2.4 Chemical derivatives of $N@C_{60}$

Comparison of chemical reactivity with C_{60}

Due to the isolation of the fullerene and nitrogen electronic orbitals in $N@C_{60}$, its chemical reactivity is ostensibly identical to that of C_{60}. The principal consideration that must be made when attempting chemical functionalization of nitrogen doped fullerenes is their reduced thermal and photostability compared to the empty fullerene analogues. This often means that modification of the synthetic protocols used for empty fullerene is required to minimise the exposure of $N@C_{60}$ to elevated temperatures. Additionally, the restricted availability of highly enriched nitrogen doped endohedral fullerenes means that the reaction scale that can be used lies within a few tens of micrograms rather than the multi-gram scale which is possible for empty fullerenes. This makes purification and characterisation non trivial and consequently relatively few examples of chemical derivatives of endohedral nitrogen fullerenes exist to date.

Exo ring-adducts

Cyclopropane exohedral adducts

The first example of successful functionalization of $N@C_{60}$ was published by Hirsch and co-workers in 1997 using a Bingel type nucleophilic cyclopropanation reaction (see Figure 1.8.a).[34] The reactivity of

$N@C_{60}$ is reported to be identical to C_{60} along with no measureable spin loss after the functionalization reaction. The ESR spectra of the mono-adduct shows the presence of extra spectral features due to the lowering of the cage symmetry. Hirsch and co-workers went on to synthesise the hexa-adduct analogue of the above $N@C_{60}$ derivative (see Figure 1.8.b) using an analogous protocol.[53] An ESR study of the hexa-adduct shows the effect of increasing the cage symmetry compared to the mono adduct raises the T_1 and T_2 coherence times by a factor of two;[53] illustrating a potential benefit of using a multiply substituted $N@C_{60}$ derivative to create $N@C_{60}$ dimers for use in quantum computation systems.

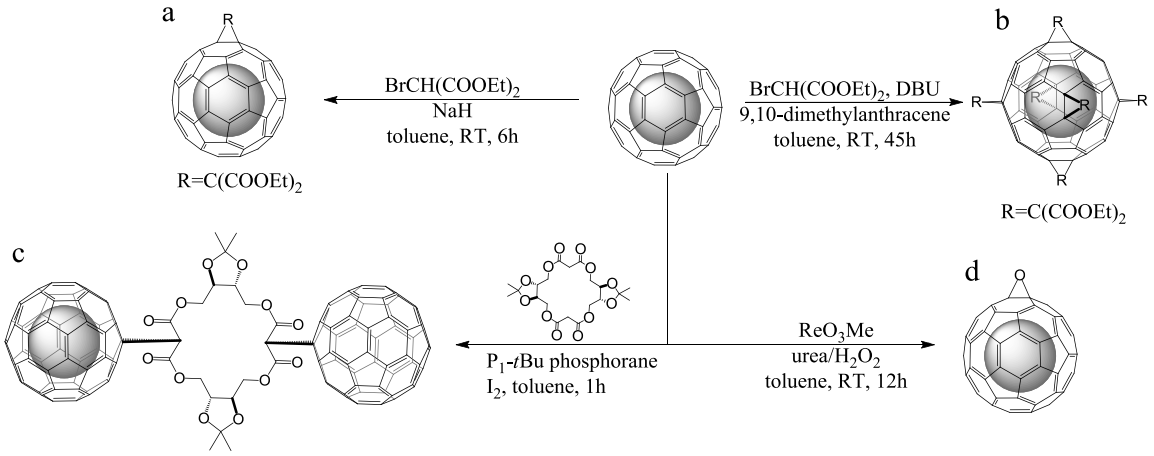


Figure 1.8 Examples of reaction schemes used to synthesise cyclopropane derivatised $N@C_{60}$ molecules. a[53],b[53], c[54]and d[55].

A bis-cyclo propane adduct has also been used to form a semi-rigid $N@C_{60}$-C_{60} dimer molecule using hindered phosphazene base *tert*-butyliminotris(dimethylamino)phosphorane (P1-*t*Bu) and iodine to reduce both the formation of charged fullerene salts and the reaction time[54] (see Figure 1.8.c). Despite using these optimised conditions, the $N@C_{60}$ purity was reduced by 50% after the reaction. This result combined with the rapid decomposition of $N@C_{60}O$ (see Figure 1.8.d) seen at temperatures sufficient for spontaneous opening of the epoxide ring to occur to form a biradical suggest an instability of $N@C_{60}$ to radical and charge formation on the fullerene cage.[55]

Pyrrolidine exohedral adducts

The most widely used method to functionalise $N@C_{60}$ is using a Prato 1,3-dipolar cycloaddition to create an exohedral five membered pyrrolidine ring adduct[56] (see Figure 1.28 for reaction mechanism).

This method has gained popularity for two reasons. The reaction is a “one pot" reaction and is compatible with a wide variety of aldehyde and amino acid precursors allowing specific functionality to be introduced easily. Additionally, the reaction has been proven to conserve a relatively high proportion of N@C_{60} spin centres, ranging between 70-80%, in the functionalized product with good long term stability when kept in the dark and at room temperature. Figure 1.9 gives an overview of the type of N@C_{60} pyrrolidine derivatives that have been synthesised to date, most of which use the readily available methyl-glycine amino acid as a reaction precursor.

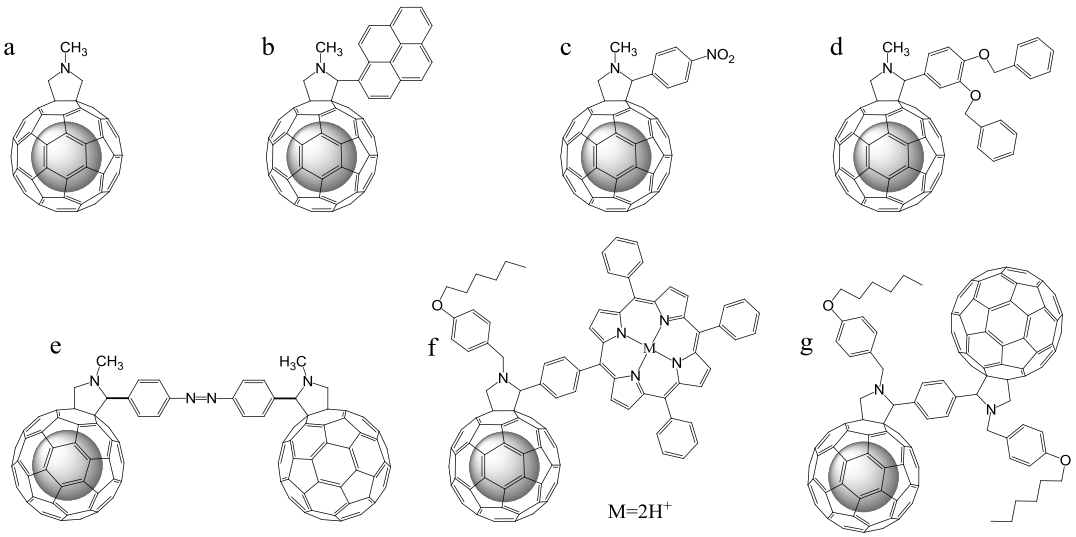


Figure 1.9 Examples of the variety of N@C_{60} pyrrolidine derivatives that have been synthesised using a Prato 1,3-dipolar cycloaddition. a[57], b[52], c[58], d[57], e[59], f[60], g[29].

ESR studies

Solution state CW ESR spectra of functionalised N@C_{60} look almost identical to pristine N@C_{60} due to the rapid tumbling of the molecule on the time scale of the measurement. However, given a suitably high resolution spectrometer, it is possible to observe a slight broadening of the hyperfine lines caused by electron-nuclear coupling to the protons attached to the adduct.[53] When the motion of the fullerene is restricted by either measuring the CW ESR in a solid state or frozen solution, the effect of the distortion of the fullerene cage can be seen by the appearance of satellite peaks adjacent to each of the hyperfine lines caused by the presence of additional transitions due to ZFS (see Figure 1.10). The

size of the axial ZFS component (D) has been shown to lie within the range of 6-17 MHz with the rhombohedral distortion (E) much smaller at between 0.4-0.9 MHz.

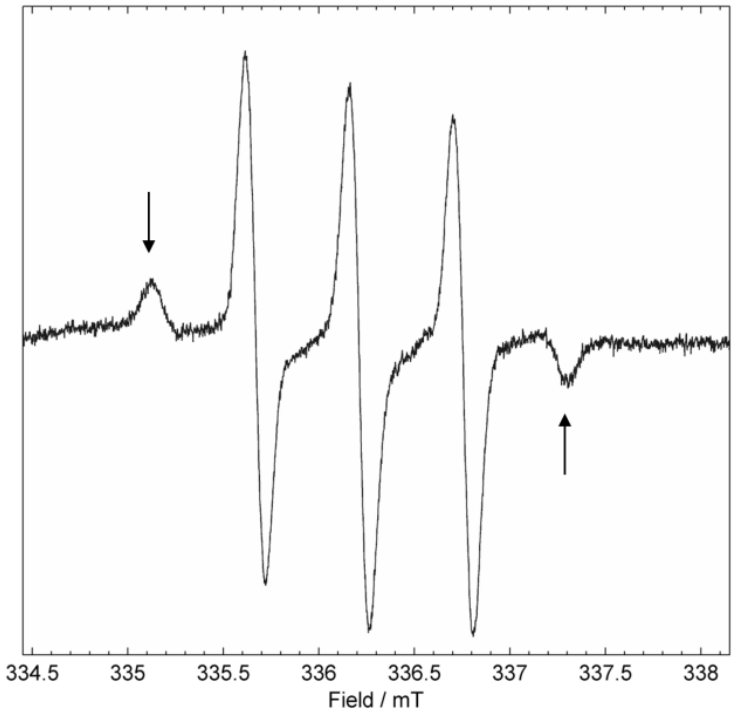


Figure 1.10 Frozen solution (77K) CW ESR spectrum recorded from a $^{14}N@C_{60}$ pyrrolidine adduct. The additional peaks due to zero field spitting (ZFS) are clearly visible (indicated by arrows). Spectra collected using a modulation amplitude of 0.6 G and a microwave attenuation of 35dB (16 μW microwave power).

A clear correlation between the size of ring formed between $N@C_{60}$ and different adducts on the ESR ZFS magnitude is shown in Table 1.1. The trend shows an increase in ZFS going from 3-4-5 membered ring exo-adducts formed with the fullerene cage. This observation was rationalised by considering the overlap of the exohedral bonds with the radial *p* orbital of the fullerene.[57] As the overlap increases, the proportion of fullerene electron density shifted to the substituent also increases, leading to a greater perturbation of the environment of the nitrogen atom and therefore to a larger ZFS parameter.

Molecule	Exohedral ring size	A_{iso} / MHz	D / MHz	E / MHz
$^{14}N@C_{60}$		15.73[46]	-	-
$^{15}N@C_{60}$*		22.35[61]		
$^{14}N@C_{70}$		15.00[53]	5.5[47]	-
1.8.c[54]	3	15.73	8.6	0.45
1.8.d[55]	3	15.45	6.6	0.5
1.8.a[53]	3	-	6.1	0.45
1.48.b[62]	4	15.55	14	0.56
1.9.a[57]	5	15.95	16.4	0.4
1.9.b[52]	5	$A_{yy/xx}$=16.44, A_{zz}=14.7	16.75	0.93
1.9.c[58]	5	$A_{yy/xx}$=14.2, A_{zz}=18.5	17	0.8
1.9.d[57]	5	15.95	17.2	0.6
1.9.e[59]	5	$A_{yy/xx}$=14.6, A_{zz}=18.6	16.1	0.7
1.9.f[60]	5	-	16.3	0.4
1.9.g*[29]	5	A_{xx} = 22.6, A_{yy} = 21.7, A_{zz} = 22.0	14.6	0.56

Table 1.1 Electron spin environment of chemically functionalized $N@C_{60}$ derivatives. All derivatives use $^{14}N@C_{60}$ apart from of those marked with an (*), which use $^{15}N@C_{60}$.

Stability

The thermal stability of $N@C_{60}$ adducts has been shown to vary for different derivatives. The cyclopropane linked adduct shown in Figure 1.8.a has a similar stability compared to pristine $N@C_{60}$, decomposing at around 500 K[63] with the stability increasing when multiple adducts are present (as in Figure 1.8.b) to provide stability up to 570 K.[63] Pyrrolidine derivatives such as described in Figure 1.9a-d however decompose rapidly[57-58] above 410 K. DFT simulations of the reaction coordinate for the escape of nitrogen from both ring sizes (see Figure 1.11) show that the energy for formation of an adduct with the inside of the cage and subsequent flip from endo-nitrogen to exo-nitrogen has a significantly lower activation barrier for the pyrrolidine derivative compared to a cyclo propane analogue owing to the difference in ring size formed in the transition state.[64]

The photostability of N@C_{60} derivatives shows a behaviour similar to their thermal stability. Pyrrolidine groups accelerate the photodecomposition by more than an order of magnitude compared to pristine N@C_{60}, while cyclopropane derivative show comparable stability to N@C_{60}.[52]

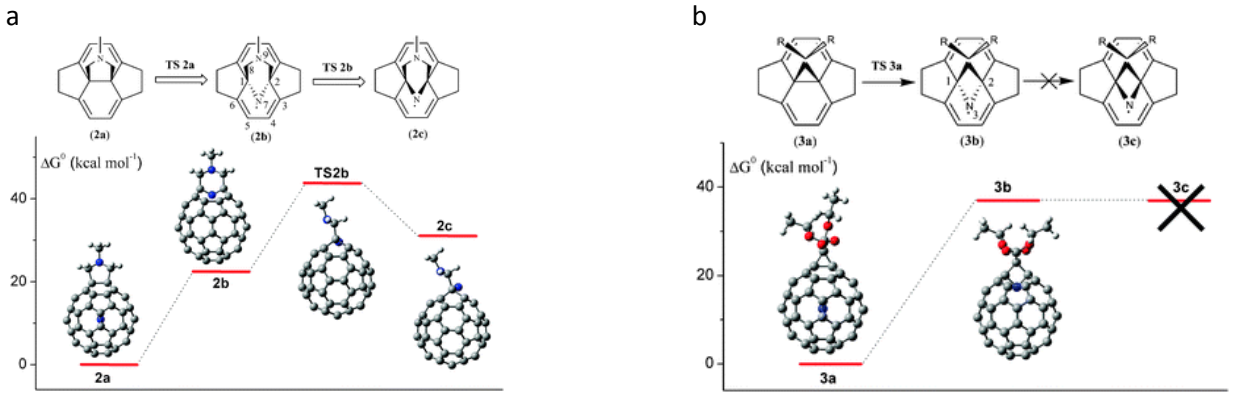


Figure 1.11 DFT simulated reaction coordinates for the escape of nitrogen from the fullerene cage when attached with either (a) a pyrrolidine ring or (b) a cyclopropane ring. Reproduced from Lui *et al.*[64]

1.3 C_{60} dimers

One method to create a controlled coupling between N@C_{60} centres is to chemically link the molecules. Owing to the identical reactivity of N@C_{60} and C_{60}; I will now provide an overview of the key areas of the vast body of work that has been undertaken in the synthesis of covalently linked C_{60} molecules, in particular focusing on linking two fullerenes together to form a 'dimer'.

1.3.1 Directly bonded dimers

The simplest and most naturally abundant C_{60} dimer is $(C_{60})_2$ Experimental and theoretical studies have shown that the most energetically favourable bonding mechanism between two C_{60} molecules is a [2+2]cycloaddition between short (6,6) bonds on adjacent fullerenes. This creates a square four-membered ring link between the two molecules, giving the structure D_{2h} symmetry (see Figure 1.12).[65] The most effective method of $(C_{60})_2$ synthesis uses a solid state mechano-chemical scheme, whereby KCN is added to solid C_{60} and reacted using a high speed vibrational milling technique.[66] The exact mechanism by which the dimerisation reaction proceeds is still debated and is thought to occur via

either a nucleophilic addition or an electron transfer step.[65] $(C_{60})_2$ is sparingly soluble in a number of organic solvents and readily forms dark brown crystals. The dimer has moderate thermal stability, fully decomposing to C_{60} at 175 ^{o}C after 15 minutes, decaying slowly under ambient light and immediately reverting back to C_{60} on electrochemical reduction.[66]

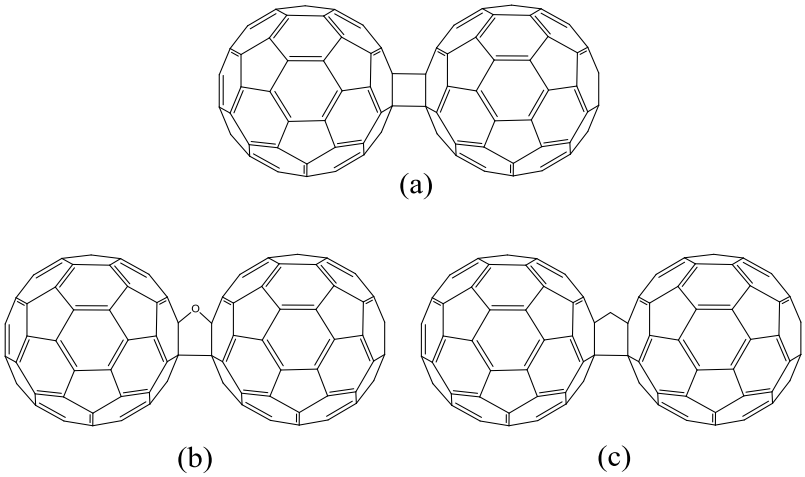


Figure 1.12 Most studied directly bonded fullerene dimers: (a) $(C_{60})_2$,[66] (b) $(C_{60})_2O$[67] and (c) $(C_{60})_2(CH_2)$.[68-69]

The naturally occurring fullerene dimer $(C_{60})_2O$ has also been extensively characterised. It is found when solid state C_{60} is kept under ambient conditions, in up to 1% abundance. It has been proposed to form when an $C_{60}O$ epoxide is thermally excited and adds across the (6,6) bond of an adjacent C_{60} molecule through a [2+2]cycloaddition.[67] X-ray characterisation of the dimer confirms its structure. Electrochemical study of $(C_{60})_2O$ shows that the reduction of the cage occurs in two different waves as an electron is added to each cage, indicating that the two fullerene conjugated systems could have significant overlap across the oxide bridge. An all-carbon analogue of $(C_{60})_2O$, $(C_{60})_2CH_2$, was discovered at the same time, being produced under the same conditions (heat and an excess of C_{60}) using $(C_{60})CH_2$ as a precursor instead of $(C_{60})O$ (see Figure 1.12).[68-69]

1.3.2 Dumbbell dimers

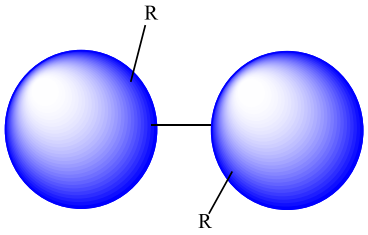


Figure 1.13 General structure of dumbbell dimers formed by radical addition.

The next level of complexity for the construction of fullerene dimers uses radical recombination of two $RC_{60}^{\bullet}$ (R= alkyl fluoroalkyl, halo or H) species to create a fullerene dumbbell structure (see Figure 1.13).[70] From observing the positive correlation of radical ESR signal and temperature, it was suggested that the dimer structure exists in equilibrium with the monomeric radicals. By studying the correlation of signal intensity with temperature and dilution with fixed temperature, the position of the equilibrium was assessed when different R groups were present. The bond strength calculated from the equilibrium measurements showed a dependency between the strength of the bridging C-C and the size of the R substituent.[71] The rotation about the inter-cage bond has been studied by Osawa *et al.* using a series of different sized R substituent ($RC_{60}C_{60}R$, R = H, Me, *t*-Bu).[72] Their findings show that the more sterically demanding *gauche* conformation of the bulky *t*-Bu substituted dimer is in fact the most stable (see Figure 1.14). The unexpected stability was ascribed to an effect that was particular to single C-C bond linked fullerene dimers.[72]

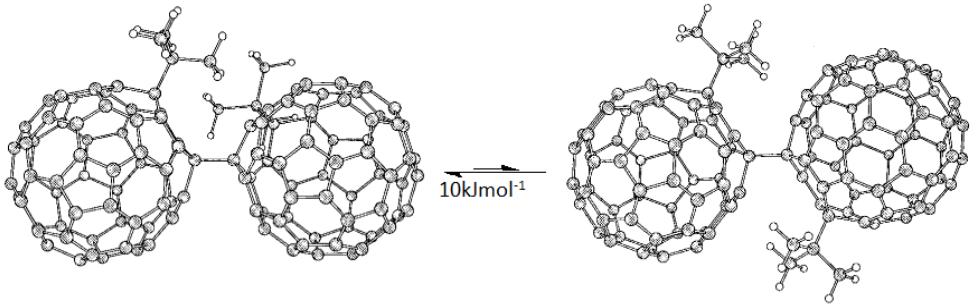


Figure 1.14 Model showing the position of equilibrium of the gauche and trans rotamers of (C_{60}*t*-Bu)$_2$.Reproduced from Osawa *et al.*[72]

Dumbbell dimers with bridging lengths greater than those found in the RC_{60}-$C_{60}R$ dimers have been created using mono- and di-acetylene linking units by Komatsu *et al.* and Diederich *et al.* respectively. Komatsu *et al.* produced a dimer with a single acetylene linker using dilithioacetylene and C_{60} in refluxing toluene (see Figure 1.15.a). The di-anion was then treated with dodecyl-iodide in refluxing toluene to create the bis-*ortho* substituted dimer (see Figure 1.15.b). The dimer yield from this method was however particularly poor.[73] Cyclic voltammetry on this compound showed a single reduction peak indicating that the acetylene bridge does not facilitate any direct exchange through conjugation between the two fullerene centres.[73] The absence of electron exchange is further supported by the lack of additional features in the dimer's electronic spectra compared to the corresponding monomer.

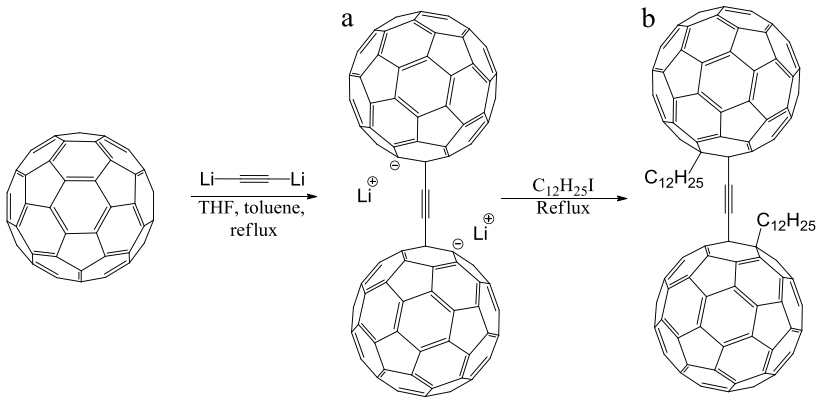


Figure 1.15 Mono acetylene bridged fullerene dimer, formed using dilithium acetylide and subsequent trapping of the dianion using an alkyhalide.[73]

Diederich *et al.* used a two-step method to form their buta-1,3-diynediyl bridged dumbbell dimer. Initially, a 1-1ithio-2-trimethyl-silyl-ethynyl-fullerene intermediate was formed selectively at a (6,6) bond of the cage via a nucleophilic addition of lithium-trimethyl-silyl-acetylide to C_{60}. After deprotection of the silyl group and quenching of the cage anion with H^+ or RBr, the monomers were homo-coupled using the Hay catalyst (CuCl-TMEDA-O_2) TMEDA = N,N,N′,N-tetra-methylenediamine in chlorobenzene to afford the target dimer structure shown in Figure 1.16.[74] As with the Komatsu dimer, the electrochemical reduction trace of the dimer suggested that negligible electronic interaction between the two fullerene cages was present.

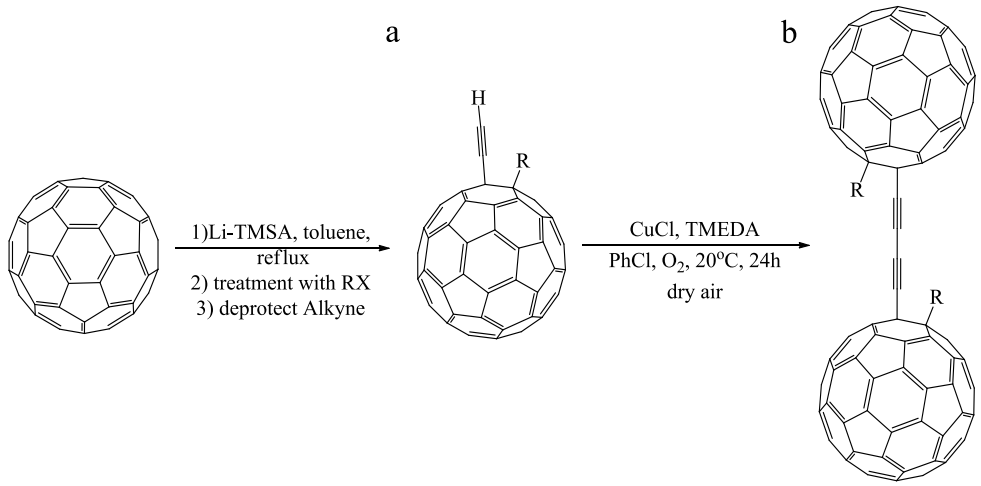


Figure 1.16 Two-step method for synthesis of buta-1,3-diynediyl bridged dumbbell dimer.[74]

Purely acetylene linked dumbbell dimers that use bridging units with greater than two diethynyl units have not been reported, possibly owing to the tendency of extended ethynyl molecular wire systems to polymerise and decompose. An example of this tendency to polymerise was reported by Abhijit *et al.* who showed that hetero-aromatic terminated octatetraynes units undergo cross-polymerisation via topo-chemical 1,2 additions at a temperature of 150° C and 198° C when the aromatic cap used was thiophene or quinoline respectively,[75] with the octatetrayne molecular wires undergoing significant decomposition after only a month of being stored under ambient conditions.

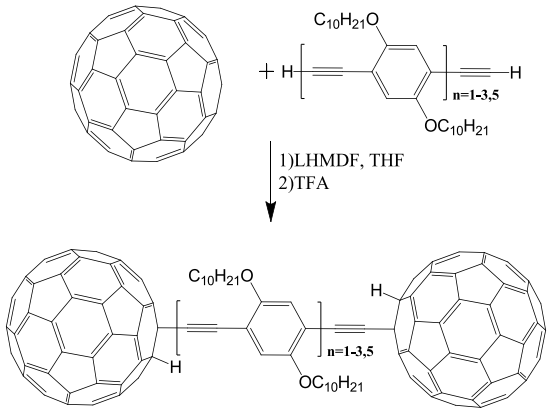


Figure 1.17 Synthesis of dumbbell dimers using oligo(*p*-phenylene-polyethylene)$_n$ (OPE) bridging units and an *in situ* lithium acetylide generation method.[75]

By synthesising dumbbell dimers using oligo(*p*-phenylene polyethynylene)$_n$ (OPE) bridging units of the form depicted in Figure 1.18, Tour *et al.* increased the maximum accessible separation of fullerene cages whilst maintaining many of the properties reported for the shorter acetylide dimers.[76] The OPE

bridging units were formed via two strategies[77] (see Figure 1.18). For n=2, OPE(2) the method scheme sequentially extended an asymmetrically protected 1,4-dialkynldialkoxybenzene unit (b) by selective alkyne deprotection, followed by Sonogashira cross-coupling to the mono iodo-4-alkynyldialkoxybenzene unit (a). For n=3,5, however, the mono deprotected products (c) and OPE(2) respectively were coupled using standard Sonogashira conditions [$PdCl_2(PPh_3)_2$, CuI, Et_3N in THF] to a 1,4-diiododialkoxybenzene central unit to create the symmetric bis-adducts, OPE(3) OPE(5). All OPE units were then attached to fullerenes via their terminal acetylenes using a variant of the Komatsu *et al.* lithium acetylide addition reaction.[78] Tour *et al.* found that the previously reported method for lithium acetylide addition produced an unsatisfactory yield of dimer products. This led Tour to develop an *in situ* method for addition of the lithium acetylide species to C_{60} using lithium hexamethyldisilazide (LHMDS) in THF. UV-Vis characterisation of the OPE dimers showed a slight shift in the absorption profile compared to a simple sum of the profiles of the corresponding bridging unit and pristine C_{60}.

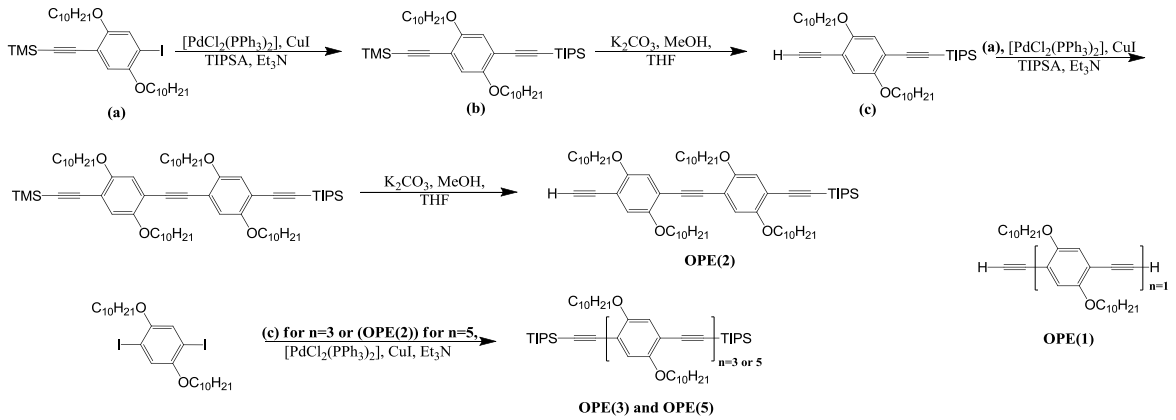


Figure 1.18 Synthetic strategy for the construction of long OPE bridging units used by Tour *et al.*[77]

This was suggested to be due to weak electronic interactions between the fullerene cage and the OPE backbone. However, the presence of only three reduction events in the cyclic voltammograms of the OPE dimers indicates that the π systems of the fullerene and OPE moieties do not overlap, a conclusion that is in agreement with the findings of previous studies. The third order non-linear properties and two photon absorption (TPA) cross sections of the OPE dimers were probed using femto second Kerr spectroscopy. The findings showed that the n=5 dimer has both an unusually large third order

hyperpolarisibility and TPA cross sections. This was suggested to be caused by either a periconjugation or charge transfer from the OPE to fullerene in the excited state.

Using a similar approach as Tour *et al.*, Zhou and co-workers synthesised a number of dumbbell dimers using different length OPE bridging units.[79] In contrast to Tour's work, the OPE precursors created by Zhou contained central poly-acetylene units which range from butadiyne to dodecahexayne size. The thermal stability and tendency of the OPE dumbbell dimers to form topo-chemical cross-coupled arrays in the solid state were explored using differential scanning calorimetry (DSC), UV-Vis spectroscopy and atomic force microscopy. The DSC scan of dimer [Figure 1.19.*b, n=1*] showed no decomposition/polymerisation feature until above 150° C compared to the OPE precursors which are unstable at ambient conditions.

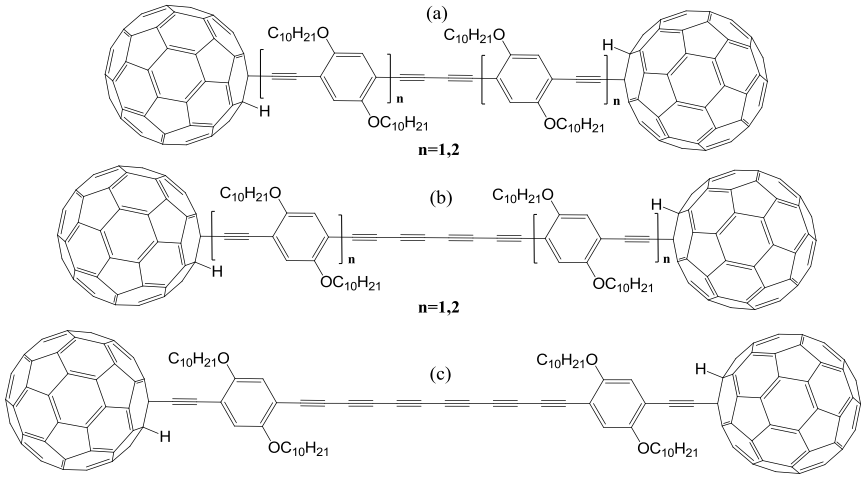


Figure 1.19 Structure of extended acetylene bridged OPE fullerene dimers created by Zhou *et al.*[79]

The UV-Vis absorption profiles at 135° C and 160° C support the assignment of the feature at 150° C to an acetylene decomposition event, with the higher thermal stability of the dimer versus the OPE precursor assumed to lie in the increased steric bulk of the fullerene cages. Annealing of a thin film of the octatetrayne dimer at 160° C for 1 h on a mica surface led to the formation of a highly ordered array of nanospheres 15-20 nm high (see Figure 1.20). The authors noted that the longer dodecahexyne bridged dimer (Figure 1.19.c) was highly unstable even at room temperature.[80]

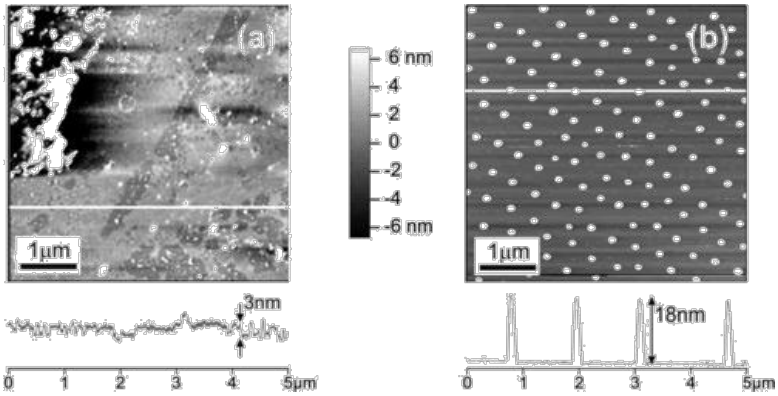


Figure 1.20 AFM images (5 μm × 5 μm) and corresponding height profiles of thin films of dimer [(b, n=1) of Figure 1.19]; (a) recorded before thermal annealing, and (b) after thermal annealing at 160 °C for 1 h. White lines indicate where the height profiles were recorded from. Reproduced from Zhou *et al.*[80]

1.3.3 Methanofullerene attached dimers

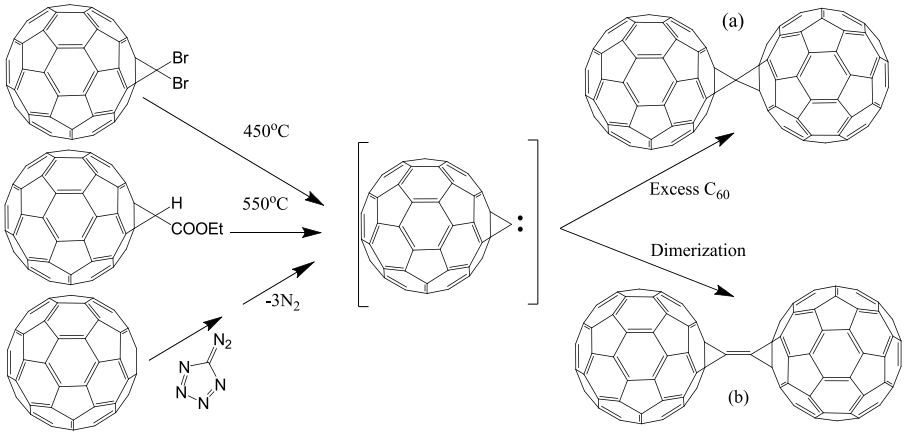


Figure 1.21 Synthetic approaches for creating the methanofullerene dimers (a) C_{60}-C-C_{60}[81] and (b) C_{60}-C_2-C_{60}[82]

The simplest fullerene dimers, which are attached using a cyclopropyl geometry, use a methanofullerene derived from either the carbene [1+2]addition, addition-elimination or [3+2]cyclysation then extrusion of N_2 [83] of a substituted methano molecule across the (5,6) bond of C_{60}. The methanofullerene derivative is then forced to undergo elimination to form a reactive methanofullerenecarbene intermediate. This intermediate carbene readily adds to either C_{60} to produce C_{60}-C-C_{60}, or to another methanofullerenecarbene to yield C_{60}-C_2-C_{60} (see Figure 1.21). Using diazotetraazole to form the intermediate carbene C_{60}C: Strongin *et al.* characterised C_{60}-C_2-C_{60}as a black solid which became a dark yellow solution when dissolved in toluene.[82] The spectroscopic study was consistent with the expected D_{2h} symmetry of C_{60}-C_2-C_{60}. Dragoe *et al.* showed that when using either $C_{60}CBr_2$ or $C_{60}CHCO_2Et$ as the carbene precursor, the ratio of C_{60}-C_2-C_{60} to C_{121} could be reduced by

increasing the excess of C_{60}. By using a 10-fold excess of C_{60}, the formation of C_{60}-C_2-C_{60} could be completely suppressed. Dragoe then went on to spectroscopically characterise C_{60}-C-C_{60}, confirming its C_{2v} symmetry.[81]

In 1992, Suzuki *et al.* reported that both *meta* and *para*-bis(diazo(phenyl)methyl)benzene bridging units could be used to form methanofulleroid dimers in good yield 39 % and 51 % respectively.[84] By adding the diazo compound to the fullerene suspended in toluene, the reaction proceeded at room temperature (see Figure 1.22). The authors reported that the broadness of the ^{1}H NMR spectra indicates that initially a number of isomers are present. However, after refluxing in toluene, the ^{1}H NMR spectra becomes well defined which is then assigned as a single isomer. Later studies predict that the resulting isomer is likely to be the thermodynamically most stable (6,6) fullerene isomer.[83, 85] Both dimers are brown-black solids which are sparingly soluble in most organic solvents and moderately soluble in CS_2. UV-Vis and electrochemical characterisation of both dimers were indistinguishable from that of the mono fulleroid analogue.

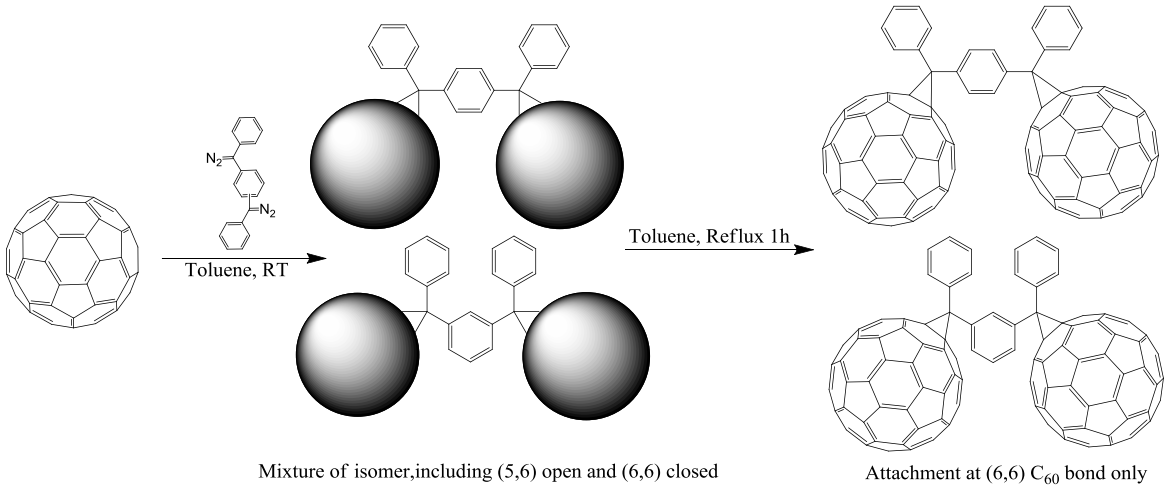


Figure 1.22 Methanofullerene dimer incorporating *meta* and *para*-bis(diazo(phenyl)methyl)benzene bridging units.[84]

In 2000, Knol *et al.* documented a more complete characterisation of a dimer very similar to Figure 1.22.[85] Addition of a solubilising alkoxy-substituent to the terminal phenyl addends (see Figure 1.23) showed the initially formed (5,6) open bis-fulleroid (36%) was characterised using ^{1}H NMR. After refluxing in ODCB the (6,6) closed dimer was recovered in 94% yield and characterised using both ^{1}H

and ^{13}C NMR, consistent with previous findings suggesting the greater thermodynamic stability of (6,6) closed bridged methanofullerenes over the (5,6) open analogue.[83] The main feature of Knol's article was to report the propensity for [2+2]cycloadditions between two cages in close proximity when irradiated by a sodium lamp. Upon irradiation, the (6,6) dimer converted to the final product (see Figure 1.23) with a 60 % yield, being characterised using ^{1}H , ^{13}C NMR and by comparison of UV-Vis data from another detailed study.[86] The [2+2]cycloaddition mechanism was proposed to occur via the triplet methanofullerene excited state, rationalised by the severe reduction of the yield when oxygen was introduced. The almost complete [2+2]cycloreversion after 15 minutes of refluxing ODCB found, is consistent with the behaviour reported for C_{120}.[65]

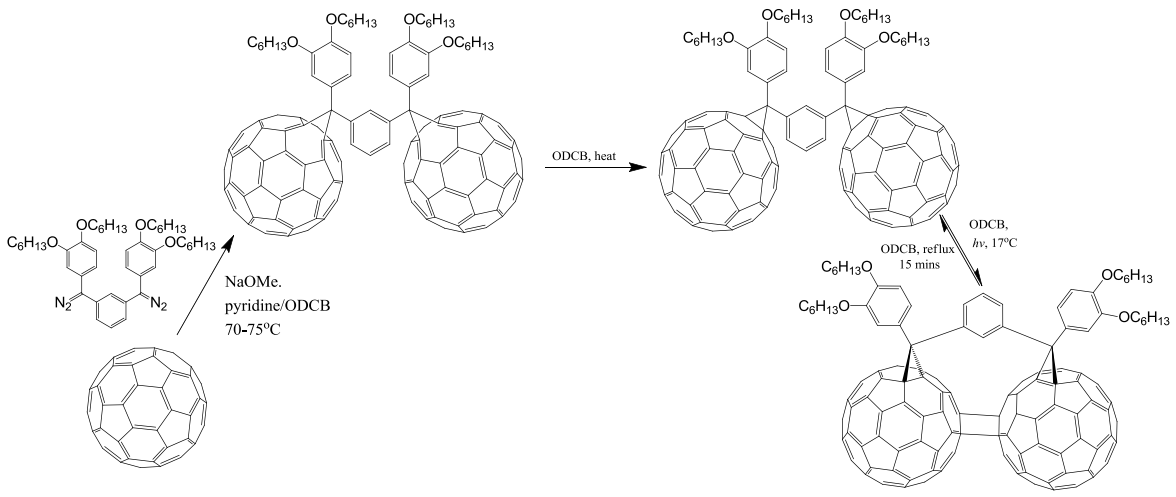


Figure 1.23 Synthesis of soluble benzene bridged dimer, showing a propensity for a [2+2]cycloaddition between the two fullerene cages when irradiated with a sodium lamp.[85]

A novel method for rigid methanofullerene dimer formation (see Figure 1.24) was realised through the self-assembly of two dipyridine functionalised fullerene monomers.[87] The incorporation of five diethyl malonate units onto the cages was shown to be sufficient to address the poor solubility of rigid fullerene dimers, allowing for the use of standard characterisation techniques. The Bingel reaction conditions (DBU at 20^{o} C) were used to attach all six substituents. The monomers were then reported to quantitatively form the dimer complex, depicted in Figure 1.24**,** within 5 minutes after the introduction of [*cis*-Pt$(PEt_3)_2(OTF)_2$]. The X-ray crystal structure solved for the dimer complex, shown in Figure 1.25, provides compelling evidence for its reported structure, with the high deviation from ideal

Pt(II) square-planar geometry of 90° to an angle of only 81.6° between N-Pt-N bonds highlighted as unusual.

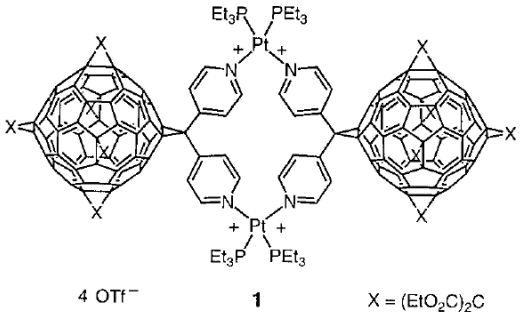


Figure 1.24 Bis-platinum bridged methano- fullerene dimer. Reproduced from Habicher *et al.*[87]

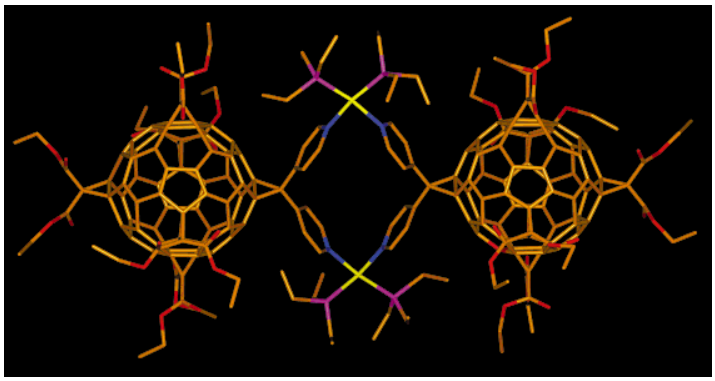


Figure 1.25 X-ray crystal structure of bis-platinum bridged methanofullerene dimer 1. Orange (carbon), red (oxygen), blue (nitrogen), yellow (platinum). Reproduced from Habicher *et al.*[87]

Using an acetylene molecular wire, Diederich and colleagues have created a cyclopropyl anchored dimer with an all-carbon bridging unit longer than one carbon double bond.[74] The method is based on a scheme developed by Rubin *et al.* whereby a trimethylsilylethynylmethanocarbene, generated from the corresponding tosylhydrazone, adds across a (6,6) fullerene bond.[88] Diederich however used an asymmetrical silyl protected analogue to allow for selective deprotection of only one of the two ethynyl functional groups. The resulting deprotected monomer is then homo-coupled using a Hay catalyst to produce the dimer shown in Figure 1.26, in a 37 % yield. The reported X-ray structure confirms the trans geometry and electron absorption spectra, indicating that minimal electronic interaction is present between the two cages.[89] Diederich *et al.* also highlight the appreciable solubility

of the dimer in organic solvents such as CS_2, toluene and cyclohexane compared to most other reported dimers.

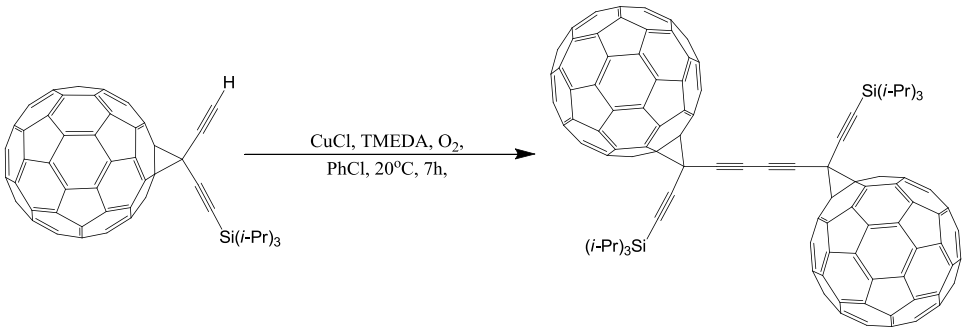


Figure 1.26 Dimer formation reaction using the Hay coupling condition with two acetylene terminated methanofullerene monomers.[89]

A novel example of an enantio-pure methanofullerene dimer was created by Segura *et al.* using an enantio 1,1'binaphthyl core.[90] The bridging unit precursor (Figure 1.27. a) was formed from a reduction of the enantio-pure bis-aldehyde.[91] The corresponding diazo-compound was then created *in situ* from the tosylhydrozone (Figure 1.27. a) using a Bamford Stevens protocol. The diazo intermediate was then attached to the fullerene species via a 1,3-dipolar cycloaddition[83] (see Figure 1.27). Cyclic voltammograms identified that the fullerene cages were electronically isolated from each other and confirmed the presence of two fullerene species.

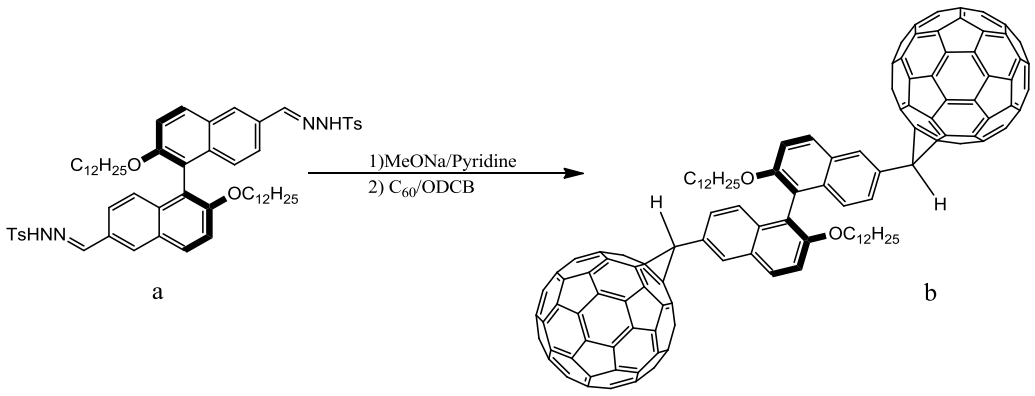


Figure 1.27 Rare example of enantio-pure methanofullerene dimer.[83]

1.3.4 Prato [2+3]cycloadditions

In 1993, Prato *et al.* showed the first successful addition of a pyrrolidine functional group to a C_{60} cage.[56] The reaction occurs via the [3+2]cycloaddition of an azomethane ylide that is generated *in situ* from an amino acid derivative and aldehyde (see Figure 1.28). As with most other cycloadditions, the ylide was found to exclusively add across the (6,6) fullerene bonds, producing monoadducts with only one regioisomer, in good yield and excellent thermal stability. Owing to the stability of pyrrolidine-fullerene species and compatibility of the reaction with a large number of different amino and aldehyde precursors, the Prato reaction has become one of the most popular methods of exohedral functionalisation of C_{60} and higher fullerenes. As a result, the reaction has been widely employed in the synthesis of fullerene dimer systems.

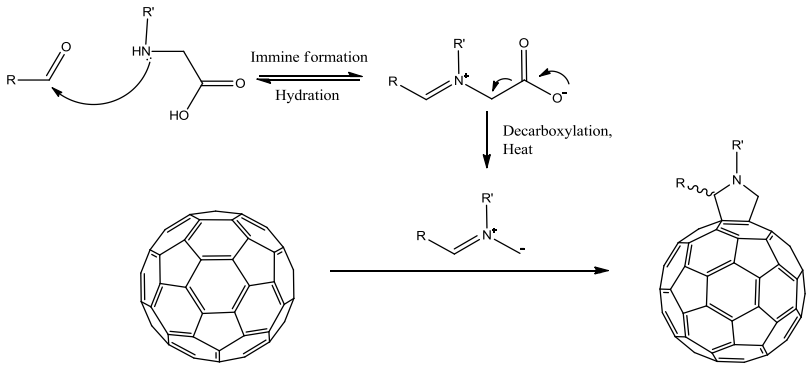


Figure 1.28 General mechanism for a [3+2]cycloaddition of an azomethane ylide to the (6,6) bond of a fullerene, known as the Prato reaction.

The first example of a dimer created using pyrrolidine functionalised C_{60} was reported by Martin and co-workers in 1996, using the procedure illustrated in Figure 1.29.[92] This dimer was also reported to be the first example of a fullerene dimer that incorporated a double donor bridging unit. The poor solubility of the dimer in organic solvents was highlighted, as was the incompatibility of the dimer with mass spectrometry. Cyclic voltammetry measurements suggested little interaction of the bridge with the fullerenes occurred in the ground state.

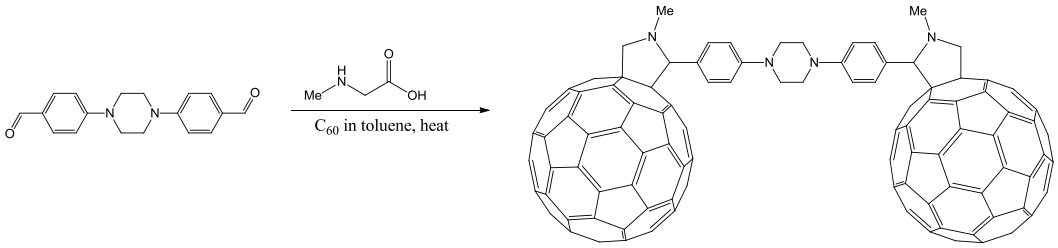


Figure 1.29 One-step reaction to form the first Pyrrolidine functionalised fullerene dimer.[92]

Soon after Nazario, Yongping and co-workers reported the first pyrrolidine dimer that was bridged via the nitrogen of the pyrrolidine ring.[93] Dimers with both *meta* and *para* attachment to the bridging benzene ring were created. The synthesis was accomplished in three steps as shown in Figure 1.30. The authors noted that both dimers exhibit only very minor deviations from the ground state near infra red (NIR) spectrum and first three reduction potentials of pristine C_{60}, attributing the deviations to solvation and cage proximity effects. The ESR spectra of the *meta* dimer dianion showed additional *triplet* satellite peaks which were assumed to be caused by intramolecular dipolar spin-spin coupling. These features were also weakly seen in the *para* dianion ESR spectra, suggested to be caused by intermolecular spin-spin coupling. The authors then went on to reassign the triplet feature to the formation of a bond between the two C_{60} as a triplet pattern with an identical hyperfine coupling parameter is seen in the corresponding ESR spectra[94] recorded from C_{60}^{2-}, possibly disproportionating into $(C_{60})_2^{2-}$. The possible formation of an intramolecular bond in the *meta* dimer is further supported by the results of the photochemical study of a similar dimer by Knol *et al.* highlighted earlier in this section.[85]

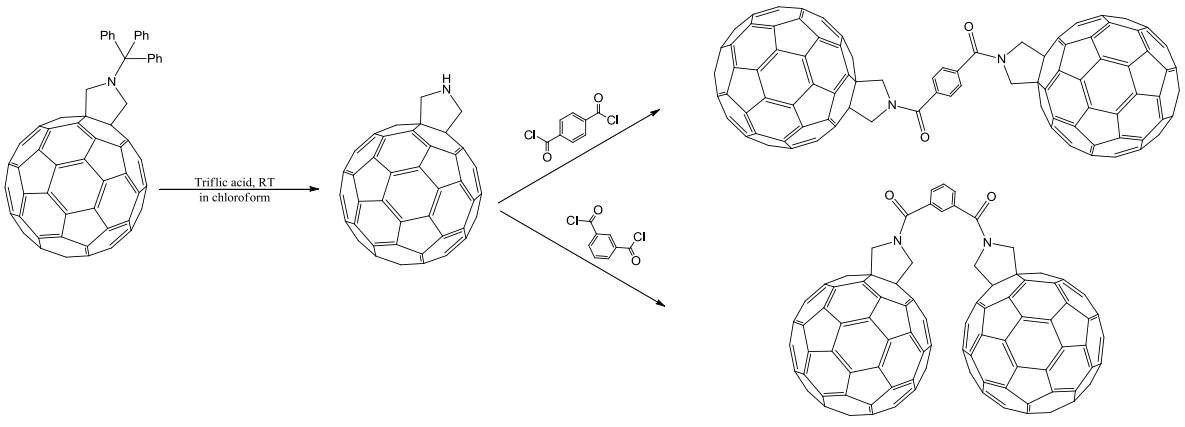


Figure 1.30 The first nitrogen bridged pyrrolidine fullerene dimer.[93]

In 1998, Sakata *et al.* published one of the first examples of rigid pyrrolidine functionalised dimers with an electroactive bridging unit[95]. Sakata *et al.* used *cis* and *trans* di-benzaldehyde substituted porphyrins as the central bridging unit precursors. These are then attached to the fullerene units via a 1,3-dipola cycloaddition (Figures 1.31.a-b). The group reported strong quenching of the fluorescence spectra of both dimers compared to the separated photoactive units. A comparison of the fluorescence intensities of the dimers with the porphyrin-C_{60} dyad (see Figure 1.31.c) showed the beneficial effect that the presence of two fullerene cages has on the rate of nonradiative photo-physical processes, such as forming charge separated states.

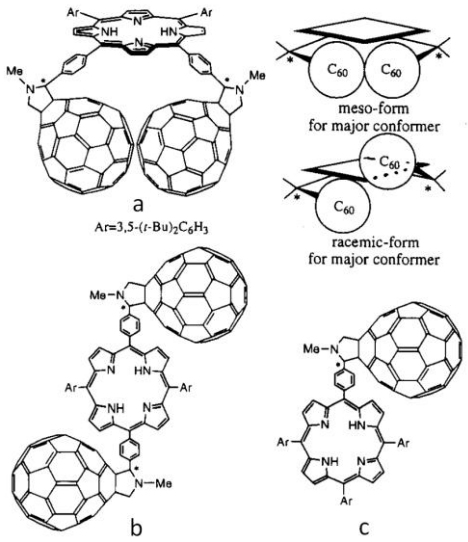


Figure 1.31 Pyrrolidine attached fullerene dimers using either (a) *cis* substituted porphyrin bridging unit or (b) *trans* substituted bridging unit. c) Corresponding fullerene porphyrin dyad. Adapted from Higashida *et al.*[95]

Another example of a pyrrolidine-attached dimer bearing an electroactive bridge was published by Martin and co-workers in 1999, using the highly fluorescent[96] bis-aldehyde (see Figure 1.32). As mentioned by previous authors, the alkoxy-substituents were noted as being very effective solubilising groups for the rigid, highly insoluble dimer core. The cyclic voltammetry of the dimer showed an increase in negativity of the reduction potentials with respect to the parent C_{60} values, a feature common to many 1,2-dihydrofullerenes.[97] While the dimer absorption spectrum indicates that as expected no intramolecular charge transfer is taking place in the ground state, the almost total quenching of the fluorescence spectrum corresponding to the excitation of the bridge (398 nm) when

recorded in dichloromethane, suggests that charge separation is significantly faster than back transfer, making the dimer potentially useful for photovoltaic applications.

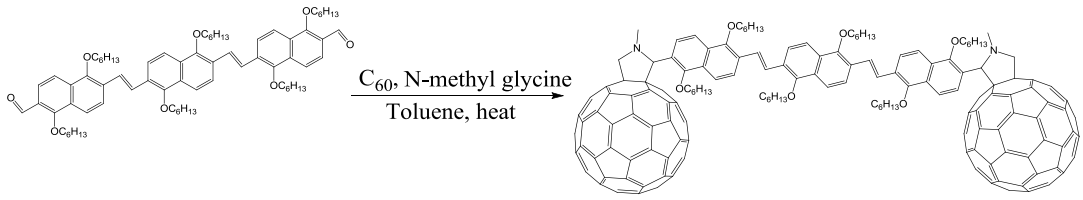


Figure 1.32 Pyrrolidine-attached dimer bearing a planar conjugated electroactive bridge.[96]

In the following year, Janssen and co-workers published a more complete photo-physical study of a family of electroactive bridged dimers which used variable length oligothiophenes bridges (T), denoted as C_{60}-nT-C_{60}, n=3, 6 or 9 (see Figure 1.33).[98] Photoexcitation of all three dimers, when dissolved in an apolar solvent, exhibit energy transfer reactions to the fullerene cage with rates between 10^{12} and 10^{13} s^{-1}. Upon an increase in the polarity of the solvent, an intramolecular charge transfer state is seen for the n=6 and 9 but not for n=3. The rate of charge separation is calculated to at most 10^{11} s^{-1}.

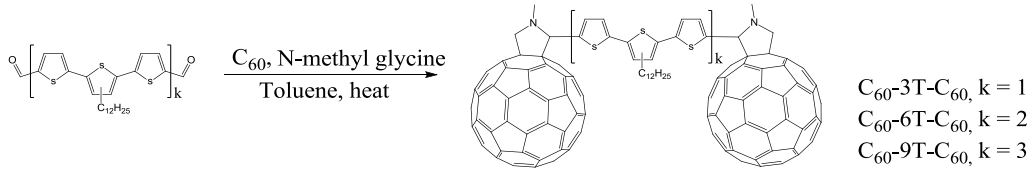


Figure 1.33 Synthesis of C_{60}-nT-C_{60} fullerene-oligothiophene-fullerene dimers.[98]

In addition, the lifetime of the charge separated state recorded for C_{60}-nT-C_{60}, n=6 or 9 in polar solvent is significantly smaller when compared to the millisecond lifetime of the corresponding state measured after photoexcitation of a thin film of either dimer. The long lifetime of the solid state sample is attributed to the intermolecular migration of the radicals to adjacent dimers. More recently, the same authors created another related set of dimers which use thiophene-pyrrole-thiophene bridging units[99] (see Figure 1.34). A detailed photochemical study of all three dimers[100] revealed that the rate constant for the creation of the charge separated states (k_{CS}) was highly dependent of the polarity of the solvent, the fastest of which was calculated to be in the range of k_{cs}= 10^{9} - 10^{10} s^{-1}. A transient photoinduced

absorption study of the dimers identified that charge recombination (k_{CR}) was short, with the upper bound calculated to be k_{CR}=2 x 10^{10} s^{-1}.

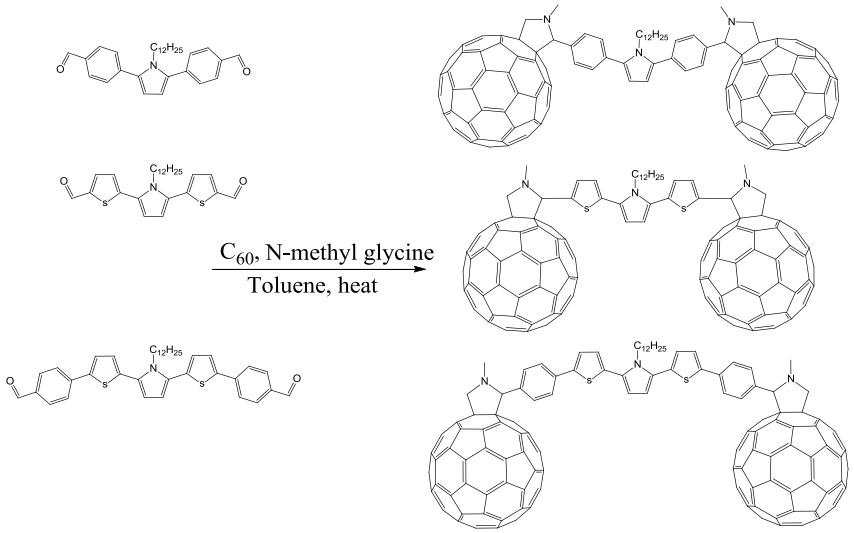


Figure 1.34 Range of thiophene bridged fullerene dimers. Figure adapted from Dhanabalan *et al.*[99]

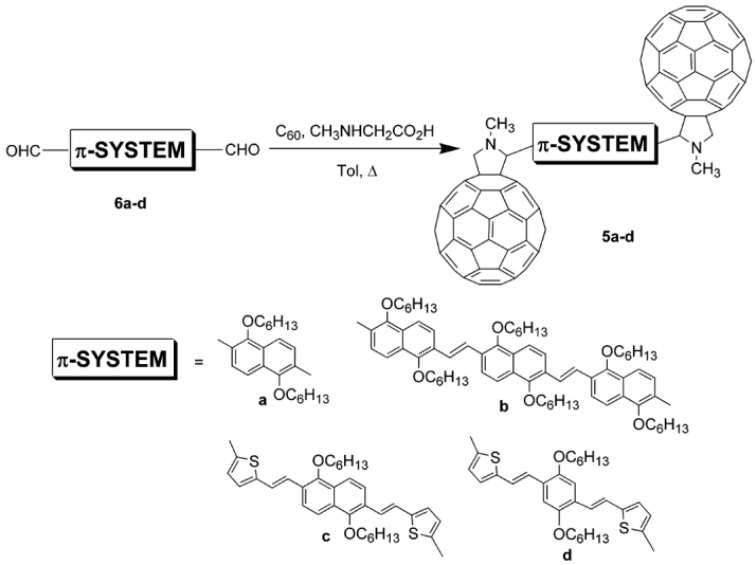


Figure 1.35 Synthesis of a selection of fullerene dimers used in a systematic study into the effect that a change to the absorption wavelength and oxidation potential of the bridging unit has on the rate constants for the various decay pathways of the photoexcited dimers. Figure reproduced from Guldi *et al.*[101]

Guldi and co-workers published a systematic study into the effect that a change to the absorption wavelength and oxidation potential of the bridging unit has on the rate constants for the various decay pathways of the photoexcited dimers.[101] The study was conducted using the dimers in Figure 1.35, the

synthesis of the bridging units was reported[102] with the dimer having being previously mentioned in this chapter. The report suggests that the red shift observed in the ground state fluorescence spectra compared to those of the separate bridging unit analogues indicates a strong electronic coupling between the fullerene and bridging unit, a conclusion that is in contrast to previous findings.[103] In addition, the absence of any additional reduction features in the cyclic voltammograms is a well documented indicator of negligible ground state electronic coupling. Using transient spectroscopy, the authors highlighted a strong dependency between the polarity of the solvent and the observed decay mechanism. All four dimers have a dominant singlet-singlet energy transfer from the oligomer unit to fullerene cage when solvated using either toluene of THF. However, when highly polar benzonitrile is used as the solvent (Figure 1.35.5c) the presence of both energy and electron transfer photoproducts can be detected, while Figure 1.35.5d switched entirely across to an electron transfer deactivation mechanism**.** This trend was rationalised through the decrease in oxidation potentials of the oligomeric spacing units along the series 5a-5d (Figure 1.35) which lowers the energy of formation of a charge separated state.

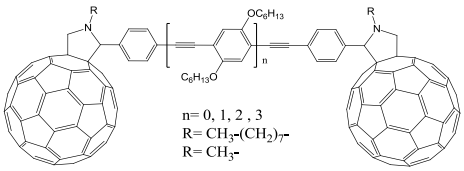


Figure 1.36 Pyrrolidine attached fullerene dimers that incorporate electroactive (OPE) bridging units ranging from three to seven phenyl units.[104]

In the following year, Guldi and co-workers published the synthesis and characterisation of another family of pyrrolidine attached fullerene dimers, which incorporated electroactive OPE bridging units ranging from three to seven phenyl units[104] (see Figure 1.36). The bridging units were synthesised using a similar iterative method as Tour *et al.* published[76] then using Sonogashira coupling conditions to attach a benzaldehyde unit to the terminal acetylenes to create the diformyl terminated spacers. A photo-physical study of the dimers, using fluorescence and transient absorption spectroscopy, showed that the dominant deactivation mechanism for all of the dimers, irrespective of the polarity of the

solvent, was via an energy transfer process. This was explained by the more thermodynamically favourable, lower energy of the $^{1*}C_{60}$-(OPE)-C_{60} state compared with charge separation energy. For a schematic illustration of the reaction decay pathways see Figure 1.37.

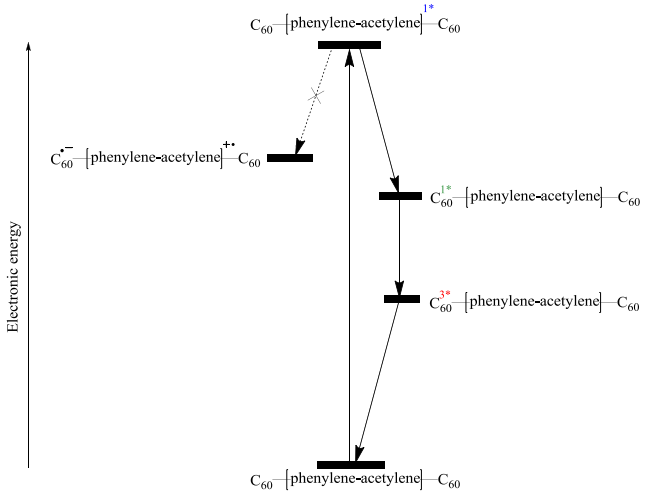


Figure 1.37 Schematic illustration of the reaction pathways available to the photoexcited C_{60}-(OPE)-C_{60} compounds shown in Figure 1.36. Diagram adapted from Atienza et al.[104]

1.3.5 Other [3+2]cycloadditions

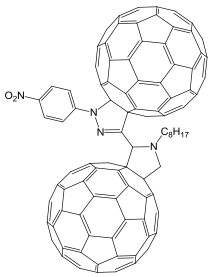


Figure 1.38 The first example of a C_{60}-C_{60} dimer linked through a asymmetric 2-pyrazolino-pyrrolidino bridge.[105]

Delgado and co-worker created the first example of a C_{60}-C_{60} dimer, linked through an asymmetric 2-pyrazolino-pyrrolidino bridge[105] (see Figure 1.38). The chosen two-step synthetic strategy first formed the formyl functionalised C_{60} monomer using previously described conditions,[106] which was then attached to another C_{60} cage with N-octylglycine via a [1,3] dipolar cycloaddition in a 70 % yield. As might be expected, UV-Vis spectra show a two-fold increase in molar absorptivity compared to the C_{60} pyrazolino precursor. The study highlights the appreciable decomposition of the dimer via a retro-cycloaddition reaction when subjected to heat or on the addition of a metal Lewis acid such as copper

(II) triflate. The results indicate the prevalence of retro-cycloaddition in both experiments, with the pyrrolidinofullerene much more susceptible to retro-cyclisation than the 2-pyrazolinofullerene unit.[107]

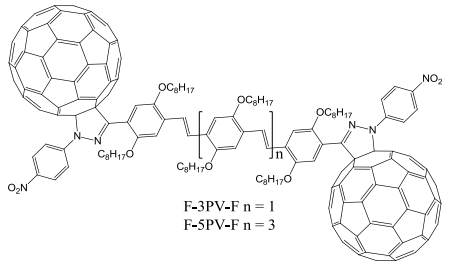


Figure 1.39 Symmetric 2-pyrazolinofullerene dimers that incorporate a oligophenylenevinylene (OPV) bridging unit.[108]

Two symmetric 2-pyrazolinofullerene dimers that incorporate an oligophenylenevinylene (OPV) bridging unit were synthesised and extensively characterised by Langa and co-workers.[108] The synthesis of the two bridging units was accomplished using a convergent approach that utilised Wittig-Horner conditions followed by catalytic treatment with iodine to give desired *E* selectivity across the alkenes. The two dimers and their corresponding dyad analogues were formed by reacting with the bis-nitrilimine intermediates at room temperature to give yields of 27 % and 10 % of the F-3pv-F and F-5PV-F dimers respectively (Figure 1.39).[109] Electrochemical analysis showed both fullerenes to be electronically isolated despite probable conjugation between the OPV and pyrazoline ring. Photo-physical characterisation of the dimers and dyads indicated the presence of charge separation occurring between the fullerene and OPV moieties on photoexcitation of the OPV unit. The mechanism for charge separation was suggested to take place via a two-step process. Firstly, the excited OPV unit undergoes a singlet energy transfer to the fullerene cage, which is then quenched by a pyrazoline to fullerene electron transfer process.[110] The effect of the second fullerene substituent markedly increases the rate of OPV→ C_{60} energy transfer, while increasing the length of the bridging unit has an inverse effect.

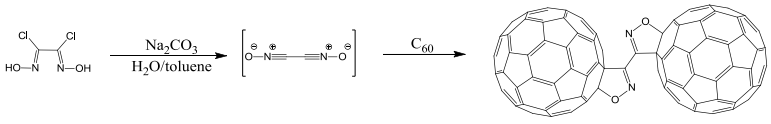


Figure 1.40 Route to Isoxazolo attached fullerene dimer.[111]

Irngartinger and co-workers are the only group to have successfully synthesised isoxazolofullerene dimers. Their initial work in 1996 used dichloroglyoxime as precursor for the *in situ* formation of cyanogen di-N-oxide which then undergoes a [3+2]cycloaddition with a (6,6) bond of the fullerene (see Figure 1.40).[111] Purification was carried out with HPLC, using toluene as the eluent. As expected, the solubility of the dimer in Figure 1.40 was very poor in most organic solvents, however, a 1-chloronaphthalene/2-chloronaphthalene 9:1 v/v solvent system provided sufficient solubility to facilitate characterisation by ^{13}C NMR. Irngartinger and co-workers later synthesised longer dimers, illustrated in Figure 1.41.[112] Interestingly, both synthetic schemes carried out the dimer reaction under very dilute conditions with a large excess of C_{60}, illustrating the sparing solubility of the product dimers in toluene and the high propensity of the intermediate monomeric species to couple to another fullerene cage. The authors highlight that due to the steric hindrance of the anthracene unit the dimer forms as one of two separable isomers in a 9:1 ratio.

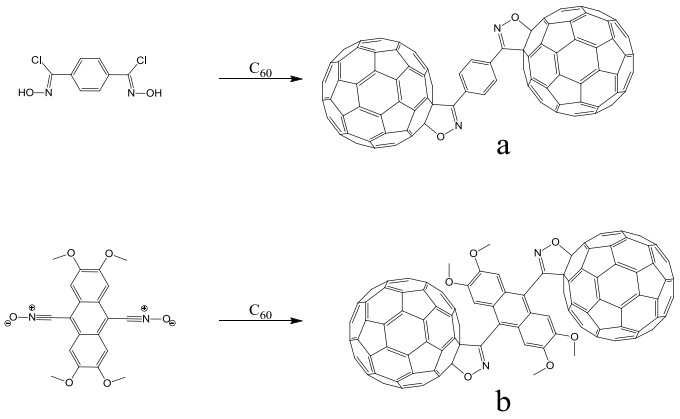


Figure 1.41 Synthesis of Isoxazolofullerene dimers using benzene and anthracene units incorporated into the linker.[112]

1.2.6 [4+2]cycloadditions

In addition to the popular Prato fullerene functionalisation method, a variety of other cycloaddition reactions have been used to link a rigid spacer molecule to two fullerene cages. The first C_{60} dimer that was formed via a Diels-Alder [4+2]cycloaddition was reported by Müller and co-workers in 1993, who used a highly reactive o-quinodimethane radical as the bridging unit precursor.[113] The O-quinodimethane was created *in situ* using an iodine-induced 1,4-elimination of 1,2-

bis(bromomethyl)benzene[114] (see Figure 1.42.a). The authors highlight the need to use the phase transfer catalyst [18]crown-6 to allow the reaction to proceed in refluxing toluene. Due to the low solubility of dimer (a), only basic characterisation using Gel permeation chromatography ,^{1}H NMR and mass spectrometry was achieved. Three years later, Müller and co-workers created a significantly more soluble dimer analogue (see Figure 1.42.b) by functionalising the o-quinodimethane precursor with alkoxy chains.[115] In addition to the dimer, longer oligomers with up to seven fullerenes were also created. The more in-depth characterisation of dimer (b) eluded to the presence of two conformations at temperatures below 30^{o} C, with the fullerene cages adopting either a *cis* or *trans* relative geometry. Using a similar methodology to Müller, Parquette and co-workers attached two fullerenes to novel 1,4-cyclohexadienyl ladders of varying length, creating a family of semi-rigid dimers (see Figure 1.42.c).[116] The authors commented on the high yield of the dimers formed (40-70 %) and the tendency for the dimers to undergo retro Diels-Alder reaction when heated in toluene. More recently, our group used the bridging precursor molecule 2,3-bis(bromomethyl)-1,4-dibromo-2-butene and an analogous iodine induced elimination technique [113] to create a shorter dimer length than either of the previous groups in a 12 % yield, (see Figure 1.42.d).[117]

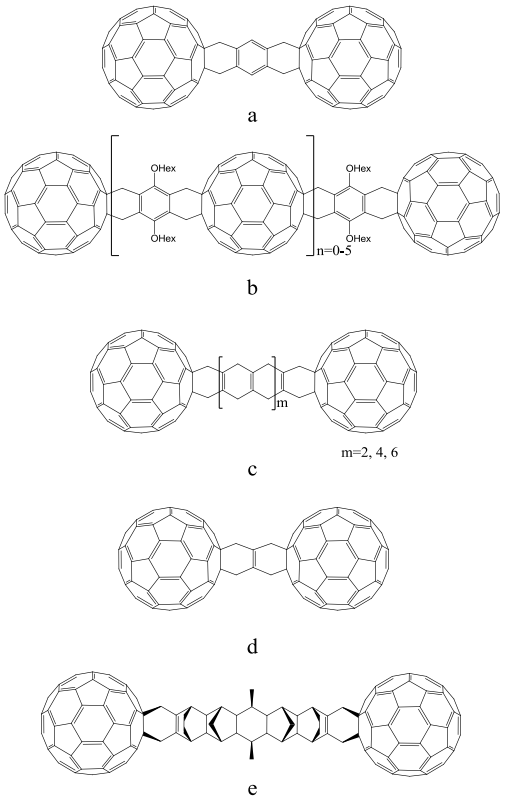


Figure 1.42 A range of ladder type dumbbell dimers attached via a [4+2]cycloaddition.[114-118]

Furthering Parquette's work, Lawson *et al.* used a bis-diene with a rigid central unit to create a dimer (see Figure 1.42.e) that only permits bending at the sp^3 carbon centres adjacent to the fullerene cage.[118] The [4+2]cycloaddition dimer reaction was highlighted as only yielding an amorphous insoluble polymer when toluene was used as the solvent, whereas when ODCB was used in combination with a higher temperature, a significant yield of dimer was recovered. The authors suggest that this pronounced change in reactivity is due to the greater solvating power of ODCB and the reversibility of the [4+2]cycloaddition reaction at the higher temperature, allowing the thermodynamically more stable dimer to become the dominant product. Three force field models of the dimer were computed to predict the relative stability of the three different conformations, all of which indicated the Folded-Folded geometry as being the most thermodynamically stable by at least 7.3 $kJmol^{-1}$, presumably due to strong π-π interactions between the two fullerene cages.

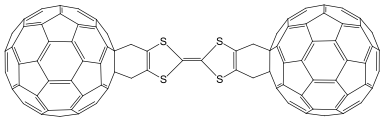


Figure 1.44 Incorporation of a strong π donor tetrathiafulvalene (TTF) into the bridging unit of a fullerene dimer.[119]

Lui and co-workers incorporated the strong π donor tetrathiafulvalene (TTF) into the bridging unit of a fullerene dimer using Diels-Alder cycloadditions of a bis diene-TTF species to two fullerene cages[119] (see Figure 1.43). The bis-diene was created *in situ* from tetrakis(bromo-methyl)TTF using a naked iodine reduction method.[113] The authors commented on the difficulty of purification and characterisation that resulted from the dimer's poor solubility and low thermal stability, primarily attributed to the prevalence of the retro Diels-Alder reaction. UV-Vis spectral features were consistent with an adduct forming with C_{60} across a 6,6 bond. The ESR signal of the anion and cation radicals produced from electro-reduction at -0.8 V (vs Ag/AgCl) and electro-oxidation at +0.7 V of the dimer, respectively, were recorded. The anion radical signal was consistent with previous literature pertaining to C_{60} cycloadducts while the five features seen in the cation radical were assigned as originating from coupling from the four equivalent axial methylenic protons of the cyclohexane bridges within the dimer.

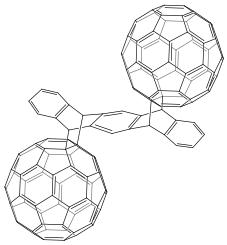


Figure 1.44 Fullerene dimer created using HSVM and pentacene.[120]

Using the same high speed vibration milling technique that was used to synthesis $(C_{60})_2$ as mentioned earlier, Komatsu formed a dimer using pentacene as the linking unit. As with the $(C_{60})_2$experiment, the reaction was carried out in the solid state by combining C_{60} with petacene and subjecting it to HSVM for 1 hour, the [4+2]cycloaddition dimer shown in Figure 1.44 was recovered.[120] The dominant conformation of the dimer was assumed to place the C_{60} substituents in an *anti* geometry rather than *cis*, with the authors basing their assignment on the slightly lower energy of the *anti* relative to *cis* of

0.36 kJ mol^{-1}. Cyclic voltammetry indicated simultaneous reduction of both fullerene cores, suggesting no appreciable electron interaction between the fullerene cores.

1.2.7 Metal-bridged dimers

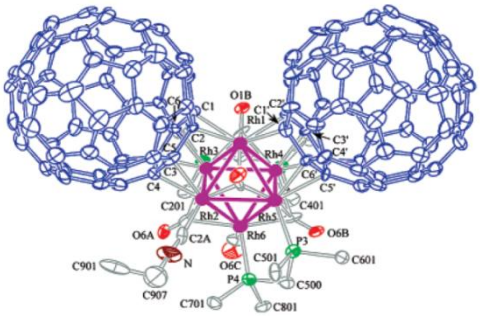


Figure 1.45 Dimer bridged by a $Rh_6(CO)_5(dppm)_2(CNR)(C_{60})_2$ complex. Reproduced from Lee *et al.*[121]

There are few examples of directly bonded metal bridged fullerene dimers, possibly due to the limited number of metal complexes that can accommodate both the bulk of two fullerenes and their innate electron deficiency. The first example of a metal centred C_{60} dimer was published by Lee and co-workers in 2002.[121] The octahedral rhenium cluster, $Rh_6(CO)_9(dppm)_2(\mu_3\text{-}\eta_2,\eta_2,\eta_2\text{ -}C_{60})$ was reacted with excess C_{60} in refluxing chlorobenzene. This product was then treated with CNR (R = $CH_2C_6H_5$) to yield the fullerene dimer $Rh_6(CO)_5(dppm)_2(CNR)(C_{60})_2$ (see Figure 1.45). The X-ray crystal structure indicates that although both fullerenes bond to the Rh_6 cluster in a $\mu_3\text{-}\eta^2,\eta^2,\eta^2$ geometry the coordination environment of each fullerene is distinct. A cyclic voltammogram of the dimer shows three pairs of reversible reduction events between -1 V and -2.5 V (vs Fc/Fc^+). The authors used the reduction pattern recorded to infer the presence of strong intramolecular coupling between the fullerene cages. Lee and co-workers went on to create another metallo-bridged fullerene dimer based on an Ir_4 cluster. Unlike the previous Rh_6 dimer this method added both fullerene cages to the cluster in a one pot reaction using the precursor $Ir_4(CO)_8(PMe_3)_4$, CNR (R) $CH_2C_6H_5$ and an excess of C_{60}. An X-ray study of the resulting green fullerene dimer $Ir_4(CO)_3(\mu_4\text{-CH})(PMe_3)_2(\mu\text{-}PMe_2)(CNR)(\mu\text{-}\eta^2,\eta^2\text{-}C_{60})\text{-}(\mu_4\text{-}\eta^1,\eta^1,\ \eta^2,\eta^2\text{-}C_{60})$, (see Figure 1.46, b) illustrates the substantially different coordination environment of the two fullerene cages. As with the former dimer, the cyclic voltammogram presented six reversible one electron redox waves. This redox behaviour is primarily attributed as arising from the different levels of

back bonding that each cage receives. In addition however, the authors used the significant increase in voltage separation within each redox pair as the molecule is reduced from C_{60}^{1-}-C_{60}^{1-} to C_{60}^{2-}-C_{60}^{2-} to C_{60}^{3-}-C_{60}^{3-} to suggest the presence of significant electron communication between the two fullerene cages. The presence of electronic communication is further substantiated by theoretical calculations of the HOMO and first +5 LUMO density maps.[122]

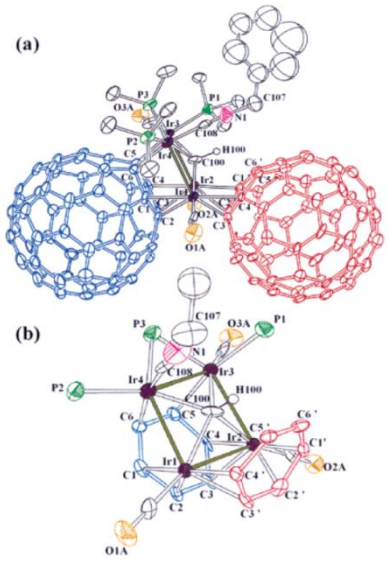


Figure 1.46 (a) Dimer bridged by an $Ir_4(CO)_3(\mu_4\text{-}CH)(PMe_3)_2(\mu\text{-}PMe_2)(CNR)(\mu\text{-}\eta^2,\eta^2\text{-}C_{60})\text{-}(\mu_4\text{-}\eta^1,\eta^1,\ \eta^2,\eta^2\text{-}C_{60})$ complex (b) Expansion of the coordination environment of the iridium with the fullerenes. Reproduced from Park *et al*.[122]

An example of a metallo-bridged fullerene dimer that was almost entirely geometrically and electronically symmetric with respect to the fullerene cages was published by Jin and co-workers. Constructed around either a single Mo(0) or W(0) centred complex, the fullerene cages were found to bond *trans*, with η^2 coordination and have the general formula $[M(\eta^2\text{-}C_{60})_2(CO)_2(dbcbipy)]$ [M = W and Mo, dbcbipy = 4,4'-di(butyl carboxyl)-2,2'-bipyridine] (see Figure 1.47). An in-depth electrochemical study of the molybdenum dimer by Zanello *et al.* showed the presence of stepwise redox events at each fullerene core albeit less distinct as those seen in the other metallo bridged dimer mentioned so far.[123] Owing to the almost identical environments of both fullerene cages, the authors assigned the stepwise redox behaviour as arising from an electronic interaction between the two fullerenes, also commenting that the principal mechanism is likely a "through space interaction" and not a direct exchange interaction mediated by the bridge.

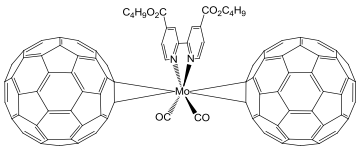


Figure 1.47 Metal bridged fullerene dimer; [Mo(η^2-C_{60})$_2$(CO)$_2$(dbcbipy)].[123]

1.3.8 Summary

The appreciable volume of literature that has been published on the formation of C_{60} dimers provides a robust foundation for the design and prediction of properties for any future C_{60} dimer research. The early work on directly bonded dimers shows the ability of C_{60} to react with itself, in the case of $C_{120}O$ even under ambient conditions. Two features common to all directly bonded C_{60} dimers are their extremely poor solubility, even relative to pristine $C_{60,}$ and the presence of significant ground state interactions between the two fullerene cages. The solubility issue has been repeatedly overcome through incorporating solubilising alkyl groups into either the fullerene cages or the bridging unit. However, the requirement for the fullerene cages to be in close proximity to one another to observe ground state C_{60}-C_{60} electronic interactions has only been suggested to partly relax when the bridging unit is a transition metal or metal cluster. The lack of electronic communication seen between the two fullerene units is most likely a result of negligible overlap between the fullerene π system and the attached bridging unit. This lack of ground state interaction between the bridging unit and C_{60} cage appears to be a major cause for the extremely long lived charge separated states that have been reported for a number of C_{60} dimers that incorporate an electroactive donor bridge.

1.4 N@C_{60} dimers

1.4.1 N@C_{60}-C_{60} dimers

The first N@C_{60}-C_{60} dimer was synthesised by Goedde *et al*. in 2001 using a mechano-chemical method to produce a directly bonded dimer[62] (see Figure 1.48 and compound). The authors showed that the dimer yield was maximised (17%) when water was rigorously excluded from the reaction mixture using desiccants such as $CaCl_2$ or P_2O_5. The mechanism was suggested to proceed via a N@C_{60}/C_{60} radical

intermediate owing to the significant reduction in dimer yield that was observed when the radical trap hydroquinone was added. No indication of the degree of decomposition of $N@C_{60}$ that occurred during the reaction. Recreation of this experiment in my group research group found that significant $N@C_{60}$ decomposition occurred during the reaction. This is commensurate with the suggestion that $N@C_{60}$ is unstable to exohedral radical formation on the carbon cage.[55] The reaction scale was large using 60mg of $N@C_{60}/C_{60}$ starting material and might explain why only unenriched $N@C_{60}/C_{60}$ was used in the reaction. I have calculated that this reaction to produce at most 10 ppb $N@_{60}$-$N@C_{60}$, therefore no ESR spectra would be expected to be resolvable from the two spin centre product component.

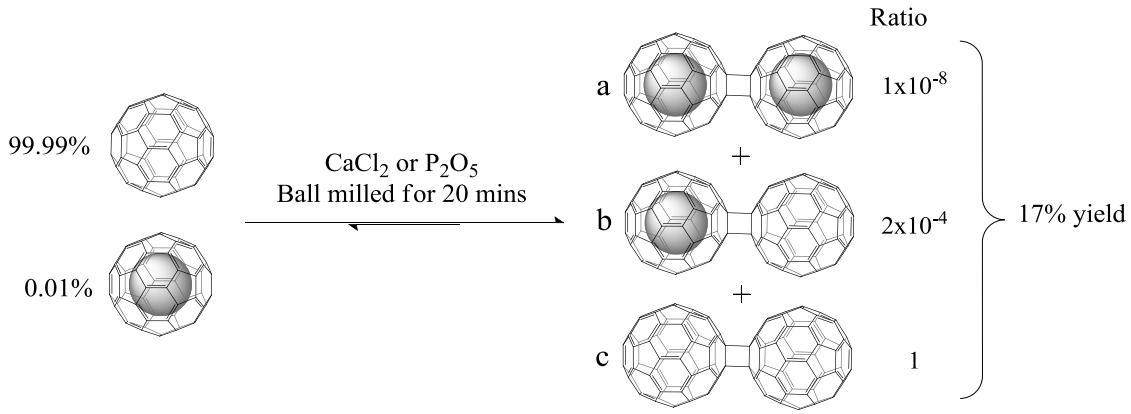


Figure 1.48 Reaction scheme for the first $N@C_{60}$-C_{60} dimer synthesised using a mechano-chemical method.[62] Calculated maximum yield of $N@_{60}$-$N@C_{60}$ dimer to be 10 ppb of dimer product. See Table 1.1 for fitted spin Hamiltonian parameters for dimer product mixture, dominated by (b).

The second $N@C_{60}$-C_{60} dimer was synthesised in 2008 by Zhang *et al.* who incorporated a photo-isomerisable azobenzene linker using standard Prato reaction conditions. The specific reaction conditions for the $N@C_{60}$-C_{60} dimer are given, however the paper states that it was produced in an 'analogous fashion' to the C_{60}-C_{60} test reaction also described in the paper. This would suggest that the reaction proceeded under the conditions shown in Figure 1.49 using a 6 fold excess of amino acid and a 50% excess of $N@C_{60}/C_{60}$ relative to the bis-aldehyde linker in refluxing toluene for two days. This reaction used semi enriched 1 % $N@C_{60}/C_{60}$ starting material to produce at least 5 mg of $N@C_{60}$-C_{60} product. The reaction was reported to cause 30 % of the $N@C_{60}$ centres to decompose. Based on the enrichment level of the $N@C_{60}/C_{60}$ used, around 0.01% of the dimer product mixture would be

expected to be present, this is 200 times less than the single spin centre component N@C_{60}-C_{60} making its presence near impossible to confirm. The fitted one spin centre model parameters are shown in Table 1.1 as compound 1.9.e

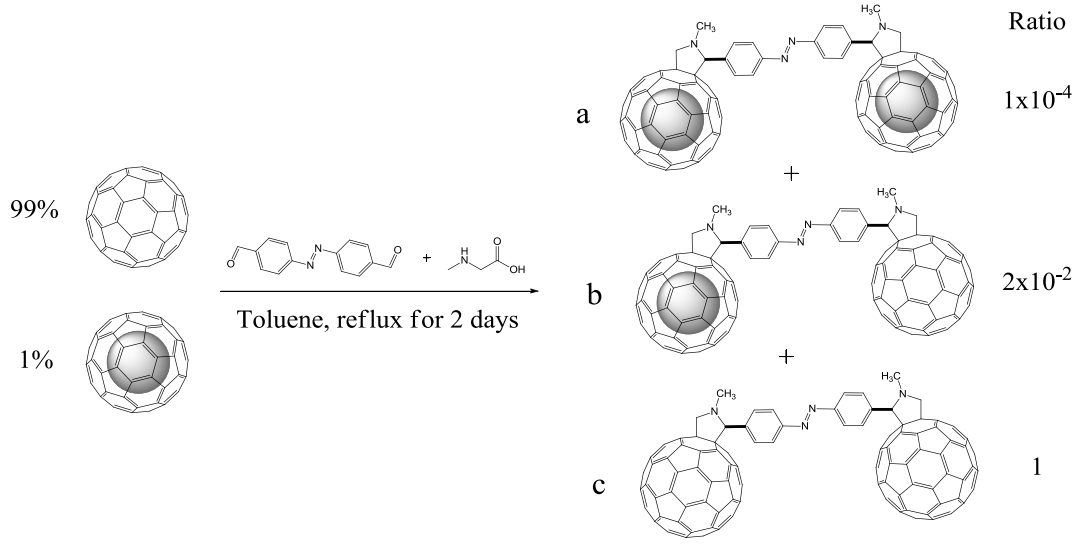


Figure 1.49 Reaction scheme for the synthesis of an aza-bridged N@C_{60}-C_{60} dimer using Prato reaction conditions and a ratio of N@C_{60}/C_{60} : bis-aldehyde : amino acid of 3 : 1 : 6.[59] ESR spectra of N@$_{60}$-C_{60} product component expected to be 200 times stronger than for N@$_{60}$-N@C_{60}, hence two spin centre N@$_{60}$-N@C_{60} component undetectable via ESR. The fitted one spin centre model parameters are shown in Table 1.1 as compound 1.9.e.

A cyclo-propane N@C_{60}-C_{60} dimer was synthesised by Hörmann *et al.* using a cyclo[2]malonate as the linker. The reaction used between 5-25 mg of 0.1% N@C_{60} in C_{60}, with scheme for the synthesis is shown in Figure 1.8.c. The reaction yield for the N@C_{60} reaction isn't given however the C_{60} analogue is given as 18%. The author reports that a 50 % decomposition of the N@C_{60} spin centres occurs during the reaction despite the optimisation of the reaction time to 1 h. The purity of N@C_{60} used was 0.01% in C_{60} resulting in the maximum expected two spin centre component of the dimer product mixture to be 2000 times less than the single spin centre component N@C_{60}-C_{60} and its abundance in the product mixture to be 1 ppm, far too low to be detectable. The fitted one spin centre model parameters are shown in Table 1.1 as compound 1.8.c. Hörmann also showed that the mono C_{60}-cyclo[2]malonate adduct could be isolated and then subsequently reacted with C_{60} to produce the dimer, offering a future pathway to the synthesis of an ^{14}N@C_{60}-^{15}N@C_{60} dimer.

Subsequent to the work described in this thesis Plant *et al.* showed that an $^{15}N@C_{60}$-C_{60} dimer can be synthesised using the amino acid N-(4-(hexyloxy)benzyl)glycine (as used in this thesis) and terephthalaldehyde via a bis Prato addition in a 15 min time period using unenriched 10 ppm $^{15}N@C_{60}/C_{60}$ starting material (see Figure 1.50).[29] The key finding of the paper is the demonstration that the double Prato reaction can be stopped at the monoadduct $^{15}N@C_{60}$-ald using a reaction time of 2 mins, then subsequently heated for 15 mins with additional N-(4-(hexyloxy)benzyl)glycine and one molar equivalent of unenriched 10ppm $^{14}N@C_{60}/C_{60}$ to create a mixture of $^{15}N@C_{60}$-C_{60} and $^{14}N@C_{60}$-C_{60} single spin centre dimers. This demonstrates sufficient control over the Prato reaction to theoretically form an $^{15}N@C_{60}$-$^{14}N@C_{60}$ asymmetric dimer. Neither the yield nor actual reaction scale used is provided however the author states that the reaction has been trialled using only 6 μg of C_{60}. The fitted spin Hamiltonian parameters for the $^{15}N@C_{60}$-C_{60} dimer are given in Table1.1 entry 1.9.g.

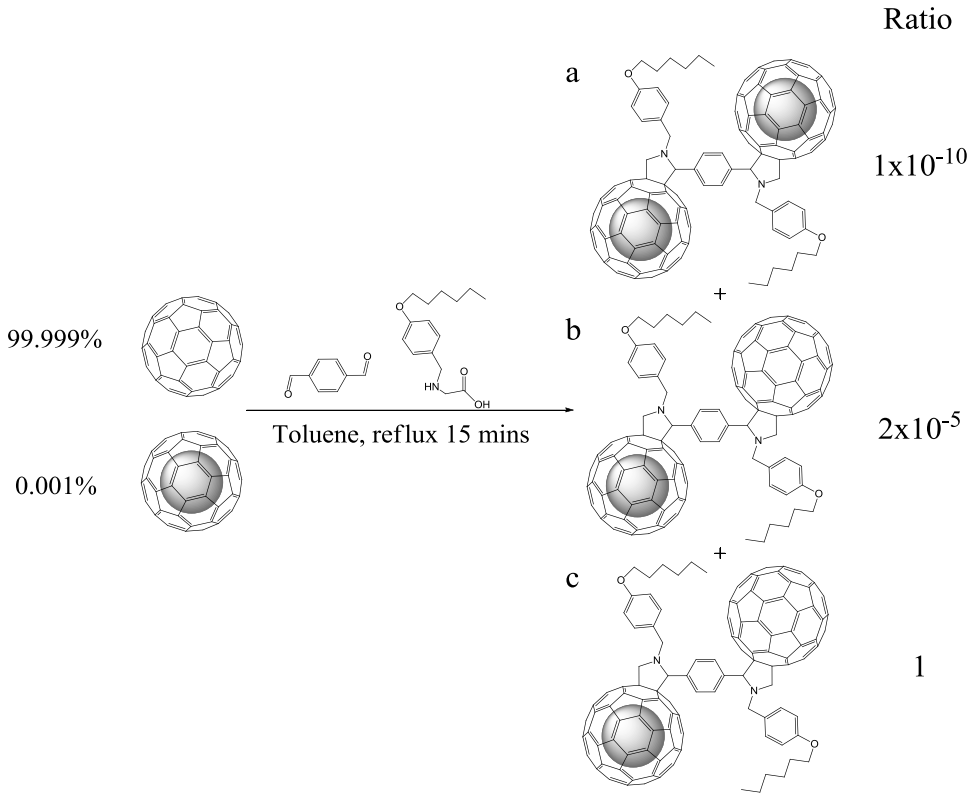


Figure 1.50 Reaction scheme for the synthesis of the first isotopically enriched $^{15}N@C_{60}$-C_{60} dimer using 10 ppm $^{15}N@C_{60}$ in C_{60}.[29] 0.1 ppb of dimer product calculated to contain two spin centre $^{15}N@C_{60}$-$^{15}N@C_{60}$ system. [29]

All $N@C_{60}$-C_{60} dimers that have been synthesised todate use no more than 1 % $N@C_{60}$ in C_{60} enriched starting material. Due to the statistical nature of the distribution of $N@C_{60}$ in the dimer products no more than 1/10,000 of the dimer molecules would be expected to contain two $N@C_{60}$ spin centres. This is orders of magnitude too small to see using ESR spectrometry and is compounded by the relative abundance of single spin centre $N@C_{60}$-C_{60} dimers present in each dimer sample. Due to the similarity of chemical and physical properties of $N@C_{60}$ and C_{60} it has not been possible to separate each of the one and two $N@C_{60}$ dimer components after the reaction.

The ideal properties of an $N@C_{60}$-$N@C_{60}$ dimer can be split into two area's synthetic and QIP:

Synthetic:

1. Synthesis and purification methods must be compatible with the very small quantities (10's of micrograms) of highly enriched $N@C_{60}$ available.
2. Reaction conditions must be compatible with the thermal and photo-stability of $N@C_{60}$.
3. Reaction must not be reversible under normal ESR measurement and storage conditions.
4. Produced molecules must have at comparable or better solubility to $N@C_{60}$/C_{60} to facilitate solution processing and characterisation.

QIP:

1. Fixed dipolar coupling between two centres, requiring:
    a. Conformational restraint.
    b. Macroscopic alignment of Inter spin-centre dimer vectors in one or more dimensions.
2. Long electron spin T_2 relaxation lifetimes compared to time required to implement universal quantum gate.
3. Each of the two electron spin centres should be magnetically distinct to allow selective addressing and readout of each Qubit.

All of the dimers created so far have an isotropic orientation distribution. As such any dipolar coupling between two spin centres would be distributed over a range that is proportional to the maximum dipolar coupling magnitude (see Figure 2.2) leading to a reduction in the number of spin centre transitions per Gauss and a decrease in the signal to noise of any ESR spectrum. Since the quantities of $N@C_{60}$ that are accessible are so small it is not possible to simply create a larger ensemble of $N@C_{60}$-$N@C_{60}$ molecules to measure. To increase the signal to noise the only free and controllable parameter is the maximum dipolar coupling magnitude which is governed by the separation of the two spin centres (see Equation 2.12). For an $N@C_{60}$-$N@C_{60}$ dimer the optimum separation between spin centres in an isotropic distribution of orientations has been calculated to be around 3 nm.[124]

1.4.2 $N@C_{60}$- hetero spin centre dimers

Current systems

To date the only one example of a multi paramagnetic centre molecule containing $N@C_{60}$ has been synthesised by Liu *et al.* [60] This system was created to probe the effect that a single adjacent spin centre has on the ESR spectrum of $N@C_{60}$. The synthesis of this ststem took place via a Prato reaction using 0.1% $N@C_{60}$ in C_{60} starting material, an aldehydye functionalised porphyrin, N-(4-(hexyloxy)benzyl)glycine, and heat for 15 mins (see Figure 1.51) . The yield of the reaction is not given hovever the C_{60} anololouge reaction using the same conditions was found to give a 28 % yield. The electron dipole-dipole interaction between the $N@C_{60}$ centre and Cu^{2+} ion within the porphyrin was found to induce such significant relaxation broadening of the $N@C_{60}$ transition that the resulting CW ESR spectrum was unresolvable. The inability to observe the $N@C_{60}$ spin environment was further compounded by the significant overlap of the Cu^{2+} and $N@C_{60}$ spectra. The broadening however was shown to be reversible by demonstrating that after chemical demetalation of the porphyrin moiety the characteristic three $N@C_{60}$ hyperfine lines return with 82 % of the initial intensity.[60]

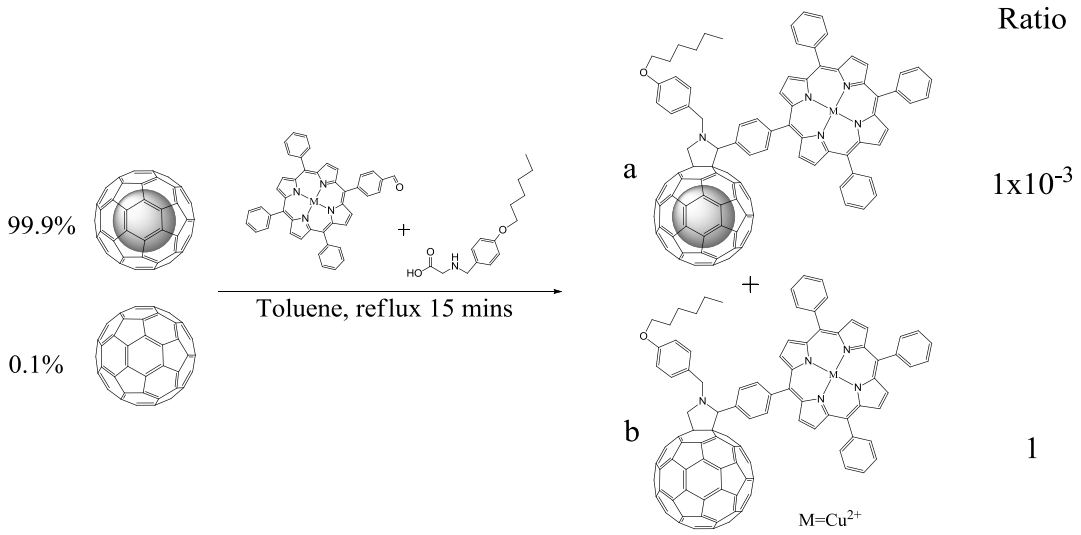


Figure 1.51 Reaction scheme for the synthesis of a Cu^{2+} porphyrin-$^{14}N@C_{60}$ dimer.[60]

Cr_7Ni rings - an ideal test hetero spin centre

Cr_7Ni antiferromagnetic rings belong to the family of antiferromagnetically (AF) coupled metallic ring compounds that were first discovered over 100 years ago with three Cr metal centres arranged in a triangular geometry.[125] This group of compounds has the general formula $[M_3O(OOCR)_6(L)_3]^z$ and is compatible with a wide range of metals and ligands.[126] Examples of larger AF metallic ring started to be investigated 25 years ago[127-128] with structures based on iron $Fe_{10}(OMe)_{20}(O_2CCH_2Cl)_{10}$ and chromium rings $Cr_8F_8(O_2CCMe_3)_{16}[(CH_3)_2CO]_2$. Homometallic rings typically have an even number of metal centres and consequently have an S=0 ground state due to the complete antiferromagnetic coupling around the ring (Figure 1.52). Heterometallic rings, of the form $[R_2NH_2][Cr_7MF_8(O_2C^tBu)_{16}]$,[129] where one of the metals has been substituted, do not result in complete antiferromagnetic ordering and therefore give rise to magnetic ground states with S≠0 making them paramagnetic at low temperatures.[130]

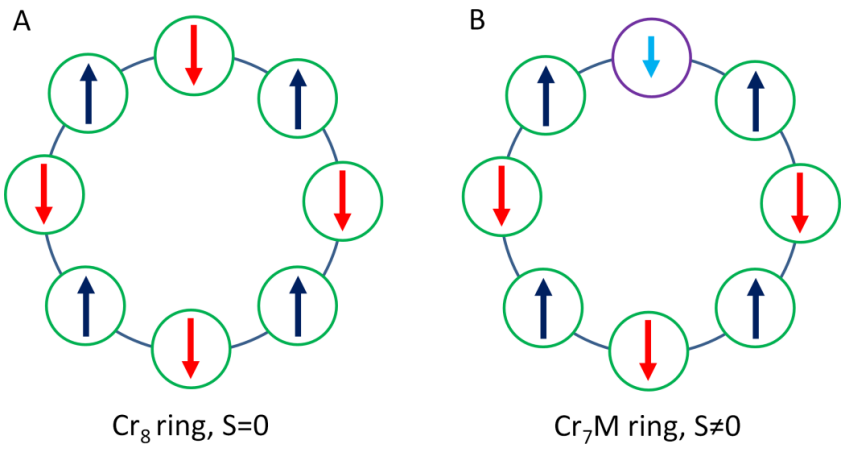


Figure 1.52 (A) Cartoon of complete antiferromagnetic ordering in homometallic Cr_8 ring complex. (B) Effect of substitution of one of the metal centres to cause incomplete antiferromagnetic ordering, giving rise to a magnetic ground state of S≠0.

One particular subgroup based on a Cr_7Ni ring structure has attracted considerable attention as a potential system to use in QIP.[131-134] The particular physical properties of this system are its 99% pure $S_{1/2}$ ground state[135], ability to retain a T_m of up to 15 µs at 1.5 K,[136-137] and unusually narrow ESR spectrum for a metal centred molecular magnet.[137] It has also been shown to be possible to link multiple Cr_7Ni units together via either threading the rings onto a long molecule to create a rotaxane or by substituting one of the axial ligands on the nickel site for either one that has chemical functionality or provides an active site for complexation.[132] To form a ring with a labile site at the nickel atom the chiral templating agent *N*-ethyl-D-glucamine is used to displace five of the fluoride ions and one pivalate ligand (see Figure 1.53), leaving water coordinated to the axial site of the nickel and an overall formula of $[Cr_7NiF_3(Etglu)(O_2CCMe_3)_{15}(H_2O)]$. The resulting complex acts as a Lewis acid, readily forming dative covalent bonds with Lewis bases such as pyridine. By using bridging groups with different geometries and a number of pyridine substituents it is possible to create multi-ring complexes with up to four Cr_7Ni rings.[138]

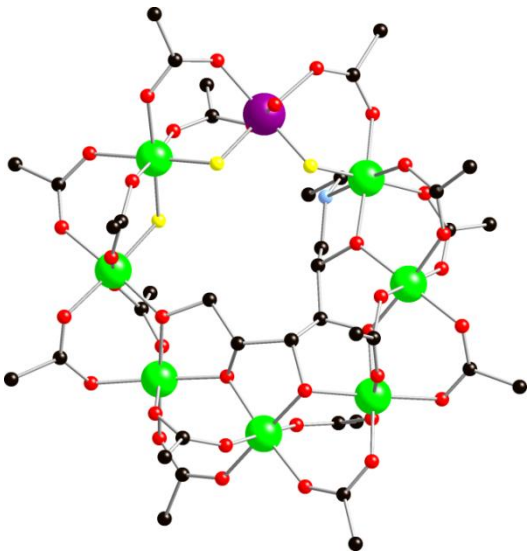


Figure 1.53 Crystal structure of Cr_7Ni ring with formula $[Cr_7NiF_3(Etglu)(O_2CCMe_3)_{15}(H_2O)]$, Etglu=*N*-ethyl-D-glucamine.[138] (black) carbon, (red) oxygen, (yellow) fluorine, (blue) nitrogen, (purple) nickel, (green) chromium. All hydrogen atoms and terminal methyls of pivalate groups are hidden for clarity.

The magnetic structure of Cr_7Ni has been both theoretically and experimentally explored.[130, 135] The first excited state is $S_{3/2}$ 1.2 meV (10 cm^{-1}) above the $S_{1/2}$ ground state, corresponding to an activation barrier of 13 K.[139] Above the first excited state, the magnetic structure is complex with eight further excited states closely spaced within the range of 22-40 cm^{-1} [135, 139] (see Figure 1.54). Additionally, the spin density has been shown to be uniformly distributed across all of the metal centres of the ring.[140]

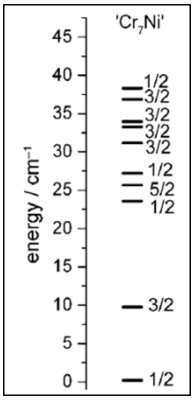


Figure 1.54 Calculated zero field energy spectrum of the ten lowest lying spin states of Cr_7Ni with formula $[R_2NH_2][Cr_7NiF_8(O_2C^tBu)_{16}]$. Adapted from Piligkos et al.139

The combination of pure $S_{1/2}$ ground state, reasonable T_1 and T_2 relaxation lifetimes, negligible ESR spectral overlap with $N@C_{60}$ and the potential ability to use coordination chemistry to link it to an $N@C_{60}$ moiety make it a very attractive system to use in an $N@C_{60}$ hetero dimer.

1.5 Thesis Motivation and Aims

To make further progress in assessing $N@C_{60}$ for use in a future QIP architecture the DiVincenzo criteria 3, 4 and 5 must be satisfied. To do this the creation of controlled entanglement between electron spins in an array of at least two magnetically distinct $N@C_{60}$ centres with fixed electron-electron coupling is required.[27] The ability to construct such a test system has up to now proved elusive. A two qubit array would already be sufficiently complex to test the implementation of key quantum logic elements such as the creation of a universal CNOT gate.[27] As 98% of the spin density of the unpaired electrons resides inside the fullerene cage, the most significant coupling interaction is expected to occur via electron-electron dipolar coupling rather than exchange coupling processes.[17] Since the magnitude of dipolar coupling is both distance dependant and angularly dependent with respect to the applied magnetic field[141] both of these parameters must be accurately controlled to fix the electron coupling interaction energy.[141] To date, macroscopic alignment has only been achieved on isolated $N@C_{60}$ and $N@C_{70}$ molecules using liquid crystal and single crystal matrices[22-23, 142-143] with no control over the local dipolar interaction of spin centres. The aims of this thesis are therefore as follows:

1. Construct an ensemble of two $N@C_{60}$ centre molecules with fixed spin spatial separation.
2. Model the spin coupling interaction between two weakly coupled $N@C_{60}$ centres.
3. Explore methods to create macroscopic alignment in two $N@C_{60}$ centre molecules.
4. Measure the impact that a weakly coupled hetero spin centre has on the length of time $N@C_{60}$ can store quantum information in a two qubit array.

Chapter 2 Analytical and Preparative Techniques

This chapter provides an introduction to the experimental techniques used in this thesis. I first detail the methods used to synthesise and purify N@C_{60}. I then introduce the theory behind CW and pulsed ESR spectroscopy, and polarised Raman spectroscopy. Finally I outline other common characterisation techniques used such as UV-Vis and FTIR spectroscopy, mass spectrometry, and 1D and 2D NMR.

2.1 Ion implantation of N@C_{60}

All ^{14}N@C_{60} and ^{15}N@C_{60} used in this thesis was synthesised using a custom built ion implantation set-up equipped with a low beam energy Oxford Applied Research DC 25s ion source and both $^{15}N_2$ and $^{14}N_2$ gas feeds (see Figure 1.1). The operation of the equipment is as follows. Initially, 0.5 g of 99% pure sublimated C_{60} purchased from MER is placed inside the effusion cell crucible below the centre of the target. The chamber is then sealed and evacuated to a pressure of between 10^{-5} and 10^{-6} Torr using a combination of diffusion pump and rotary pump over a period of around 12 hours. The temperature controller (Eurotherm 2200) is then set of the crucible to 200 ^{o}C for 20 minutes to bake out any moisture from the fullerene powder. The temperature is then ramped up to 375^{o}C at 10 ^{o}C min^{-1}, just below the temperature at which C_{60} sublimes. The N_2 gas source is turned on and the flow rate set to 0.2 CCM, causing the pressure inside the chamber to rise to between 7-10 x 10^{-5} Torr.

The ion source is set to a N^+ beam energy of 40 eV and an acceleration voltage of 500 V, providing an N^+ beam current of 0.5-1.2 mA incident on the target. The temperature controller is then set to ramp up very slowly to 520^{o}C at 0.1^{o}C min^{-1} to maintain a constant deposition rate of 0.5-2 Ås^{-1}. After a period of 24 hours, a 5 μm film of implanted C_{60} has been deposited on the target, implantation the apparatus is then turned off and the fullerene film scraped from the target to yield approximately 200

mg of carbon material. Of this material, 100-150 mg is soluble and primarily contains a mixture of $N@C_{60}/C_{60}$ in the ratio of 6×10^{-5} : 1, determined by ESR spectroscopy.

2.2 HPLC purification

2.2.1 Introduction

High Pressure Liquid Chromatography (HPLC), also known as High Performance Liquid Chromatography, is a well established versatile liquid chromatographic technique that can be use as both a quantitative analytical tool as well as a reproducible method for preparative scale purification. HPLC is the principal method used to enrich $N@C_{60}$ and purify all fullerene derivatives synthesised in this thesis.

Figure 2.1 illustrates the main components common to all HPLC instrumentation. Initially, the sample for analysis/ purification is dissolved using a minimum quantity of mobile phase and injected into the instrument upstream of the column. The mobile phase is then drawn from the solvent reservoir and pressurised to between 80-150 atm. The sample is transported first to a guard column whereby any compounds that have too greater an affinity to the stationary phase of the column, known as 'sticking to the column', are retained and removed from the sample. The sample then passes on to the column and the different components are separated based on their strength of interaction with the stationary phase. The stronger the interaction the longer it is retained on the column. Each compound has a characteristic 'retention time' using a particular set of condition that can be used for its identification and isolation. The composition of the eluent mixture is subsequently probed using a UV-Vis or IR spectrometer to yield an absorption vs time trace of the mixture. If the difference in retention time between components is sufficient then the eluting mixture exits the instrument and each compound can be collected as a different fraction. If however incomplete separation of the components is apparent then the eluting mixture can be circulated back onto the column using a recycling valve to increase separation.

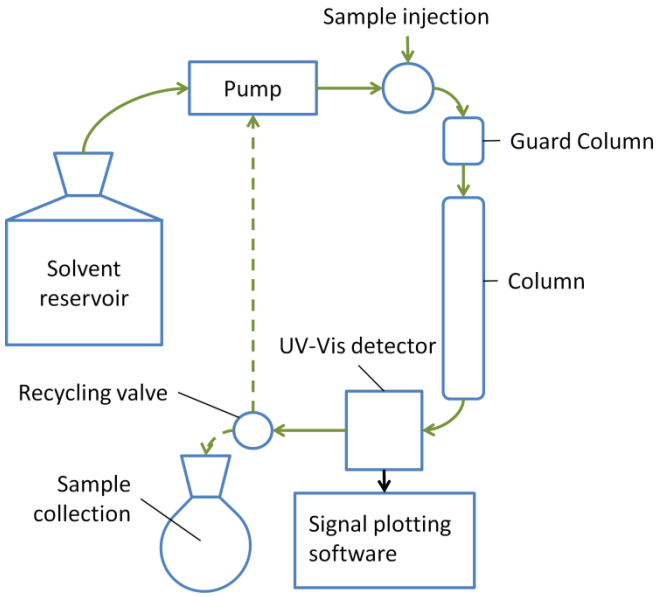


Figure 2.1 Schematic of an HPLC instrument with recycling mode.

2.2.2 Purifying N@C_{60}

The C_{60} film recovered from ion implantation is dissolved in toluene over night and filtered using a 0.22 µm filter. The soluble component of this extraction primarily contains a mixture of N@C_{60}/C_{60} in the ratio of 6 x 10^{-5}:1. As noted in Chapter 1, C_{60} and N@C_{60} have very similar physical and chemical properties, making it difficult to isolate the trace quantity of N@C_{60} from the C_{60} bulk. To achieve complete separation, I used a two stage iterative recycling HPLC purification procedure.

The first stage uses a large preparative scale JAI LC-200 HPLC instrument equipped with a 100 mm x 500 mm 15 PBB column to efficiently separate 95 % of the C_{60} bulk from the N@C_{60}. 20-150 mL of concentrated N@C_{60}/C_{60} toluene solution (~2 mg mL^{-1} concentration) is loaded onto the column and recycled twice. On the third cycle, the peak is collected and split in half at the apex with the second fraction containing ≈95 % of the N@C_{60} molecules. The second half of the peak is retained and concentrated to 2 mg mL^{-1} using a rotary evaporator. This procedure is repeated until the entire sample has been processed which was 11 times for the +50 % purity N@C_{60} sample used in chapter 3. The enrichment of N@C_{60} to C_{60} achieved from one stage is 1.4-1.5. To remove 95 % of C_{60} component, the procedure is repeated a further seven times retaining and injecting the second half of the peak each time. Each injection takes 3 hours to run from injection to collection plus an additional 3 hours to

recover the 12 L of solvent that is collected and to concentrate the $N@C_{60}$ containing fraction before reinjection using three 2L bench top rotary evaporators in parallel.

The second stage uses a preparative JAI LC 908-W HPLC instrument equipped with a 25 x 250 mm 5 μm PBB Cosmosil column to purify the partially enriched $N@C_{60}/C_{60}$ mixture to up to near 100 % pure $N@C_{60}$. 0.4-2.5 mL sample volume is loaded onto the column and recycled between 5-6 times. Due to the smaller size of the silica gel particles, 5 μm instead of 15 μm used in stage 1, the separation of peaks is enhanced, with the smaller column cross section improving the signal to noise of the HPLC trace. On the final cycle, the peak is collected and split in half at its apex with the second fraction containing ≈95 % of the $N@C_{60}$ molecules. The second half of the peak is retained and concentrated using a rotary evaporator. This procedure is repeated until the entire sample has been processed. The enrichment of $N@C_{60}$ to C_{60} achieved from one stage is 1.55-1.6. To isolate a +50 % purity $N@C_{60}$ component the procedure is repeated a further 14 times retaining and injecting the second half of the peak each time. The time required to achieve a 50 % purity sample from 3 g of raw implanted material using this setup is between 2 and 3 months. The theoretical yield of the enrichment process from 60 ppm $N@C_{60}$ in C_{60} to 50 % $N@C_{60}$ is $(95\ \%)^{22}$=32 % i.e. from 3 g of 60 ppm material it should be possible to produce 96 μg of 50 % $N@C_{60}$ in C_{60}. This theoretical yield is achieved for enrichment up to around 1% $N@C_{60}$ in C_{60} however as the purity of $N@C_{60}$ is increased further, the yield after each enrichment step reduces significantly. In the case of the +50 % $N@C_{60}$ sample produced in this thesis, from 3 g of 60 ppm $N@C_{60}$ in C_{60} only 10 μg of +50 % $N@C_{60}$ material was produced giving a total yield of 3.2 %. The cause of this yield reduction is currently not known, but is an issue that must be addressed.

2.3 ESR spectroscopy

2.3.1 CW ESR

Continuous Wave (CW) Electron Spin Resonance (ESR) Spectroscopy is used throughout this thesis to probe the distribution of spin transition present in the ground state of N@C_{60}. By sweeping the static magnetic field, the energy separation between spin states is modulated. If the energy separation is resonant with the applied fixed microwave (mw) frequency the sample absorbs a fraction of the mw radiation in the resonator. Since the resonator is critically coupled all of the incident mw radiation is absorbed, reflecting none back to the detector. When the sample absorbs a fraction of the radiation, the resonator becomes detuned and a fraction of the mw radiation is reflected back to the detector, producing a signal. All N@C_{60} CW spectra recorded in this thesis use X-band frequency mw radiation (~9.5 GHz) with $B_0 \approx 0.33\ T$. The two spectrometers used were a Magnetech ms200 and Bruker EMX.

2.3.2 Static Spin Hamiltonian

To interpret the observed CW ESR spectrum of N@C_{60}, the energy and density of spin transitions must be characterised. The total distribution of energies within the ground state of a paramagnetic molecule that has a particular electron spin quantum number *S* and *m* nuclei with nuclear spin numbers *I* can be expressed generally in terms of the static spin Hamiltonian (Equation 2.1)

$$\hat{\boldsymbol{H}} = \hat{H}_{EZ} + \hat{H}_{ZF} + \hat{H}_{HF} + \hat{H}_{NZ} + \hat{H}_{NQ} + \hat{H}_{NN} \quad (2.1)$$

With $\hat{H}_{EZ}$: the electron Zeeman interaction; $\hat{H}_{ZF}$: zero-field splitting; $\hat{H}_{HF}$: the hyperfine coupling interactions between the electron spin and *m* nuclei; $\hat{H}_{NZ}$: nuclear Zeeman interactions; $\hat{H}_{NQ}$: nuclear quadrupole interaction and $\hat{H}_{NN}$: the dipolar and exchange interaction between pairs of nuclear spins.

This thesis deals with systems that contain two interacting electron spin systems that are weakly coupled. In these systems it is common to treat each of the spin centres as having a well defined spin, S_1 and S_2, with an associated spin Hamiltonian of the form of Equation 2.1 and introduce two additional

cross coupling terms; $\widehat{H}_{EX}$: an electron spin exchange interaction and $\widehat{H}_{EE}$: an electron spin dipole-dipole interaction (Equation 2.2)

$$\widehat{\boldsymbol{H}}(S_1, S_2) = \widehat{\boldsymbol{H}}(S_1) + \widehat{\boldsymbol{H}}(S_2) + \widehat{H}_{EX} + \widehat{H}_{EE} \qquad (2.2)$$

At the static field strengths of around 0.3 T (X-band) used in this thesis, the most dominant term in a spin Hamiltonian of N@C_{60} is the electron Zeeman interaction. This term characterises the interaction between the electron spin and the static applied magnetic field $\boldsymbol{B}_0$, note that a tilde ($\widetilde{}$) is used to indicate the transpose i.e. $\widetilde{\boldsymbol{B}}_0$. The strength of this interaction is governed by the symmetric tensor $\boldsymbol{g}$ with three principal values g_x, g_y, g_z known as g-values. For the I_h high symmetry environment of N@C_{60} these three values are identical hence can be defined as a single scalar value $g_{iso} = g_x = g_y = g_z$ (Equation 2.3). For first row p-block centred paramagnetic molecules, like N@C_{60}, g-values are typically close to that of the free electron value of $g_e = 2.002319$.

$$\widehat{H}_{EZ} = \frac{\mu_B \widetilde{\boldsymbol{B}}_0 \boldsymbol{g} \boldsymbol{S}}{\hbar} \qquad (2.3)$$

When the symmetry of N@C_{60} is reduced by chemical modification, the degeneracy of the $S_{3/2}$ ground state is lifted due to the electrostatic dipolar coupling between the unpaired electrons. This interaction is called *zero-field splitting,* since this interaction is an electrostatic in origin, the magnitude of the splitting is independent of the applied B_0 field.

$$\widehat{H}_{ZF} = \widetilde{\boldsymbol{S}} \boldsymbol{D} \boldsymbol{S} \qquad (2.4)$$

The zero-field splitting interaction tensor ***D*** tensor is both symmetric and traceless. By using the principal axis system of the ***D*** tensor it is possible to describe the tensor using two scalar parameters D and E. D is known as the axial zero-field splitting term with a value of $D = 3D_z/2$ and E is known as the rhombohedral term with a value of $E = (D_x - D_y)/2$.

$$\widehat{H}_{ZF} = D_x S_x^2 + D_y S_y^2 + D_z S_z^2 = D\left\{S_z^2 - \frac{1}{3}S(S+1)\right\} + E\left(S_x^2 - S_y^2\right) \qquad (2.5)$$

The coupling between the electron and nuclear spins is known as the hyperfine interaction and is characterised by the tensor ***A***. ***A*** is composed of two forms of interaction, an isotropic Fermi contact interaction a_{iso}, with $\mathbb{I}$ equal to the identity operator, and the electron-nuclear dipolar coupling tensor ***T***.

$$\widehat{H}_{HF} = \sum_{i=1}^{m} \tilde{\boldsymbol{S}}\boldsymbol{A}\boldsymbol{I}_i \; ; \; \boldsymbol{A} \quad = a_{iso}\mathbb{I} + \; \boldsymbol{T} \qquad (2.6)$$

In the case of N@C_{60}, $g_x \approx g_y \approx g_z$, permitting **T** to be transformed to use the hyperfine principal axis system to traceless diagonal tensor that can be described by axial and rhombohedral parameters, much like the zero field interaction. Since 98% of the spin density of N@C_{60} is located on the nitrogen nuclei the hyperfine interaction can be approximated to only a single interaction of the electron spin with the central ^{14}N or ^{15}N nuclei.

The nuclear Zeeman term describes the interaction of the nuclear spins with the static magnetic field. Each nucleus has a fixed nuclear g-factor g_n and nuclear spin quantum number *I*, giving rise to a characteristic coupling strength at a particular $\mathbf{B}_0$ static field. Table 2.1 has the g_n and *I* values for a selection of common isotopes. The nuclear Zeeman interaction magnitude of the isotopes in Table 2.1 is between 650 – 9000 times smaller than the electron Zeeman interaction. Due to this the nuclear Zeeman term contribution to the ESR spectrum is usually small.

$$\widehat{H}_{NZ} = -\sum_{i=1}^{m} \frac{g_n^i \mu_N \tilde{\boldsymbol{B}}_0 \boldsymbol{I}_i}{\hbar} \qquad (2.7)$$

Isotope	*I*	g_n	Natural abundance %
^{1}H	1/2	5.5857	99.9885
^{2}H	1	0.8574	0.0115
^{13}C	1/2	1.4048	1.07
^{14}N	1	0.4037	99.632
^{15}N	1/2	-0.5664	0.368
^{19}F	1/2	5.2577	100

Table 2.1 Nuclear spin quantum numbers and nuclear g-values for common isotopes. Values taken from.[144]

The nuclear quadrupole interaction tensor $\boldsymbol{Q}$ characterises the non-spherical charge distribution of $I > 1/2$ nuclei with the surrounding electric field gradient. In $^{14}N@C_{60}$ this term is usually neglected so will be omitted from the model spin Hamiltonians used here.

$$\widehat{H}_{NQ} = \sum_{\boldsymbol{I_i}>\frac{1}{2}} \tilde{\boldsymbol{I}}_{\boldsymbol{i}} \boldsymbol{Q} \boldsymbol{I}_{\boldsymbol{i}} \qquad (2.8)$$

The nuclei-nuclei coupling interaction is expressed as a sum of all pair wise interactions of the nuclei present. The magnitude of this interaction is governed by the nuclei-nuclei coupling tensor **P.** In an organic molecule, this term usually has by far the largest number of elements (m^2-m), which in a isotropic solid state ESR spectrum must be averaged over all orientations with respect to B, due to the angularly dependent dipole-dipole interaction contribution to **P**. This is very computationally expensive; however since this interaction is too small to be detected in an ESR spectrum it will also be omitted from the spin Hamiltonian.

$$\widehat{H}_{NN} = \sum_{i \neq h}^{m} \tilde{\boldsymbol{I}}_i \boldsymbol{P}^{(\boldsymbol{i},\boldsymbol{h})} \boldsymbol{I}_h \qquad (2.9)$$

As mentioned at the beginning of the section when two weakly coupled electron spin centres are present S_1 and S_2, two additional cross-coupling terms are included in the Hamiltonian. The exchange interaction term $\widehat{H}_{EX}$ characterises the strength and nature of the overlap between the electronic wave functions of the two-spin centres. $\widehat{H}_{EX}$ is usually dominated by the isotropic Heisenberg exchange interaction in organic molecules which is described by the scalar term K_{iso}. In the case of $N@C_{60}$ only 98% of the electron spin density resides on the nitrogen atom. This leads to the expectation that the importance of this term to be less than for a typical nitrogen centred radical such as ^{14}N nitroxides for which $\widehat{H}_{EX}$ is significant when the spin centres are either delocalised in a conjugated system or separated by less than about 15 Å.[145]

$$\widehat{H}_{EX} = K_{iso} \tilde{\boldsymbol{S}}_1 \boldsymbol{S}_2 \qquad (2.10)$$

The electron-electron dipolar interaction term $\widehat{H}_{EE}$ is characterised by the tensor $\boldsymbol{J}$ (see Equation 2.11). If the two spins are well localised, the point dipole approximation can be applied and $g_x \approx g_y \approx g_z$ then $\boldsymbol{J}$ can be transformed to use the dipole-dipole principal axis system to form a diagonalised traceless tensor $\boldsymbol{J}^{diag}$. $\boldsymbol{J}^{diag}$ has a single coupling term j_{dip} with $r_{1,2}$ equal to the separation of the two-spin centres (2.12).

$$\widehat{H}_{EE} = \tilde{\boldsymbol{S}}_1 \boldsymbol{J} \boldsymbol{S}_2 \qquad (2.11)$$

$$\boldsymbol{J}^{\boldsymbol{diag}} = j_{dip} \begin{pmatrix} -1 & & \\ & -1 & \\ & & 2 \end{pmatrix}; \; j_{dip} = \frac{\mu_0 \mu_B^2 g_{iso}^{(1)} g_{iso}^{(2)}}{4\pi\hbar r_{1,2}^3} \qquad (2.12)$$

For a simple two $S_{1/2}$ spin centre system the dipolar interaction energy ω_{EE} can be described as the polar angle θ_{dip} between the static magnetic field direction $\boldsymbol{B}_0$ and the vector connecting the centre of S_1 with S_2 using Equation 2.13. The angular dependence for two dipolar coupled $S_{1/2}$ electron spin centres is plotted in Figure 2.2. For S > ½ systems such as N@C_{60} ($S_{3/2}$) the interaction is more complicated.[146] One reason is that dipolar coupling to S > ½ systems give rise to multiple ω_{EE} angular distributions for each of the 2S+1 eigenstates of the system.[146] In this thesis I have used the 'pepper' simulation function of the EasySpin Matlab toolbox[147] developed by Stefan Stoll and Arthur Schweiger to simulate all ESR spectra that include a $\widehat{H}_{EE}$ dipolar interaction term with at least one S>½ spin centre. The 'pepper' function is specifically designed to simulated solid state ESR spectra and is capable of dealing with systems that contain multiple nuclei that contain S > ½ spin centres.[147]The ability for the 'pepper' function to correctly simulate the dipolar coupling interaction between two free $S_{3/2}$ electron spin centres, with no nuclei, was qualitatively tested for by simulating the spectra of varying angles of the inter-spin axis with respect to B_0 to confirm that the expected 2S+1 transitions are observed.

$$\omega_{EE} = j_{dip} \left(3\cos^2\left(\theta_{dip}\right) - 1 \right) \qquad (2.13)$$

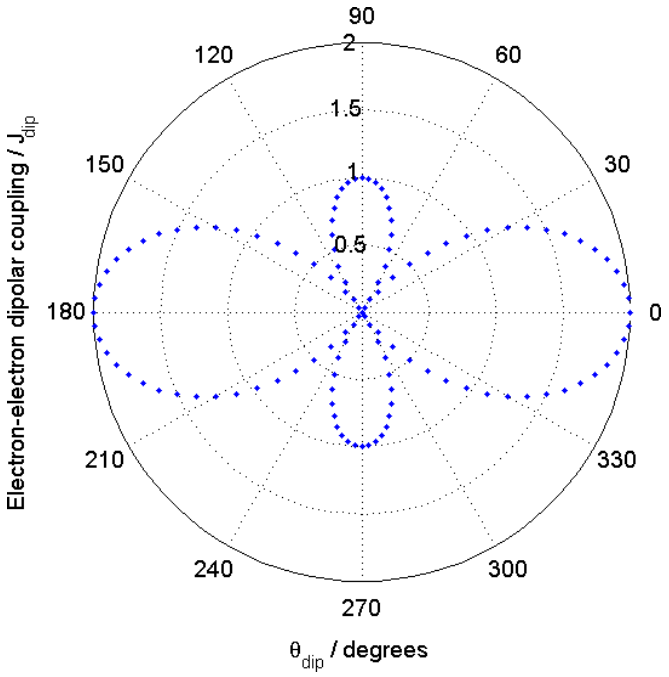


Figure 2.2 Plot of electron-electron dipolar coupling energy ω_{EEI} between two $S_{1/2}$ spin centres as a function of the angle θ_{dip} of the inter-spin vector with the direction of the applied static magnetic field B_0.

2.3.3 Pulsed ESR

Pulsed ESR is a powerful technique for manipulating and measuring the transient magnetisation of paramagnetic centres using microwave radiation. It is the sole method used in Chapters 4 and 5 to measure the longitudinal (T_1) and transverse (T_2) magnetisation relaxation time of N@C_{60}. It is also the most common method used to create, manipulate and read out the entangled electron-spin quantum states required to implement an electron spin based quantum computer.[18, 20, 132-133, 148-151] Owing to these points it is worth explaining, using a simple vector representation, how pulsed ESR can manipulate and measure the magnetisation of an ensemble of spin centres.

I will start by defining the magnetic moment of the simplest spin system, a single electron, as $\mu = -g_e \mu_B \boldsymbol{S}$. In an ensemble of many magnetic moments, the net magnetic moment per unit volume is defined as the macroscopic magnetisation $\boldsymbol{M}$. When a static magnetic field is applied $\boldsymbol{B}_0$, **M** will evolve according to the following equation until the angle ϑ between $\boldsymbol{M}$ and $\boldsymbol{B_0}$ is minimised, while conserving angular momentum.

$$\frac{d\boldsymbol{M}}{dt} = \frac{-g_e\mu_B}{\hbar}(\boldsymbol{M} \times \boldsymbol{B}_0) = \frac{-g_e\mu_B}{\hbar}(|\boldsymbol{M}||\boldsymbol{B}_0| \cdot \sin\,\vartheta) \qquad (2.14)$$

Once a stationary state is reached, $\boldsymbol{M}$ can be thought of as precessing on a cone about $\boldsymbol{B}_0$ with angle ϑ and angular frequency ω_s.

$$\omega_s = \frac{g_e\mu_B\boldsymbol{B}_0}{\hbar} \qquad (2.15)$$

If the frame of reference is now shifted from the laboratory frame to that of a rotational frame which rotates about the direction of $\boldsymbol{B}_0$ at ω_s, the physical effect of applying a linearly polarised microwave pulse with angular frequency $\omega_{mw} = \omega_s$ can be visualised. Hence from now on I will use the x, y and z rotating frame coordinate system rather than the laboratory axes, with the direction of $\boldsymbol{B}_0$ taken as the z-axis of the rotating frame. A linear polarised microwave pulse in the x-axis can be thought of as a superposition of two oppositely handed circularly polarised electromagnetic fields. Only the component that rotates in the same direction as ω_s will have an angular frequency of $\omega_{mw} = \omega_s$ and will interact significantly with $\boldsymbol{M}$. In the rotating frame, this circularly polarised component of the microwave field $\boldsymbol{B}_1$ is static and exerts an additional precession of $\boldsymbol{M}$ about the x-axis with angular frequency ω_1.

$$\omega_1 = \frac{g_e\mu_B\boldsymbol{B}_1}{\hbar} \qquad (2.16)$$

The effect of applying a linearly polarised microwave pulse in the x-axis for duration t_p on the components of $\boldsymbol{M}$ - M_x, M_y, M_z with an equilibrium magnetisation of M_z^0 equal to M_Z is represented in Equation 2.17.

$$\begin{cases} M_x = 0 \\ M_y = -M_z^0 sin(\omega_1 t_p) \\ M_z = \ M_z^0 \cos\,(\omega_1 t_p) \end{cases} \qquad (2.17)$$

The application of a mw pulse rotates M_z^0 in the zy plane by an angle $\omega_1 t_p$ known as the tip angle. The resulting magnetisation after a tip angle of π or $\frac{\pi}{2}$ is shown in Equation 2.18 and pictorially in Figure 2.3:

$$t_p\begin{cases}M_x=0\\M_y=0\\M_z=-M_z^0\end{cases}\xleftarrow[\omega_1 t_p=\pi]{}t_0\begin{cases}M_x=0\\M_y=0\\M_z=M_z^0\end{cases}\xrightarrow[\omega_1 t_p=\frac{\pi}{2}]{}t_p\begin{cases}M_x=0\\M_y=-M_z^0\\M_z=0\end{cases}\qquad(2.18)$$

Since the tip angle depends on both ω_1 and t_p it can be controlled in two ways. Changing the power of the mw pulse alters the field $\boldsymbol{B}_1$, so modifying $\omega_1$according to (2.16). Alternatively, the length of t_p can be changed. Owing to the easier fast manipulation of the duration of t_p rather than the magnitude of $\boldsymbol{B}_1$, experimental measurements are usually made using a fixed $\boldsymbol{B}_1$ and a variable pulse length t_p to produce the desired tip angle.

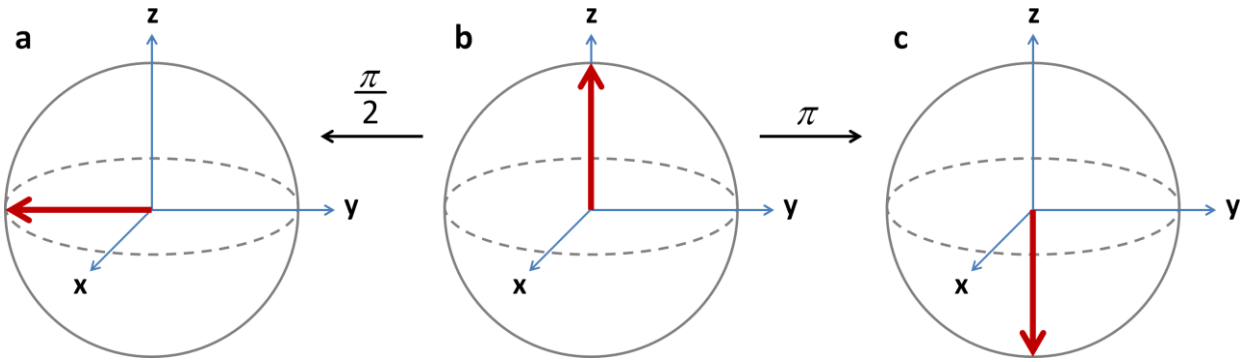


Figure 2.3 Vector representation of the resulting change in magnetisation on a Bloch sphere after a $\frac{\pi}{2}$ (a) or π (c) pulse along the x-axis with initial magnetisation M_z^0 (b).

2.3.4 Relaxation

So far, I have only discussed an ideal system in which $\omega_{mw}=\omega_s$ and $\frac{dM_z^0}{dt}$ = 0. In a real Pulsed ESR experiment this is not true, causing the magnetisation to evolve in the time after a mw pulse. The principal effect of this is to relax the sample to a lower energy state. The two main mechanisms for relaxation are *longitudinal relaxation* characterised by a time T_1 and *transverse relaxation* characterised by a time T_2. Longitudinal relaxation causes M_z to exponentially relax towards M_z^0 at a rate $\frac{dM_z}{dt}=\frac{-(M_z-M_z^0)}{T_1}$ (see Figure 2.4 a-b). This relaxation mechanism occurs via the change of the magnetic quantum number of a spin system. To do this, each spin system must absorb or emit the corresponding quanta of energy ω_s. This is achieved though coupling to the surrounding environment or 'lattice' and exchanging the required quanta of energy ω_s via local magnetic fluctuations of the

environment. For this resonant exchange interaction, the T_1 lifetime increases as the amplitude of the magnetic fluctuations at ω_s decreases.

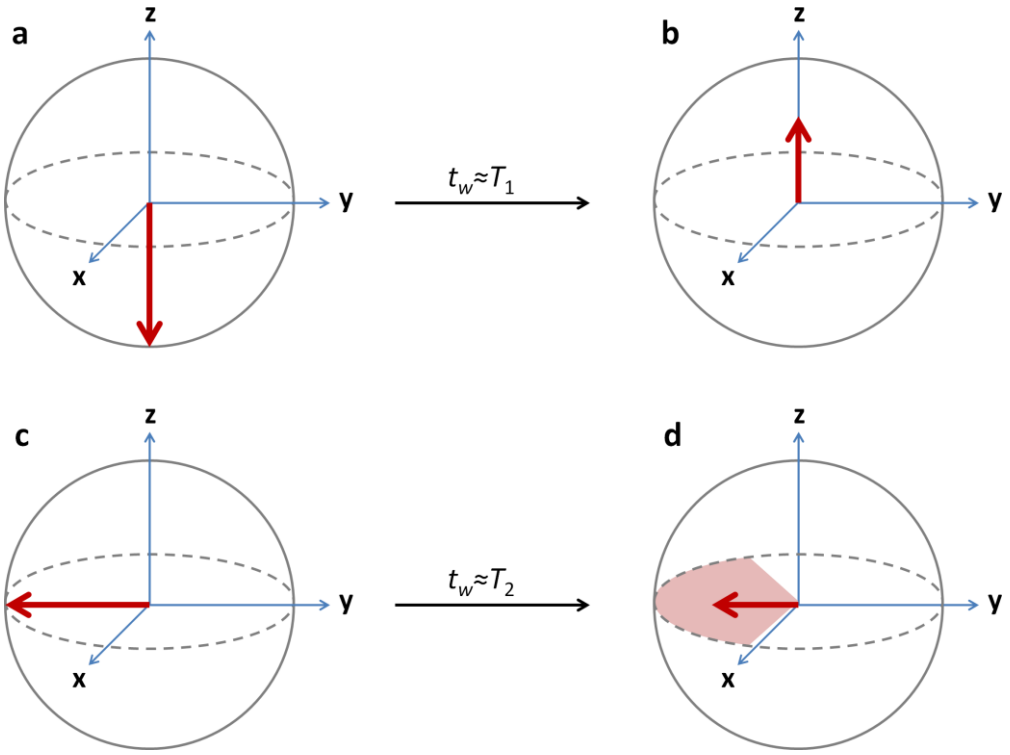


Figure 2.4 Vector representation of an xy-magnetised spin packet (a) undergoing T_2 relaxation (b) after a t_w time comparable to T_2. After an initial π pulse(c) the T_1 relaxation of M_z towards the equilibrium magnetisation (d) is observed after a t_w time comparable to T_1.

The transverse relaxation time T_2 characterises the rate that coherent magnetisation in the xy plane is lost. This arises in part through the same energy exchange process governing T_1. However, since $T_2 \ll T_1$, particularly in solids and at low temperature, this is normally neglected. The principal mechanism occurs via the change in local magnetic environment of the individual spin centres during the course of a measurement, causing a distribution in ω_s to occur. This can be thought of as a 'fanning out' of the xy components of spin centres about the z axis and a net reduction in the magnitude of the xy magnetisation component (see Figure 2.4.c-d). When the relative motion is fast and the correlation time is small compared to the inverse of the magnetic interaction between spin centres, i.e. the liquid state, transverse relaxation normally occurs via spin-spin relaxation whereby a pair of spin centres exchange energy and states. In the solid-state, transverse relaxation is usually dominated by dipolar coupling with the surrounding nuclei and electron spins. This can give rise to distribution of relaxation

rates that is strongly dependent on the lattice. Owing to this it is common to discuss transverse relaxation using a phenomenological parameter T_m known as the phase memory time and characterises the shape of the echo decay profile (see *Hahn Echo* below) with time; T_m can be influenced by a number of processes which include:

Spectral diffusion - this refers to the processes that move spin magnetisation between different locations in the ESR spectrum. If this process moves the magnetisation to a frequency outside of the excitation bandwidth centred at ω_{mw} then the T_m appears reduced. This can occur in both electron-electron and electron-nuclear processes.

Instantaneous diffusion - refers to the process whereby an excited spin is coupled to another spin centre with a frequency inside of the excitation bandwidth centred at ω_{mw} which is then flipped during the refocusing pulse of an echo detection sequence. This causes the local magnetic field of the initially excited spin to change and so appear as a reduction in T_m.

Nuclear spin diffusion - refers to the process by which pairs of nuclei with similar Zeeman energy exchange magnetic states. This interaction changes the hyperfine interaction and so changes ω_s, leading to T_m dephasing.

A lorentzian broadening of the spin packet is also seen by the T_1 relaxation of adjacent dipolar coupled electron-spin centres which are not excited during a pulse sequence.

The measurement of relaxation can be achieved using a number of different pulse sequences. The two that are used in this thesis are *inversion recovery* to measure T_1 and *Hahn echo* to measure T_m. The *inversion recovery* pulse sequence works by inverting M_z by applying a π puse in the x-axis then waiting a fixed time t_d and then performing a Hahn echo to measure $M_z^{t_d}$. The pulse sequence is as follows: $\pi - t_d - \frac{\pi}{2} - \tau - \pi - \tau - echo$. By incrementing t_d, the decay of M_z can be measured, permitting T_1 to be extracted by fitting the profile to $M_z^{t_d} - M_z^0 \propto e^{\frac{-t_d}{T_1}}$. The *Hahn echo* works by removing the time

independent transverse dephasing processes after a $\frac{\pi}{2}$ pulse by applying a π pulse at time τ to reverse the dephasing processes and form and 'echo' at time 2τ. The sequence is as follows: $\frac{\pi}{2} - \tau - \pi - \tau - echo$. The length of τ is incrementally increased and the echo decay profile is recorded, which T_m can be fitted to. All pulsed measurements used in this thesis were made using a Bruker Elexsys E680 spectrometer using one of two resonators, either a Bruker X-band pulse-ENDOR dielectric resonator (EN 4118X-MD4) or an X-band dielectric resonator (EN 4118X-MD5).

The T_1 and T_2 lifetimes for a radical also have a significant impact on the shape of CW ESR line width, with the intrinsic line width of a transition proportional to the sum of the T_1 and T_2 lifetimes $[\frac{1}{T_1} + \frac{1}{T_2}]$. In the case of N@$C_{60}$ at room temperature and in solution, both T_1 and T_2 are long, giving rise to a line width that is extremely narrow, experimentally determined[47] to be < 0.3 μT. The long T_1 and T_2 times for N@C_{60} also cause the CW ESR spectrum to 'saturate' (i.e. deplete the ground state of a resonant transition away from thermal equilibrium resulting in a distorted spectral line shape) under much smaller applied microwave fields than typical nitrogen centred radicals. Typical room temperature solution CW ESR spectrums of N@C_{60} at X-Band are collected using an applied microwave field of 0.3 mW together with the smallest modulation amplitude achievable given the inhomogeneity of B_0 with a particular spectrometer, which is typically 100-200 mG. This leads to line widths of ≈150 mG as shown in figure 1.6.

2.5 Polarised Raman spectroscopy.

In Chapter 4, I use polarised Raman spectroscopy to characterise the alignment of an C_{60}-C_{60} dimer molecule within an elastomer host matrix. I will now explain the basic theory of Raman spectroscopy and how this technique can be used to measure the alignment of a molecular system.

Raman spectroscopy is based on the inelastic scattering of photons from a sample. Under normal conditions, this process occurs via the excitation of the ground state of a molecule to a virtual state by

a photon hv_{ex}, which subsequently relaxes back to the ground electronic state via the emission of a photon. The majority of the relaxation is elastic, emitting a photon hv_r with equal energy to the incident energy $hv_r = hv_{ex}$, this is known as Rayleigh scattering. When relaxation from the virtual state is inelastic the photon either gains or losses a quantum of energy corresponding to an increase or decrease in the vibrational state of the molecule (see Figure 2.5). If relaxation results in an increase in vibrational state hv_{vib} a photon with energy $hv_s = hv_{ex} - hv_{vib}$ is emitted, producing a band of photons with slightly less energy than hv_{ex} corresponding to vibrational states of the molecule, this is known as the Stokes band. When the vibration state of the molecule decreases, the emitted photon $hv_{as} = hv_{ex} + hv_{vib}$, forming a band of photons with slightly more energy than hv_{ex} known as the Antistokes band. At room temperature the majority of molecules are in the ground vibrational state causing the stokes band to be more intense than Antistokes. [152] Owing to this, the Stokes band is the band that is commonly used in Raman spectroscopy.

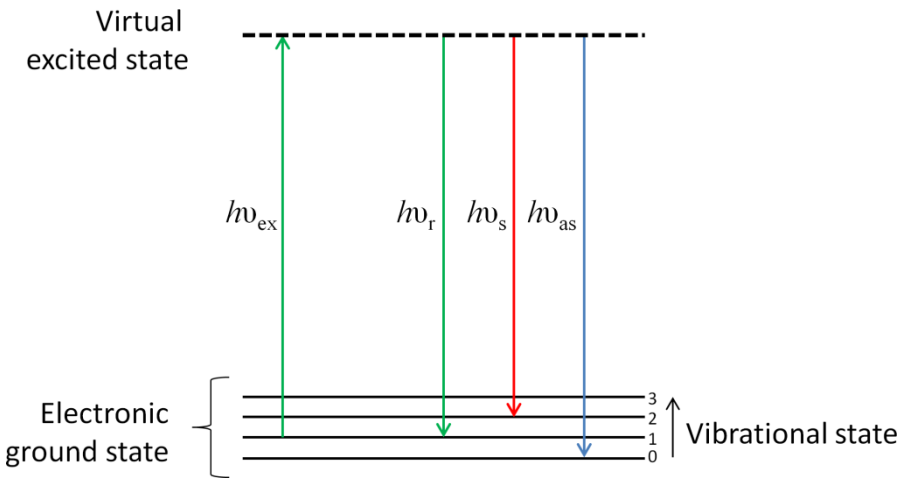


Figure 2.5 Different scattering processes that occur during Raman scattering. hv_{ex} – Excitation energy. hv_r – Rayleigh scattering. hv_s – Stokes scattering. hv_{as} – Antistokes scattering.

For Rayleigh scattering the strength of the induced dipole moment $\boldsymbol{\mu_i}$ is related to the incident radiation $\boldsymbol{E}$ by the symmetric polarisability tensor $\boldsymbol{\alpha}$ by $\boldsymbol{\mu_i = \alpha E}$**.** For a vibration to be Raman active the transition moment dipole operator must transform as one or a combination of the quadratic symmetry terms $x^2, y^2, z^2, xy, yz, zx$ with the component of the t μ_k^{vib} equal to:

$$\mu_k^{vib} = \left(\frac{d\boldsymbol{\alpha}}{dQ}\right)\boldsymbol{E} = \boldsymbol{\alpha}'\boldsymbol{E} \qquad (2.19)$$

With Q being the magnitude of the spatial displacement of the atoms in the molecule from their equilibrium position during the vibration. Like $\boldsymbol{\alpha}$ the first derivative $\boldsymbol{\alpha}'$ is also symmetric. By only measuring vibrational bands which are totally symmetric (i.e. only transform as combinations of x^2, y^2, z^2) only the principal diagonal component of $\boldsymbol{\alpha}'$ are non zero, adding further simplification.[153] The effect of rotating a single molecule in the xy-plane by an angle (θ) on the intensity I of the Parallel (I_{zz}) and perpendicular (I_{yz}) components of scattered light can be visualised using a simple model system. The model assumes that the molecule is an ideal rod-like shape, with $\alpha'_{xx} = \alpha'_{yy} = 0$, $\alpha'_{zz} \neq 0$ and the incident radiation polarised in the z-direction E_z. The angular dependence of the induced dipole at this frequency is thus greatly simplified too.[154]

$$\mu'_{zz}(\theta) = \alpha'_{zz} E_z cos^2\theta \qquad (2.20)$$

Since $I \propto \mu^2$the intensity of I_{zz} and I_{yz} are given by[153]:

$$I_{zz}(\theta) \propto \alpha'^2_{zz} cos^4\theta \qquad (2.21)$$

$$I_{yz}(\theta) \propto \alpha'^2_{zz} cos^2\theta sin^2\theta \qquad (2.22)$$

The form of the resulting I_{zz} and I_{yz} angular intensity profiles for this ideal single molecular system can be seen in Figure 2.6.

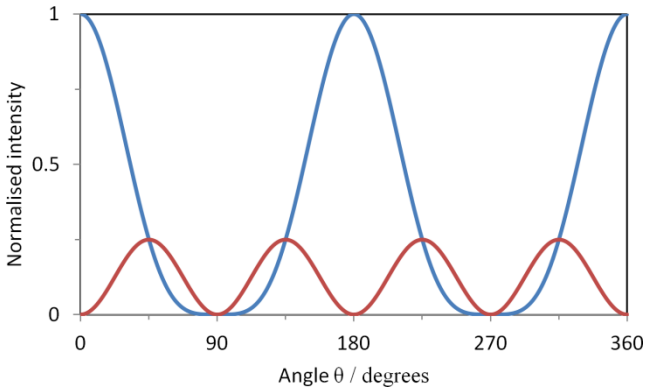


Figure 2.6 Angular dependence of I_{zz} and I_{yz} (red) components of scattered light, calculated from Equations 2.21 and 2.22 for single molecule oriented along the z-axis with only $\alpha'_{zz} \neq 0$ and the incident light polarised along the z-axis also.

In a real sample, the orientation of the molecules may be distributed in three dimensions. For a cylindrically symmetric molecule this Orientation Distribution Function (ODF) can be expressed in terms of the polar angle β about a vector and two orientation parameters P_2 and P_4 (2.23). If the directional vector for β is chosen as the alignment direction of a system (stretch direction of a polymer) then P_2 is equivalent to the Herman's orientation factor which is often used to characterise the degree of alignment in a system.

$$ODF(\beta) = \frac{1}{8\pi^2}\left\{1 + \frac{5}{2}\langle P_2\rangle(3cos^2\beta - 1) + \frac{9}{8}\langle P_4\rangle(3 - 30cos^2\beta + 35cos^4\beta)\right\} \qquad (2.23)$$

The relationship between θ and β in the experimental set-up used in Chapter 4 is shown in Figure 2.7. In addition to the molecules being distributed in three dimension, a real cylindrically symmetric molecule has $\alpha'_{xx} = \alpha'_{yy} \neq 0$, $\alpha'_{zz} \neq 0$. The resulting expression for the θ dependence of I_{zz} and I_{yz} can be expressed as a depolarisation ratio[153, 155] $R(\theta)$ in terms of the parameters of the ODF and the ratio $r = \frac{\alpha'_{yy}}{\alpha'_{zz}}$.

$$R(\theta) = \frac{I_{\parallel}(\theta)}{I_{\perp}(\theta)} = \frac{I_{YZ}(\theta)}{I_{ZZ}(\theta)} = \frac{(-1+r)^2[-56-40\langle P_2\rangle+(105cos\,4\theta-9)\langle P_4\rangle]}{-56(8r^2+4r+3)+40(4r^2-r-3)(1+3\cos 2\theta)\langle P_2\rangle-3(r-1)^2(9+20\cos 2\theta+35\cos 4\theta)\langle P_4\rangle} \qquad (2.24)$$

By fitting Equation 2.24 to the measured $R(\theta)$ profile of a sample, the orientation distribution of the polarisability ellipsoid can be calculated in terms of P_2, P_4 and *r* parameters. If the relation between the polarisability ellipsoid and the vibration normal coordinates is known then the orientation distribution of the molecular unit can be inferred.

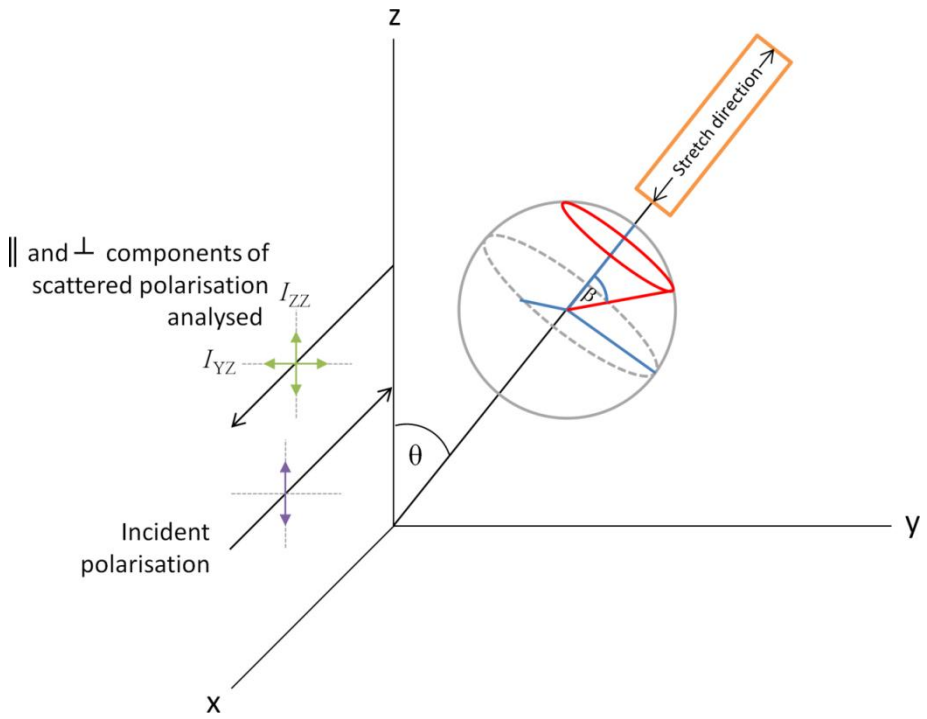


Figure 2.7 Experimental set-up used in this thesis, indicating the E_z direction of the incident polarisation as well as the two analyser polariser directions to collect I_{zz} and I_{yz} scattering intensities. Both angles θ and β are with respect to the host elastomer matrix stretch direction. θ is confined to the zy-plane.

2.6 UV-Vis spectroscopy

UV-Vis spectroscopy is used to probe the electronic structure of molecules that contain π-bonds or nonbonding electrons. π-bonds and nonbonding *n*-electrons are higher in energy than σ-bonds making the energy required to excite π and *n* electrons to antibonding π* or σ* orbitals sufficiently small to correspond to wavelengths in the UV and visible spectrum.

As well as characterising the electronic structure of molecules, the Absorbance (A_{absorb}) at a particular wavelength of a compound can be used in conjunction with the Beer-Lambert law to calculate the concentration c of a solution once the extinction coefficient ε and path length L are known.

$$\frac{A_{absorb}}{\varepsilon L} = c \qquad (2.25)$$

2.7 FTIR Spectroscopy

Fourier Transform Infra Red Spectroscopy (FTIR) is used to probe the frequency of vibrational transitions within a molecule. It is particularly useful for identifying the presence of different functional groups within a molecule by the existence of particular characteristic vibrational frequencies in the spectrum.[156] Infra-red spectroscopy is a complementary technique to Raman spectroscopy since the selection rules for the symmetry of IR active vibrations are different requiring the vibration to transform as a linear combination of x, y, z and a change in dipole of the molecule upon excitation.

2.8 Mass Spectrometry

In this thesis, two mass spectrometry ionisation techniques are used: Electro-spray Ionisation (ESI) and Matrix Assisted Laser Desorption/Ionisation (MALDI). Both of these techniques are considered to be 'soft ionisation' techniques that cause little fragmentation of the sample.[107]

MALDI using a *trans*-2-[3-(4-*tert*-butylphenyl)-2-methyl-2-propenylidene] malononitrile (DCTB) matrix in negative mode is a widely used ionisation method for fullerene derivatives.[157] ESI has also been used for fullerene derivatives[107] however it is typically used for more polar molecules that easily decompose such as the Cr_7Ni antiferromagnetic rings used in Chapter 5.[138]

2.9 NMR

Nuclear Magnetic Resonance (NMR) spectroscopy works on the same principal as ESR however it is optimised to probe the nuclear spin transition energies rather than of the electron. While there are a large number of nuclei that can be interrogated this thesis only makes use of the two most commonly probed nuclear isotopes, ^{1}H and ^{13}C. All measurements were performed on either a 300 MHz or 500 MHz Agilent Mercury 300 or Bruker DRX500 spectrometer at room temperature in solution.

2.9.1 1D ^{1}H NMR and ^{13}C NMR

1 dimensional (1D) NMR are the simplest experiments used to probe the local magnetic environment of a particular nuclear isotope. The frequency of the nuclei resonances are reported in the magnetic field invariant unit of parts per million (ppm) from the chemical shift of an internal reference, normally the resonance of the solvent. In most organic systems, there are a significant number of proton nuclei, making ^{1}H NMR the primary nuclei to probe. The most common features of a ^{1}H NMR spectrum that are used to elucidate a molecular structure are: relative peak area, isotropic exchange coupling patterns and magnitude and chemical shift. For organic compounds the range of chemical shifts is typical between 0 and 10 ppm, paramagnetic compounds can have much greater chemical shifts of +/- several hundred ppm.

A 1D ^{13}C NMR spectrum is typically performed in a proton decoupled mode. This mode removes the splitting that arises from coupling to adjacent protons, greatly simplifying the spectrum and making adjacent peaks easier to identify. All ^{13}C spectra in this thesis were recorded in this mode. The most common features of a ^{13}C NMR spectrum that are used to elucidate a molecular structure are the number of carbon environments and their chemical shift.

2.9.2 2D COSY and me-HSQC NMR

2D (^{1}H,^{1}H) Correlation spectroscopy (COSY) is used to identify ^{1}H nuclei that are exchange coupled.[158] The experiment plots ^{1}H chemical shift on both x and y axis. When two proton environments are exchanged coupled, an off-diagonal peak is observed between the two resonances, known as a ‘cross peak’.

2D (^{1}H,^{13}C) multiplicity-edited Hetero-nuclear Single Quantum Correlation (me-HSQC) spectroscopy is used to correlate the ^{1}H and ^{13}C spectra of a molecule via the appearance of cross peaks. HSQC works by transferring ^{1}H coherence to and then from the attached ^{13}C nuclei.[159] It has a particularly high sensitivity as it is based on the detection of the ^{1}H resonance. me-HSQC also has the added benefit of

providing information on the number of protons attached to a particular carbon.[160] If the carbon has one or three protons attached then the cross peak has a positive intensity. If however there are two protons attached to a carbon then the cross peak is negative.

Chapter 3 Synthesis of $^{14}N@C_{60}$ dimers with controlled separation

To further explore the potential of $N@C_{60}$ as a quantum computing element, the ability to construct an array of at least two $N@C_{60}$ centres with fixed separation is required to permit the interaction of neighbouring spin centres with one another to be measured. In this chapter, I describe the synthesis and characterisation of three different C_{60} dimer compounds that contain rigid oligo(p-phenylene polyethylene) (OPE) spacers. I identify optimum reaction conditions to form the dimers and apply them to $N@C_{60}$ containing samples. The electron spin environments of two $N@C_{60}$ containing dimers are subsequently characterised using CW ESR, finding that they are similar. The reaction is finally applied to a high purity $N@C_{60}$ sample ($\sim 50\%$ $N@C_{60}$) using a 10 µg reaction scale and the addition of extra spin transitions are observed in the ESR spectra. I go on to show that these extra spectral features can be predominatly accounted for by the inclusion of a dipolar coupling term between two $S_{3/2}$ $N@C_{60}$ centres in the spin Hamiltonian.

3.1 Introduction

Owing to a number of synthetic challenges associated with $N@C_{60}$, experimental electron spin resonance studies have previously been restricted to probing the interaction of ensembles of molecules that each contain a single $N@C_{60}$ spin centre. These challenges centre on the low yielding production methods available to synthesise $N@C_{60}$, producing at best a 500 ppm $N@C_{60}/C_{60}$ mixture,[37, 45] and the time consuming processing techniques currently required to enrich the ratio of $N@C_{60}$ to C_{60}.[41, 43] In addition, compared to C_{60}, chemically functionalized $N@C_{60}$ derivatives have significantly lower thermal and photostability.[52,24, 148-149] To further explore the potential of $N@C_{60}$ as a quantum computing element, the ability to test points 4 and 5 of the DiVincenzo criteria is needed. To achieve this, an array of at least two $N@C_{60}$ centres with fixed separation is required to permit the interaction of the two-spin centres with one another to be studied.

As detailed in Section 1.4, a number of $N@C_{60}$-C_{60} dimers[29, 54, 62, 161] have been previously synthesised, these are summarised in Figure 3.1.

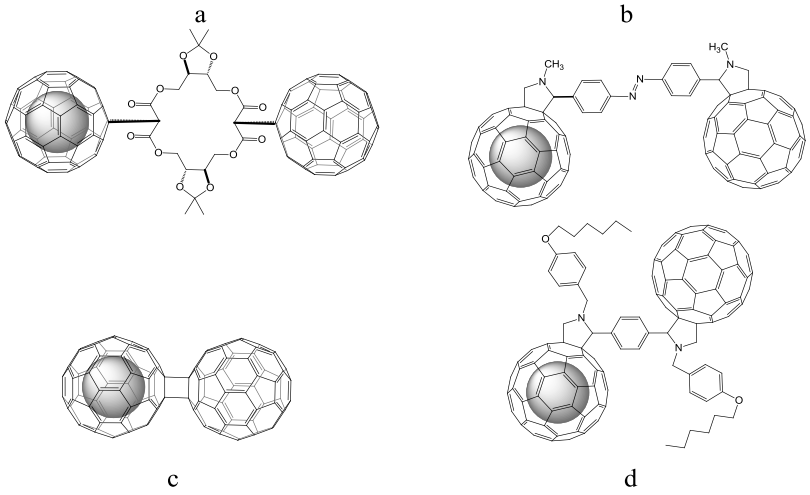


Figure 3.1 Chemical structure of previously characterised $N@C_{60}$-C_{60} dimer molecules [29, 54, 62, 161]

To apply this technique to synthesise a two-spin centre $N@C_{60}$-$N@C_{60}$ dimer molecule, avoiding decomposition of the $N@C_{60}$ during the reaction is of great importance. This is best illustrated through a simple thought experiment. If one were to synthesise an $N@C_{60}$-$N@C_{60}$ dimer using 100% pure $N@C_{60}$ and during the reaction there was a 50% probability that each of the $N@C_{60}$ molecule decomposes only $(0.5)^2$= 25% of the molecules would have two-spin centres and 50% would have one. However if the probability of decomposition is reduced, to for example 20% , the fraction of the sample that would contain two-spin centre molecules would instead be increased to $(0.8)^2$=64% with 32% single spin centre molecules. The effect of improving the retention of $N@C_{60}$ spin centres from 50% to 80% therefore corresponds to a four-fold increase in the relative contribution of the signal in a CW ESR spectrum arising from $N@C_{60}$-$N@C_{60}$ compared to that of the singly filled $N@C_{60}$-C_{60}. Of the methods used to synthesise the dimer molecules in Figure 3.1 only the bis-pyrrolidine derivative 3.1.b was explicitly shown to retain a significant fraction of the $N@C_{60}$ centres after the reaction, showing that only 30% of the $N@C_{60}$ centres decomposed.[33, 59]

3.2 Synthesis approach overview

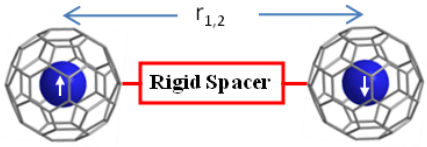


Figure 3.2 Cartoon of approach used to create $N@C_{60}$-$N@C_{60}$ centre dimer molecule with controlled separation of the two-spin centres ($r_{1,2}$).

The approach used in this work, uses a rigid molecular spacer to covalently link the two $N@C_{60}$ molecules (see Figure 3.2). By using spacers with different lengths, the coupling between the spin centres can be controlled. The Prato 1,3-dipolar cycloaddition reaction[56] was chosen to attach the spacer to the two fullerenes owing to its proven compatibility with the stability of $N@C_{60}$[33, 52, 57-60] and a wide rage of aldehyde and amino acid reagents[92, 95-96, 98-99, 101, 104, 162]. To minimise the number of steps needed to synthesise the molecule, the reaction was optimised to form the target dimer compounds in one reaction step, shown in Figure 3.3

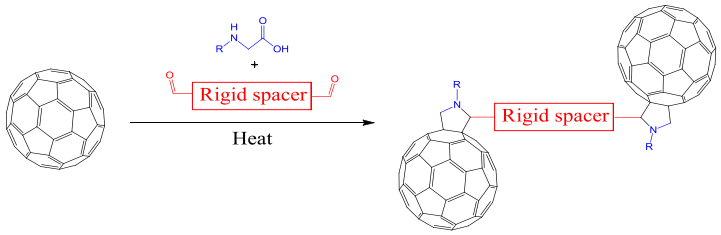


Figure 3.3 Reaction scheme for a 'one pot' bis addition of fullerenes to an aldehyde terminated rigid molecule unit using two Prato 1,3-dipolar cycloaddition reactions.

To produce a double $N@C_{60}$-$N@C_{60}$ containing molecules of the form depicted in Figure 3.3, a number of bis-aldehyde precursors and C_{60} dimer analogues were synthesised to permit structural characterisation and reaction optimisation. In this chapter, the synthesis and characterisation of three bis-aldehyde molecular wire spacer units are detailed. The structures of these bridging units are shown in Figure 3.4 with their designated names Ald-3bz, Ald-5bz, and Ald-3bzo. Using these aldehyde precursors, the corresponding bis-fullerene dimer adducts were synthesised with their designated names Dimer-3bz, Dimer-5bz and Dimer-3bzo (see Figure 3.4). Using partially enriched $^{14}N@C_{60}$, two single spin centre $^{`14}N@C_{60}$-C_{60} dimers were then created and characterised, these are referred to as

$^{14}N@C_{60}$-C_{60} Dimer-3bz and $^{14}N@C_{60}$-C_{60} Dimer-5bz (see Figure 3.4). Finally, the target double spin labelled molecule was synthesised and is referred to as $^{14}N@C_{60}$-$^{14}N@C_{60}$ Dimer-3bz (see Figure 3.4).

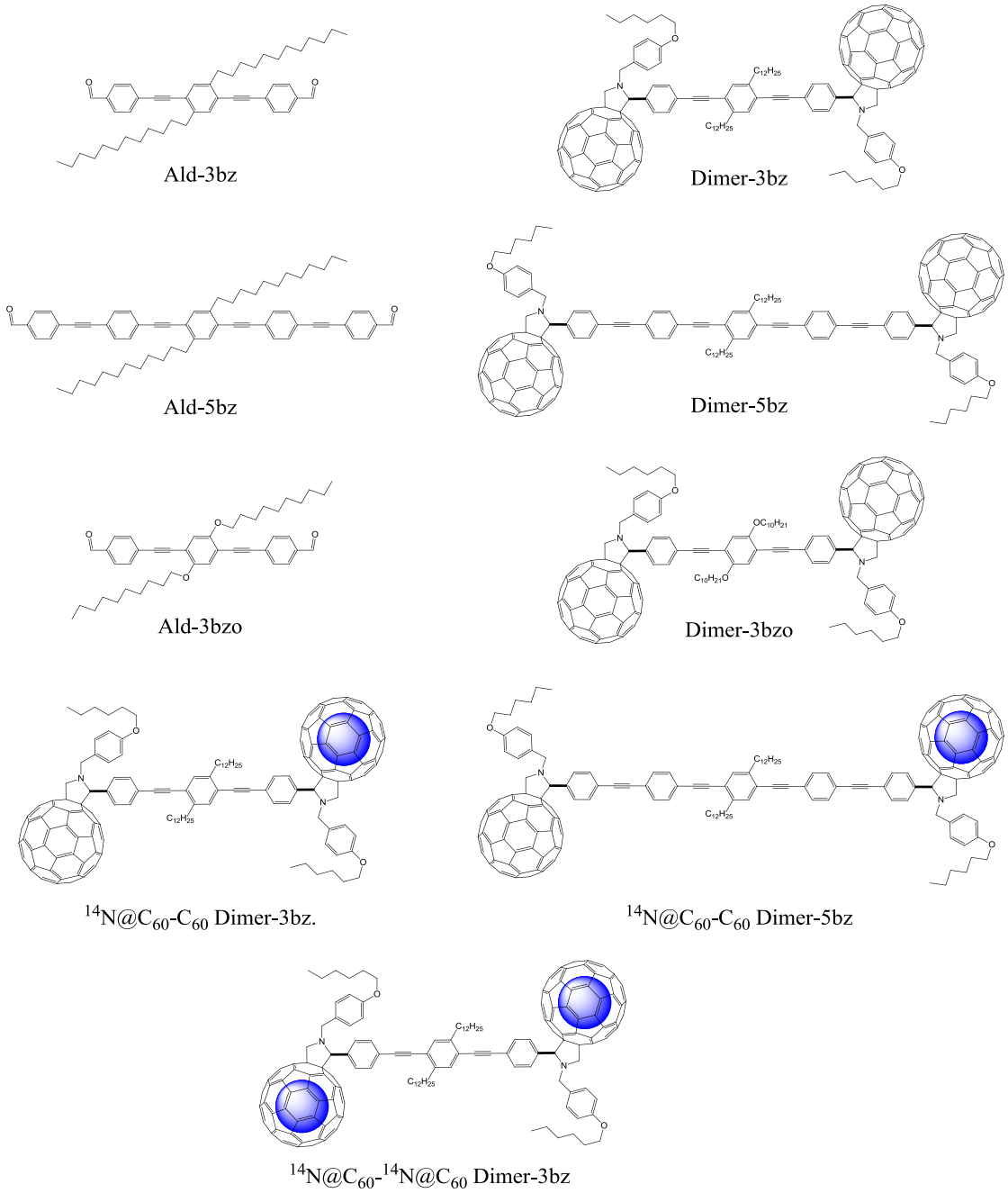


Figure 3.4 Chemical structures and corresponding abbreviations of all molecules characterised in this chapter.

3.3 Synthesis and characterisation of bridging units

Dibenzaldehyde terminated oligo(*p*-phenylene polyethynylene) (OPE) molecules were chosen for use as spacing units due to their inherent rigidity, modular construction and good photo and thermal

stability. Two different length OPE briging units were synthesised one 1.9 nm and the other 3.2 nm, the shorter unit was created in two variants due to the availability of the starting materials. Ald-3bz and Ald-5bz were synthesised via a double Sonagashira coupling of 4-iodobenzaldehyde to 1,4-didodecyl-2,5-diethynylbenzene and 4,4'-((2,5-didodecyl-1,4-phenylene)bis(ethyne-2,1-diyl))bis(ethynylbenzene) respectively, (see Figure 3.5).

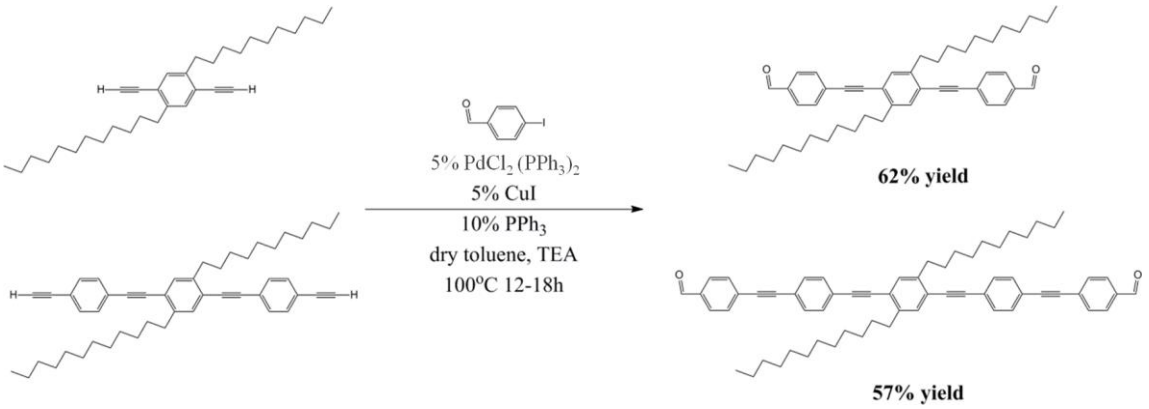


Figure 3.5 Reaction conditions used to synthesise Ald-3bz and Ald-5bz.

The limited availability of 1,4-didodecyl-2,5-diethynylbenzene led to a second 1.9 nm bridging unit to be synthesised, hence forth referred to as Ald-3bzo, containing alkoxy rather than alkyl substituents on the central benzene ring. The synthetic scheme for Ald-3bzo consists of two stages (Figure 3.6), initially a Sonagashira coupling of 2-(4-bromophenyl)-1,3-dioxolane with ethynyltrimethylsilane followed by trimethylsilyl (TMS) deprotection using potassium fluoride. The resulting 4-ethynylbenzaldehyde was Sonagashira coupled in a bis-addition to the commercially availble 1,4-dibromo-2,5-bis(decyloxy)benzene to form Ald-3bzo. This scheme was used in preference to direct addition of ethynyltrimethylsilane to 1,4-dibromo-2,5-bis(decyloxy)benzene as it was found that the mono- and bis-acetylene adducts were difficult to separate using standard flash silica chromatography due to their similar polarity.

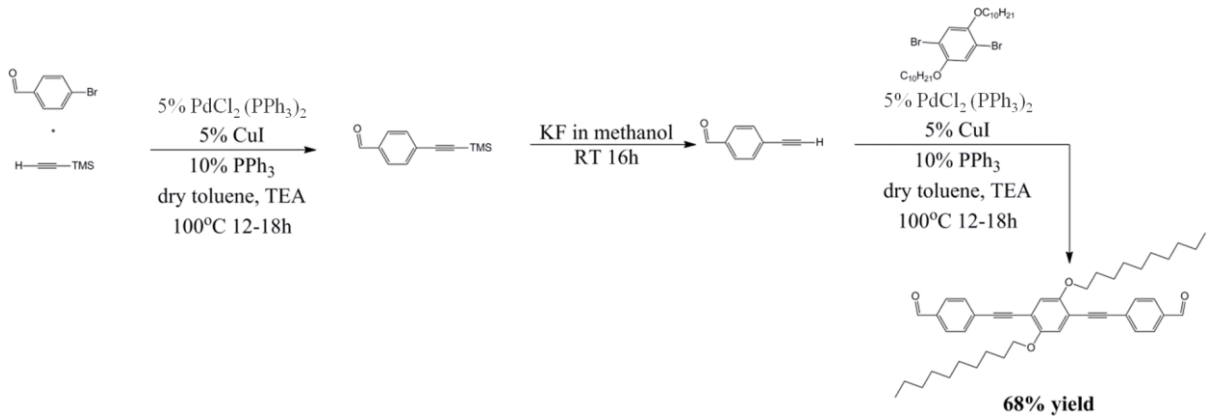


Figure 3.6 Reaction conditions used to synthesise Ald-3bzo.

3.2.2 Characterisation

All three OPE bridging units were characterised using ^{1}H and ^{13}C Nuclear Magnetic Resonance (NMR), Fourier Transform Infrared Spectroscopy (FTIR) and Electro-Spray Ionisation (ESI) mass spectrometry. Due to the structural similarity of all three units I shall discuss the characterisation of all three OPE molecules together.

The ^{1}H NMR spectra of the three bridging units (see Figure 3.7) will be discussed from lowest to highest chemical shift. The triplet at 0.87-0.88 ppm, J= 6.9-7.1 Hz is present in all molecules and is assigned (based on chemical shift , J coupling magnitude and integral height) to the terminal methyl groups of the aliphatic chain substituents attached to central benzene ring. The peaks between 1 ppm and 5 ppm are all assigned to the remainder of the aliphatic central chains. As expected, these peak multiplicities shapes and ppm shifts are almost identical for both Ald-3bz and Ald-5bz, with an increasing chemical shift as the protons become closer to the aromatic group. The increased low field shift for the aliphatic protons in Ald-3bzo can be attributed to the inductive effect of the oxygen α to the aromatic ring. The two aromatic protons of the ring are assigned to the singlets situated at 7.04-7.41 ppm, with an upfield shift of 0.4 ppm observed in Ald-3bzo due to a positive mesomeric effect of the adjacent alkoxy substituent. The pair of J coupled doublets at 7.53 ppm and 7.55 ppm (J=8.2 Hz) are only present in Ald-5bz and are assigned to the four protons on the additional pair of benzene rings present. The pair of J coupled doublets in each spectra between 7.9 ppm and 7.67 ppm are assigned to the four protons

on the aromatic ring adjacent to the aldehyde group, with the pair *ortho* to the aldehyde experiencing the higher ppm shift due to the stronger negative mesomeric and inductive effect of the aldehyde group. Finally the 10.03-10.04 ppm singlet peaks in each spectrum are assigned to the aldehyde proton based on the multiplicity and characteristic chemical shift.

^{1}H NMR

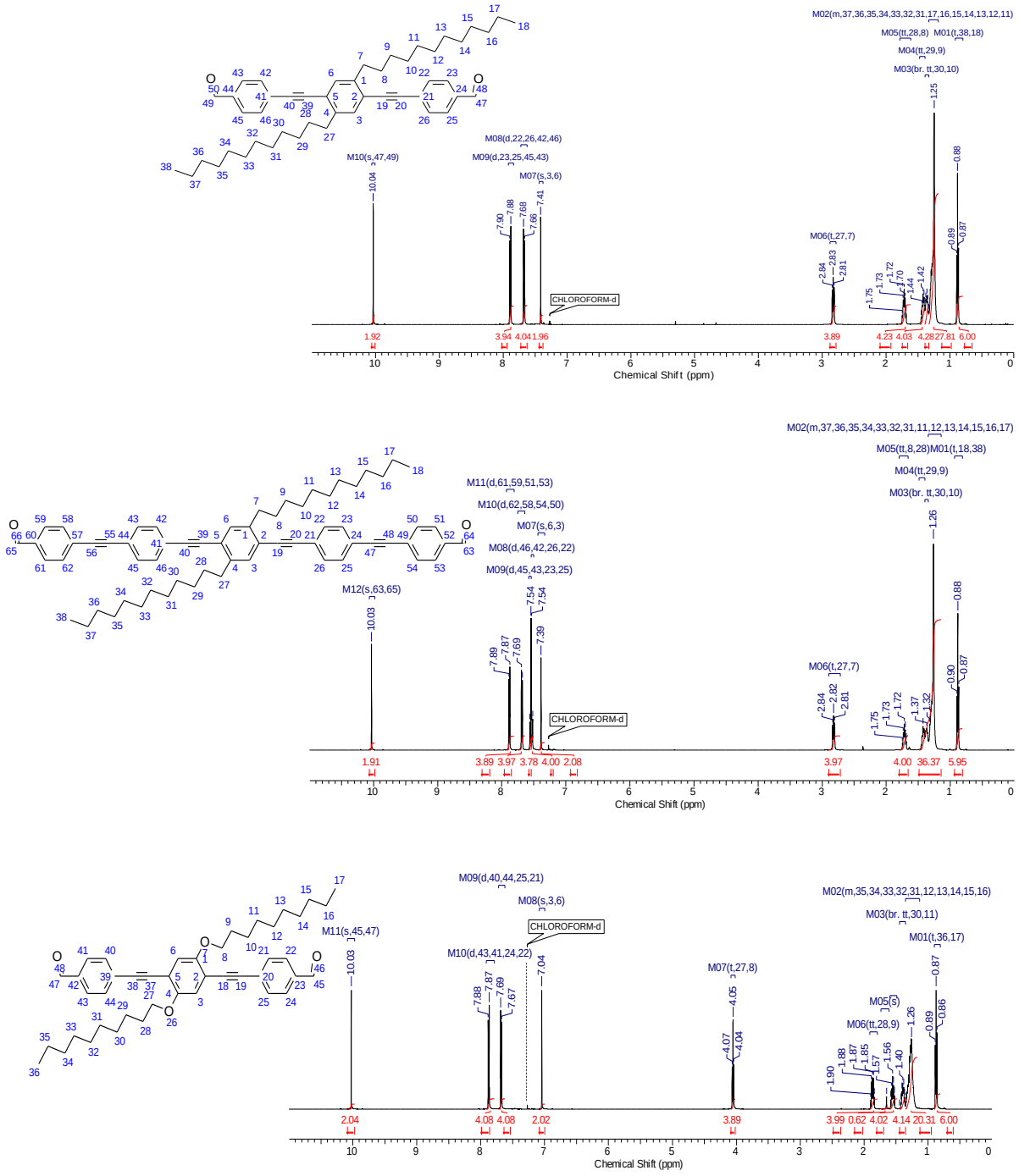
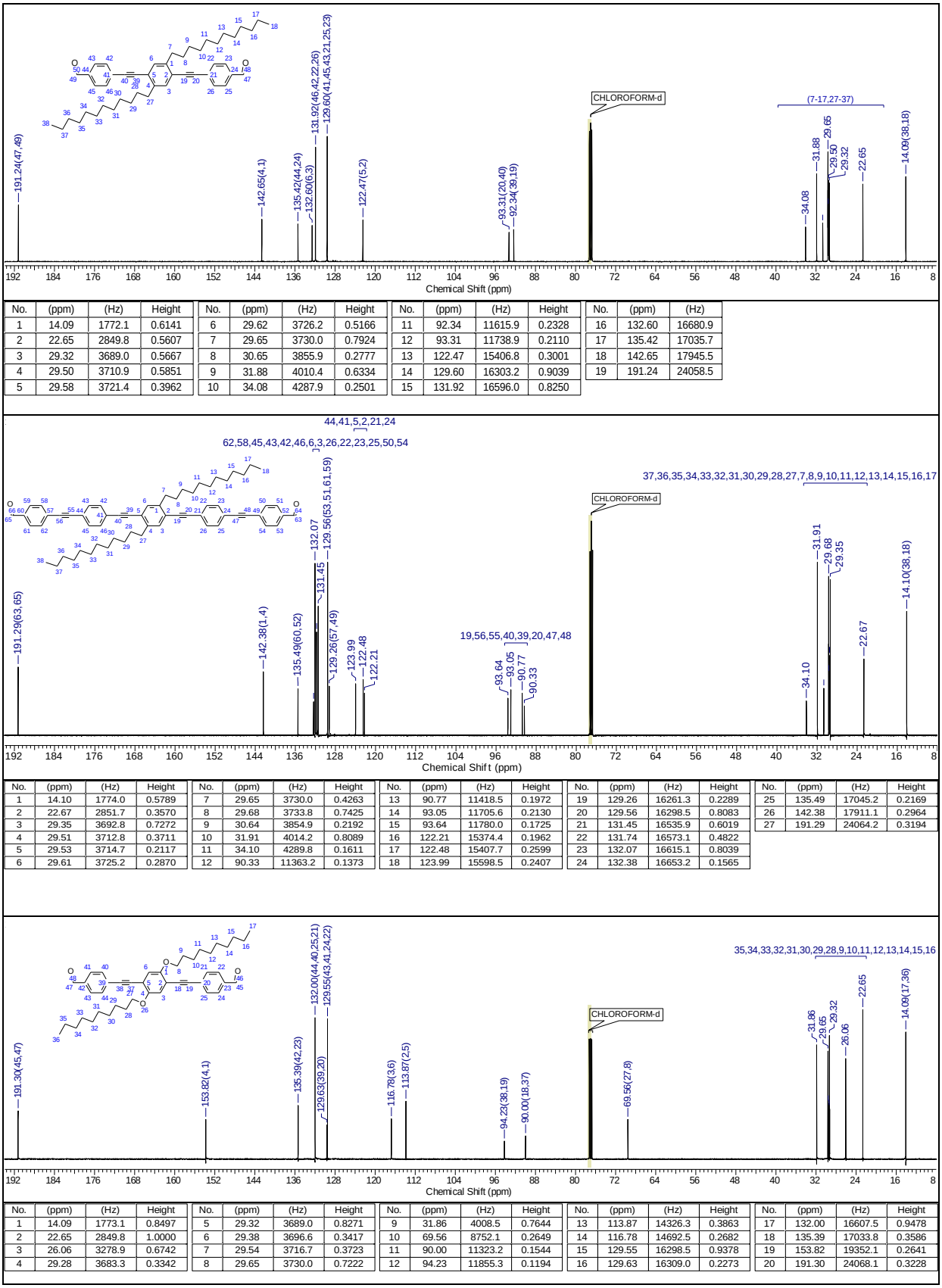


Figure 3.7 500MHz ^{1}H NMR spectra recorded in chloroform-d from a) Ald-3bz, b) Ald-5bz, c) Ald-3bzo. The integrals and assignments are overlaid.

^{13}C NMR



No.	(ppm)	(Hz)	Height
1	14.09	1772.1	0.6141
2	22.65	2849.8	0.5607
3	29.32	3689.0	0.5667
4	29.50	3710.9	0.5851
5	29.58	3721.4	0.3962

No.	(ppm)	(Hz)	Height
6	29.62	3726.2	0.5166
7	29.65	3730.0	0.7924
8	30.65	3855.9	0.2777
9	31.88	4010.4	0.6334
10	34.08	4287.9	0.2501

No.	(ppm)	(Hz)	Height
11	92.34	11615.9	0.2328
12	93.31	11738.9	0.2110
13	122.47	15406.8	0.3001
14	129.60	16303.2	0.9039
15	131.92	16596.0	0.8250

No.	(ppm)	(Hz)
16	132.60	16680.9
17	135.42	17035.7
18	142.65	17945.5
19	191.24	24058.5

No.	(ppm)	(Hz)	Height
1	14.10	1774.0	0.5789
2	22.67	2851.7	0.3570
3	29.35	3692.8	0.7272
4	29.51	3712.8	0.3711
5	29.53	3714.7	0.2117
6	29.61	3725.2	0.2870

No.	(ppm)	(Hz)	Height
7	29.65	3730.0	0.4263
8	29.68	3733.8	0.7425
9	30.64	3854.9	0.2192
10	31.91	4014.2	0.8089
11	34.10	4289.8	0.1611
12	90.33	11363.2	0.1373

No.	(ppm)	(Hz)	Height
13	90.77	11418.5	0.1972
14	93.05	11705.6	0.2130
15	93.64	11780.0	0.1725
16	122.21	15374.4	0.1962
17	122.48	15407.7	0.2599
18	123.99	15598.5	0.2407

No.	(ppm)	(Hz)	Height
19	129.26	16261.3	0.2289
20	129.56	16298.5	0.8083
21	131.45	16535.9	0.6019
22	131.74	16573.1	0.4822
23	132.07	16615.1	0.8039
24	132.38	16653.2	0.1565

No.	(ppm)	(Hz)	Height
25	135.49	17045.2	0.2169
26	142.38	17911.1	0.2964
27	191.29	24064.2	0.3194

No.	(ppm)	(Hz)	Height
1	14.09	1773.1	0.8497
2	22.65	2849.8	1.0000
3	26.06	3278.9	0.6742
4	29.28	3683.3	0.3342

No.	(ppm)	(Hz)	Height
5	29.32	3689.0	0.8271
6	29.38	3696.6	0.3417
7	29.54	3716.7	0.3723
8	29.65	3730.0	0.7222

No.	(ppm)	(Hz)	Height
9	31.86	4008.5	0.7644
10	69.56	8752.1	0.2649
11	90.00	11323.2	0.1544
12	94.23	11855.3	0.1194

No.	(ppm)	(Hz)	Height
13	113.87	14326.3	0.3863
14	116.78	14692.5	0.2682
15	129.55	16298.5	0.9378
16	129.63	16309.0	0.2273

No.	(ppm)	(Hz)	Height
17	132.00	16607.5	0.9478
18	135.39	17033.8	0.3586
19	153.82	19352.1	0.2641
20	191.30	24068.1	0.3228

Figure 3.8. 125 MHz proton decoupled ^{13}C NMR spectra recorded in chloroform-d from a) Ald-3bz, b) Ald-5bz, c) Ald-3bzo.

The ^{13}C NMR spectra recorded from the three bridging units (see Figure 3.8) will be discussed together, from lowest to highest chemical shift. The peaks at 14.09-14.010 ppm are assigned to the terminal carbons on the alkyl chains, based on the chemical shift. The peaks within 22-70 ppm are assigned to the remaining carbons on the alkyl chains. Similar to the proton spectra, these peaks are virtually identical for both Ald-3bz and Ald-5bz, while the carbon α to the oxygen attached to the ring is shifted down field to 69.56 ppm owing to the negative inductive effect of the oxygen. The peaks between 90.00-94.23 ppm are assigned to the alkyne carbons, with the extra two peaks in the Ald-5bz spectrum assigned to the two additional alkyne carbons present. All of the peaks within the region 113-154 ppm were assigned to the aromatic ring carbons. The assignment was achieved by correlating the observed peaks to those predicted by using an NMR prediction package (ChemDraw). All of the predicted lines fell within 1 ppm of those observed. Finally, the peaks at 191.24-191.30 ppm were assigned to the aldehyde carbon based on the characteristic chemical shift.

IR

FTIR using an ATR diamond crystal configuration was recorded from each of the bridging units (see Figure 3.9). The strong bands at 2914-2918 cm^{-1} and 2847-2852 cm^{-1} are indicative of alkyl C-H vibrations[156] and are therefore assigned to the alkyl substituents on the central benzene rings. The 2207-2212 cm^{-1} weak band is assigned to the alkyne stretches,[163] the weakness is due to the small dipole of the bond. The 1691-1697 cm^{-1} strong band is characteristic of an aldehyde C=O stretch and is therefore assigned to the terminal aldehyde units. Lastly, the bands at 1593-1597 cm^{-1} are assigned to the symmetric stretch of the aromatic rings, also known as the 'breathing mode'. [164]

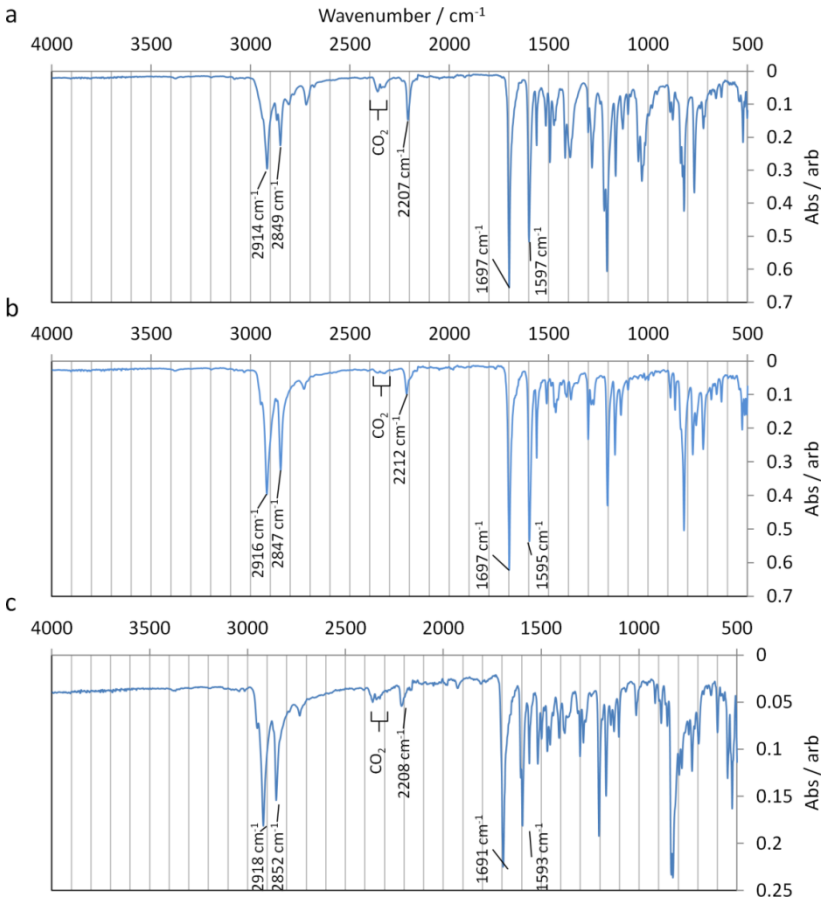


Figure 3.9 FTIR spectra of a) Ald-3bzo b) Ald-3bz c) Ald-5bz, recorded at room temperature.

Mass Spectra

The mass spectra of all three bridging molecules were recorded (see Figure 3.10) and compared to the theoretical isotope distribution for the expected molecular formula. The results indicate an excellent agreement between both the peak positions and isotope profile for all three molecules, confirming the correct structural composition of each bridging unit.

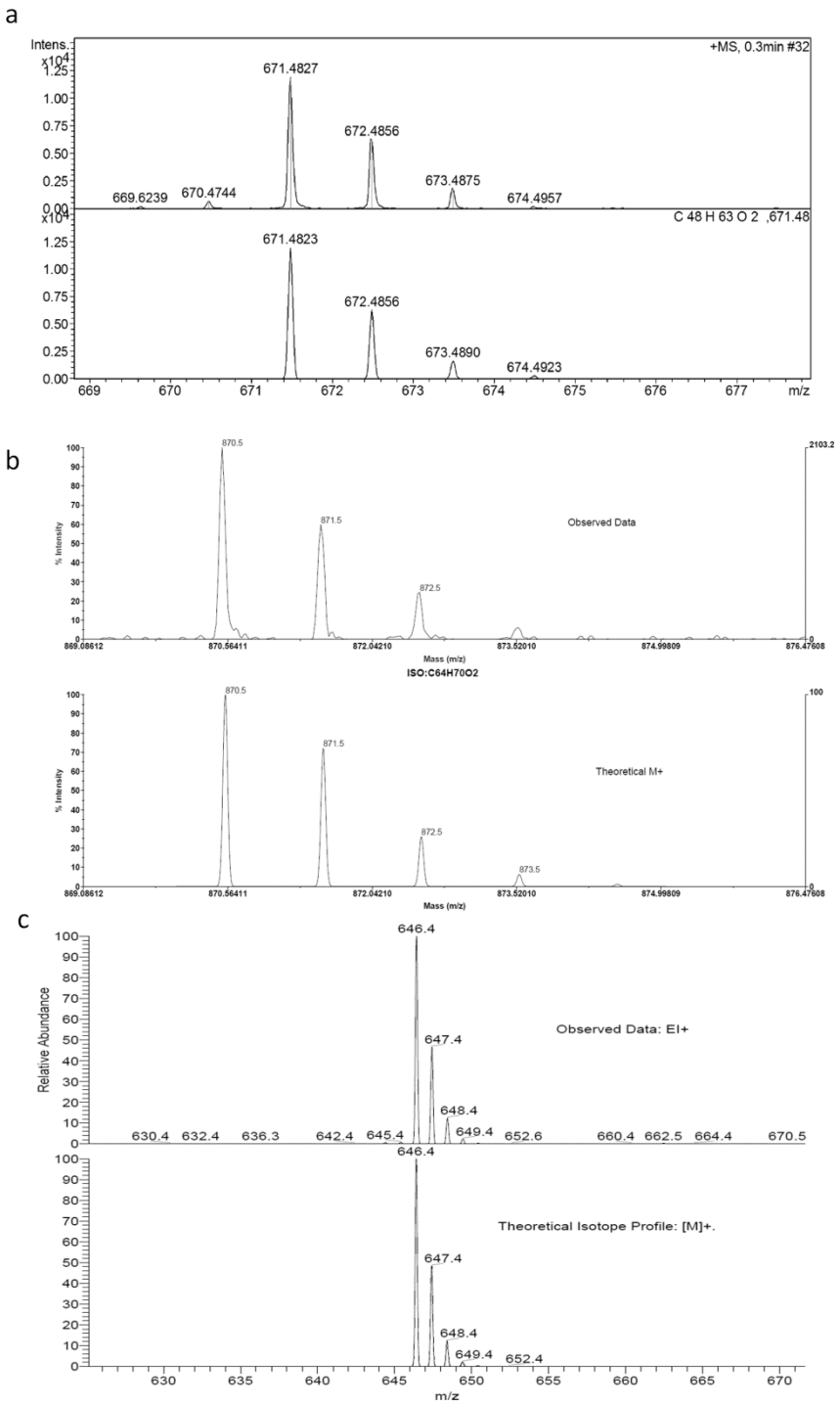


Figure 3.10 a) recorded Isotope distribution peaks for a) Ald-3bz using ESI, b) Ald-5bz using MALDI-ToF, c) Ald-3bzo using EI. Expected isotope distribution is plotted below each spectrum.

3.4 Synthesis and characterisation of C_{60}-C_{60} dimers

Using the aldehyde bridging units Ald-3bz, Ald-5bz and Ald-3bzo, three C_{60}-C_{60} dimer molecules were synthesised (see Figure 3.11) in one step using a double [3+2]cycloaddition. The amino acid derivative used in the reaction was N-(4-(hexyloxy)benzyl)glycine. This was chosen as it shows a significant reaction rate enhancement when compared to more commonly used amino acid derivatives such as N-ethylglycine (see Section 3.3.3).

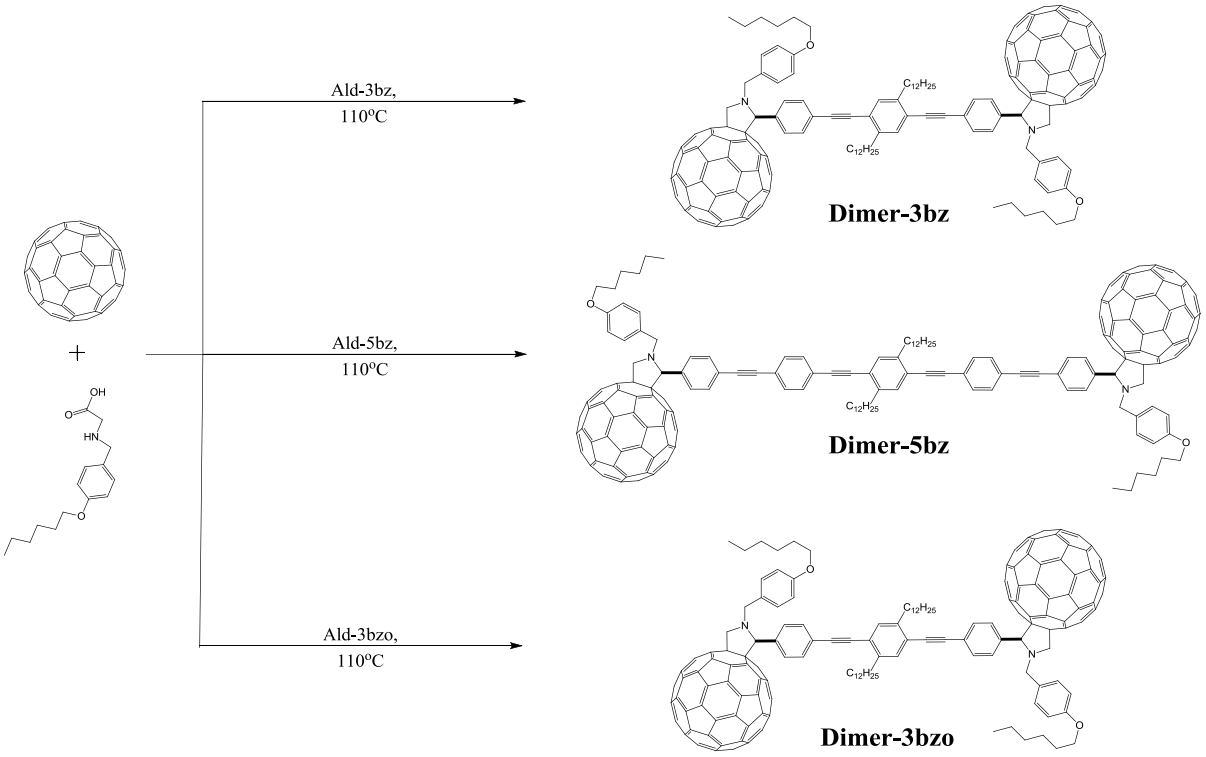


Figure 3.11 Reaction scheme for the synthesis of C_{60}-C_{60} molecules, Dimer-3bz (40% yield), Dimer-5bz (40% yield) and Dimer-3bzo (26% yield) using N-(4-(hexyloxy)benzyl)glycine as the amino acid reagent.

3.4.1 Characterisation

All three dimer molecules were characterised using HPLC, ^{1}H and ^{13}C NMR, FTIR, UV-Vis spectroscopy and MALDI-ToF mass spectrometry. Due to the related molecular structure of all three units it is pertinent to discuss the characterisation of the dimer molecules together.

HPLC

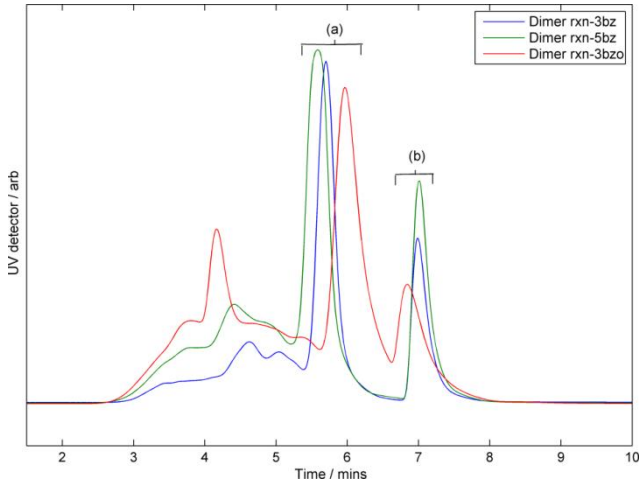


Figure 3.12 Overlaid HPLC traces of product mixtures for three dimer reactions Using N-(4-(hexyloxy)benzyl)glycine. Peak (a) was retained and characterised as the C_{60}-C_{60} dimer molecule. Peak (b) was taken to be unreacted C_{60} based on peak retention time and the characteristic purple colour. The reaction mixture was passed through a short silica plug using toluene as eluent prior to HPLC analysis. Column: Buckyprep-M 20 x 250 mm. Eluent: Toluene. Flow rate:18 mL min^{-1}.

The HPLC traces of each of the dimer product mixtures are shown in Figure 3.12. The overall appearance of the traces is similar for all three reactions with the peaks between 5.58-5.98 minutes isolated and confirmed as the C_{60}-C_{60} dimer product. The retention time of the dimer peaks are all shorter than pristine C_{60} (retention time 6.85-7.02 minutes), in contrast to previously characterised C_{60}-C_{60} dimer molecules using the same mobile phase and similar HPLC columns which have close to double the retention time of C_{60}.[59, 62, 68] An increased retention time is also consistent with what would be expected by simply considering the larger conjugated π system of the dimer molecules compared to C_{60}. This unusual behaviour is suggested to be predominantly due to a disruptive interaction of the long alkyl chains of the bridging units with the fullerene surface. This interaction would cause a reduction of the effective surface area of the fullerene conjugated π system that is available to interact with the stationary phase of the column so reducing the retention time of dimer molecule.

The ^{1}H NMR spectra of the dimer bridging units (see Figure 3.13) will be discussed from lowest to highest chemical shift. The two triplets between 0.85-0.94 ppm, present in all of the dimer spectra, are assign to the terminal methyl protons of the alkyl chains on the bridging unit and the hexyloxybenzene substituent of the pyrrolidine group based on expected shift splitting pattern and integrated signal

height. The lower field triplet is assigned to the hexyloxybenzene methyl group due to closer proximity to the aromatic and oxy groups. All of the peaks in the range 1.23-4.04 ppm excluding the doublet between 3.66-3.83 ppm are assigned to the remaining alkyl protons on the bridging unit and hexyloxybenzene substituents. The assignments are based on the relative signal heights, comparison with the peak positions of the aldehyde precursor and the assumption that the most deshielded triplet could be assigned to the hexyloxybenzene O-CH_2-R protons, owing to the –ve inductive effect of the oxy group. The four doublets between 3.66 and 4.95 ppm are assigned to vicinal coupling of the two N-CH_2-R groups of the pyrrolidine group. The pair of doublets with the lower average chemical shift and the larger coupling magnitude of 13-13.5 Hz are assigned to the N-CH_2-hexyloxybenzene protons.[56] This assignment is rationalised on the basis of the reduced –ve inductive effect of the fullerene moiety and the greater π-donation (known to increase the +ve vincinial coupling magnitude) from the amine lone pair caused by the enhanced rotational freedom of the N-CH_2 bond compared to the rigid geometry of the N-CH_2 within the pyrrolidine ring. The pair of doublets with the larger average chemical shift and the smaller coupling magnitude of 7.5-9.5 Hz are assigned to the N-CH_2 group within the pyrrolidine ring and is in good agreement with the assignments of previously reported fullerene pyrrolidine derivatives.[56, 58, 92] The singlet at 5.18-5.26 ppm is assigned to the N-CH proton within the pyrrolidine ring and is also in good agreement with previously reported fullerene pyrrolidine derivatives.[56, 58, 92] The pair of doublets with $^3J_{H-H}$ 8.5-8.8 Hz at 7.02-7.05 ppm and 7.53-7.56 ppm are assigned to the protons *meta* and *ortho* to the hexyloxy substituent of the benzene ring respectively due to the mesomeric effect of the oxy substituent on the ring. The singlet at 7.35-7.36 ppm in Dimer-3bz and Dimer-5bz is assigned to the two protons on the central benzene ring of the bridging unit, the equivalent protons in dimer-3bzo are shifted up field to 6.99 ppm due to the +ve mesomeric effect of the *meta* oxy substituent on the benzene ring. These peak positions are also only marginally shifted from the corresponding protons of each of the aldehyde precursors as expected owing to the remote position of these protons from the attached fullerene substituent. The pair of doublets 7.49-7.51 ppm ($^3J_{H-H}$ 8.8Hz) are only present in the spectrum of the longer Dimer-5bz and so are assigned to the two pairs of

protons on the extra two benzene rings present in this molecule, as also seen in the aldehyde precursor spectrum. The double at 7.64-7.67 ppm is assigned to the aromatic protons on the OPV unit *meta* to the pyrrolidine substituent,[104] with the highly broadened peak at ≈8 ppm assigned to the aromatic protons *meta* to the pyrrolidine substituent. This broadening effect has been seen previously[104] and is assumed to be caused by the incomplete averaging of the interaction of the *meta* protons with the aromatic system of the fullerene cage due to rotation around the aromatic-pyrrolidine bond.

^{1}H NMR

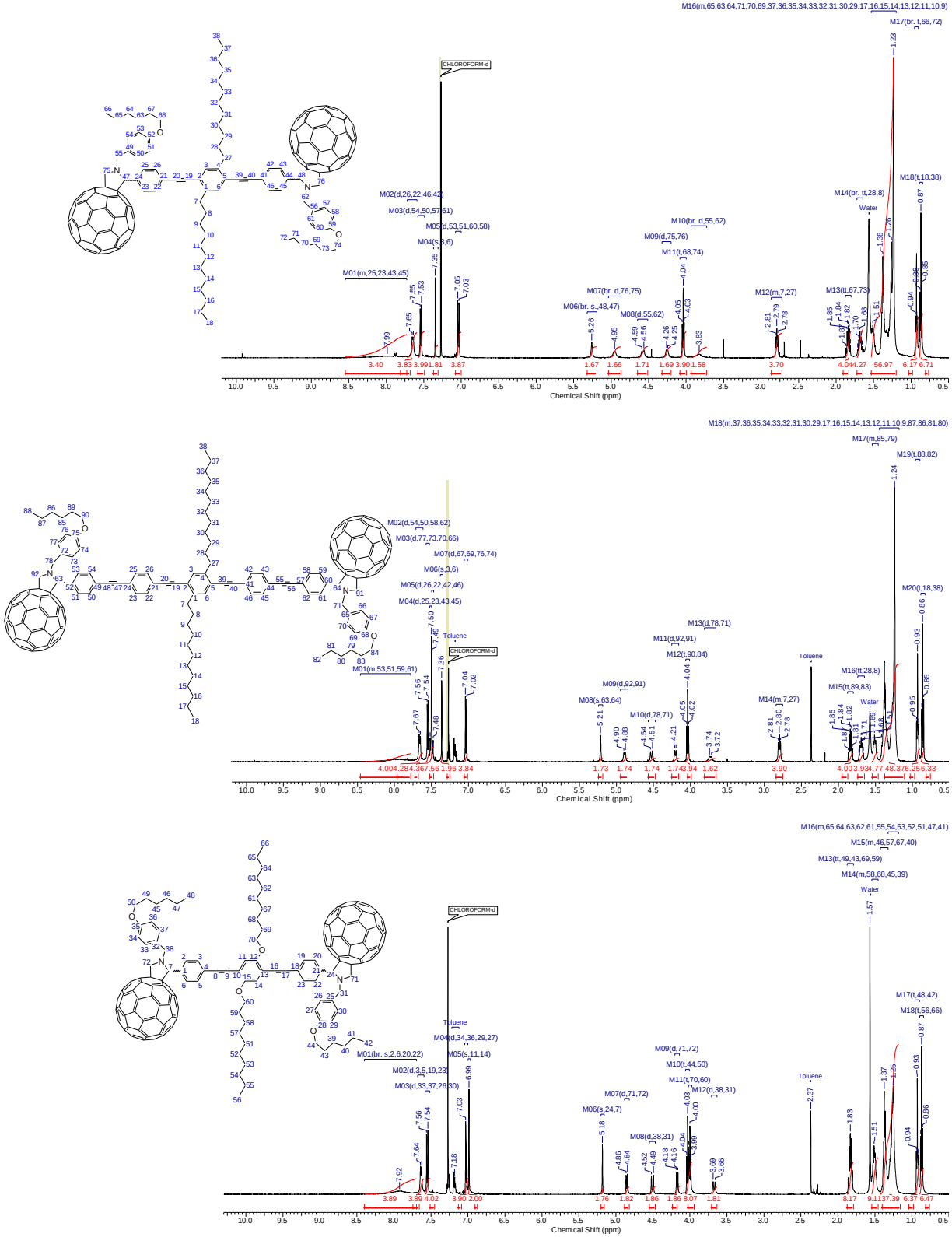
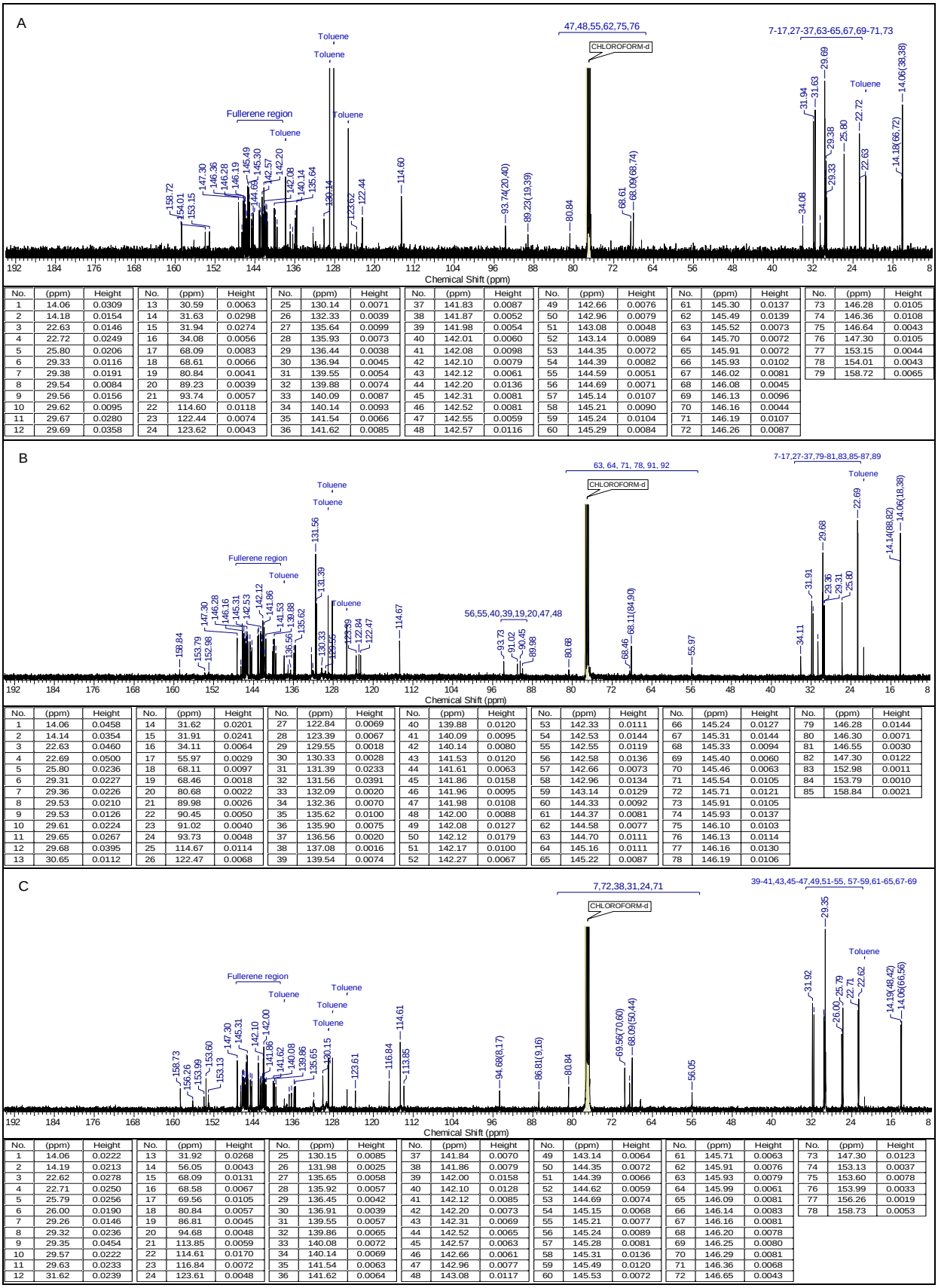


Figure 3.13 500 MHz ^{1}H NMR spectra recorded in chloroform-d from a) Dimer-3bz, b) Dimer-5bz, c) Dimer-3bzo. The integrals and assignments are overlaid.

^{13}C NMR



No.	(ppm)	Height	No.	(ppm)	Height	No.	(ppm)	Height	No.	(ppm)	Height	No.	(ppm)	Height	No.	(ppm)	Height	No.	(ppm)	Height
1	14.06	0.0309	13	30.59	0.0063	25	130.14	0.0071	37	141.83	0.0087	49	142.66	0.0076	61	145.30	0.0137	73	146.28	0.0105
2	14.18	0.0154	14	31.63	0.0298	26	132.33	0.0039	38	141.87	0.0052	50	142.96	0.0079	62	145.49	0.0139	74	146.36	0.0108
3	22.63	0.0146	15	31.94	0.0274	27	135.64	0.0099	39	141.98	0.0054	51	143.08	0.0048	63	145.52	0.0073	75	146.64	0.0043
4	22.72	0.0249	16	34.08	0.0056	28	135.93	0.0073	40	142.01	0.0060	52	143.14	0.0089	64	145.70	0.0072	76	147.30	0.0105
5	25.80	0.0206	17	68.09	0.0083	29	136.44	0.0038	41	142.08	0.0098	53	144.35	0.0072	65	145.91	0.0072	77	153.15	0.0044
6	29.33	0.0116	18	68.61	0.0066	30	136.94	0.0045	42	142.10	0.0079	54	144.39	0.0082	66	145.93	0.0102	78	154.01	0.0043
7	29.38	0.0191	19	80.84	0.0041	31	139.55	0.0054	43	142.12	0.0061	55	144.59	0.0051	67	146.02	0.0081	79	158.72	0.0065
8	29.54	0.0084	20	89.23	0.0039	32	139.88	0.0074	44	142.20	0.0136	56	144.69	0.0071	68	146.08	0.0045			
9	29.56	0.0156	21	93.74	0.0057	33	140.09	0.0087	45	142.31	0.0081	57	145.14	0.0107	69	146.13	0.0096			
10	29.62	0.0095	22	114.60	0.0118	34	140.14	0.0093	46	142.52	0.0081	58	145.21	0.0090	70	146.16	0.0044			
11	29.67	0.0280	23	122.44	0.0074	35	141.54	0.0066	47	142.55	0.0059	59	145.24	0.0104	71	146.19	0.0107			
12	29.69	0.0358	24	123.62	0.0043	36	141.62	0.0085	48	142.57	0.0116	60	145.29	0.0084	72	146.26	0.0087			

No.	(ppm)	Height	No.	(ppm)	Height	No.	(ppm)	Height	No.	(ppm)	Height	No.	(ppm)	Height	No.	(ppm)	Height	No.	(ppm)	Height
1	14.06	0.0458	14	31.62	0.0201	27	122.84	0.0069	40	139.88	0.0120	53	142.33	0.0111	66	145.24	0.0127	79	146.28	0.0144
2	14.14	0.0354	15	31.91	0.0241	28	123.39	0.0067	41	140.09	0.0095	54	142.53	0.0144	67	145.31	0.0144	80	146.30	0.0071
3	22.63	0.0460	16	34.11	0.0064	29	129.55	0.0018	42	140.14	0.0080	55	142.55	0.0119	68	145.33	0.0094	81	146.55	0.0030
4	22.69	0.0500	17	55.97	0.0029	30	130.33	0.0028	43	141.53	0.0120	56	142.58	0.0136	69	145.40	0.0060	82	147.30	0.0122
5	25.80	0.0236	18	68.11	0.0097	31	131.39	0.0233	44	141.61	0.0063	57	142.66	0.0073	70	145.46	0.0063	83	152.98	0.0011
6	29.31	0.0227	19	68.46	0.0018	32	131.56	0.0391	45	141.86	0.0158	58	142.96	0.0134	71	145.54	0.0105	84	153.79	0.0010
7	29.36	0.0226	20	80.68	0.0022	33	132.09	0.0020	46	141.96	0.0095	59	143.14	0.0129	72	145.71	0.0121	85	158.84	0.0021
8	29.53	0.0210	21	89.98	0.0026	34	132.36	0.0070	47	141.98	0.0108	60	144.33	0.0092	73	145.91	0.0105			
9	29.53	0.0126	22	90.45	0.0050	35	135.62	0.0100	48	142.00	0.0088	61	144.37	0.0081	74	145.93	0.0137			
10	29.61	0.0224	23	91.02	0.0040	36	135.90	0.0075	49	142.08	0.0127	62	144.58	0.0077	75	146.10	0.0103			
11	29.65	0.0267	24	93.73	0.0048	37	136.56	0.0020	50	142.12	0.0179	63	144.70	0.0111	76	146.13	0.0114			
12	29.68	0.0395	25	114.67	0.0114	38	137.08	0.0016	51	142.17	0.0100	64	145.16	0.0111	77	146.16	0.0130			
13	30.65	0.0112	26	122.47	0.0068	39	139.54	0.0074	52	142.27	0.0067	65	145.22	0.0087	78	146.19	0.0106			

No.	(ppm)	Height	No.	(ppm)	Height	No.	(ppm)	Height	No.	(ppm)	Height	No.	(ppm)	Height	No.	(ppm)	Height	No.	(ppm)	Height
1	14.06	0.0222	13	31.92	0.0268	25	130.15	0.0085	37	141.84	0.0070	49	143.14	0.0064	61	145.71	0.0063	73	147.30	0.0123
2	14.19	0.0213	14	56.05	0.0043	26	131.98	0.0025	38	141.86	0.0079	50	144.35	0.0072	62	145.91	0.0076	74	153.13	0.0037
3	22.62	0.0278	15	68.09	0.0131	27	135.65	0.0058	39	142.00	0.0158	51	144.39	0.0066	63	145.93	0.0079	75	153.60	0.0078
4	22.71	0.0250	16	68.58	0.0067	28	135.92	0.0057	40	142.10	0.0128	52	144.62	0.0059	64	145.99	0.0061	76	153.99	0.0033
5	25.79	0.0256	17	69.56	0.0105	29	136.45	0.0042	41	142.12	0.0085	53	144.69	0.0074	65	146.09	0.0081	77	156.26	0.0019
6	26.00	0.0190	18	80.84	0.0057	30	136.91	0.0039	42	142.20	0.0073	54	145.15	0.0068	66	146.14	0.0083	78	158.73	0.0053
7	29.26	0.0146	19	86.81	0.0045	31	139.55	0.0057	43	142.31	0.0069	55	145.21	0.0077	67	146.16	0.0081			
8	29.32	0.0236	20	94.68	0.0048	32	139.86	0.0065	44	142.52	0.0065	56	145.24	0.0089	68	146.20	0.0078			
9	29.35	0.0454	21	113.85	0.0059	33	140.08	0.0072	45	142.57	0.0063	57	145.28	0.0081	69	146.25	0.0080			
10	29.57	0.0222	22	114.61	0.0170	34	140.14	0.0069	46	142.66	0.0061	58	145.31	0.0136	70	146.29	0.0081			
11	29.63	0.0233	23	116.84	0.0072	35	141.54	0.0063	47	142.96	0.0077	59	145.49	0.0120	71	146.36	0.0068			
12	31.62	0.0239	24	123.61	0.0048	36	141.62	0.0064	48	143.08	0.0117	60	145.53	0.0072	72	146.65	0.0043			

Figure 3.14 127 MHz proton decoupled ^{13}C NMR spectra recorded in chloroform-d from a) Dimer-3bz, b) Dimer-5bz, c) Dimer-3bzo. See Figure 3.13 for carbon numbering used.

The ^{13}C spectra (see Figure 3.14) will be discussed in a similar manner to the proton spectra, from lowest to highest chemical shift. The two peaks between 14.06-14.19 ppm are assigned to the methyl carbons of the alkyl chains of the bridging unit and the hexyloxy substituent attached to the fullerene cage. This assignment is based on the expected shift for alkyl chain methyl carbons and the assumption that the longer chain bridging unit will have the lower chemical shift. The peaks between 22.63-34.11 ppm in Dimer-5bz and Dimer-3bz are assigned to the remaining alkyl carbons of the bridging unit and hexyloxy substituent (excluding the carbon α to the ether). Of the 15 expected magnetic environments, 14 peaks are resolvable in this region. For Dimer-3bzo, the analogous region lies between 22.62-31.92 ppm for which 12 magnetic environments are expected and 11 are resolvable. All of the carbons α to the ether on the hexyloxy groups are significantly down field shifted to between 69.09-69.11 ppm and the carbons α to the ether on the decyloxy group of Dimer-3bzo showing the same shift as was found in the ald-3bzo precursor of 69.56 ppm. The three remaining peaks between 56-81 ppm are assigned to the three carbon atoms α to the nitrogen of the pyrrolidine group. The 56 ppm peak is poorly resolved in Dimer-3bz, due to the reduced signal to noise and so was not assigned. In both Dimer-3bz and Dimer-3bzo there are two peaks between 86.81-94.68 ppm which are assigned to the two alkyne carbons in the bridging unit. The +ve mesomeric effect of the *ortho* oxy group on the central benzene ring of Dimer-3bzo can be seen to move the high field peak upfield relative to Dimer-3bz by a similar amount to that seen in the aldehyde precursors. As with Ald-5bz, two additional resonances are seen in this region in Dimer-5bz due to the additional two alkyne environments present. The presence of up to 60 peaks in the region around 142.8 ppm have been observed in other exohedrally derivatised fullerene molecule. The identification of 43-45 peaks between 139-148 ppm in these dimer spectra are therefore consistent with the presence of a functionalised fullerene molecule.

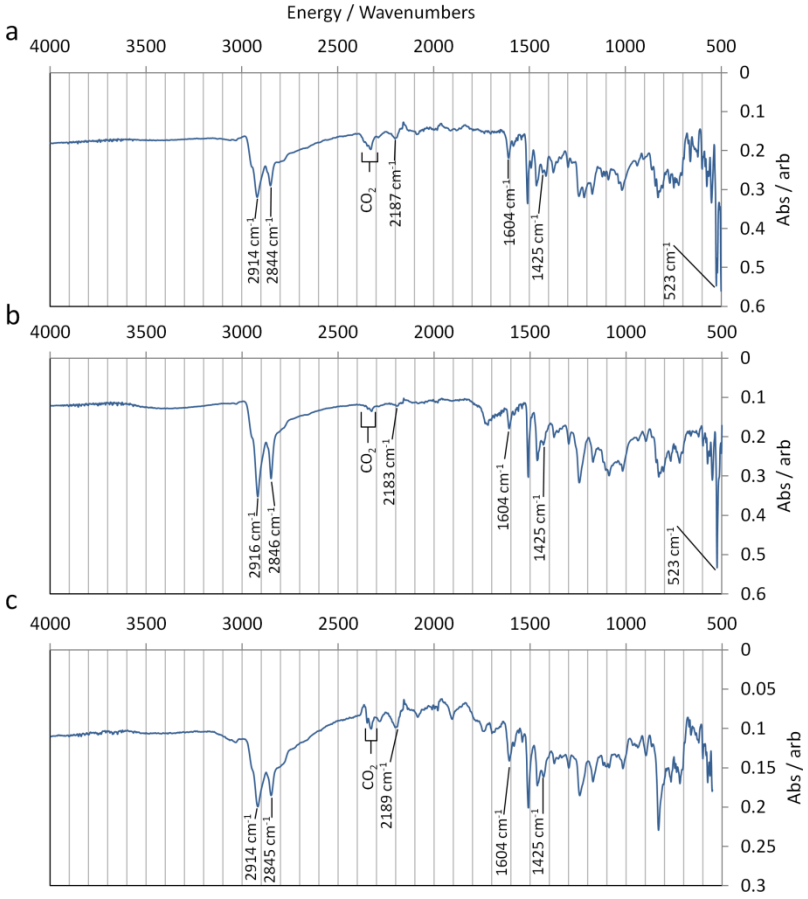


Figure 3.15 FTIR spectra of a) Dimer-3bzo b) Dimer-3bz c) Dimer-5bz, recorded at room temperature.

FTIR using an ATR diamond crystal configuration was recorded from each of the bridging units (see Figure 3.15). The strong bands at 2914-2916 cm^{-1} and 2844-2856 cm^{-1} are indicative of alkyl C-H vibrations and are therefore assigned to the alkyl substituents on the central benzene rings. The 2183-2189 cm^{-1} weak band is assigned to the alkyne stretches, the weakness is due to the small dipole of the bond. This peak is better resolved in Dimer-3bzo using Raman spectroscopy (see Chapter 5 for corresponding Raman analysis). The 1604 cm^{-1} band is assigned to the symmetric stretch of the aromatic rings of the bridging unit, also known as the 'breathing mode'.[164] The 1425 cm^{-1} band is assigned to the $T_{1u}(4)$ stretching mode of the fullerene unit and the 523 cm^{-1} band is assigned to the $T_{1u}(1)$ mode of the fullerene unit.[165]

UV-Vis

The UV-Vis absorption spectra were recorded for each of the dimer molecules (see Figure 3.16). The appearance of the absorption profiles are similar to the position of the maximum absorbance due to a combination of absorption of the fullerene cage at 350 nm and the main absorption peak of associated with the OPE bridging units. The characteristic 435 nm peak associated with the exohedral functionalisation of the fullerene cage[56]is present in all three molecules.

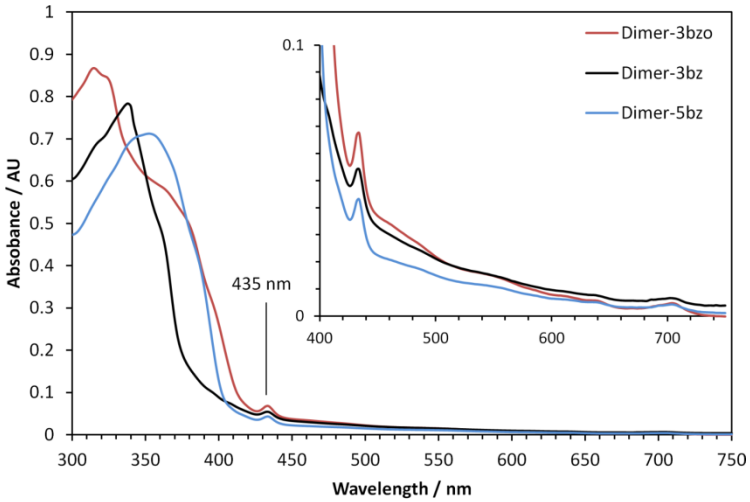


Figure 3.16 UV-Vis spectra of Dimer-3bzo (red), Dimer-3bz (black), Dimer-5bz (blue), recorded in toluene.

Mass Spectra

The mass spectra of all three dimer molecules was recorded (see Appendix Figures A.1-A.4) and compared to the theoretical isotope distribution for the expected molecular formula. The results are in good agreement with both the peak positions and isotope profile for all three dimer molecules, confirming the correct structural composition of each bridging unit.

3.4.2 Reaction optimisation for small scale

Owing to the reduced thermal stability and availability of $N@C_{60}$ compared to $C_{60,}$ the reaction parameters were optimised to minimise both the reaction scale and reaction time. The first step was to confirm the suitability of the chosen amino acid derivative in the dimer forming reaction. Figure 3.17 illustrates the significant rate enhancement that using N-(4-(hexyloxy)benzyl)glycine as the amino acid precursor has on the rate of the [2+3]cycloaddition reaction compared to when a more commonly used amino acid such as N-(ethyl) glycine is used. When N-(ethyl) glycine is used, after a reaction time of 60 minutes most of the C_{60} and Ald-3bz remains unreacted. However, when N-(4-(hexyloxy)benzyl)glycine is employed, only a 10 minute reaction time is required to yield a 50% conversion of C_{60} to Dimer-3bz. The dependence of the yield of C_{60} and Dimer-3bz on the reaction time (see insert of Figure 3.17) indicates that the reaction has gone ≈90% to completion after only 5 minutes of heating. At longer reaction times the yields of both C_{60} and Dimer-3bz are reduced and the HPLC peaks before 5:30 minutes grow in height. This suggests that at longer reaction times, the Dimer-3bz product starts to be consumed, probably via the formation of multiple pyrrolidine adducts on the fullerene cage. To reduce the formation of these side reactions, an excess of C_{60} is often used. However, since the scale of an $N@C_{60}$ analogue reaction will be determined by the quantity of $N@C_{60}$ obtainable, the option of using an excess of fullerene starting material is not available. Owing to this, an optimal reaction time of 5 minutes was decided on as it produces the highest dimer yield whilst keeping side reactions to a minimum.

The difficulty in synthesising high purity $N@C_{60}$ means that the scale of the dimer reaction needed to be reduced to be compatible with only 10-20 μg of fullerene starting material. To maintain a high concentration of fullerene starting material, as used in the large scale experiments, the volume of the reaction vessel needed to be correspondingly reduced. This was achieved by using a 5mm NMR tube as the reaction vessel, permitting solvent volumes down to 10 μl to be accommodated.

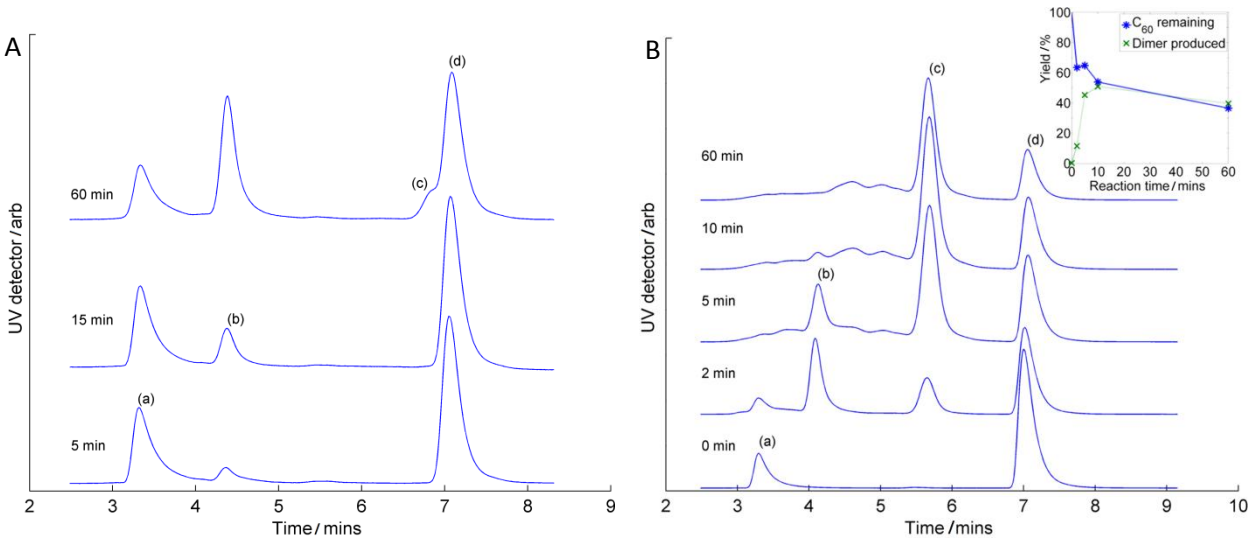


Figure 3.17 Reaction progress for the formation of C_{60}-C_{60} dimer-3bz, followed using HPLC over 60 min. (a) unreacted bis-aldehyde, (b) mono-3bz, (c) dimer-3bz, (d) unreacted C_{60}. A) Dimer-3bz reaction using N-(ethyl) glycine as amino acid reagent. B) Dimer-3bz reaction using N-(4-(hexyloxy)benzyl)glycine, insert: calculated yield based on the integrated peak heights of (c) and (d). HPLC column: Buckyprep-M 20 x 250 mm, Eluent: Toluene, flow rate 18 mL min^{-1}.

The Dimer-3bz reaction was scaled down in two steps, firstly to use 100 µg of C_{60} and then 20 µg. To manipulate and measure such small quantities of reagents it was found easiest to make up stock solutions of Ald-3bz and C_{60} in dry degassed toluene and then use a 100 µl syringe to measure out the desired number of moles of each reagent into the NMR tube reaction vessel. Due to the tendency for the amino acid to oligomerise when left in solution it was found to be more reliable to weigh the required mass of amino acid for each reaction separately using a seven decimal place microbalance. The HPLC traces of the reactant products (see Figure 3.18) for both scales show the presence of both C_{60} and Dimer-3bz. As the scale of the reaction is reduced from 30 mg-0.1 mg-0.02 mg the yield of dimer-3bz decreases from 45%-20%-8% respectively. This reduction in yield is accompanied by an increase in the size and number of peaks between 3-5 minutes. To increase the sensitivity of the HPLC UV-spectrometer an analytical 4.6 mm x 250 mm Buckyprep-M column was purchased to perform further purification. In addition, to improve the isolation of the dimer peak, the change to eluting the reaction products using a binary solvent system of hexane and toluene was used. The effect of increasing the ratio of hexane to toluene on the relative retention time of dimer-3bz and C_{60} can be seen in Figure 3.19. Using a 35:65 ratio of hexane to toluene was found to significantly enhance the separation between C_{60} and Dimer-3bz peaks.

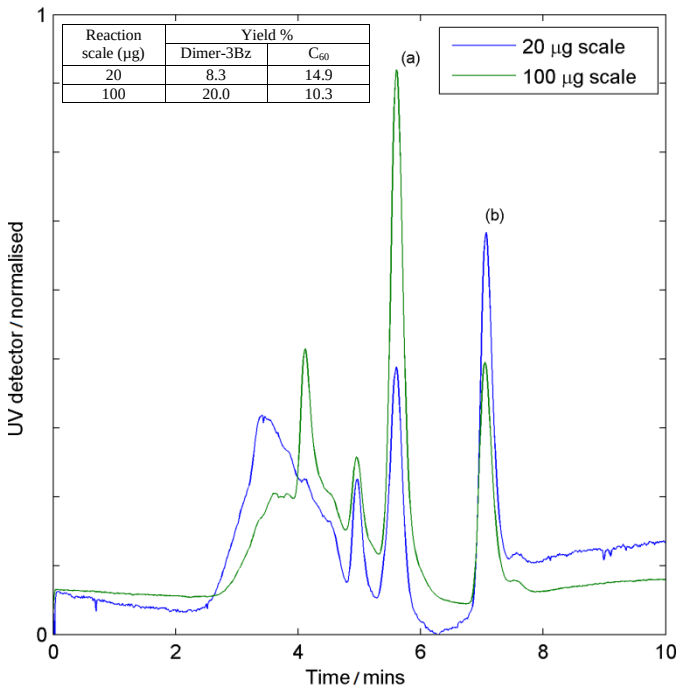


Figure 3.18 HPLC traces of product mixtures after 5 minute reaction time of the formation of C_{60}-C_{60} Dimer-3bz using 20 µg and 100 µg reaction scales with respect to C_{60}. (a) Dimer peak. (b) C_{60} peak. Insert: calculated yield based on the integrated peak areas of (c) and (d). Column Buckyprep-M 20 x 250 mm. Eluent Toluene. Flow rate 18 mL min^{-1}.

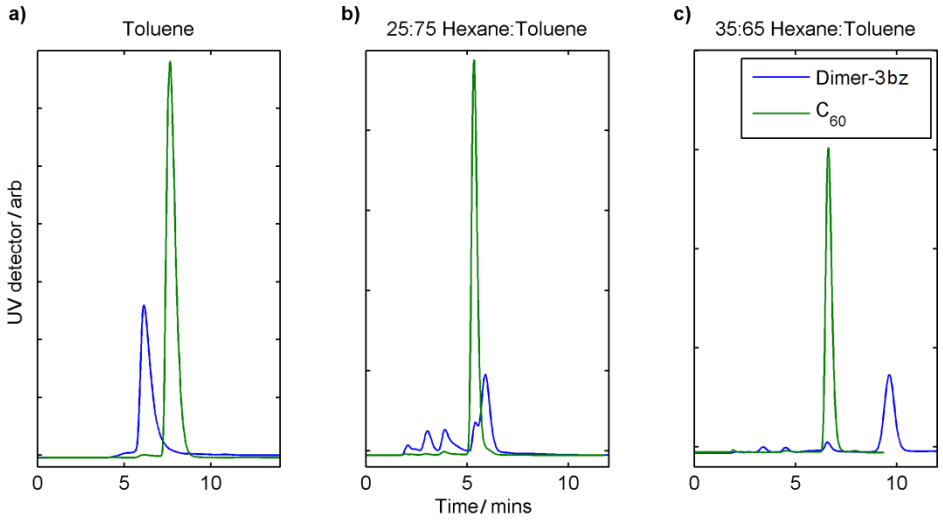


Figure 3.19 HPLC traces showing the effect which increasing the fraction of hexane in the eluent mixture has on the relative retention times of C_{60} and Dimer-3bz. Column Buckyprep-M 4.6 x 250 mm. Eluent see plot titles. Flow rate a) 1 mL min^{-1}, b+c) 2 mL min^{-1}.

3.5 Synthesis and ESR characterisation of $^{14}N@C_{60}$-C_{60} dimers

In preparation to creating two-spin centre dimer molecules, the optimised reaction conditions found for the formation of Dimer-3bz and Dimer-5bz using pristine C_{60} were applied to partially enriched $^{14}N@C_{60}$ in C_{60} starting material. The reaction was performed using two different scales, using 500 µg of 0.1% $^{14}N@C_{60}$ in C_{60} to form Dimer-5bz and 150 µg of 1% $^{14}N@C_{60}$ in C_{60} to form Dimer-3bz, which were purified using the HPLC methods developed in Section 4.3. The $N@C_{60}$ containing reactions were found to behave comparably to that of the C_{60} analogue reactions, showing a reduction in the yield of dimer product as the scale is reduced. The electron spin environments of the isolated dimer products were then characterised using RT and frozen solution CW ESR spectroscopy.

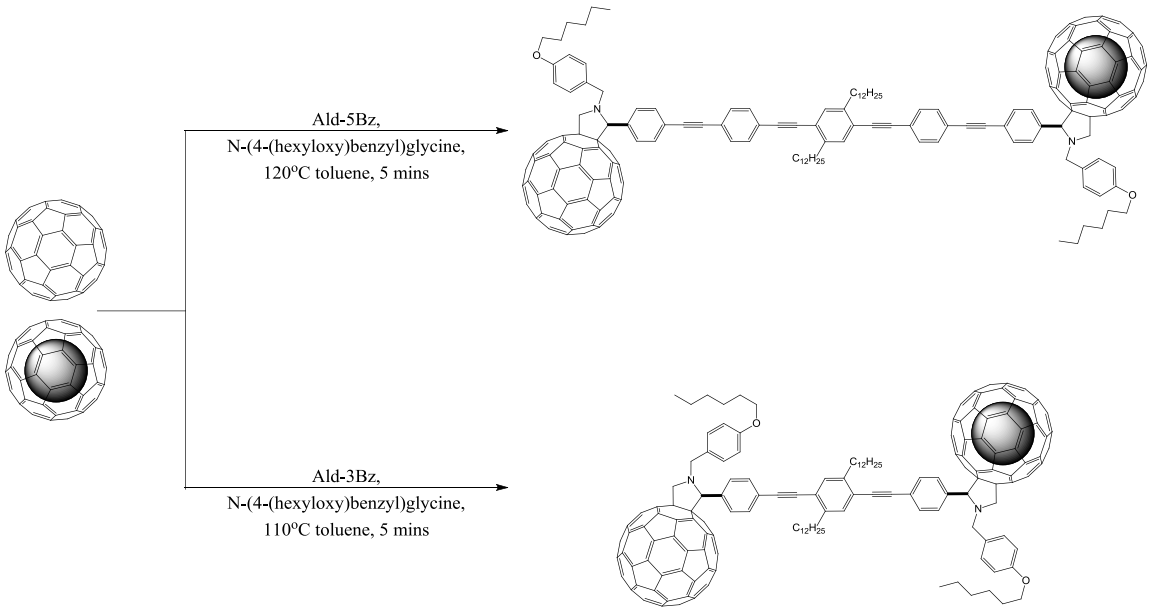


Figure 3.20 Reaction scheme for the synthesis of $^{14}N@C_{60}$-C_{60} Dimer-3bz (2 % yield) and Dimer-5bz (6 % yield) molecules, using 1 % $^{14}N@C_{60}$ and 0.1 % $^{14}N@C60$ in C_{60} starting material respectively. Both reactions retain approximately 80% of the initial $^{14}N@C_{60}$ in C_{60} enrichment level, i.e. 20 % of the spin centres decompose during the reaction.

3.5.1 $N@C_{60}$ synthesis and enrichment

The $N@C_{60}$ material was synthesised using the ion implantation experimental set-up outlined in Section 2.1. This raw $N@C_{60}$ containing material was subsequently enriched via the two stage HPLC purification method detailed in Section 2.2. First, a recycling JAI LC-200 HPLC instrument was used together with a 100 x 500 mm 15 PBB column for the initial five purification stages. Subsequently, a JAI LC 908-W HPLC

instrument was used together with a 5 PBB column to enrich to the final 0.1 or 1% $N@C_{60}$ purity used in the reactions.

3.5.2 Characterisation

The $N@C_{60}$-C_{60} dimers were characterised by HPLC, room temperature (RT) solution ESR and frozen solution ESR.

HPLC

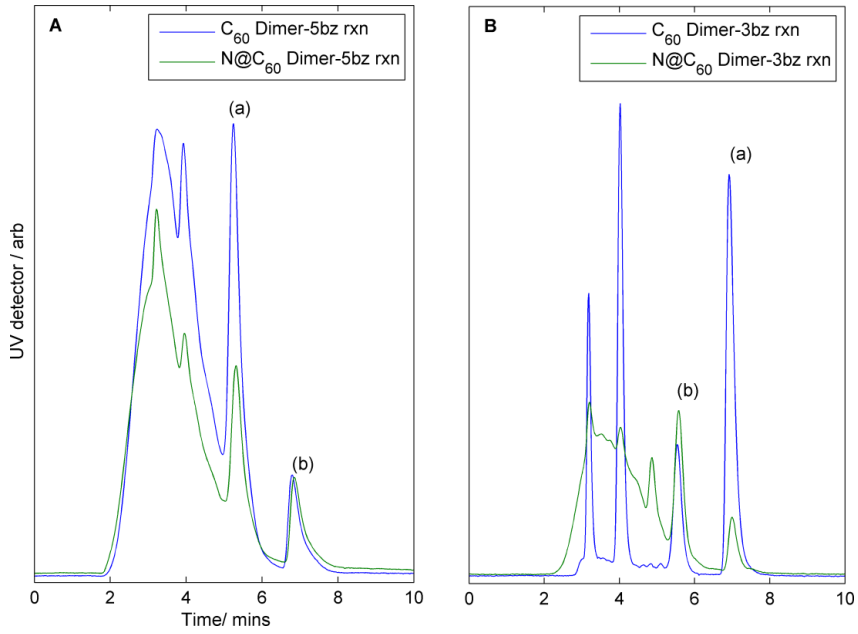


Figure 3.21 HPLC traces of product mixtures after 5 minute reaction time of the formation of (A) $N@C_{60}$-C_{60} dimer-5bz using 500 µg reaction scales with respect to $N@C_{60}/C_{60}$ (~0.1% $N@C_{60}$ purity). Column Buckyprep-M 20 x 250 mm. Eluent Toluene. Flow rate 18 mL min^{-1}. (B) $N@C_{60}$-C_{60} dimer-3bz using 150 µg reaction scales with respect to $N@C_{60}/C_{60}$ (~1% $N@C_{60}$ purity). Column Buckyprep-M 4.6 x 250 mm. Eluent 35:65 Hexane : Toluene. Flow rate 2 mL min^{-1}. (a) Dimer peak. (b) C_{60} peak.

After passing the crude product mixtures through a short silica plug to remove any amino acid derivative, the dimer molecules were isolated using HPLC. Owing to the difference in scale on which the reactions were carried out on, 500 µg for Dimer-5bz and 150 µg for Dimer-3bz respectively, a different HPLC purification protocol was used for each reaction. For the Dimer-5bz reactions, a preparative 20 x 250 mm Buckyprep-M column was used together with a single solvent eluent mixture of toluene. For the smaller scale Dimer-3bz reactions, an analytical 4.6 x 250 mm column was used together with a binary solvent mixture of 35:65 hexane : toluene. Immediately prior to purifying the $N@C_{60}$ containing reactions, a calibration HPLC trace using the product mixture of the corresponding

C_{60} test reactions was performed. Using this as a guide the exact expected position of each of the $N@C_{60}$ could be determined. As shown in Figure 3.21, the peak position of both Dimer-5bz and Dimer-3bz $N@C_{60}$ containing reaction correlate very well with the C_{60} calibration traces.

CW ESR

The room temperature (RT) solution CW ESR of both $^{14}N@C_{60}$-C_{60} Dimer-3bz and $^{14}N@C_{60}$-C_{60} Dimer-5bz were recorded using a X-band Miniscope ms200 spectrometer using toluene as solvent (see inserts Figure 3.22). Both spectra were recorded using 35 dB of microwave attenuation to provide 16 μW mw power to avoid signal saturation, and 200 mG modulation amplitude to minimise peak shape distortion. As might be expected, the solution spectra appear identical to the $^{14}N@C_{60}/C_{60}$ starting materials due the rapid tumbling of the molecular species causing an averaging out of the anisotropy (see Section 2.3). The observation of a signal due to a 5.6% $^{15}N@C_{60}$ (I=1) isotopic impurity introduced during HPLC enrichment of the starting material can be seen in the Dimer-3bz spectra. Both spectra show peak to peak hyperfine linewidths of approximately 150 mG. This observed linewidth is limited due to the inhomogeneity of the static applied magnetic field across the sample and so the natural linewidth could well be much closer to that reported for pristine $N@C_{60}$ of 30 mG.[47]

The frozen solution spectra of both Dimer-3bz and Dimer-5bz, recorded using an EMX and Miniscope ms200 spectrometer respectively. For the Dimer-3bz measurement the following parameters where used, 90K temperature, 0.8G modulation amplitude, and 54 dB microwave attenuation (0.8 μW mw power). For the Dimer-5bz measurement used a temperature of 77K, 0.6G modulation amplitude, and 30dB (50 μW mw power). In both spectra, in addition to the three hyperfine lines, satellite peaks due to the presence of a fixed ZFS term in the spin Hamiltonian arising from the distortion of the cage by the exohedral chemical functionalization is present (a more detailed description of ZFS can be found in Section 2.4). The magnitude of this fixed ZFS term has been found to correlate with the geometry of the adduct (see Table 1.1). To examine the nature of the ZFS term present in the spectra, models of the electron spin environment were created using the EasySpin software package and fitted to each

spectrum. The model uses a simplified Hamiltonian (Equation 3.1) to describe the energy of the electron spin.

$$\hat{\boldsymbol{H}} = \hat{H}_{EZ}(g_{iso}) + \hat{H}_{ZF}(D, E) + \hat{H}_{HF}(A_{iso}) \quad (3.1)$$

This model includes terms for the Electron Zeeman Interaction ($\hat{H}_{EZ}$), Zero Field Splitting ($\hat{H}_{ZF}$) and Hyperfine Interaction of the electron spin with the ^{14}N nuclear spin ($\hat{H}_{HF}$). The fitting variable used for each of the terms is shown in brackets in Equation 3.1. Isotropic terms for both the g-factor (g_{iso}) and hyperfine coupling constant (A_{iso}) were found to be sufficient to give a suitably good fit to the data. The ZFS interaction however required both axial (D) and rhombohedral (E) terms to accurately model the spectrum and is constant with previously characterised $N@C_{60}$ derivatives. [52-53, 55, 57-58, 60, 166] The only other fitting parameter that was fitted in the model was the Gaussian linewidth of each transition (lwpp), principally caused by the distribution of coupling energies of the surrounding bath of nuclear spins surrounding each molecule.[53] For the Dimer-3bz spectra an additional $^{15}N@C_{60}$-C_{60} component with a 5.6% weighting was required to account for the isotopic impurity introduced during the enrichment of the $^{14}N@C_{60}$ starting material. This second component used the same spin hamiltonian form and parameters as the $^{14}N@C_{60}$ Dimer-3bz component with the exception of a larger A_{iso} value of 21.24 MHz, consistent with previous observations.[29, 46, 124]

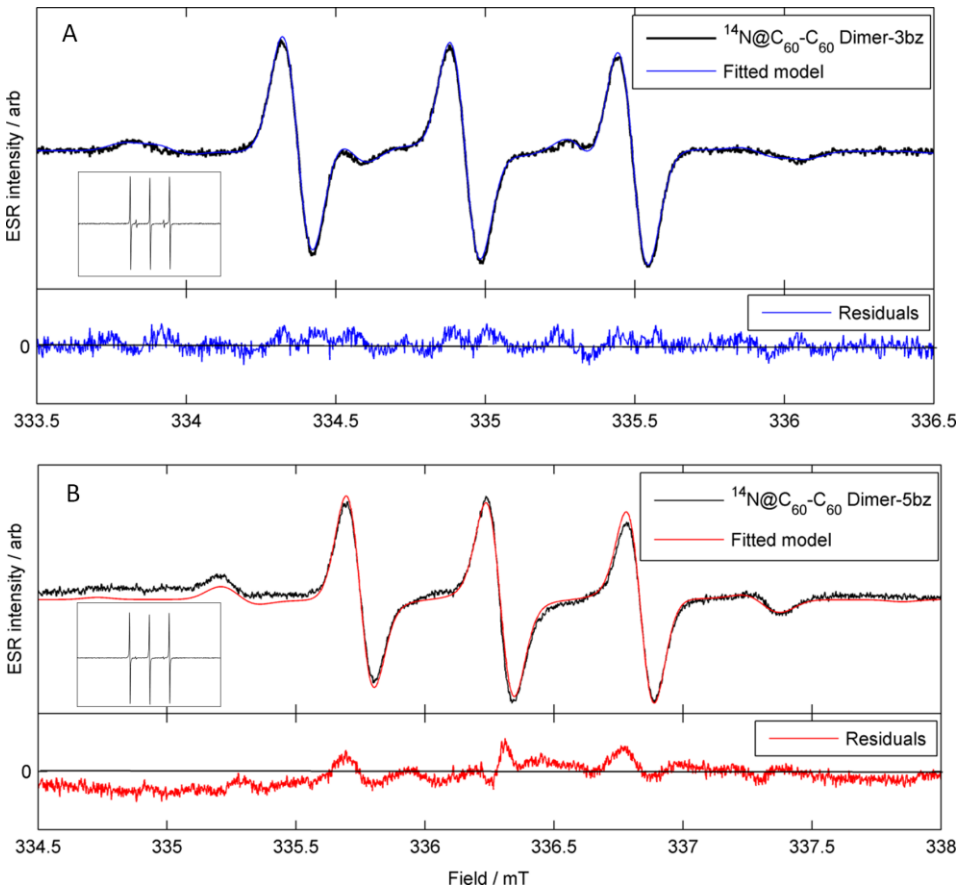


Figure 3.22. Frozen solution CW ESR spectrums of $N@C_{60}$-C_{60} dimers recorded in toluene with RT solution spectra shown as inserts. A) Frozen solution CW ESR spectra recorded at 90K using an EMX spectrometer of $N@C_{60}$-C_{60} Dimer-3bz (black) fitted to an ^{14}N model spectrum (blue) with the following parameters: hyperfine splitting term (A_{iso}= 15.736 MHz), Axial zero field term (D=14.19, E=0.74), linewidth 0.121 G and g_{iso}=2.0027 with a RMS residual fit of 0.012. The model also includes a 5.6% ^{15}N impurity component with the following parameters: A_{iso}= 21.24 MHz, D=14.19, E=0.74, linewidth 0.121 G and g_{iso}=2.0027. B) Frozen solution CW ESR spectra recorded at 77K using a Miniscope ms200 spectrometer of $N@C_{60}$-C_{60} Dimer-5bz (black) fitted to a model spectrum (red) with the following parameters: A_{iso}= 15.281 MHz, D=14.25, E=0.41, linewidth 0.1080 G and g_{iso}=2.0023 with a RMS residual fit of 0.049. Poor fitting at low field due to the presence of a small impurity in the microwave cavity (shown in figure A.5).

Since the chemical geometry of the exohedral pyrrolidine adduct of both the Dimer-3bz and Dimer-5bz is similar, the fitted models were expected to show similar electron environments. This is indeed the case for the g_{iso}, peak to peak linewidth and both ZFS D and E terms. The smaller A_{iso} term found for Dimer-5bz is suggested to be due to a minor shift in the hyperfine peak positions caused by the presence of a broad impurity in the microwave cavity used, see figure A.5, this can also be seen as a sinusoidal undulation in the residuals of the fit in figure 3.22.B. The axial ZFS term of Dimer-3bz (14.19 MHz) and Dimer-5bz (14.25 MHz) was found to be slightly smaller than that found for other pyrrolidine adducts of 16.5 MHz $\pm$1MHz.[52, 57-60] The remaining fitted parameters, g_{iso} and E, agree well with previous reports of $N@C_{60}$ pyrrolidine adducts.[52, 58-59]

3.6 Synthesis and ESR characterisation of an $^{14}N@C_{60}$-$^{14}N@C_{60}$ dimer

The similarity of the electron spin environment in Dimer-3bz and Dimer-5bz permits the decision as to which linker to use as the spacing unit to be made purely based on the expected magnitude of dipolar coupling interaction J_{dip} between each of the spin centres. It has been theoretically calculated that the optimal spin-spin separation for an $^{15}N@C_{60}$-$^{15}N@C_{60}$ dimer to resolve dipolar coupling in a CW ESR spectrum is around 3 nm in a disordered frozen solution matrix such as toluene.[124] The separation of the two spin centres can be estimated to be around 2.7 nm and 4 nm for Dimer-3bz and Dimer-5bz, respectively. Hence the chosen dimer structure for the synthesis of a $^{14}N@C_{60}$-$^{14}N@C_{60}$ dimer molecule was Dimer-3bz as it had a spin separation closest to 3 nm.

The reaction was performed using 10 µg of ~50% $^{14}N@C_{60}$ in C_{60} to form both $N@C_{60}$-C_{60} and $N@C_{60}$-$N@C_{60}$ Dimer-3bz molecules (see Figure 3.23). It was carried out using the same reaction protocol that was utilised to synthesise the single spin centre Dimer-3bz sample characterised in Section 3.4 and purified using the hexane/toluene HPLC method developed in Section 3.3. The isolated dimer product was characterised using RT and frozen solution CW ESR spectroscopy to determine the average number of spin centres in each molecule and measure the effect of spin-spin coupling on the spin Hamiltonian.

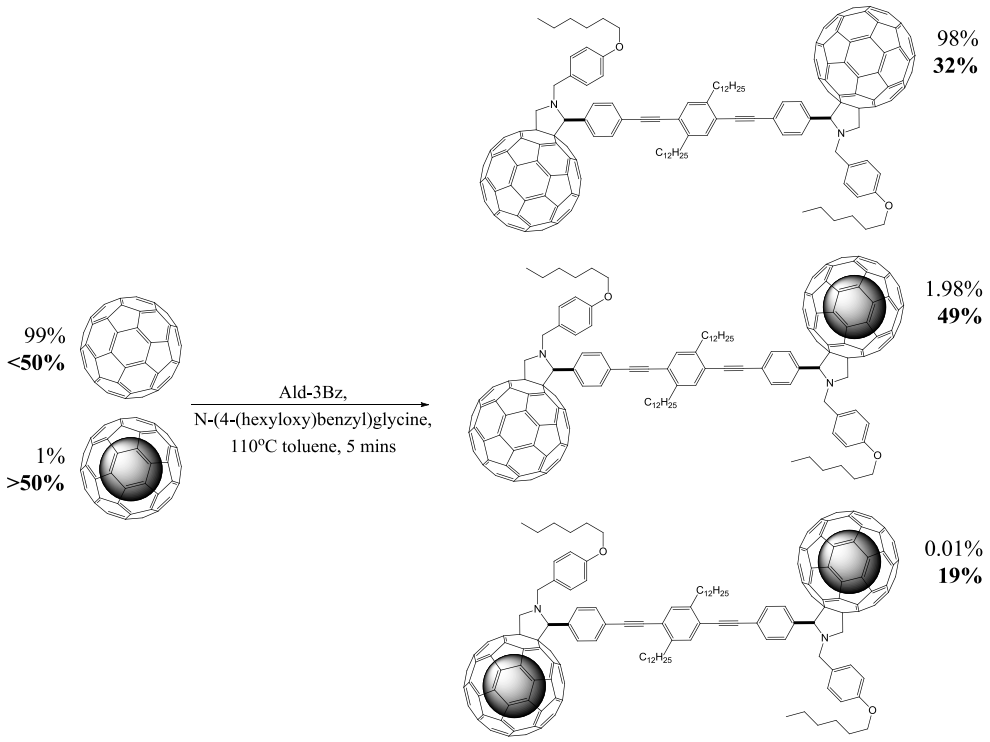


Figure 3.23. Reaction scheme for the synthesis of Dimer-3bz using 1% $N@C_{60}$ in C_{60} and +50 % $N@C_{60}$ in C_{60} (bold typeface). The scheme indicated the predicted statistical distribution of the $N@C_{60}$ in the dimers collected together as the product fraction. For the 1 % $N@C_{60}$ in C_{60} reaction the distribution was calculated using the number of $N@C_{60}$ centres per fullerene cage in the starting material (0.01); C_{60}-C_{60} = 0.99^2, $N@C_{60}$-C_{60} = 0.01 x 0.99, $N@C_{60}$-$N@C_{60}$ = 0.01^2. For the +50 % $N@C_{60}$ in C_{60} reaction the distribution was calculated from the number of $N@C_{60}$ centres per fullerene cage in the product dimer fraction, measured using HPLC peak and ESR signal integration to be 0.43(5); C_{60}-C_{60} = 0.565^2, $N@C_{60}$-C_{60} = 2*0.435 x 0.565, $N@C_{60}$-$N@C_{60}$ = 0.435^2.

3.6.1 $N@C_{60}$ synthesis and enrichment

3 grams of $N@C_{60}/C_{60}$ mixture was synthesised using the ion implantation method outline in Section 2.1.[34] This raw $N@C_{60}$ containing material was subsequently enriched via the two stage HPLC purification method (detailed in Section 2.2.) first using a recycling JAI LC-200 HPLC instrument together with a 100 x 500 mm 15 PBB column for the initial eight purification stages and subsequently using a JAI LC 908-W instrument together with a 5 PBB column to enrich the sample a further 14 stages. After 22 recycling HPLC runs, a high purity $N@C_{60}/C_{60}$ peak was isolated (see Figure 3.24.A). The integrated area of the $N@C_{60}/C_{60}$ peak indicated the total mass of $N@C_{60}/C_{60}$ to be 10 µg. With the total number of $N@C_{60}$ spin centres present calculated from the RT CW ESR spin signal intensity, a lower bound for the mass of $N@C_{60}$ was determined to be 4.6 µg (see Figure 3.24.B).

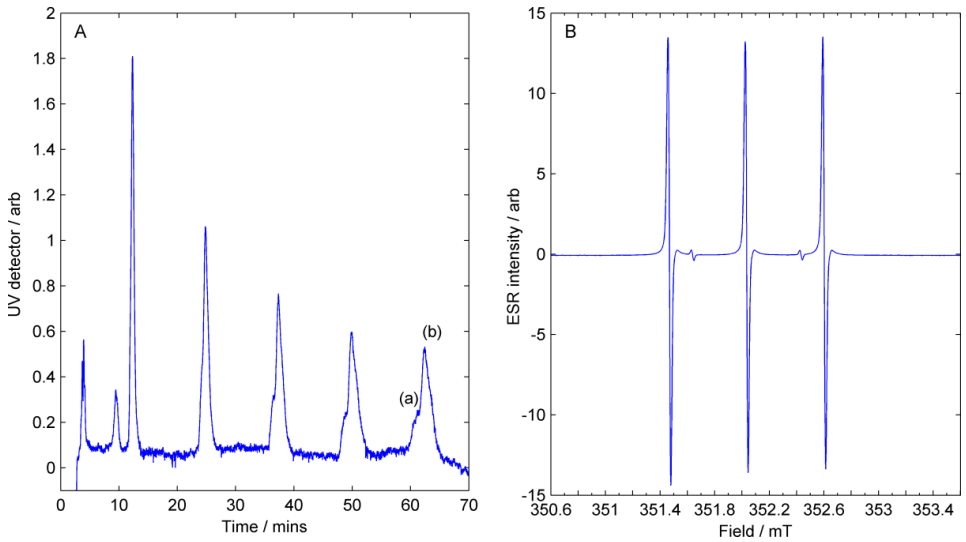


Figure 3.24 (A) Final recycling HPLC run for $N@C_{60}$ purification. (a) C_{60} and (b) $N@C_{60}$ peaks respectively. Column (5-PBB) 20 x 250 mm. Eluent toluene, flow rate 16 mL min^{-1}, final peak area intergration yields mass of $N@C_{60}$ calculated to be 10 µg. (B) RT EMX ESR spectrum recorded from $N@C_{60}$ peak collected from (A) using the following parameters, 60 dB mw attenuation (0.2 µW mw power), 0.2 G modulation amplitude, Q factor 9100 and 90 s scan time averaved over 3 scans. Using the precalibrated inbuilt software of the EMX spectrometer, double integration of the peak area yielded the total number of $N@C_{60}$ spin centres calculated to be 3.75 x 10^{15} molecules, corresponding to 4.6 µg of $N@C_{60}$.

3.6.2 Characterisation

After passing the crude product mixture through a short silica plug to remove any amino acid derivative, the $^{14}N@C_{60}$-$^{14}N@C_{60}$ containing Dimer-3bz peak was isolated using HPLC. Owing to the small scale of the reaction, an analytical 4.6 x 250 mm column was used together with a binary solvent mixture of 35:65 hexane : toluene. Immediately prior to purifying the $N@C_{60}$ containing reactions, a calibration HPLC trace using the product mixture of the corresponding C_{60} test reactions was performed. Using this as a guide the exact expected position of each of the $N@C_{60}$ peaks could be determined. As can be seen in Figure 3.25.A the peak position of both the C_{60}/$N@C_{60}$ and Dimer-3bz peaks correlate very well with the C_{60} calibration traces. Based on the peak area, the quantity of $N@C_{60}$ Dimer-3bz was 430 ng corresponding to a 2 % yield. The yield of the $N@C_{60}$ Dimer-3bz was smaller than expected while the contribution from earlier peaks was much more prominent. This could be due to either the decomposition of the $N@C_{60}$ containing molecules during the reaction or the presence of a small quantity of $C_{60}O$/$N@C_{60}O$ that is formed during storage of the fullerene starting material.

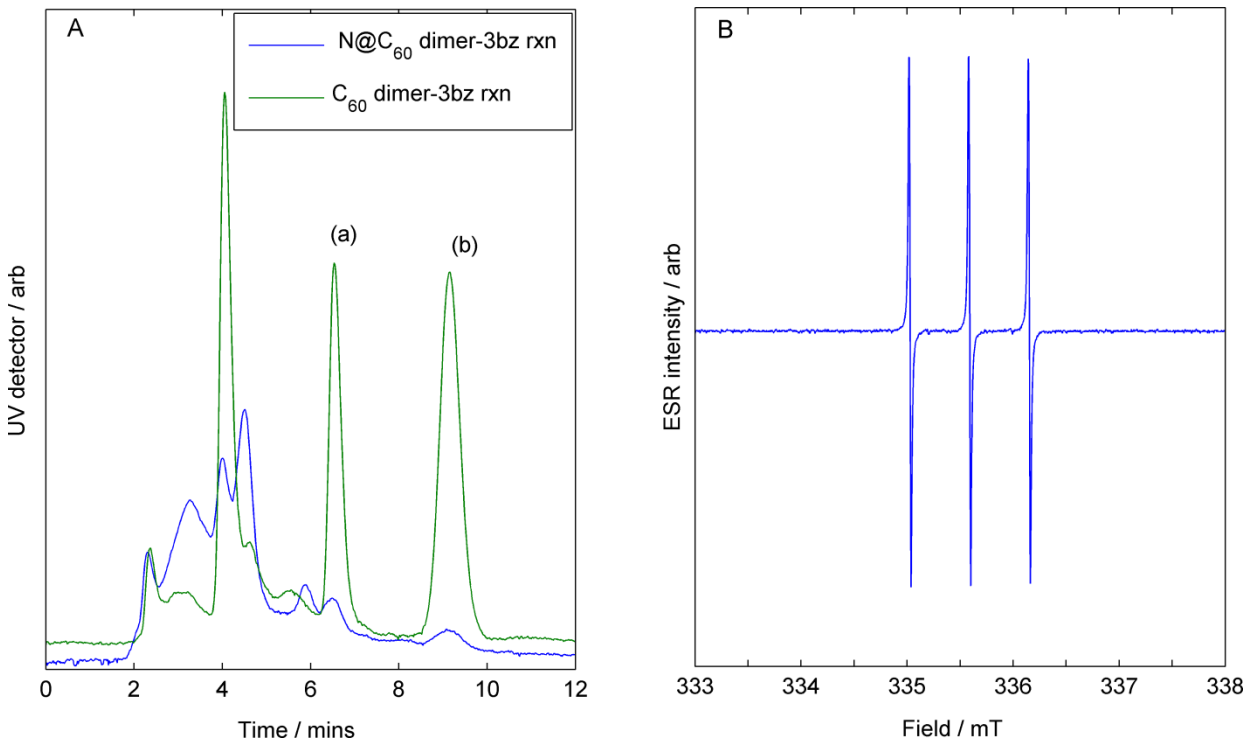


Figure 3.25 (A) HPLC trace of reaction mixture after $N@C_{60}$-$N@C_{60}$ dimer formation reaction (blue), overlayed with the analogue C_{60} marker spectrum (green) indicating that the retention time of both the $N@C_{60}$ and $N@C_{60}$ dimer peaks are located exactly where the C_{60} analogue reactions predict. (a) $N@C_{60}$/C_{60} peak. (b) $N@C_{60}$-$N@C_{60}$ dimer peak. Integration of (b) corresponds to 430 ng of Dimer-3bz. Column Buckyprep-M 4.6 x 250 mm. Eluent 35:65 hexane:toluene. Flow rate 2 mL min^{-1}. (B) RT EMX ESR spectrom recorded from peak (b) of Figure (A) using 55 dB mw attenuation (0.6µW mw power) and 0.2G mw modulation. Using the precalibrated inbuilt software of the EMX spectrometer, double integration of signal yields total number of $N@C_{60}$ containing Dimer-3bz molecules to be 1.16 x 10^{14}.

The presence of doubly filled dimer was probed using RT and frozen solution CW ESR spectroscopy. By quantifying the number of molecules of dimer produced using the reaction HPLC trace (1.01 x 10^{14}) and the total number of $N@C_{60}$ spin centres present, calculated from the double integral of the RT CW ESR spectra (1.16 x 10^{14} spin centres), the average number of spin centres per cage was calculated to be 0.43(5). By assuming similar chemical reactivity of $N@C_{60}$ and C_{60}, the fraction of $N@C_{60}$-$N@C_{60}$ dimer and $N@C_{60}$-C_{60} dimer was calculated to be 19 % and 49 % respectively (see Figure 3.23).

A 90 K frozen toluene solution ESR spectrum of the dimer fraction was recorded to probe for the expected additional spectral features arising from dipole-dipole coupling between two $N@C_{60}$ centres (see Figure 3.26). The principal features of the spectra appear very similar to those obtained from the 1 % $N@C_{60}$-C_{60} Dimer-3bz as shown in Figure 3.22.a. Initial least sqared fitting of the spectrum to the single spin centre hamiltonian used to model the 1 % $N@C_{60}$-C_{60} Dimer-3bz specta (equation 3.1) can be

seen in figure 3.26. the best fit pararameters where A_{iso}= 15.741 MHz, D=14.58, E=0.72, line-width 0.109 G, g_{iso}=2.0027. While these parameters are physically plausible they fail to accurately account for a significant proportion of the spectral signal either side of each hyperfine peak, best illustrated by looking at the residuals of the fit shown in red.

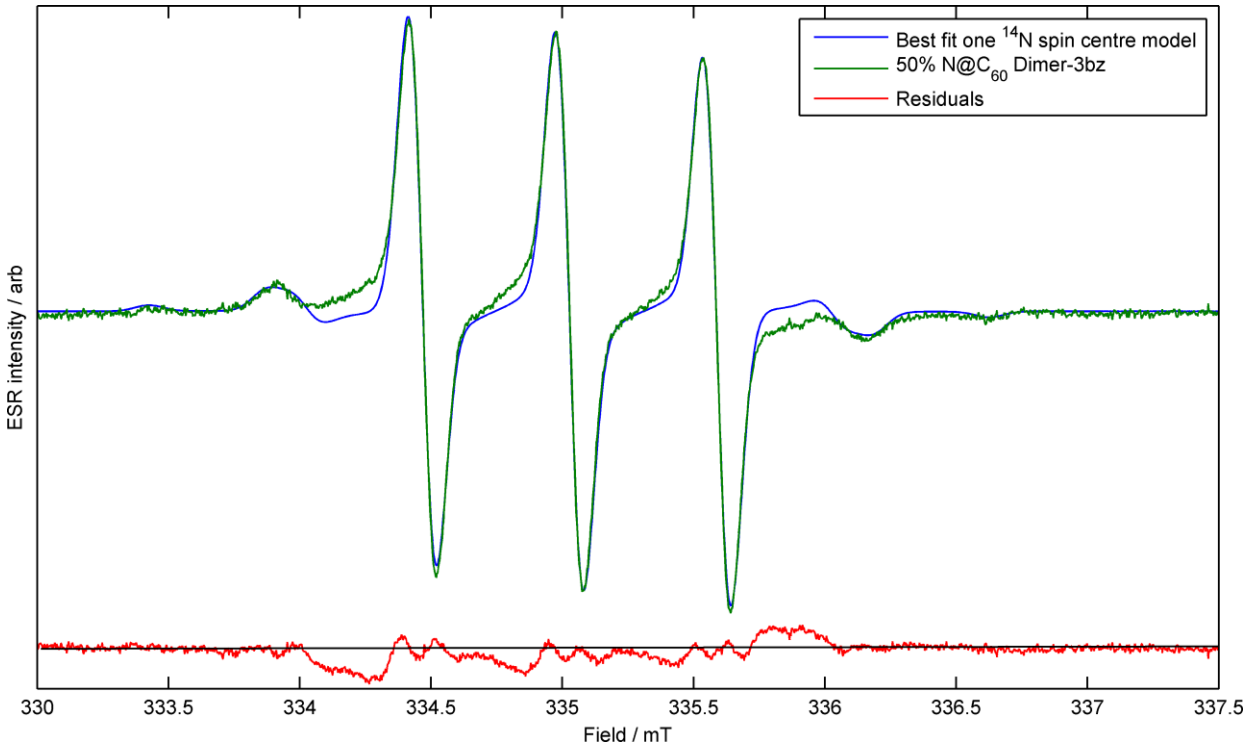


Figure.3.26 Frozen toluene solution CW ESR spectra recorded at 90 K using an EMX spectrometer of the dimer product of the +50 % $N@C_{60}/C_{60}$ Dimer-3bz reaction (green). Least squared Best fit model (blue) using a single one ^{14}N spin centre, fitted parameters are as follows A_{iso}= 15.741 MHz, D=14.58, E=0.72, line-width 0.109 G, g_{iso}=2.0027 and an RMSE 0.0232. Residuals of fit shown in red.

Figure 3.23 indicates that the dimer reaction products are expected to contain both one and two $N@C_{60}$ spin centre molecules. Owing to this it is suggested that the observed spectrum is a linear combination of a one and two spin centre components and the spectral regions that fit poorly to a one spin model are infact due to the two spin centre component.To isolate the spectral features associated with the minor $N@C_{60}$-$N@C_{60}$ Dimer-3bz component of the product mixture, the 1 % $N@C_{60}$-C_{60} Dimer-3bz spectrum was subtracted from the 50 % $N@C_{60}$-$N@C_{60}$ spectrum to give the residual spectrum shown in Figure 3.27.B.

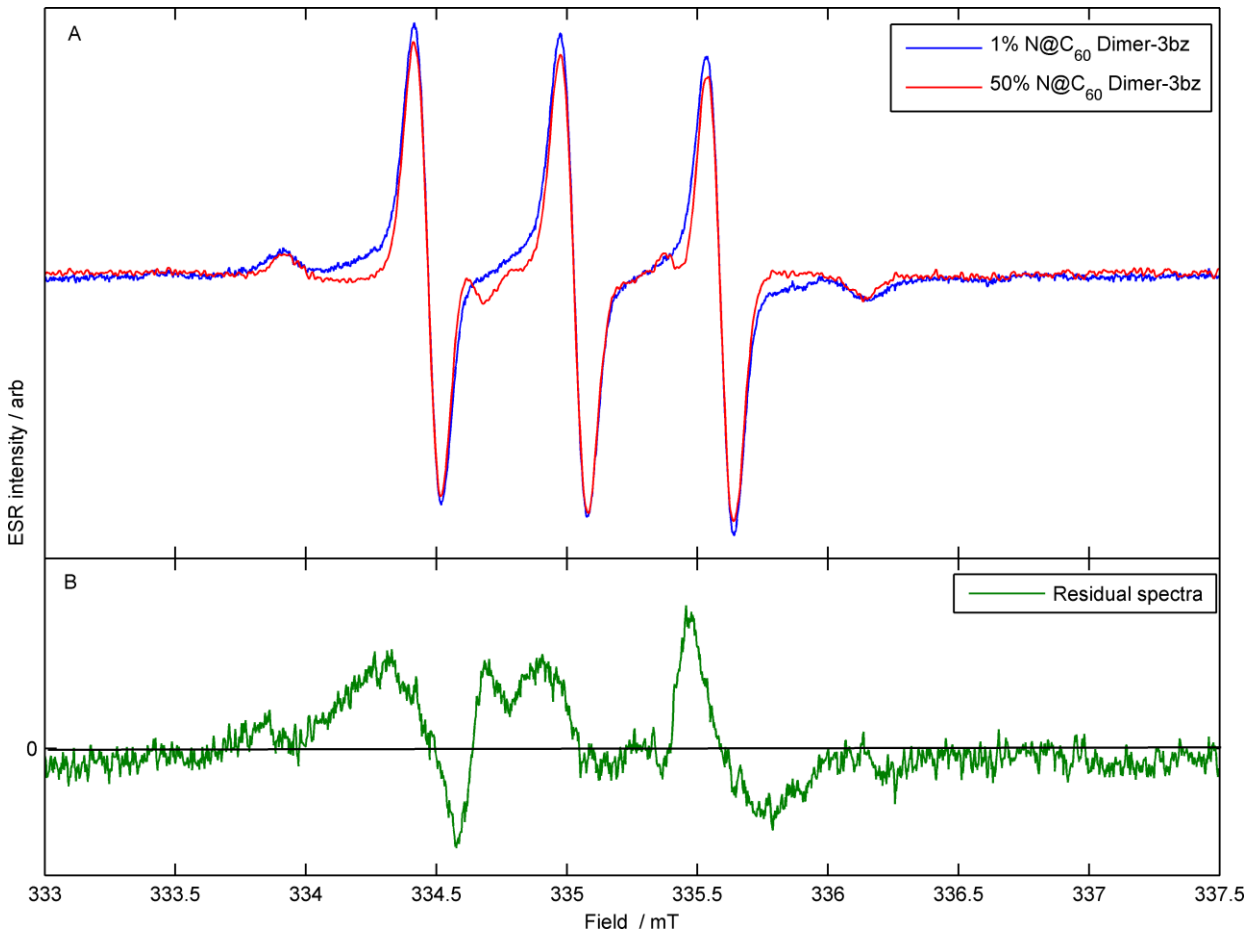


Figure 3.27 A) Frozen solution CW ESR spectra recorded at 90 K using an EMX spectrometer of, N@C_{60}-C_{60} Dimer-3bz from 1 % N@C_{60}/C_{60} Dimer-3bz reaction (blue) and a mixture of N@C_{60}-N@C_{60} and N@C_{60}-C_{60} Dimer-3bz from the +50 % N@C_{60}/C_{60} Dimer-3bz reaction (red). B) a residual plot of the difference between the two spectra (green).

A simulated ESR spectrum for a two-spin centre N@C_{60}-N@C_{60} Dimer-3bz molecule was then created using a model electron spin Hamiltonian of form shown in Equation 3.2.

$$\widehat{\boldsymbol{H}} = \sum_{i=1}^{2}\left\{\widehat{H}_{EZ}^{i}(g_{iso}) + \widehat{H}_{ZF}^{i}(D,E) + \widehat{H}_{HF}^{i}\left(A_{iso}^{I(i)}\right)\right\} + \widehat{H}_{EE}^{1,2}\left(J_{dip}\right) \qquad (3.2)$$

This Hamiltonian is of the form used to describe an isolated N@C_{60}-C_{60} Dimer-3bz spin system shown in Equation 3.1 with the addition of an interaction term arising from a fixed point dipole-dipole coupling between the two-spin centres ($\widehat{H}_{EE}^{1,2}$). The Hamiltonian includes separate, but identical Electron Zeeman Interaction ($\widehat{H}_{EZ}$), Zero Field Splitting ($\widehat{H}_{ZF}$) and Hyperfine Interaction with a single ^{14}N nuclear spin ($\widehat{H}_{HF}$) terms for each of the two-spin centres (i).

The model spectrum uses the same values for the parameters g_{iso}, D, E, A_{iso} and lwpp that were fitted to the 1 % $N@C_{60}$-C_{60} Dimer-3bz spectra in Figure 3.22 leaving only the magnitude of maximum dipole-dipole interaction (J_{dip}) to be specified. To estimate this value, a molecular model of the $N@C_{60}$-$N@C_{60}$ molecule was created and optimised using a molecular mechanics (mm2) relaxation method using the software package ChemBioDraw 3D. The most significant modulation of the separation between the two-spin centres was assumed to arise from the low dihedral barrier to rotation of the fullerene cages about the long axis of the OPE bridging unit, giving the minimum and maximum separation of the fullerene cages to be equal to the *cis* and *trans* conformations shown in Figure 3.28. This model yields the distance between the centre of the two $N@C_{60}$ units of between 2.6(3) nm (*cis*) and 2.7(5) nm (*trans*). To calculate an average value for the J_{dip} parameter, a separation of 2.7 nm was used together with Equation 2.12 to give $J_{dip} = 2.67\ MHz$ (see the blue line in Figure 3.29.A for the calculated model spectrum, for comparison the 1 % $N@C_{60}$ dimer-3bz model is also shown in red).

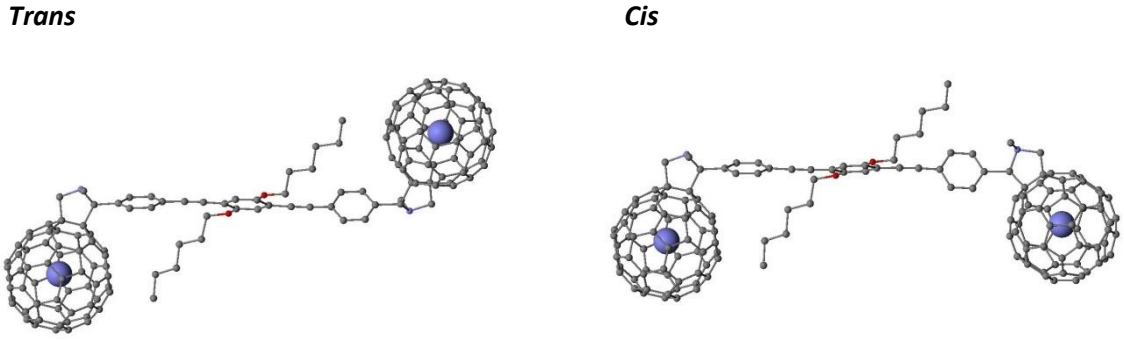


Figure 3.28 Molecular model of an $N@C_{60}$-$N@C_{60}$ Dimer-3bz molecule, with the pyrrolidine substituents omitted for simplicity and only the first six carbon atoms on the central unit shown. *Trans* conformation is calculated to have a 2.75 nm separation between the centres of the fullerene cages. *Cis* conformation is calculated to have a 2.63 nm separation between centres. Model was created using a molecular mechanics (mm2) relaxation method using ChemDraw 3D software.

Before a comparison of the model could be made with the residual spectra, a model to account for the 5.6 % $^{15}N@C_{60}$-C_{60} Dimer-3bz impurity present in the 1 %$^{14}N@C_{60}$-C_{60} Dimer-3bz ESR spectrum was constructed using the same model used as the minor ^{15}N component fitted to the 1 % $^{14}N@C_{60}$-C_{60} Dimer-3bz ESR spectrum in figure 3.22. The $^{15}N@C_{60}$-C_{60} model parameters are as follows: A_{iso}= 21.24 MHz, D=14.19, E=0.74, lwpp=1.121 G and g_{iso}=2.0027. The inverse of the calculated spectrum

is shown in black together with the $^{14}N@C_{60}$-$^{14}N@C_{60}$ Dimer-3bz and $^{14}N@C_{60}$-C_{60} Dimer-3bz models in Figure 3.29.A. The $^{15}N@C_{60}$-C_{60} model was then added to the $^{14}N@C_{60}$-$^{14}N@C_{60}$ Dimer-3bz and $^{14}N@C_{60}$-C_{60} Dimer-3bz models and overlaid onto the residual spectra of figure 3.27.B (see Figure 3.29.B). The principal features of the $^{14}N@C_{60}$-$^{14}N@C_{60}$ Dimer-3bz model and experimental data correlate well, with the calculated residual spectrum shown in figure 3.29.C. The RMS fit error is also smaller for the $^{14}N@C_{60}$-$^{14}N@C_{60}$ Dimer-3bz model (0.099) compared to the $^{14}N@C_{60}$-C_{60} Dimer-3bz model (0.132) supporting the assumption that the residual spectrum has effectively excluded the single spin centre component of the total spectrum.

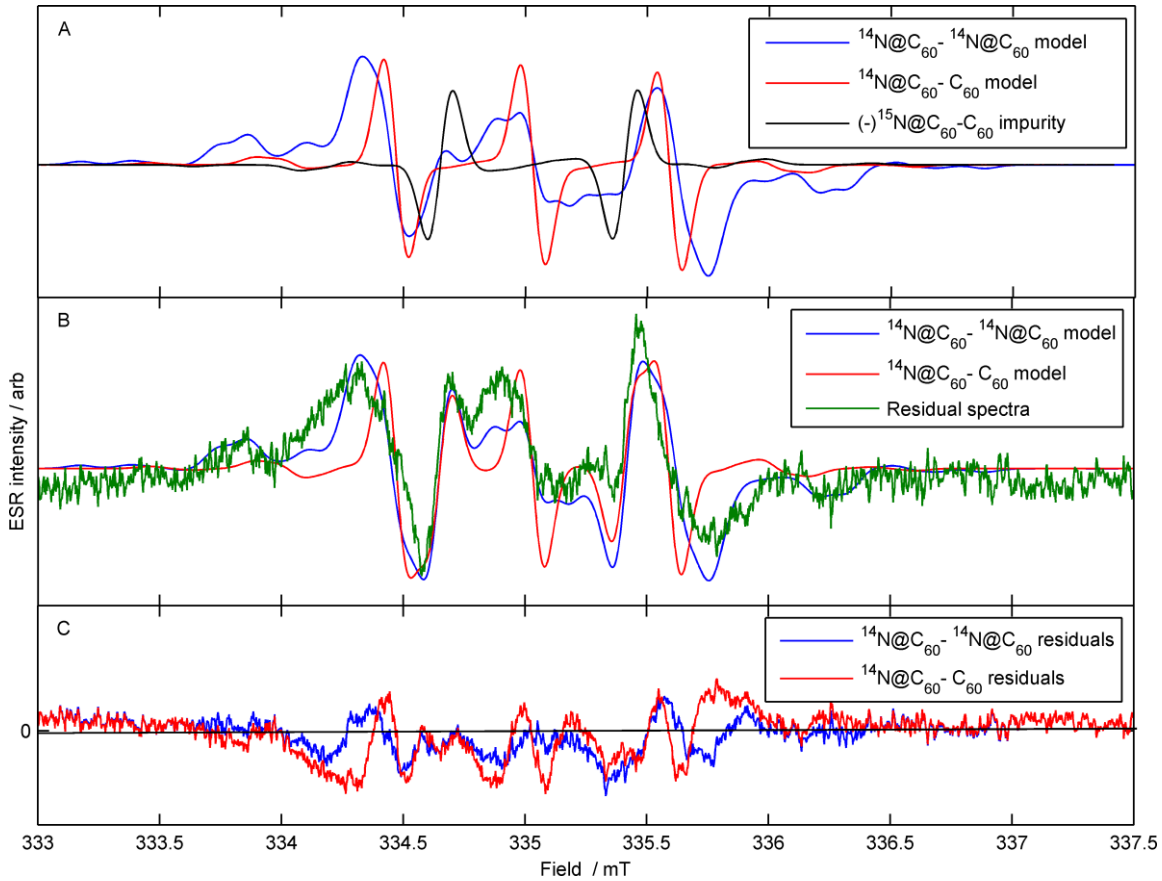


Figure 3.29. A) One (red) and two (blue) spin centre $N@C_{60}$-$N@C_{60}$ models, with following parameters: (A_{iso}= 15.736 MHz, D=14.19, E=0.74, line-width 0.121 G and g_{iso}=2.0027 the two spin centre model includes a dipolar interaction term of J_{dip}= 2.67 MHz. The inverse of the model of the 5.6 % $^{15}N@C_{60}$-C_{60} impurity present in the 1 %$N@C_{60}$-C_{60} spectrum shown in figure 3.22.A (black) was added to each of the one and two spin centre $N@C_{60}$-$N@C_{60}$ models to yield the two models in shown in (B). B) Overlay of the one and two spin centre models including the ^{15}N impurity onto the residual component shown in figure 3.27.B with the corresponding residual fits shown in (C) and RMS fit errors of 0.132 and 0.099 for the one and two spin centre models respectively.

3.7 Discussion

The combination of low thermal stability of chemically functionalised $N@C_{60}$ and the requirement (assuming the absence of a catalyst) for elevated temperature to activate the 1,3 dipolar cycloaddition reaction made optimising the rate of the dimer formation reaction key to the successful synthesis of an $N@C_{60}$-$N@C_{60}$ dimer. A comparison of the product mixture at a number of reaction time intervals using the chosen amino acid N-(4-(hexyloxy)benzyl)glycine or the more commonly used N-(ethyl)glycine in the dimer forming reaction shows that our chosen amino acid provides a substantial enhancement of the reaction rate. The addition of an aromatic substituent to the amino group can greatly enhance the rate of 1,3-dipolar cycloaddition to nanotubes;[167] rationalised by a preorganisation of the ylide with the sp^2 nanotube surface via π-π stacking. The same preorganisation is likely to be present between the fullerene cage and N-(4-(hexyloxy)benzyl)glycine. This could then produce a double rate enhancement: firstly, the probability of the three reagents meeting to react is enhanced, and secondly, the electrophilic fullerene can stabilise the formation of the ylide intermediate. It is also possible that the presence of the o-hexyl substituent enhances the reaction rate, firstly by increasing the solubility of the amino acid in the reaction solvent, permitting a greater stoichiometric ratio to be used, and additionally by enhancing the π-π interaction between the fullerene and the amino acid benzene ring through mesomeric donation of the oxygen into the benzene ring.

The similarity of the model spin Hamiltonian fitted to both the $N@C_{60}$-C_{60} Dimer-3bz and Dimer-5bz molecules in frozen matrices agrees with the expectation that the spin density remains localised on the nitrogen centre leading to the size of the OPE π-system to not influence the electron spin environment.

The ESR spectrum arising from a two-spin centre $N@C_{60}$-$N@C_{60}$ molecule suggests that the presence of two $N@C_{60}$ functionalized molecules in close proximity to one another does not significantly affect the stability of the endohedral nitrogen species. This is a fundamental requirement for the successful implementation of $N@C_{60}$ as a quantum logic element. The ability for the spin Hamiltonian for the

centre $N@C_{60}$-$N@C_{60}$ molecule to be approximated to a simple point dipole-dipole interaction will aid theorists to construct models describing larger arrays of coupled $N@C_{60}$ molecules.

Since this reaction is compatable with microgram quantities, the way is open for further chemical functionalization of high purity $N@C_{60}$. This method can be used to create two-spin centre $N@C_{60}$ molecules with the required narrow coupling strength distribution to allow $N@C_{60}$ to be exploited for quantum information processing applications. The next logical step is to orient the molecules with respect to a magnetic field, this will be investigated in Chapter 4.

3.8 Summary of Experimental Details

Synthesis of Ald-3bz. To a 50 mL two neck round bottom flask fitted with a reflux condenser, 1,4-didodecyl-2,5-diethynylbenzene 100 mg (0.2165 mmol), 4-iodobenzaldehyde 110.5 mg (0.43 mmol), bis(triphenylphosphene)palladium(II) chloride 7.6 mg (0.011 mmol), Copper(I) iodide 5.6mg (0.011 mmol), triphenylphosphene 2.1 mg (0.22 mmol) was added and purged with argon for 15 minutes. 20 mL of dry toluene and 1 mL of triethylamine were purged with argon for 20 minutes before being added via a cannula to the solid reagents. The reagent mixture was heated to 100^{o}C for 15 hours then purified using a flash silica column: 1:1 DCM:Pet. R_f=0.4. 90 mg pure product isolated (62 % yield). ^{1}H NMR (500 MHz, CHLOROFORM-*d*) δ ppm 0.88 (t, *J*=6.9 Hz, 6 H) 1.18 - 1.33 (m, 28 H) 1.36 (br. tt, *J*=7.5,7.5 Hz, 4 H) 1.42 (tt, *J*=7.5, 7.5 Hz, 4 H) 1.72 (tt, *J*=7.5, 7.5 Hz, 4 H) 2.83 (t, *J*=7.5 Hz, 4 H) 7.41 (s, 2 H) 7.67 (d, *J*=8.2 Hz, 4 H) 7.89 (d, *J*=8.2 Hz, 4 H) 10.04 (s, 2 H). ^{13}C NMR (126 MHz, CHLOROFORM-*d*) δ ppm 14.09, 22.65, 29.32, 29.50, 29.51(shoulder), 29.58, 29.63, 29.64(shoulder), 29.65, 30.65, 31.88, 34.08, 92.34, 93.31, 122.47, 129.58(shoulder), 129.60, 131.92, 132.60, 135.42, 142.65, 191.24. FTIR (ATR diamond crystal), 2914(s) and 2849(s)(C-H alk), 2207(w)(-C≡C-), 1697(s) (C=O), 1597(s)(C-C arom)HRMS (ESI) calcd for [$C_{48}H_{62}O_2$+H] 671.4823, found 671.4827 $[MH]^+$

Synthesis of Ald-5bz. To a 100 mL two neck round bottom flask fitted with a reflux condenser, 4,4'-((2,5-didodecyl-1,4-phenylene)bis(ethyne-2,1-diyl))bis(ethynylbenzene) 100 mg (0.163 mmol), 4-

iodobenzaldehyde 83 mg (0.36 mmol), bis(triphenylphosphene)palladium(II) chloride 5.7 mg (0.0081 mmol), Copper(I) iodide 5.6 mg (0.0084mmol), triphenylphosphene 2.1 mg (0.016 mmol) was added and purged with argon for 15 minutes. 20 mL of dry toluene and 1 mL of triethylamine were purged with argon for 20 minutes before being added via a cannula to the solid reagents. The reagent mixture was heated to 100°C for 16 hours then purified using a flash silica column: 7:3 DCM:Pet. R_f=0.44. 77mg pure product was isolated (57 % yield). ^{1}H NMR (500 MHz, CHLOROFORM-*d*) δ ppm 0.88 (t, *J*=7.1Hz, 6 H) 1.15 - 1.34 (m, 28 H) 1.37 (br. tt, *J*=7.3, 7.3, 7.2, 7.2 Hz, 4 H) 1.42 (tt, *J*=7.5, 7.3 Hz, 4 H) 1.72 (tt, *J*=7.7, 7.5 Hz, 3 H) 2.82 (t, *J*=7.7 Hz, 4 H) 7.39 (s, 2 H) 7.53 (d, *J*=8.2 Hz, 4 H) 7.55 (d, *J*=8.2 Hz, 4 H) 7.69 (d, *J*=8.2 Hz, 4 H) 7.88 (d, *J*=8.2 Hz, 4 H) 10.03 (s, 2 H). ^{13}C NMR (126 MHz, CHLOROFORM-*d*) ppm 14.1, 22.67, 29.35, 29.51, 29.53, 29.61, 29.65, 29.68, 30.64, 31.91, 34.1, 90.33, 90.77, 93.05, 93.64, 122.21, 122.8, 123.99, 129.26, 129.56, 131.45, 131.74, 132.07, 132.38, 135.49, 142.38, 191.29. FTIR (ATR diamond crystal), 2918(s) and 2852(s)(C-H alk), 2208(w)(-C≡C-), 1691(s) (C=O), 1593(s)(C-C arom) MALDI-ToF(DTCB matrix) calcd for $C_{64}H_{70}O_2$ 871.27, found 870.5.

Synthesis of Ald-3bzo. To a 100 mL two neck round bottom flask fitted with a reflux condenser, 1,4-dibromo-2,5-bis(decyloxy)benzene 100 mg (0.182 mmol), ethynyltrimethylsilane 52 mg (0.400 mmol), bis(triphenylphosphene)palladium(II) chloride 6.0 mg (0.0086 mmol), Copper(I) iodide 1.8 mg (0.0094 mmol), triphenylphosphene 4.6 mg (0.018 mmol) was added and purged with argon for 15 minutes. 20 mL of dry toluene and 1 mL of triethylamine were purged with argon for 20 minutes before being added via a cannula to the solid reagents. The reagent mixture was heated to 60°C for 12 hours then purified using a flash silica column: 1:1 DCM:Pet. R_f=0.50. 80 mg pure product was isolated (68 % yield). ^{1}H NMR (500 MHz, CHLOROFORM-*d*) δ ppm 0.87 (t, *J*=7.0 Hz, 6 H) 1.13 - 1.35 (m, 21 H) 1.39 (br. tt, *J*=7.5, 7.5, 4 H) 1.55 (br. tt, *J*=7.5, 7.1 Hz, 4 H) 1.65 (s, 1 H) 1.87 (tt, *J*=7.1 Hz, 4 H) 4.05 (t, *J*=7.1 Hz, 4 H) 7.04 (s, 2 H) 7.68 (d, *J*=8.2 Hz, 4 H) 7.88 (d, *J*=8.2 Hz, 4 H) 10.03 (s, 2 H). ^{13}C NMR (126 MHz, CHLOROFORM-*d*) ppm 14.09, 22.65, 26.06, 29.28, 29.32, 29.38, 29.54, 29.65, 31.86, 69.56, 90, 94.23, 113.87, 116.78, 129.55, 129.63, 132, 135.39, 153.82, 191.3. FTIR (ATR diamond crystal), 2916(s) and

2847(s)(C-H alk), 2212(w)(-C≡C-), 1697(s) (C=O), 1597(s)(C-C arom) MALDI-ToF(DTCB matrix) calcd for $C_{44}H_{54}O_4$ 646.4017, found 646.4020.

Synthesis of C_{60}-C_{60} Dimer-3bz. To a two neck 50 mL round bottom flask 10 mg (1.5 x 10^{-2} mmol) of Ald-3bz, 32 mg (4.4 x 10^{-2} mmol) of C_{60} and 32 mg (1.4 x 10^{-1} mmol) of N-(4-(hexyloxy)benzyl)glycine was added. The mixture was then sealed and degassed with a flow of argon. To a 50 mL schlenk tube, 20 mL of dry toluene added, degassed using three freeze-pump-thaw cycles and cannulared over to the solid reagents flask. The reaction mixture was sonicated for 30 minutes and was then attached to a reflux condenser and heated to 110^{o}C for 1 hour in a pre-heated oil bath. The product mixture was passed through a short silica plug then concentrated and purified using HPLC, Buckyprep-M column (20 x 250 mm), eluent toluene, flow rate 18 mL min^{-1}, retention time 5.70 minutes,15mg collected. Yield 40 %. ^{1}H NMR (500 MHz, CHLOROFORM-*d*) δ ppm 0.87 (t, *J*=6.9 Hz, 6 H) 0.93 (br. t, *J*=6.8 Hz, 6 H) 1.20 - 1.53 (m, 48 H) 1.68 (br. tt, *J*=7.7, 7.3Hz, 4 H) 1.84 (tt, *J*=7.5, 6.6 Hz, 4 H) 2.72 - 2.86 (m, 4 H) 3.83 (br. d, *J*=13.2 Hz, 2 H) 4.04 (t, *J*=6.6 Hz, 4 H) 4.26 (d, *J*=7.9 Hz, 2 H) 4.58 (d, *J*=13.2 Hz, 2 H) 4.95 (br. d, *J*=7.9 Hz, 2 H) 5.26 (br. s, 2 H) 7.04 (d, *J*=8.5 Hz, 4 H) 7.35 (s, 2 H) 7.54 (d, *J*=8.5 Hz, 4 H) 7.65 (d, *J*=6.6 Hz, 4 H) 7.73 - 8.54 (m, 4 H).^{13}C NMR (CHLOROFORM-d ,126 MHz): δ ppm = 14.06, 14.18, 22.63, 22.72, 25.8, 29.33, 29.38, 29.54, 29.56, 29.62, 29.67, 29.69, 30.59, 31.63, 31.94, 34.08, 68.09, 68.61, 80.84, 89.23, 93.74, 114.6, 122.44, 123.62, 130.14, 132.33, 135.64, 135.93, 136.44, 136.94, 139.55, 139.88, 140.09, 140.14, 141.54, 141.62, 141.83, 141.87, 141.98, 142.01, 142.08, 142.1, 142.12, 142.2, 142.31, 142.52, 142.55, 142.57, 142.66, 142.96, 143.08, 143.14, 144.35, 144.39, 144.59, 144.69, 145.14, 145.21, 145.24, 145.29, 145.3, 145.49, 145.52, 145.7, 145.91, 145.93, 146.02, 146.08, 146.13, 146.16, 146.19, 146.26, 146.28, 146.36, 146.64, 147.3, 153.15, 154.01, 158.72 ppm. MALDI [neg] (DTCB matrix) calcd for $C_{196}H_{104}N_2$ 2518.9, found 2517.4. FTIR (ATR diamond crystal), 2914(s)(C-H arom), 2844(s)(C-H alk), 2187(w)(-C≡C-), 1604(s)(C-C arom), 1425(m)(C-C fullerene), 523 (s) (C-C fullerene). CHN calcd C 93.46 %: H 4.16 %: N 1.11 %, found C 93.55 %: H 4.07 %: N 0.98 %.

Synthesis of C_{60}-C_{60} Dimer-3bzo. To a two neck 50 mL round bottom flask, 8.97 mg (1.4x 10^{-2} mmol) of 4,4'-((2,5-bis(decyloxy)-1,4-phenylene)bis(ethyne-2,1-diyl))dibenzaldehyde, 32 mg (2.8 x 10^{-2} mmol) of C_{60} and 35mg (1.32 x 10^{-1} mmol) of N-(4-(hexyloxy)benzyl)glycine was added. The mixture was then sealed and degassed with a flow of argon. To a 50 mL schlenk tube, 20 mL of dry toluene added, degassed using three freeze-pump-thaw cycles and cannulared over to the solid reagents flask. The reaction mixture was sonicated for 30 minutes then attached to a reflux condenser and heated to 110^{o}C for 30 minutes in a pre heated oil bath. The product mixture was passed through a short silica plug then concentrated and purified using HPLC, Buckyprep-M column (20 x 250 mm), eluent toluene, flow rate 18 mLmin^{-1}, retention time 5.98 minutes, 9 mg collected. Yield 26 %. ^{1}H NMR (500 MHz, CHLOROFORM-*d*) δ ppm 0.87 (t, *J*=6.9 Hz, 6 H) 0.93 (t, *J*=7.2 Hz, 6 H) 1.18 - 1.32 (m, 24 H) 1.32 - 1.43 (m, 8 H) 1.46 - 1.54 (m, 8 H) 1.83 (tt, *J*=7.8, 6.5 Hz, 8 H) 3.67 (d, *J*=13.2 Hz, 2 H) 4.00 (t, *J*=6.6 Hz, 4 H) 4.03 (t, *J*=6.7 Hz, 4 H) 4.17 (d, *J*=9.5 Hz, 2 H) 4.51 (d, *J*=13.2 Hz, 2 H) 4.85 (d, *J*=9.5 Hz, 2 H) 5.18 (s, 2 H) 6.99 (s, 2 H) 7.02 (d, *J*=8.8 Hz, 4 H) 7.55 (d, *J*=8.8 Hz, 4 H) 7.63 (d, *J*=8.5 Hz, 4 H) 7.92 (br. s, 4 H). ^{13}C NMR (CHLOROFORM-d ,126 MHz): δ ppm 14.06, 14.19, 22.62, 22.71, 25.79, 26.00, 29.26, 29.32, 29.35, 29.57, 29.63, 31.62, 31.92, 56.05, 68.09, 68.58, 69.56, 80.84, 86.81, 94.68, 113.85, 114.61, 116.84, 123.61, 125.29, 128.22, 129.03, 130.15, 131.98, 135.65, 135.92, 136.45, 136.91, 137.87, 139.55, 139.86, 140.08, 140.14, 141.54, 141.62, 141.84, 141.86, 142, 142.1, 142.12, 142.2, 142.31, 142.52, 142.57, 142.66, 142.96, 143.08, , 143.14, 144.35, 144.39, 144.62, 144.69, 145.15, 145.21, 145.24, 145.28, 145.31, 145.49, 145.53, 145.71, 145.91, 145.93, 145.99, 146.09, 146.14, 146.16, 146.2, 146.25, 146.29, 146.36, 146.65, 147.3, 153.13, 153.6, 153.99, 156.26, 158.73 ppm. MALDI [neg] (DTCB matrix) calcd for $C_{192}H_{96}N_2O_4$ 2494.8, found 2494.7. FTIR (ATR diamond crystal), 2916(s)(C-H arom), 2847(s)(C-H alk), 2193(w)(-C≡C-), 1606(m)(C-C arom), 1427(w)(C-C fullerene), 523 (s) (C-C fullerene).

Synthesis of C_{60}-C_{60} Dimer-5bz. To a two neck 50 mL round bottom flask, 15 mg (1.7 x 10^{-2} mmol) of Ald-5bz, 37 mg (5.1 x 10^{-2} mmol) of C_{60} and 36 mg (1.35 x 10^{-1} mmol) of N-(4-(hexyloxy)benzyl)glycine was added. The mixture was then sealed and degassed with a flow of argon. To a 50 mL schlenk tube, 20 mL

of dry toluene was added, degassed using three freeze-pump-thaw cycles and cannulared over to the solid reagents flask. The reaction mixture was sonicated for 30 minutes and then attached to a reflux condenser and heated to 110^{o}C for 1 hour in a pre heated oil bath. The product mixture was a passed through a short silica plug then concentrated and purified using HPLC, Buckyprep-M column (20 x 250 mm), eluent toluene, flow rate 18 mLmin^{-1}, retention time 5.58 minutes, mass collected 18 mg. Yield 39 % ^{1}H NMR (500 MHz, CHLOROFORM-*d*) δ ppm 0.86 (t, *J*=6.9 Hz, 6 H) 0.93 (t, *J*=7.3 Hz, 6 H) 1.18 - 1.45 (m, 48 H) 1.46 - 1.54 (m, 4 H) 1.69 (tt, *J*=7.6 Hz, 4 H) 1.84 (tt, *J*=7.2 Hz, 4 H) 2.75 - 2.84 (m, 4 H) 3.73 (d, *J*=13.2 Hz, 2 H) 4.04 (t, *J*=6.6 Hz, 4 H) 4.20 (d, *J*=9.5 Hz, 2 H) 4.53 (d, *J*=13.2 Hz, 2 H) 4.89 (d, *J*=9.5 Hz, 2 H) 5.21 (s, 2 H) 7.03 (d, *J*=8.5 Hz, 4 H) 7.36 (s, 2 H) 7.49 (d, *J*=8.8 Hz, 4 H) 7.51 (d, *J*=8.8 Hz, 4 H) 7.55 (d, *J*=8.5 Hz, 4 H) 7.66 (d, *J*=8.5 Hz, 4 H) 7.78 - 8.46 (m, 4 H). ^{13}C NMR (CHLOROFORM-d ,126 MHz): δ ppm 14.06, 14.14, 22.63, 22.69, 25.8, 29.31, 29.36, 29.53, 29.53, 29.61, 29.65, 29.68, 30.65, 31.62, 31.91, 34.11, 55.97, 68.11, 68.46, 80.68, 89.98, 90.45, 91.02, 93.73, 114.67, 122.47, 122.84, 123.39, 129.55, 130.33, 131.39, 131.56, 132.09, 132.36, 135.62, 135.9, 136.56, 137.08, 139.54, 139.88, 140.09, 140.14, 141.53, 141.61, 141.86, 141.96, 141.98, 142, 142.08, 142.12, 142.17, 142.27, 142.33, 142.53, 142.55, 142.58, 142.66, 142.96, 143.14, 144.33, 144.37, 144.58, 144.7, 145.16, 145.22, 145.24, 145.31, 145.33, 145.4, 145.46, 145.54, 145.71, 145.91, 145.93, 146.1, 146.13, 146.16, 146.19, 146.28, 146.3, 146.55, 147.3, 152.98, 153.79, 158.84 ppm. MALDI [neg] (DTCB matrix) calcd for $C_{212}H_{112}N_2O_2$ 2718.9, found 2718.8. FTIR (ATR diamond crystal), 2914(s)(C-H arom), 2845(s)(C-H alk), 2189(w)(-C≡C-), 1604(s)(C-C arom), 1425(m)(C-C fullerene).

Synthesis of $^{14}N@C_{60}$-C_{60} Dimer-3bz. To a new, 7inch 5mm NMR tube, 200µg (7.5 x 10^{-1}µmol) of N-(4-(hexyloxy)benzyl)glycine, 150 µg (2.07 x 10^{-1} µmol) of ~1 % pure $^{14}N@C_{60}$ in C_{60} dissolved in 100 µl of toluene and 500µl (0.137 mmolL^{-1}) of Ald-3bz in toluene were added. The reaction mixture was concentrated to a final volume of 100 µl using a flow of argon gas and a 2 x 5 mm magnetic stirrer bar was added. The reaction mixture was heated to 110^{o}C for 5 minutes in a preheated oil bath then was removed and quenched in an ice-bath. The product mixture was passed through a short silica plug to

remove amino-acid residue and then purified using HPLC (4.6 mm x 250 mm Buckyprep-M, eluent: 35 % hexane, 65 % toluene). 2 % yield (3 µg) of product was recovered.

Synthesis of $^{14}N@C_{60}$-C_{60} Dimer-5bz. To a new, 7inch 5mm NMR tube, 731 µg (2.76 µmol) of N-(4-(hexyloxy)benzyl)glycine, 500 µg (6.94 x 10^{-1} µmol) of ~0.1 % pure $^{14}N@C_{60}$ in C_{60} dissolved in 300 µl of dry toluene and 302 µg (3.47 x 10^{-1} µmol) of Ald-5bz was added. The reaction mixture was concentrated to a final volume of 100 µl using a flow of argon gas and a 2 x 5 mm magnetic stirrer bar was added. The reaction mixture was heated to 120^{o}C for 5 minutes in a preheated oil bath then was removed and quenched in an ice-bath. The product mixture was passed through a short silica plug to remove amino-acid residue and then purified using HPLC (20 mm x 250 mm Buckyprep-M, eluent: toluene). ~6 % yield (~8 µg) of product was recovered.

Synthesis of two spin centre $^{14}N@C_{60}$-$^{14}N@C_{60}$ Dimer-3bz. To a new, 7inch 5mm NMR tube, 20 µg (7.5 x 10^{-2}µmol) of N-(4-(hexyloxy)benzyl)glycine, 10 µg (1.37 x 10^{-2} µmol) of ~50 % pure $N@C_{60}$ in C_{60} disolved in 100 µl of toluene and 50µl (0.137 mmolL^{-1}) of Ald-3bz in toluene were added. The reaction mixture was concentrated to a final volume of 25 µl using a flow of argon gas and a 2 x 5 mm magnetic stirrer bar was added. The reaction mixture was heated to 110^{0}C for 5 minutes in a pre-heated oil bath then removed and quenched in an ice bath. The product mixture was passed through a short silica plug to remove amino-acid residue and then purified using HPLC (4.6 mm x 250 mm Buckyprep-M, eluent: 35 % hexane, 65 % toluene). 2 % Yield (430 ng) of product were recovered.

Chapter 4 Characterisation of C_{60} and $N@C_{60}$ dimers in polymer matrices

This chapter explores the potential to create macroscopic alignment of $N@C_{60}$ dimer molecules to exert control of the spin-spin interaction by incorporating the dimers into a uniaxially strained polymer host matrix. Using polarised Raman spectroscopy, I first characterise the macroscopic alignment of both C_{60} Dimer-3bzo and Ald-5bz molecules within a liquid crystal elastomer matrix. I then characterise the spin environment of $N@C_{60}$-C_{60} Dimer-3bzo molecules incorporated into the same elastomer using CW and pulsed ESR spectroscopy. The presence of phase separation of $N@C_{60}$-C_{60} Dimer-3bzo from the elastomer is identified, leading to the dominant mechanism for T_2 relaxation to occur via Instantaneous Spin Diffusion, limiting T_2 to 1.4 μs at 30 K. The chapter then characterises the relaxation behaviour of $^{15}N@C_{60}$ and $^{15}N@C_{60}$-C_{60} Dimer-3bzo in an ideal polymer system using a polystyrene matrix. Finding that deuteration of the polymer has a marked positive effect on the phase memory coherence time (T_m). I go on to show that deuterated polystyrene acts as a suitable polymer matrix for $N@C_{60}$-C_{60} Dimer-3bzo molecules, permitting both uniform dispersion and retention of a phase memory lifetime (T_m) of 21 μs at 40 K.

4.1 Introduction

As stated in Chapter 1, to further assess the potential of $N@C_{60}$ as a qubit in a future quantum computer, a system of two or more magnetically distinct endohedral fullerenes must be engineered to have a fixed spin-spin coupling interaction.[27] Chapter 3 describes a method to chemically link together two $N@C_{60}$ centres using a molecular wire bridging unit to create a dimer with a narrow distribution of spatial separations.[168] Chapter 3 also shows that the principal coupling mechanism in this system is via an anisotropic magnetic dipole interaction.[17] Hence for an ensemble of two-qubit molecules to exhibit a uniform intramolecular interaction the molecules must be aligned with one another and dilute.[27] The ability to exert orientational order on $N@C_{60}$ by incorporating it into an anisotropic matrix such as a

liquid crystal[169] or single crystal[22, 170-171] has so far been restricted to single spin centre arrays, with no clear route to scale up to work with multi spin centre arrays. One potential method to achieve this is to disperse rigidly separated multi spin centre molecules in a host polymer matrix. Straining the matrix uniaxially would then cause preferential orientation between polymer chains which in turn could impart macroscopic alignment on the incorporated molecules.[172-173]

4.2 Alignment of Dimer-3bzo and Ald-5bz in a silicone elastomer

There are a number of important factors that must be considered when choosing a suitable polymer matrix to align N@C_{60} containing dimer molecules. The polymer must be highly orientable when uniaxially extended. Additionally, it must permit the incorporation of the N@C_{60} molecules at around room temperature and have a sufficiently low glass transition temperature (T_g) to allow the polymer to be aligned in the absence of heat to avoid the decomposition of the spin active material. Finding a suitable material that satisfies these conditions is non-trivial as most polymers which exhibit a high propensity for alignment are either crystalline or semi crystalline. This property often causes the polymer to have a T_g of over 100^{o}C and requires hot solvent to bring it into solution, to permit dispersal of the fullerene molecules.

One family of polymer derivatives identified as having the required prerequisite properties were liquid crystalline elastomers (LCE). In their unstrained state they are elastic networks of long, cross-linked polymer chains containing short rigid units, which are easily extendable at room temperature. The action of extending a LCE allows the rigid molecular units to order, creating a high degree of macroscopic alignment between the polymer chains and the axis of deformation. Finally, the presence of chemical cross-linking between the LCE chains permits the reversible swelling of the elastomer using a solvent. This provides a route to incorporate small molecules into the LCE by using a solvent to swell the LCE and deliver the small molecules. The solvent can subsequently be evaporated to leave the molecules dispersed in the LCE.

The LCE chosen for this study was a siloxane based main chain liquid crystal elastomer (MCLCE) of the form shown in Figure 4.1, hence forth referred to as Si-LCE. Si-LCE was chosen due to its propensity to form a monodomain smectic-C phase when uniaxially extended at room temperature and its remarkable ability to retain the ordered structure without the need for secondary cross-linking or continued application of tension.[174] In the monodomain smectic-C form, the LCE shows a relatively high degree of alignment exhibiting a Hermans orientation parameter of around 0.65, making it an ideal candidate to test the ability of a polymer material to exert alignment on incorporated fullerene dimer molecules.

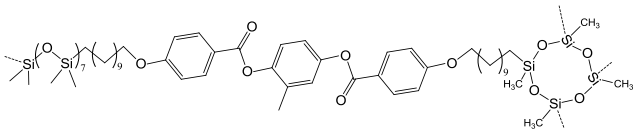


Figure 4.1 Structure of the siloxane liquid crystal elastomer (Si-LCE) used in this chapter. Containing a 10 % crosslink density.

To initially characterise the ability of Si-LCE to exert order on small molecules, the incorporation of the high aspect ratio rigid molecular wire Ald-5bz was used as an ideal system. Following characterisation of this model system, the incorporation of the target Dimer-3bzo compound was tested.

4.2.1 Sample preparation

Chloroform solutions of Ald-5bz, C_{60}-Dimer-3bzo and N@C_{60}-Dimer-3bzo were prepared using a concentration of 3.2 mg mL^{-1}. Si-LCE samples were then cut using an ASTM D638 dogbone cutter (2.8 mm x 7mm) weighing 30-40 mg. The Si-LCE samples were then immersed in the Ald-5bz and Dimer-3bzo solutions for 5 hours and significant swelling of the Si-LCE was observed. These were then removed and left to air dry for 16 hours. The Si-LCE materials was found to absorb 6.33 times its dry weight in chloroform, therefore based on the uptake of chloroform, and assuming that Si-LCE has the same propensity to absorb Ald-5bz and Dimer-3bzo as chloroform, the dry loading of the samples were calculated to be 2 % ww Ald-5bz/ C_{60}-Dimer-3bzo/ N@C_{60}-Dimer-3bzo in Si-LCE.

4.2.2 Creating orientation

To create order in the Si-LCE samples, the samples must be uniaxially deformed. This was achieved using an Instron 5900 tensile test rig. Figure 4.2 shows that the inclusion of a 2 % mass loading of either Ald-5bz or Dimer-3bzo in Si-LCE does not significantly alter the elastic behaviour of the material. The observed maximum extension ratio (*λ)* of over 2.5 is more than sufficient to form the mono domain smectic-C phase.[174] For both samples, extension of the elastomer induced an opaque to transparent transition, indicative of a disordered to crystalline transition.[174] The samples were left to equilibrate to their residual length for 15 hours, during which time the samples remained transparent, confirming the persistence of the monodomain smectic-C phase.

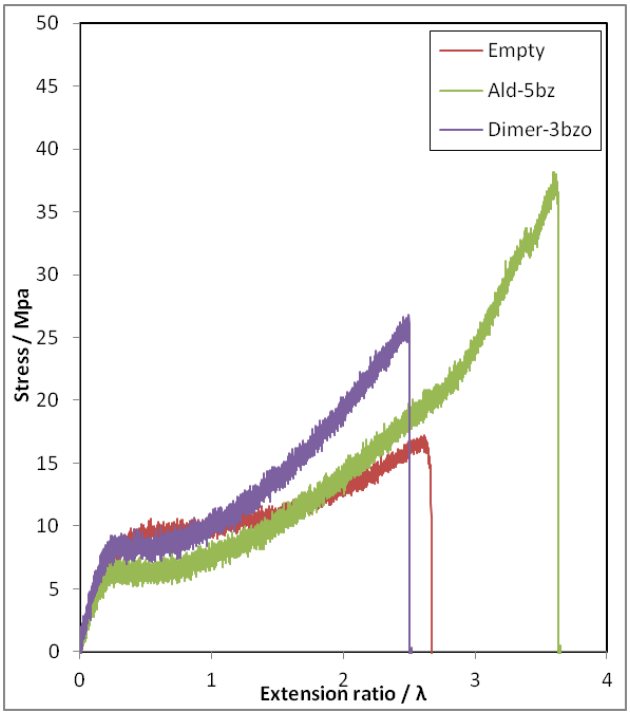


Figure 4.2 Stress vs λ measured during the uniaxial deformation of Si-LCE with 2 % Ald-5bz (green) and 2 % Dimer-3bzo. An empty sample treated in the same way, i.e. swollen with chloroform then air dried, is shown as comparison (red)

4.2.3 Probing for orientation

There are a number of methods available to measure molecular and polymer alignment including NMR[175-176], X-ray diffraction[177] and polarised optical spectroscopy. The most common optical methods are polarised UV-Vis[173, 178], polarised IR[173] and polarised Raman spectroscopy[155], all of which use the molecular symmetry dependant absorption and/or emission of photons in a particular spectroscopic

transitions, allowing for the separate characterisation of the alignment of the small molecules from host matrix. Polarised Raman spectroscopy was the method of choice for this study due to its sensitivity to symmetric acetylenes (present in both Ald-5bz and Dimer-3bzo molecules) and ability to provide greater information as to the orientation distribution of the molecular units (see Chapter 2.5).

The measurements were performed using a Kaiser Optical Systems RamanRXN1 Polarized Raman Spectrometer incorporating a manual rotary sample stage and selectable parallel/perpendicular polarised detection filter. The excitation source was an Invictus 785 nm GaAlAs diode laser. Each of the Si-LCE samples was mounted under light tension on a silicon wafer using double sided tape on the reverse of the substrate. Crystalline silicon was chosen since its Raman spectrum is well characterised and very simple, only containing one narrow peak[179] at 520 cm^{-1}. It therefore does not overlap with the region of interest in this study (1200 cm^{-1}-2500 cm^{-1}).

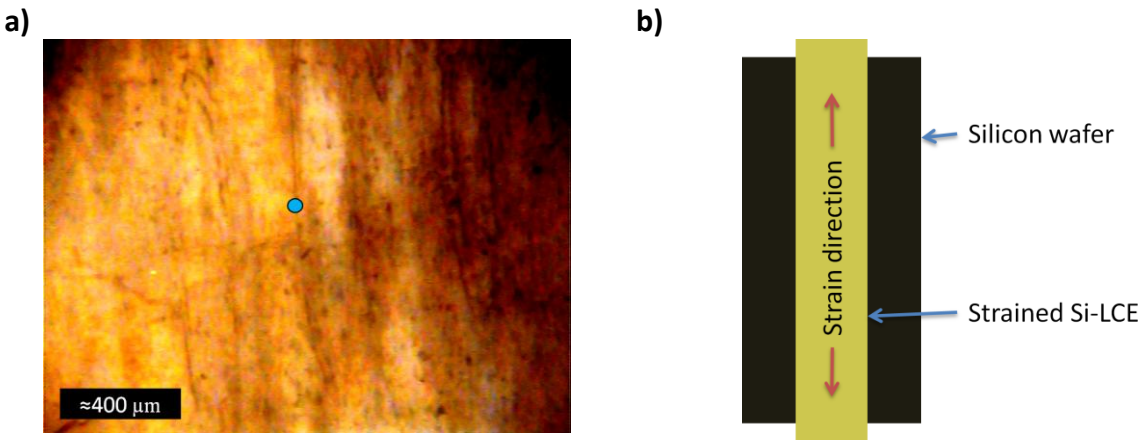


Figure 4.3 a) optical image of 2 % Ald-5bz in Si-LCE recorded using Raman microscopy. The blue spot highlights the centre of the region that is excited using by the 785 nm laser. b) Schematic of sample geometry used for polarised Raman spectroscopy.

The Raman spectrum for each sample was recorded from a centrally selected region of each sample (see Figure 4.3.a) between 100 cm^{-1} to 3500 cm^{-1}, with the dark intensity profile subtracted. 10, 10 second exposures were accumulated for both VH and HH polarization configuration. This was then repeated at 10 degree increments of the sample stage for either 180 or 360 degrees.

Ald-5bz in Si-LCE

Comparison of a pristine Si-LCE and the 2 % Ald-5bz in Si-LCE Raman spectra allowed for the separation of the two spectra (see Figure 4.4) and the selection of suitable bands to study. For the Ald-5bz unit the peak centred at 2203 cm^{-1} was assigned to the symmetric stretch of the $-C \equiv C -$ bonds [163] and the shoulder centred at 1597 cm^{-1} was assigned to the symmetric stretch of the benzene rings.[164] To study the orientation of the Si-LCE matrix, the peak at 1607 cm^{-1} was assigned to the symmetric stretch of the benzene rings in the 1,4-phenylene bis(4-alkoxybenzoate) rigid mesogen unit of the liquid crystal (the same normal mode as the 1597 cm^{-1} vibration).[164] Both of these vibrational modes transform as *A* symmetry with their major change in polarisability (α') being parallel to the long axis of the molecular units.[153, 164] Owing to these properties, the Raman tensor can be approximated as cylindrically symmetric and hence the simplest form of orientation distribution function (ODF) can be used (see Equation 2.23). This allows the anisotropic distribution of the principal axis of Raman tensor to be characterised with respect to the extension direction of the Si-LCE in terms of the polar angle β only.[153, 155] The orientation parameters $\langle P_2 \rangle$ and $\langle P_4 \rangle$ are found by fitting the angular dependence of the measured peak depolarisation ratio $(\mathrm{R}(\theta))$ to Equation 2.24, leaving r ($r = \frac{\alpha'_{yy}}{\alpha'_{zz}}$), $\langle P_2 \rangle$ and $\langle P_4 \rangle$ as fitting parameters.

All peaks were isolated by fitting each of the bands to a sum of lorentzian peaks using the Galactic spectra analysis software program (GRAMS). This deconvolution was particularly important for the 1607 cm^{-1} and 1597 cm^{-1} peaks due to the significant overlapped present (see Figure 4.5)

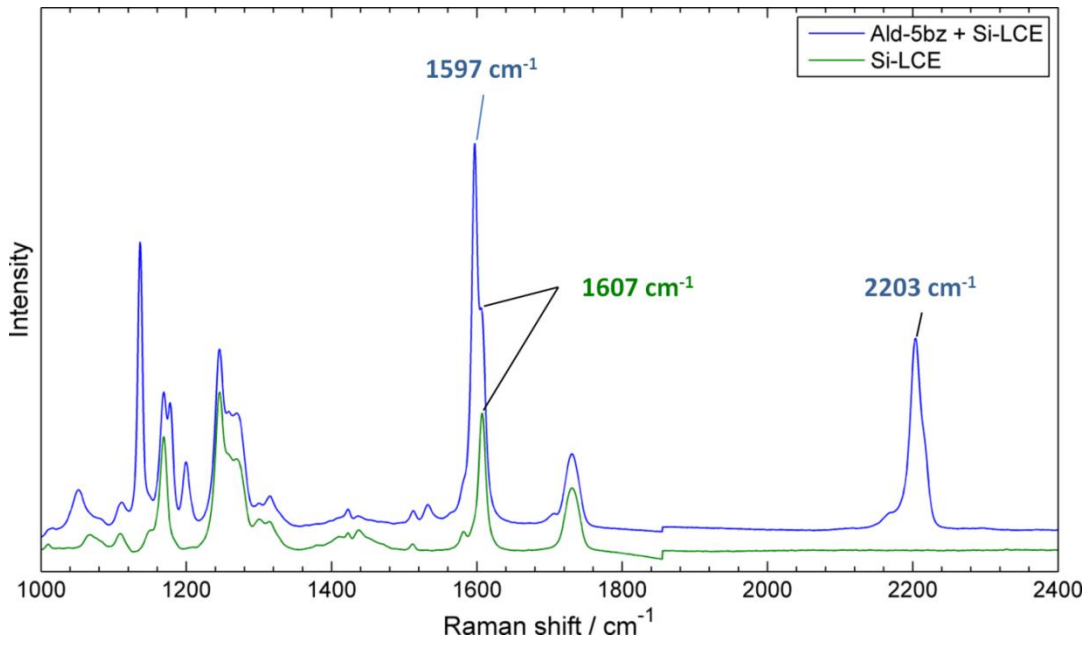


Figure 4.4 Raman spectrum recorded from a pure untreated Si-LCE sample (green) and a Si-LCE with 2 % Ald-5bz dispersed within it (blue). 2203 cm^{-1} and 1597 cm^{-1} bands are assigned to the symmetric stretch of the $-C \equiv C -$ and benzene units respectively within Ald-5bz. The 1607 cm^{-1} band is assigned to the symmetric stretch of the benzene rings in the 1,4-phenylene bis(4-alkoxybenzoate) rigid mesogen unit of the liquid crystal.

The peak intensity was taken to be equal to the area of each fitted peak. I_{VH}/I_{HH} was then plotted as a function of θ to yield the experimentally determined depolarisation ratio (*R*). Figure 4.6 shows the experimentally determined I_{HH}, I_{VH} and *R* angular dependencies for both Ald-5bz peaks. These are overlaid with the best fit parameters for P_2, P_4 and *r* using Equation 5.2. Both depolarisation profiles

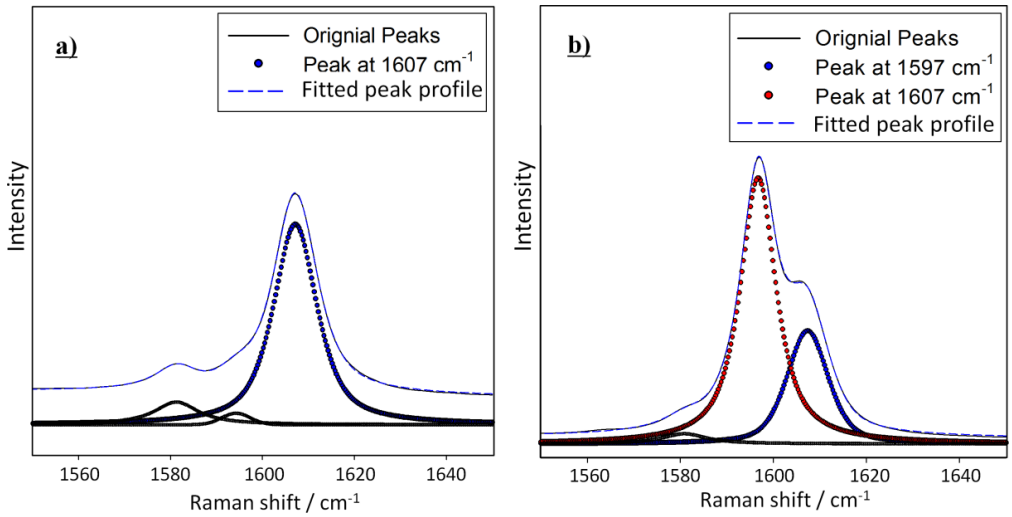


Figure 4.5 Raman band at 1607 cm^{-1} of a) pure Si-LCE and b) Si-LCE with 2 % loading of Ald-5bz. The peaks at 1597 cm^{-1} and 1607 cm^{-1} were isolated from one another in b) by modelling the band as a sum of two principal lorentzian peaks. The agreement between the fitted model and experimental spectrum is excellent.

are similar with bimodal maxima about 90° and conform to a form previously observed.[155] The calculated order parameters are similar, with $P_2 = 0.55$ and 0.27, and $P_4 = 0.27$ and 0.24 for the 2203 cm^{-1} and 1597 cm^{-1} peaks respectively. This is attributed to the adjacent location of the molecular units responsible for the 2203 cm^{-1} and 1597 cm^{-1} peaks within the rigid molecular backbone of Ald-5bz.

An identical fitting procedure was performed on the 1607 cm^{-1} peak of the Ald-5bz containing sample to characterise the alignment of the Si-LCE host matrix. The depolarisation ratio is plotted in Figure 4.7. The form of the depolarisation profile differs from that of the 1597 cm^{-1} Ald-5bz peaks with only a single maximum centred at 90°, however it also conforms to an expected distribution shape.[155]

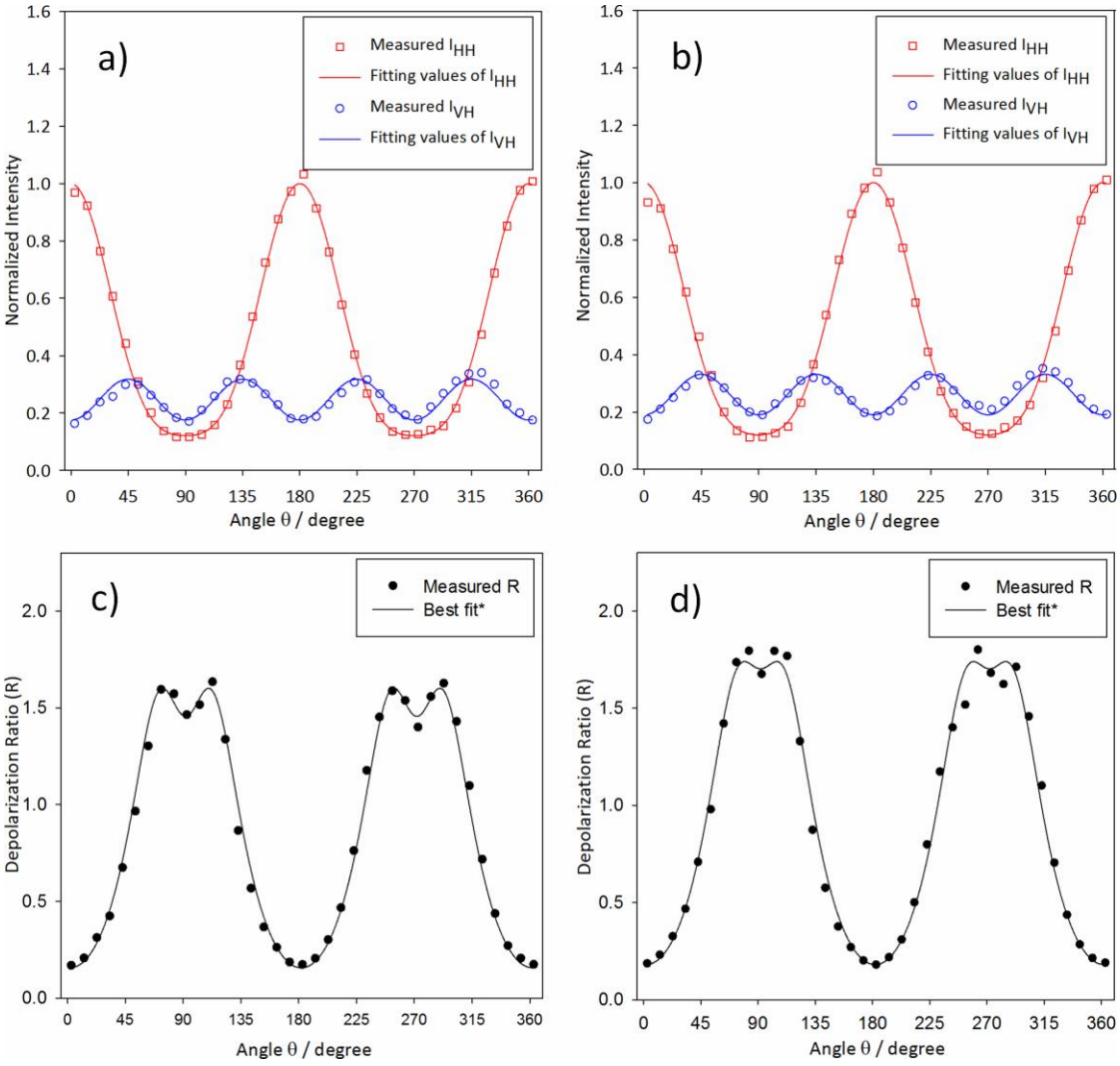


Figure 4.6 I_{HH} and I_{VH} angular dependence of Ald-5bz peaks. a) 2203 cm^{-1} peak with calculated intensity profile using fitted values from c) overlaid. b) 1597 cm^{-1} peak with calculated intensity profile using fitted values from d) overlaid. c) and d) angular dependence of R for 2203 cm^{-1} (c) and 1597 cm^{-1} (d). *fitted to Equation 2.24 using the polynomial regression function in SigmaPlot. Regression fitting carried out by M. Park.

The fitted order parameters were $P_2 = 0.66$ and $P_4 = 0.30$. The P_2 orientation parameter (also known the Hermans orientation function) is in very good agreement with that found using X-ray diffraction 0.65[174] and confirms that the incorporated small molecules at the 2 % loading level do not appear to disrupt the smectic-C phase. A positive P_2 parameter characterises the presence of anisotropic order with preferential alignment parallel to, in our study, the elastomer stretch direction. The larger the positive value, the greater the degree of alignment with P_2 = 1 indicating perfect alignment. The difference in P_2 value measured in Si-LCE and Ald-5bz can be rationalised by considering that the elastomer imposes order on the dispersed small molecules. This transfer of alignment is not 100 % efficient, hence the P_2 value measured for Ald-5bz is slightly smaller than for the host Si-LCE matrix.

The P_2 and P_4 parameters can be considered together to characterise the shape of the ODF.[180] The P_2 and P_4 values for both Si-LCE and Ald-5bz lie in a region where the ODF is expected to have one maximum at β = 0° that monotonically decreases from $0^o \leq \beta \geq 90^o$ to a minimum at β = 90°.[155, 180]

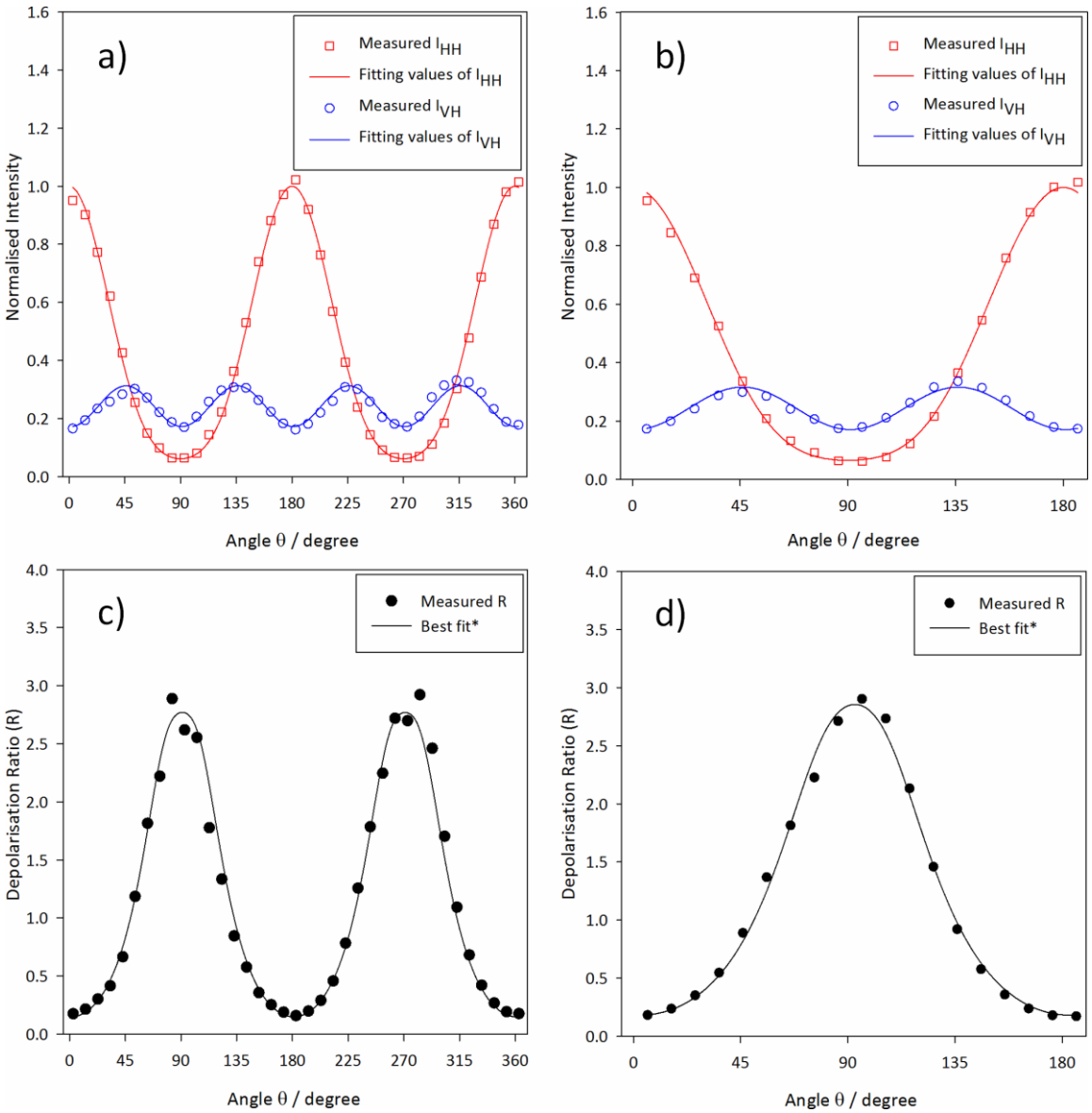


Figure 4.7 I_{HH} and I_{VH} angular dependence of Si-LCE peak at 1607 cm^{-1}. a) Ald-5bz + Si-LCE sample with calculated intensity profile using fitted values from c) overlaid. b) Dimer-3bz + Si-LCE sample with calculated intensity profile using fitted values from d) overlaid. c) and d) show angular dependences of R for Ald-5bz + Si-LCE (c) and Dimer-3bz + Si-LCE (d). *fitted to Equation 2.24 using the polynomial regression function in SigmaPlot. Regression fitting carried out by M. Park.

Dimer-3bzo in Si-LCE

The characterisation of alignment of the Si-LCE matrix was achieved using the same 1607 cm^{-1} band as used in the Ald-5bz in Si-LCE sample. The resulting depolarisation ratio as a function of θ is almost identical in form to that of the Ald-5bzo Si-LCE sample with a single peak at $\theta = 90^{o}$. The fitted P_2 and P_4 values are also very similar at 0.65 and 0.25 respectively, suggesting that the Dimer-3bzo molecule does not disrupt the crystallinity of Si-LCE.

The initial band chosen to characterise the orientation of the Dimer-3bzo was the 2220 cm^{-1} band, assigned the $-C \equiv C -$ symmetric stretch (see Figure 4.8). However, due to the weakness and broadness of the band it could not be included in the study. The more intense 1463 cm^{-1} band is assigned to the fullerene $A_g(2)$ mode also known as the 'pentagon pinch' mode.[181] The functionalisation of the fullerene reduces its symmetry to C_{2v} and so lifts the degeneracy of the principal polarisability tensor components. For this analysis, I will assume that $\alpha_{xx} = \alpha_{yy}$ and the major change in polarisability (α') is parallel to the C_2 axis of the fullerene unit.

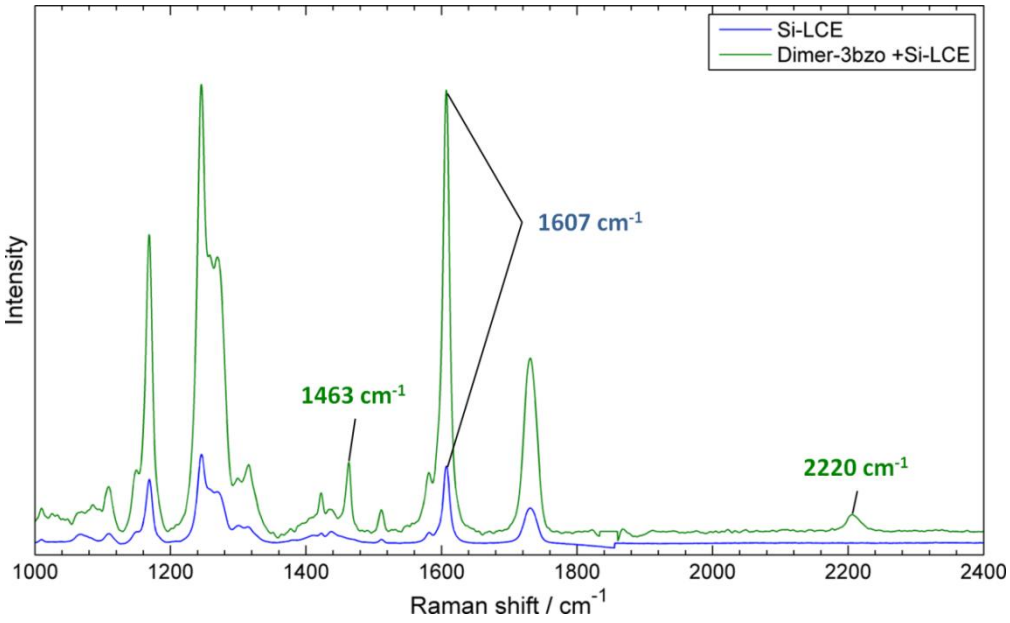


Figure 4.8 I_{HH} Raman spectrum recorded from a pure untreated Si-LCE sample (blue) and a Si-LCE with 2 % Dimer-3bz dispersed within it (green). 2220 cm^{-1} and 1463cm^{-1} bands are assigned to the symmetric stretch of the $-C \equiv C -$ and the pentagon pinch mode of the fullerene unit respectively within Dimer-3bzo. The 1607 cm^{-1} band is assigned to the symmetric stretch of the benzene rings in the 1,4-phenylene bis(4-alkoxybenzoate) rigid mesogen unit of the liquid crystal. The significant background has been subtracted for clarity.

Peak fitting was performed on the 1463 cm^{-1} band to characterise the alignment of the fullerene unit of the Dimer-3bzo molecules. The depolarisation ratio is plotted in Figure 4.9. The form of the depolarisation profile differs from that of the 2203 cm^{-1}, 1597 cm^{-1} and 1607 cm^{-1} showing two maxima at 44° and 130° and three minima at 0°, 90°, 180°. Interestingly, the I_{HH} and I_{VH} profiles are similar in form to those measured in the 873 cm^{-1} (C-COO stretch in polymer backbone) band of uniaxially deformed films of poly($_L$-lactic acid)[155] (PLLA) when aligned in its α-helix[182] crystalline phase.

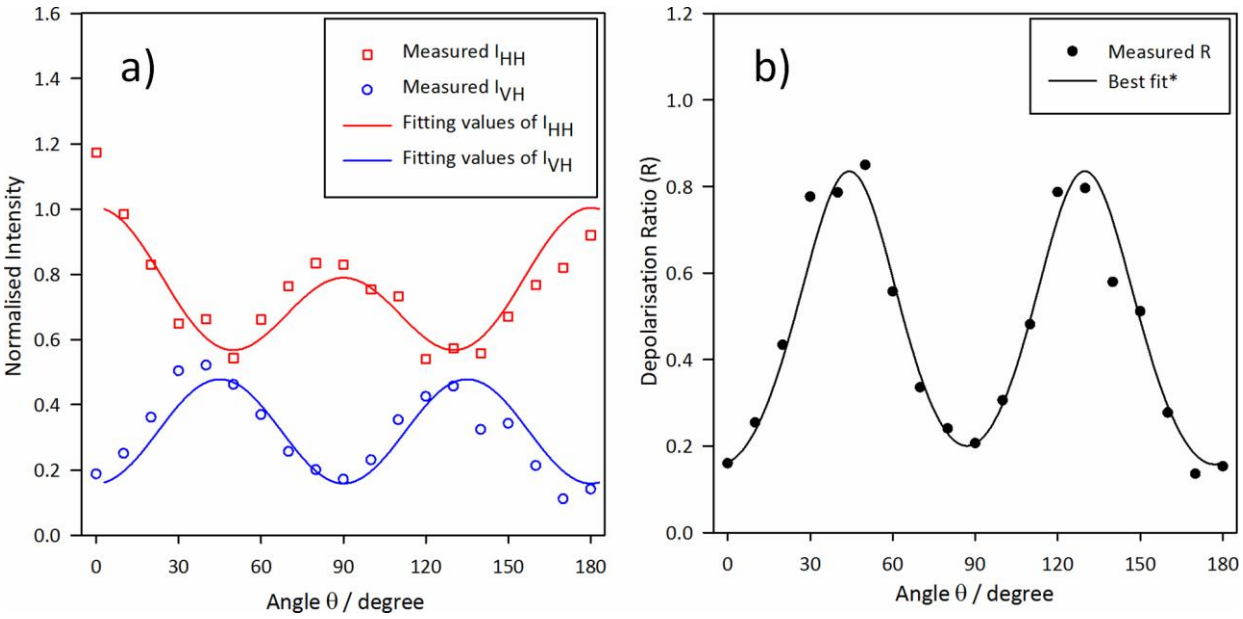


Figure 4.9 a) I_{HH} and I_{VH} angular dependence of 1463 cm^{-1} peak of Dimer-3bz + Si-LCE sample with calculated intensity profile using fitted values from (b) overlaid. b) shows angular dependences of R for the Dimer-3bz + Si-LCE 1463cm^{-1} peak. *fitted to Equation 2.24 using the polynomial regression function in SigmaPlot.

The calculated fitted orientation parameters obtained from Equation 2.24for the 1463 cm^{-1} band are P_2=0.01 and P_4=0.28. This corresponds to an ODF that has at least one minimum between $0^o \leq \beta \geq 90^o$. The small P_2 value can partly be accounted for by the rotational freedom of the fullerene unit about the long axis of the molecule. The observation of an anisotropy in the ODF supports that the Si-LCE matrix is aligning the Dimer-3bzo molecules to some extent. However, the direction and degree of alignment of the rigid molecular backbone is not resolvable.

4.2.4 N@C_{60} Dimer-3bzo in Si-LCE

An ^{15}N@C_{60}-Dimer-3bzo molecule (see Figure 4.10) was synthesised using 0.1 % ^{15}N@C_{60} in C_{60} as described in Chapter 3. This spin active sample was then dispersed in Si-LCE to give a 2 % loading using the same solvent swelling method used to synthesis the Dimer-3bzo and Ald-5bz samples that were interrogated using polarised Raman spectroscopy.

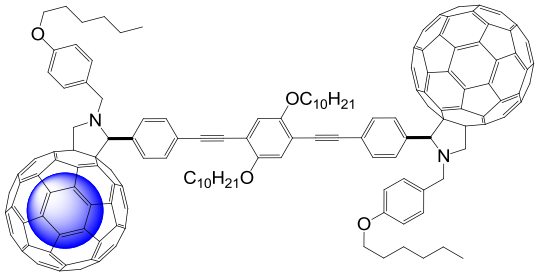


Figure 4.10 Structure of ^{15}N@C_{60}-Dimer-3bzo synthesised using partially enriched N@C_{60}.

This sample was then probed using pulsed ESR spectroscopy to characterise the effect of the elastomer matrix on the phase coherence lifetime (T_2) of the N@C_{60} molecules. The T_2 lifetime was measured using a standard Hahn echo sequence of the form $P_{\frac{\pi}{2}} - \tau - P_\theta - \tau - echo$, τ being the wait time between pulses and P_θ equal to a π pulse, with $\frac{\pi}{2} = 56\ ns$ and $\pi = 112\ ns$. The T_2 was found to have a weak temperature dependence that lay in the range of 0.950 µs - 1.4 µs between 295 K – 5 K at room temperature (see inset of Figure 4.11). This is shorter than that reported for other N@C_{60} derivatives in the solid state with a more typical phase coherence time of 3 µs-24 µs being observed.[23, 53, 58-59] One possible reason for this is that phase separation of the fullerene molecules from the elastomer has occurred. This would result in the local concentration of N@C_{60} to be significantly increased, causing the relaxation mechanism to be dominated by electron spin dipolar coupling. This mechanism of relaxation is known as Instantaneous Spin Diffusion (ISD) and can be probed for by measuring the effect of reducing the duration (tip angle) of the P_θ pulse in a standard Hahn echo sequence on T_2[17]. As the tip angle is reduced, the probability of flipping two adjacent spins during the P_θ refocusing pulse is also reduced, lowering the effective spin concentration of the sample.[17, 183] The connection between T_2 and P_θ for spin ½ systems is well understood.[184] However, to account for the larger effective magnetic moment of high spin ^{15}N@C_{60}, a modified scale factor (ε) is required. A scale factor derived form $\varepsilon = \sqrt{S(S+1) + 0.25}$ has been previously employed to yield the following expression:[185]

$$\frac{1}{T_2} = \frac{\varepsilon \mu_0 \pi g^2 \mu_B^2 C}{9\sqrt{3}\hbar} sin^2\left(\frac{P_\theta}{2}\right) \qquad (4.1)$$

Where μ_0 is the vacuum permittivity of free space, μ_B is the Bohr magneton, g is the ^{15}N@C_{60} g-factor and C is the spin concentration of each hyperfine line. By fitting a linear equation to a plot of $\frac{1}{T_2}$ vs $sin^2\left(\frac{P_\theta}{2}\right)$ a value for C can be calculated from Equation 4.3. The corresponding plot for this sample is shown in Figure 4.11, with the fitted gradient corresponding to a spin concentration per hyperfine line of $1.25 \times 10^{17} spins\ cc^{-1}$. This is far closer to the value of $2.4 \times 10^{17}\ spins\ cc^{-1}$, expected if phase separation had occurred and the local density of Dimer-3bzo molecules was approximated to $1\ g\ cc^{-1}$, than that of $1.7 \times 10^{15}\ spins\ cc^{-1}$, calculated for homogenously distributed Dimer-3bzo molecules in the elastomer matrix. This strongly suggests that a substantial fraction of the Dimer-3bzo molecules have phase separated from the Si-LCE matrix and as a result the T_2 lifetime is limited by ISD processes.

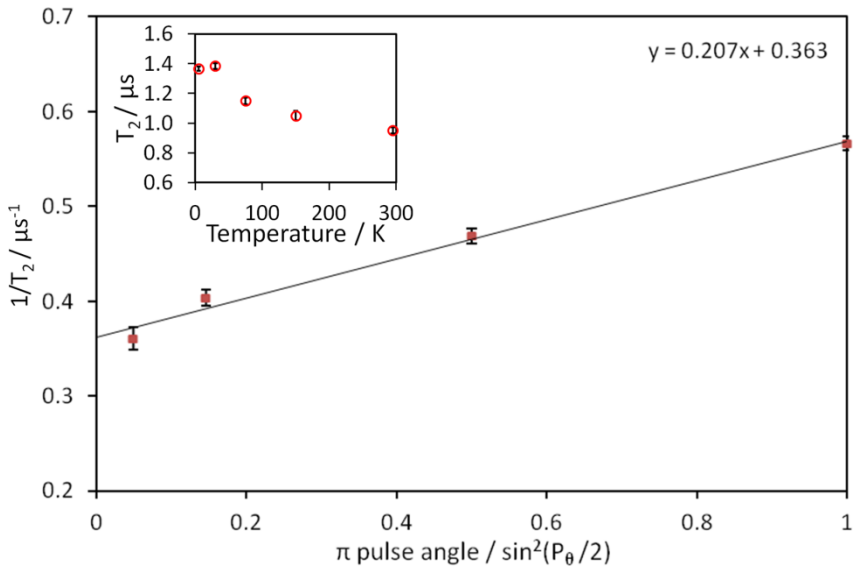


Figure 4.11 Dependency of T_2 lifetime on π pulse tip angle of N@C_{60}-Dimer-3bzo in Si-LCE (2 % loading), measured to probe for the contribution of Instantaneous Spin Diffusion (ISD). Inset: T_2 temperature dependence of same sample.

4.3 ESR characterisation of N@C_{60} in a polystyrene matrix.

4.3.1 Sample preparation

The ^{15}N@C_{60}/C_{60} was synthesised using an ion implantation method outlined in Section 2.1, yielding an average purity of 60 ppm of N@C_{60} in C_{60}. Purification of this sample followed using HPLC.[42] After 13 recycling HPLC runs, a 0.9 % purity N@C_{60}/C_{60} peak was isolated. This material was then used to

synthesise an ^{15}N@C_{60}-Dimer-3bzo molecule illustrated in Figure 4.10 using the double 1,3-dipolar cycloaddition method discussed in Chapter 3.

Atactic deuterated polystyrene (D-ps) with an M_w= 21600 and M_w/M_n=1.08 was purchased from Polymer Source Inc, while the protonated polystyrene analogue (H-ps) had an M_w=20000 and a M_w/M_n=1.01 was sourced from Sigma-Aldrich.

Pristine N@C_{60} and N@C_{60}-C_{60} compounds were dispersed in the polymer matrices by the following method: for each sample, 1.32 nmol of 0.9 % pristine ^{15}N@C_{60} or ^{15}N@C_{60}-Dimer-3bzo was dissolved in 100 µl of d_8-toluene. In a separate vial, 150 µg of either deuterated or protonated polystyrene was sonicated at room temperature in 300 µl of d_8-toluene for 1 hour to ensure complete dissolution. The N@C_{60} solution was then added to the polystyrene containing vial and sonicated for 30 minutes to ensure uniform dispersion. This mixture was then precipitated from methanol. The resulting white powder was dried under vacuum for at least 24 hours to ensure the complete removal of residual methanol and toluene. About 70 mg of each sample was then sealed under vacuum in a 4 mm quartz ESR tube.

4.3.2 CW ESR study

Room temperature (294 K) X-band CW ESR measurements were recorded for both of the D-ps and H-ps N@C_{60} samples using a Bruker EMX spectrometer. A microwave attenuation of 47 dB (4µW mw power) was used together with modulation amplitude of 0.02 mT and 0.04 mT to record the spectra of the D-ps and H-ps N@C_{60} samples, respectively (see Figure 4.12). A model spin Hamiltonian of the form shown in Equation 4.2 was fitted to the recorded spectra using the EasySpin software package.[147]

$$\widehat{\boldsymbol{H}} = \widehat{H}_{EZ}(g_{iso}) + \widehat{H}_{ZF}(D_{strain}) + \widehat{H}_{HF}(A_{iso}) \qquad (4.2)$$

This model includes terms for the Electron Zeeman Interaction ($\widehat{H}_{EZ}$), Zero Field Splitting ($\widehat{H}_{ZF}$) and Hyperfine Interaction of the electron spin with the ^{15}N nuclear spin ($\widehat{H}_{HF}$). The fitting variable used for each of the terms is shown in brackets in Equation 4.2. The g-factor (g_{iso}) and isotropic hyperfine

interaction (A_{iso}) parameters were found to be consistent with previous reports of ^{15}N@C_{60}.[61] A zero centred D_{strain} parameter was also included to account for a broadening seen at the base of each hyperfine peak. The line shape of each transition was fitted using a Gaussian distribution. The dominant hyperfine line broadening mechanism is attributed to the dipolar coupling of the molecular spin to the surrounding bath of nuclear spins of the host polymer,[53] providing a distribution of ESR transition energies that depends on the strength of the electron-nuclear coupling magnitude. The 2.9(4) fold reduction from 0.83 G to 0.28 G of the linewidth that occurs upon deuteration of the polymer is explained by the smaller gyro-magnetic ratio of deuterium compared to hydrogen $\left({}^{\gamma_H}/_{\gamma_D} = 6.6\right)$, reducing the distribution of ESR transition energies. This ratio of linewidth is similar to that previously reported for deuterated and protonated cyclopropane mono- (2.8) and hexa- (3.7) adducts of N@C_{60}.[53] measured in a powder form.

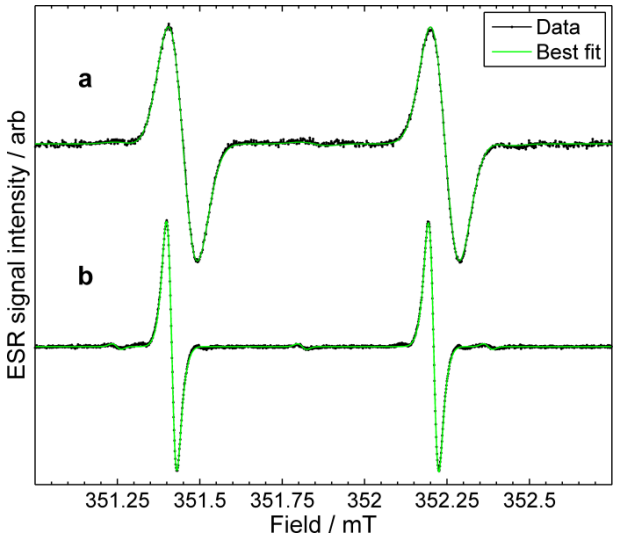


Figure 4.12 X-band ESR spectra of a) ^{15}N@C_{60} in H-ps and b) ^{15}N@C_{60} in D-ps, recorded at 294 K using an EMX spectrometer. Fitted models overlaid in green with 1 % minor component of ^{14}N@C_{60} included in model. RMS fit error in (a) and (b) of 0.014 and 0.0070 respectively.

The narrow linewidth (0.28 G) of the N@C_{60} in D-ps host reveals a Gaussian ZFS strain, $|\mathbf{D}_{strain}|$= 0.49 MHz; this appears as a broadening of the base of the hyperfine lines. $|\mathbf{D}_{strain}|$ is related to the axial and rhombohedral strains, D_{strain} and E_{strain} respectively by:

$$|\boldsymbol{D}_{\boldsymbol{strain}}| = \sqrt{\tfrac{2}{3}{D_{strain}}^2 + 2{E_{strain}}^2} \qquad (4.3)$$

The presence of a ZFS D_{strain} term indicates that the host polymer matrix induces a local deformation of the fullerene cage restricting its rotational motion,[186] which suggests a significant interaction of the polystyrene pendant groups and the fullerene surface.

The CW ESR spectrum of the ^{15}N@C_{60}-Dimer-3bzo in D-ps sample was recorded under similar conditions as the pristine N@C_{60} samples (see Figure 4.13) using a Miniscope ms200 spectrometer at 294 K with 30dB mw attenuation (50µW mw power) and 0.4 G mw attenuation. The model spin Hamiltonian however required the addition of a fixed ZFS term to account for the distortion to the fullerene cage by the pyrrolidine group. The fitted axial and rhombohedral components, D=16.41 MHz and E=0. 46 MHz respectively, were in good agreement with previously reported pyrrolidine N@C_{60} derivatives.[58, 168] The comparable $|\mathbf{D_{strain}}|$ parameter extracted from both the pristine N@C_{60} and N@C_{60}-Dimer-3bzo D-ps samples signifies that the polystyrene matrix is distorting both endohedral systems by a similar amount.

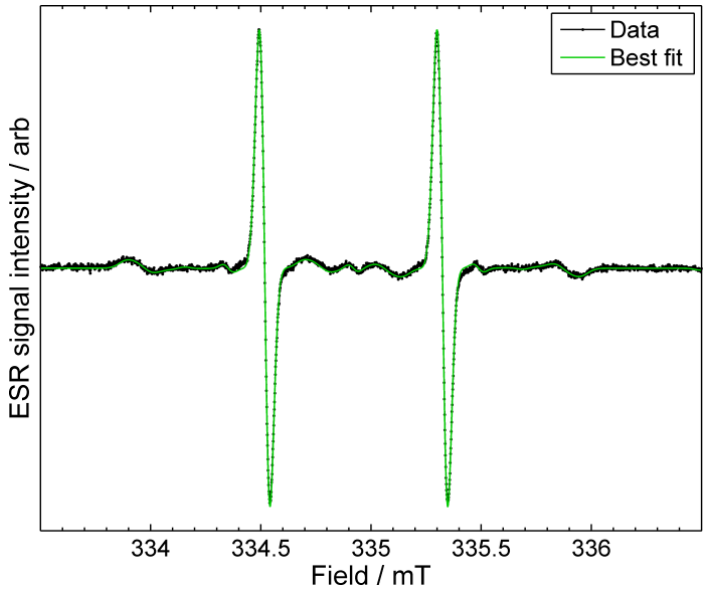


Figure 4.13. X-band ESR spectra of ^{15}N@C_{60}-Dimer-3bzo in D-ps, recorded at 294 K using a Miniscope ms200 spectrometer. Fitted models overlaid in green with 1 % minor impurity of ^{14}N@C_{60} included in model. RMS fit error 0.00081.

System	*g*	A_{iso} / *MHz*	*LW peak to peak* / G	Zero field splitting / MHz				
				D	E	D_{strain}	E_{strain}	$\lvert D_{strain} \rvert$
N@C_{60} in D-ps	2.0023(9)	22.25(0)	0.28	-	-	0.6	-	0.49
N@C_{60} in H-ps	2.0023(2)	22.26(2)	0.83	-	-	0.72	-	0.59
N@C_{60} – C_{60} In D-ps	2.0022(1)	22.60(9)	0.49	16.41	0.46	0.38	0.48	0.56

Table 4.1 Spin Hamiltonian Models fitted to frozen solution CW ESR spectra N@C_{60} in polystyrene matrices.

4.3.3 Pulsed ESR study

The temperature dependences of the spin-lattice relaxation (T_1) and phase memory (T_m) times for each of the three systems, ^{15}N@C_{60}-Dimer-3bzo in D-ps, ^{15}N@C_{60} in D-ps and ^{15}N@C_{60} in H-ps were measured between 20 K and 294 K, using pulse lengths of 80 ns and 160 ns for $\frac{\pi}{2}$ and π rotations, respectively. T_1 was measured using an inversion-recovery pulse sequence[17] and was extracted using a simple mono-exponential fit to the decay profile.[17] All systems showed identical T_1 temperature dependences (see Figure 4.14), exhibiting a similar fast exponential temperature dependence below 100 K as found for N@C_{60} in a glassy CS_2:S_2Cl_2 matrix.[186]

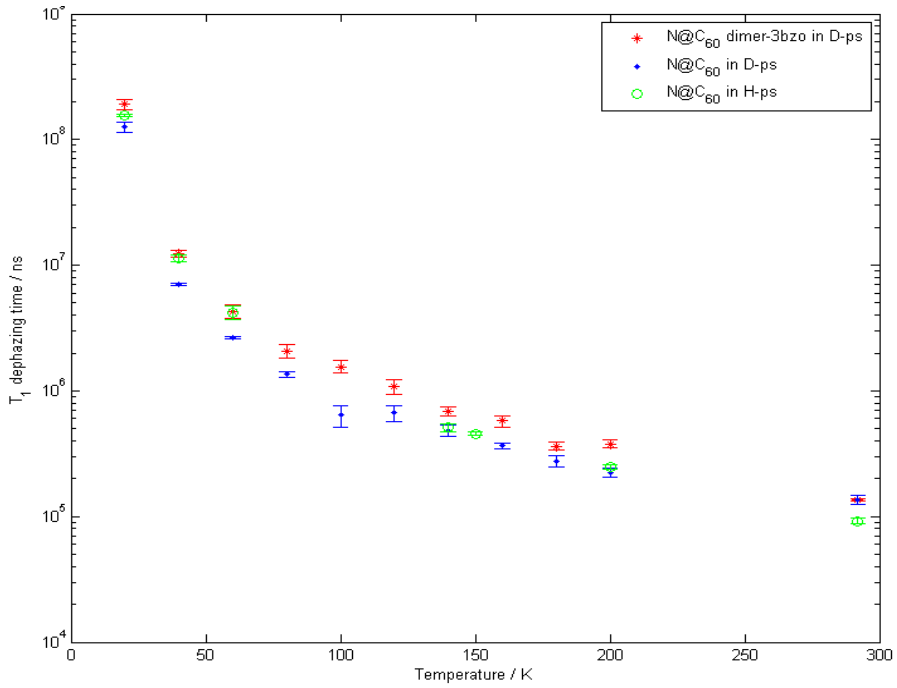


Figure 4.14 Temperature dependence of T_1 with 95 % confidence bounds shown.

T_m was measured using a standard Hahn echo sequence, employing a 2-step phase cycle to remove unwanted contributions from the free induction decay and to provide a zero offset baseline for the echo decay profile. The decay profiles were found to fit well to a stretched exponential function of the form

$$Y(2\tau) = Y(0) \cdot e^{-(2\tau/T_m)^n} \qquad (4.4)$$

With $Y(2\tau)$ corresponding to the echo intensity measured for a pulse separation τ, $Y(0)$ the extrapolated echo intensity at $\tau = 0$, and n the stretch parameter. After fitting this function to the decay profiles, both T_m and the corresponding stretch parameter *n* were extracted, which are plotted in Figure 4.14.

The uniformity of the dispersion of the fullerene molecules in the polystyrene matrix was measured by plotting the dependence of T_m on the π pulse tip angle (P_θ) of the refocusing pulse of the Hahn echo sequence. For All three systems systems, T_m was found to be independent of tip angle (see Figure 4.15.a inset), indicating that instantaneous spin diffusion was not contributing significantly to the dephasing rate.[187] This confirms that the fullerenes were well dispersed and were not phase separating from the host matrix.

Comparison of the two pristine ^{15}N@C_{60} samples indicates that deuteration of the polymer increases T_m by a factor of 6.5 at 20 K to 48.5 µs (see Figure 4.15). The difference in the stretch parameter for the two hosts (*n* = 1.34 for D-ps, *n* = 2.12 for H-ps at 20 K) indicates that the dominant relaxation mechanisms differ, since dynamical processes are associated with stretch parameters around 1, and a stretch parameter of 2-3 is characteristic of nuclear spin diffusion.[188] Both the phase memory time and the stretch parameter are largely insensitive to temperature below 200 K for the H-ps host, indicating that nuclear spin diffusion dominates the relaxation over a wide temperature range.

The ^{15}N@C_{60}-Dimer-3bzo in D-ps sample exhibits a maximum T_m of 21 µs measured at 40 K, very similar to that measured for other N@C_{60} pyrrolidine derivatives in a frozen solution.[58-59] This maxima

coincides with the largest stretch parameter measured for the system of $n \cong 2$ suggesting that nuclear spin diffusion processes is limiting the maximum T_m lifetime achieveable.[188] Over almost the entire temperature range studied, the stretch parameter for the ^{15}N@C_{60}-Dimer-3bzo sample lies between the values for ^{15}N@C_{60} in H-ps and D-ps hosts. The dimer molecule includes a significant number of protons in the molecular wire bridging unit with many of these protons geometrically constrained to lie in close proximity to the paramagnetic centre. These protons could contribute significantly to the spin relaxation, particularly at lower temperatures where a larger stretched parameter is observed. I therefore suggest that the maximum T_m attainable might be increased by synthesising a fully deuterated analogue of the ^{15}N@C_{60}-Dimer-3bzo.

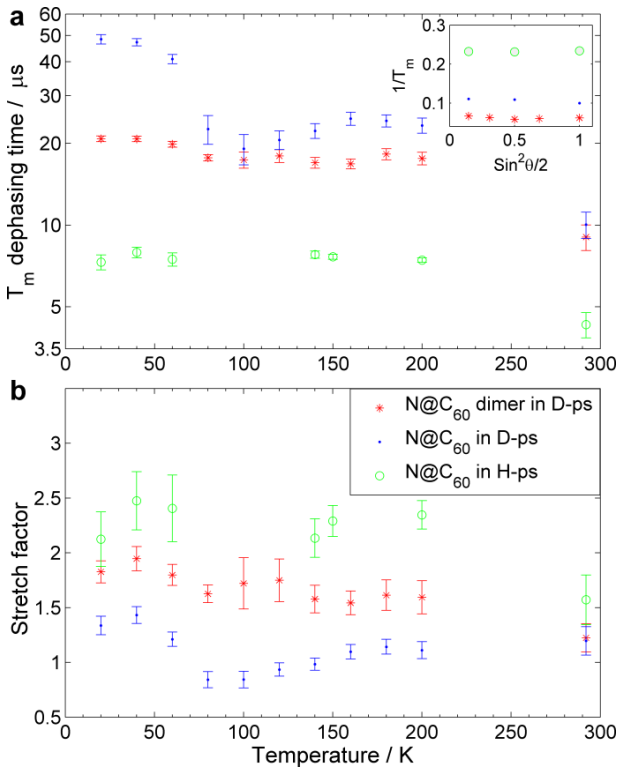


Figure 4.15 a) T_m Temperature dependence of ^{15}N@C_{60}-Dimer-3bzo in D-ps (red), ^{15}N@C_{60} in D-ps (blue) and ^{15}N@C_{60} in H-ps (green) with 95 % confidence bounds shown. b) Stretch parameter *n* fitted for each T_m parameter with 95 % confidence bounds shown.

4.4 Discussion

The alignment of the rigid molecule Ald-5bz using a silicone liquid crystal elastomer was successful, producing a Herman's orientation parameter of 0.55, close to that measured for the host Si-LCE of

0.65. The alignment of fullerene dimer molecules however proved challenging. Firstly, it was found that the expected $-C \equiv C -$ and benzene bond stretches were too weak to use for characterisation. While the origin of this weakness is not known, it is noted that a significant background emission originating from the dimer molecules was observed possibly causing saturation of the spectrometer detector CCD, so reducing the spectrum signal-to-noise. This background emission is attributed to the fluorescence spectra of the fullerene unit between 600 - 1000 cm^{-1}. Emission in this spectral range has been reported for both pristine[189] C_{60} and the C_{60}-OPE-C_{60} dimer molecules[104] shown in Figure 1.36, which are structurally very similar to Dimer-3bzo. The absence of a Raman acetylene band has also been observed in a previous preliminary report on fullerene OPE molecules.[190] If the fullerene emission between 600 - 1000 cm^{-1} is responsible for the poor resolution of the $-C \equiv C -$ band then repeating the measurements using an excitation wavelength outside of this range such as 1064 nm from a Nd : YAG laser could greatly improve spectral signal to noise. The inability to satisfactorily resolve the $-C \equiv C -$ band led characterisation via the use of the less well understood, but more intense, 'pentagon pinch' mode of the fullerene cage at 1465 cm^{-1}. The resulting P_2 and P_4 order parameters of 0.01 and 0.28 are difficult to interpret due to the rotational freedom of the fullerene cage about the OPV bridging unit and the unknown axis of the principal polarisability component. A qualitative conclusion that can be drawn is that the degree of alignment of the Dimer-3bzo molecules is significantly lower than found for Ald-5bz, since if significant alignment of the long axis of the molecule with the stretch direction had occurred, a large negative or positive P_2 parameter would be expected.

Synthesising a Si-LCE composite containing N@C_{60} Dimer-3bzo proves that the solvent swelling technique is indeed compatible with the low thermal stability of N@C_{60} derivatives. The results of the instantaneous diffusion experiment demonstrate that using a loading of 2 % fullerene dimers in Si-LCE matrix results in phase separation and a suppression of T_2 to 1.4 µs at 40 K. This poor dispersion would also contribute to the low alignment of the dimer in Si-LCE matrix.

I have shown that polystyrene offers a suitable polymer host matrix for $N@C_{60}$ and $N@C_{60}$-C_{60}, permitting both uniform dispersion of the magnetic molecules and, when the polystyrene is deuterated, long phase memory times of up to 21 μs. In Chapter 3, I have demonstrated that a two-qubit $^{14}N@C_{60}$-$^{14}N@C_{60}$ dimer of the form of Dimer-3bzo exhibits a coupling of about 2.7 MHz. Theoretical studies on a two qubit $N@C_{60}$ system with a dipolar interaction of 3MHz offer an estimate of the time needed to implement an entanglement-forming CNOT gate between the qubits of about 11 μs,[27] which is shorter than our measured phase memory time for $^{15}N@C_{60}$-Dimer-3bzo in D-ps of 21 μs. If a deuterated polymer matrix that permits the dispersal of $N@C_{60}$ and induces alignment of fullerene dimers can be identified, it should be possible to preserve a sufficiently long T_2 time to implement a universal quantum gate in an ensemble of $^{15}N@C_{60}$-$^{15}N@C_{60}$ Dimer-3bzo molecules to test the 4th and 5th DiVincenzo criteria, i.e. the ability to implement a universal set of quantum gates and separately measure the two qubit states.

Chapter 5 Synthesising a heterospin centre N@C_{60}-Cr_7Ni complex.

An optimal electron spin based QIP architecture might well comprise of a number of different types of molecular-based qubits that each have different ideal properties. However, little is known about how the spin environment of N@C_{60} is affected when coupled to a magnetically dissimilar qubit building block. This chapter therefore focuses on the synthesis and characterisation of two fullerene-antiferromagnetic ring complexes linked via a pyridine terminated bridge. The first complex C_{60}(py)-Cr_7Co is only weakly paramagnetic, while the second complex N@C_{60}(py)-Cr_7Ni contains two spin centres. I start by synthesising and characterising the pyridine terminated fullerene derivative, C_{60}(py) and the complex C_{60}(py)-Cr_7Co using NMR and Mass Spectroscopy. I then repeat the synthesis procedure to create the spin active N@C_{60}(py) molecule and N@C_{60}(py)-Cr_7Ni complex. The CW ESR and echo detected field sweep spectra of N@C_{60}(py) and N@C_{60}(py)-Cr_7Ni are compared along with their T_1 and T_m temperature dependences to examine the effect of the dynamic magnetic structure of the antiferromagnetic ring on the N@C_{60} centre.

5.1 Introduction

The previous two chapters of this thesis have focused on creating controlled coupling between two N@C_{60} spin centres. This chapter shifts the focus to controlling the interaction between N@C_{60} and another molecular spin system, a Cr_7Ni antiferromagnetic ring magnet, to assess the potential of an electron spin based quantum computing architecture that consists of a range of magnetically dissimilar weakly coupled qubits.

By chemically linking the N@C_{60} and Cr_7Ni spin centres the dipolar coupling distribution can be controlled and modelled in the same way as achieved in chapter 3 with a homo ^{14}N@C_{60}-^{14}N@C_{60}, with the goal being to gain a greater understanding of the interaction between an ^{14}N@C_{60} centre and a

hetero spin centre. Once synthesised the effect of a single hetero spin centre on the T_1 and T_m lifetimes of $^{14}N@C_{60}$ can then be studied, to evaluate the future capability of a multi spin centre QIP architecture that uses $N@C_{60}$ as a computational element.

5.2 C_{60}(py)-Cr_7Co

To permit characterisation of the Lewis base functionalised fullerene molecule, the synthesis scheme was first applied to pristine C_{60} before $N@C_{60}$. This 2,3 dipolar cycloaddition reaction uses similar conditions to that optimised for the dimer forming reaction in Chapter 3, together with the amino acid N-(4-(hexyloxy)benzyl)glycine (see Figure 5.1). Lewis base functionality was introduced via the use of 4-(pyridin-4-yl)benzaldehyde as the aldehyde precursor, chosen due to its rigidity, effective length, low steric bulk and ready availability. A pyridine derivative was chosen due to its extensive use as a ligand for the Cr_7M family of molecular magnets,[138] forming a dative covalent bond.

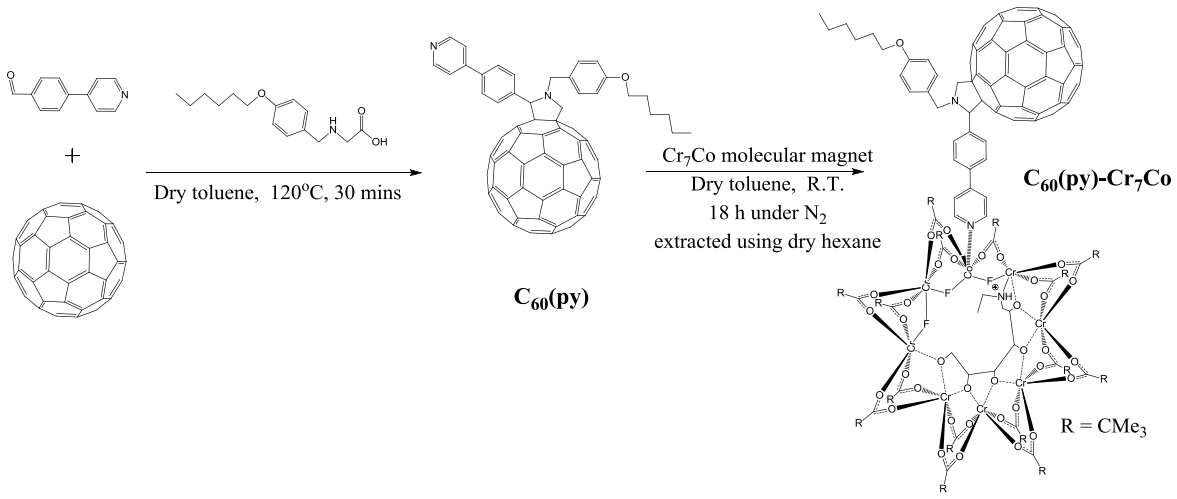


Figure 5.1 Reaction scheme used to synthesise C_{60}(py)-Cr_7Co complex.

For the complex forming reaction step, the structurally and chemically similar Cr_7Co molecular magnet was chosen rather than the paramagnetic Cr_7Ni analogue (see Figure 1.53). Cr_7Co was chosen since due to the rapid relaxation of the Co(III) centre, it is only weakly paramagnetic and therefore permits characterisation via ^1H NMR.[191-192] The complexation reaction was performed by Dr G. Timco at the University of Manchester. The procedure was entirely carried out at room temperature and consisted

of dissolving both the fullerene and molecular magnet molecules in dry toluene over night, then subsequently removing the toluene and extracting the product mixture into dry hexane for which the uncomplexed C_{60}(py) is only sparingly soluble. The resulting solution was dark brown.

5.2.1 Characterisation of C_{60}(py)

For HPLC purification both Buckyprep and Buckyprep-M columns were trialled using toluene as eluent, finding that the Buckyprep column gave better consistency of retention times between different injections and less peak tailing. This is presumed to be due to the complete end capping that is present on the silica stationary phase of the Buckyprep but not Buckyprep-M column. The HPLC chromatogram of C_{60}(py)using both Buckyprep and Buckyprep-M is show in Figure B.1 in the Appendix.

The molecule C_{60}(py) was principally characterised via NMR using 1D ^{1}H NMR, ^{13}C NMR, 2D (^{1}H,^{1}H) COSY and (^{1}H,^{13}C) me-HSQC NMR experiments. Additionally, MALDI-ToF mass spectrometry and UV-Vis spectroscopy were used.

Assignment of the ^{1}H NMR spectrum (see Figure 5.2) was made in combination with the results from the (^{1}H,^{1}H) COSY (see Figure 5.3) and (^{1}H,^{13}C) me-HSQC (see Figure 5.4) experiments. Each assignment will be discussed from lowest to highest chemical shift. Triplet M17 is assigned to the terminal methyl group (23) based on the chemical shift, splitting pattern and multiplicity with the COSY and HSQC experiments also supporting this assignment. The multiplets M16-14 and M12 are assigned to the remaining centres of the alkyl chain (20-22) and (24-25) with the chemical shift increasing with proximity to the oxy group. This assignment is consistent with the chemical shifts observed and the relative peak area. The COSY spectrum supports this assignment by indicating that each multiplet is on an adjacent carbon, with the lowest chemical shift coupled to the terminal methyl group. Me-HSQC also confirms that each of the corresponding carbons has two protons.

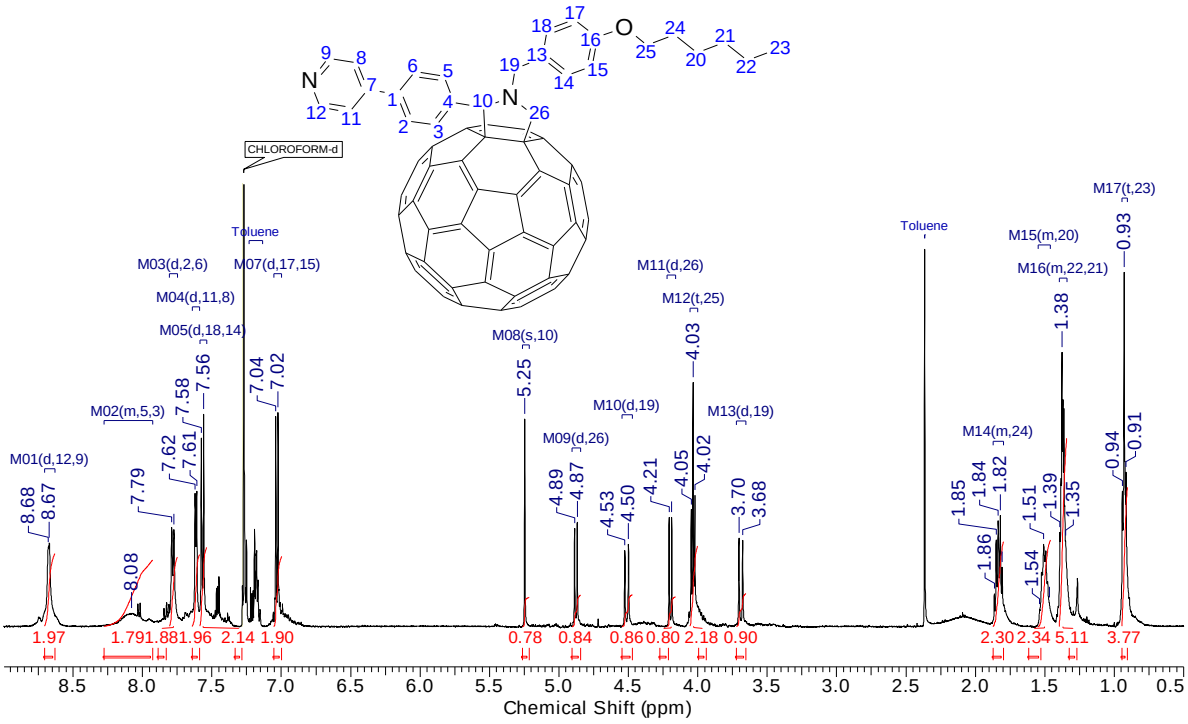


Figure 5.2 500MHz R.T. ^{1}H NMR collected from C_{60}(py) in chloroform-d.

The pair of doublets M13 and M10 with $^2J_{HH}$=13.2 Hz are assigned to each of the protons at position 19[56] with the coupling confirmed by COSY cross peaks. This assignment is rationalised on the basis of the reduced –ve inductive effect of the fullerene moiety and the greater π-donation (known to increase the +ve vincinial coupling magnitude) from the amine lone pair caused by the enhanced rotational freedom of the N-CH_2 bond compared to the rigid geometry of the N-CH_2 within the pyrrolidine ring. Confirmation that these protons are germinal stems from the HSQC assignment of both M13 and M10 proton environments to the same carbon resonance. The pair of doublets M11 and M9 with the smaller coupling magnitude of 9.5-9.8 Hz are assigned to the N-CH_2 within the pyrrolidine ring (26) based on the presence of COSY cross peaks and the HSQC assignment of both proton environments are α to the same carbon resonance. This assignment is also in good agreement with that of previously reported fullerene pyrrolidine derivatives.[56, 58, 92] The singlet M8 is assigned to (10) and is also consistent with previous reports.[56, 58, 92] The pair of doublets M7 and M5 with $^3J_{HH}$ = 8.5 Hz are assigned to the protons *meta* (18, 14) and *ortho* (15, 17) to the hexyloxy substituent of the benzene ring, respectively. The significant difference in chemical shift is primarily accounted for by the mesomeric effect of the oxy substituent on the ring, with the chemical shifts closely matching those found in all of

the fullerene dimer compounds characterised in Chapter 3. The doublet M4 and broad doublet M1 are assigned to the protons *ortho* (12, 9) and *meta* (11, 8) to the pyridine ring, based on proximity to the negative inductive effect of the nitrogen.[193] Although the broadening of M1 prevents an accurate $^3J_{HH}$ coupling constant from being extracted, the cross peak in the COSY experiment supports the assignment. The double M3 is assigned to the aromatic sites (2, 5) *ortho* to the pyrrolidine substituent[104] with the highly broadened peak M2 assigned to the aromatic protons *meta* to the pyrrolidine substituent. This broadening effect has been seen previously[104] and is assumed to be caused by the incomplete averaging of the interaction of the *ortho* protons with the aromatic system of the fullerene cage due to rotation about the aromatic-pyrrolidine bond. The significant broadening of M2 prevents its observation in the COSY experiment so preventing the anticipated cross peak with M3.

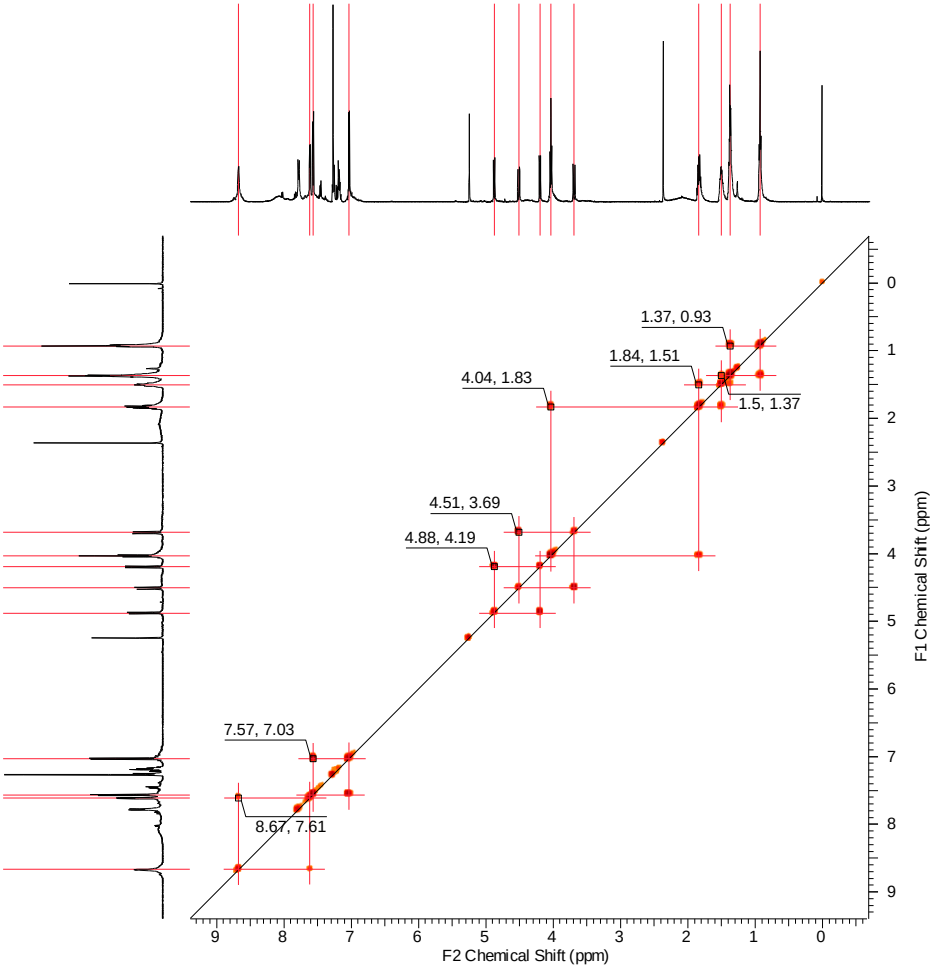
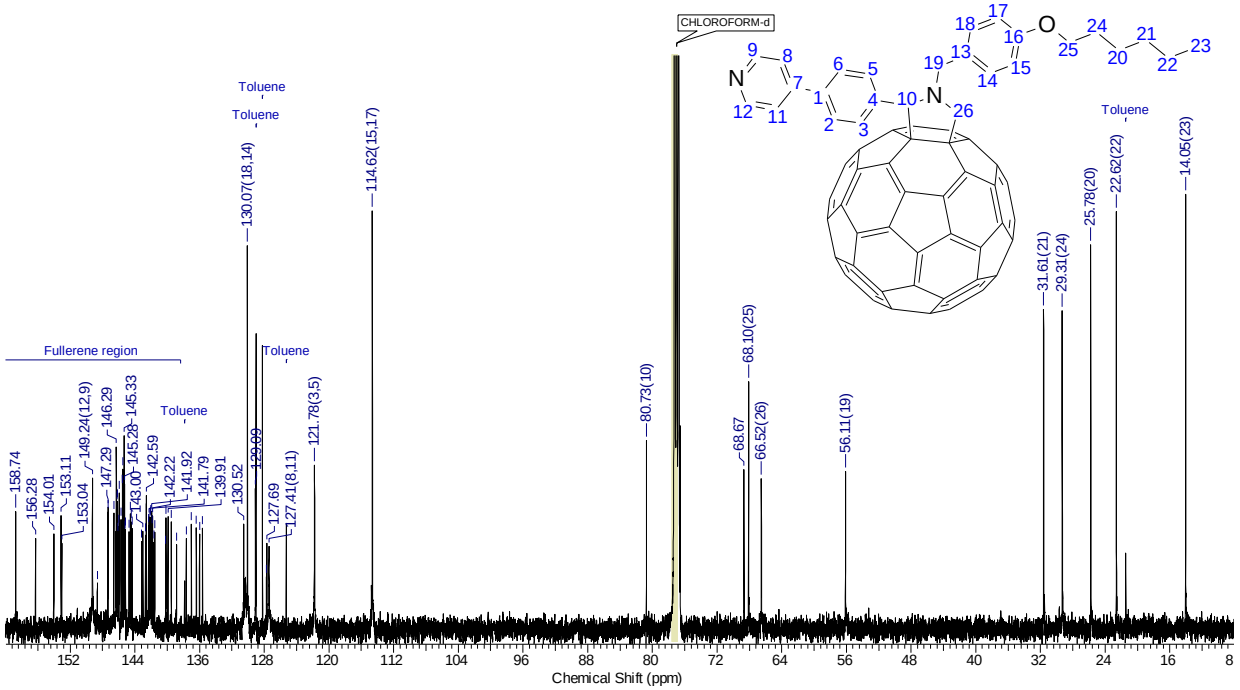


Figure 5.3 R.T. (^{1}H,^{1}H) COSY NMR plot recorded from C_{60}(py) in chloroform-d. Points counted (512, 256).

Partial assignment of the ^{13}C NMR spectrum (Figure 5.4) was made by correlation with the assigned ^{1}H NMR multiplets using the (^{1}H,^{13}C) HSQC experiment shown in Figure 5.4. Using this method all carbon resonances between 14.05 ppm and 121.41 ppm bar one at 68.67 could be assigned to carbons with proton substituents. 50 of the 62 remaining unassigned carbon environments lie in the aromatic region between 138 ppm and 160 ppm, which is characteristic of the presence of a functionalised fullerene molecule.



No.	(ppm)	Height
1	14.05	0.0292
2	22.62	0.0280
3	25.78	0.0258
4	29.31	0.0214
5	31.61	0.0215
6	56.11	0.0106
7	66.52	0.0101
8	68.10	0.0166
9	68.67	0.0107
10	80.73	0.0126
11	114.62	0.0281
12	121.78	0.0110
13	127.41	0.0055

No.	(ppm)	Height
14	127.69	0.0058
15	127.75	0.0035
16	129.09	0.0094
17	130.07	0.0257
18	130.52	0.0070
19	135.62	0.0068
20	136.00	0.0064
21	136.39	0.0068
22	136.99	0.0070
23	137.65	0.0061
24	138.84	0.0057
25	139.49	0.0072
26	139.91	0.0075

No.	(ppm)	Height
27	140.14	0.0075
28	140.19	0.0054
29	141.54	0.0065
30	141.65	0.0058
31	141.79	0.0076
32	141.88	0.0068
33	141.92	0.0079
34	142.01	0.0061
35	142.04	0.0075
36	142.06	0.0074
37	142.11	0.0062
38	142.14	0.0073
39	142.22	0.0076

No.	(ppm)	Height
40	142.31	0.0069
41	142.56	0.0084
42	142.59	0.0089
43	142.69	0.0063
44	143.00	0.0066
45	143.16	0.0059
46	144.33	0.0067
47	144.42	0.0072
48	144.54	0.0077
49	144.72	0.0065
50	145.15	0.0067
51	145.21	0.0065
52	145.28	0.0097

No.	(ppm)	Height
53	145.33	0.0130
54	145.49	0.0107
55	145.52	0.0104
56	145.53	0.0095
57	145.69	0.0073
58	145.95	0.0091
59	145.99	0.0069
60	146.11	0.0063
61	146.13	0.0086
62	146.19	0.0071
63	146.21	0.0084
64	146.29	0.0122
65	146.34	0.0065

No.	(ppm)	Height
66	146.60	0.0078
67	147.29	0.0082
68	147.33	0.0078
69	148.64	0.0031
70	149.24	0.0101
71	153.04	0.0057
72	153.11	0.0076
73	154.01	0.0064
74	156.28	0.0061
75	158.74	0.0079

Figure 5.4 125 MHz carbon NMR spectrum recorded from C_{60}(py) in chloroform-d.

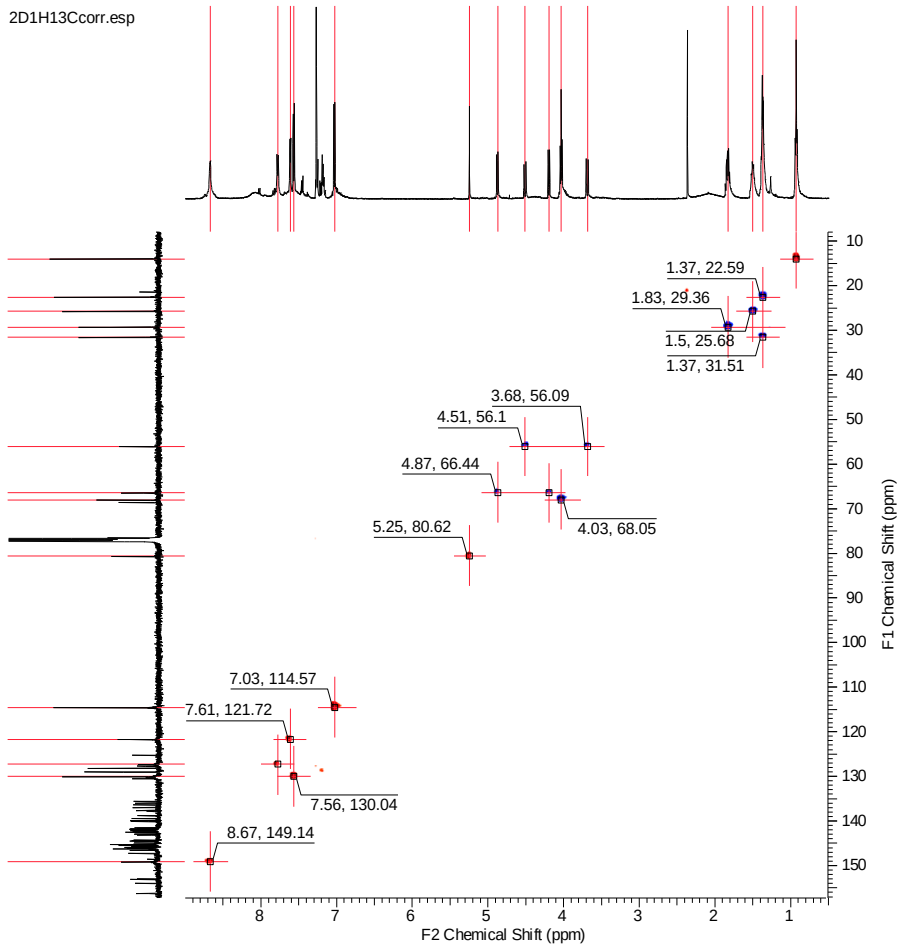


Figure 5.4 (^{1}H,^{13}C) HSQC NMR experiment recorded from C_{60}(py) in chloroform-d. Red contours indicate an odd number of carbons α to aliphatic carbon, blue contours indicate 2 carbons α to aliphatic carbon. (512,256) points collected.

The overall appearance of the UV-Vis absorption spectrum of C_{60}(py) (Figure 5.5) is very similar to that of the dimer compounds characterised in Chapter 3, showing the characteristic peak associated with exohedrally functionalised fullerene derivatives at ≈ 435 nm.[56]

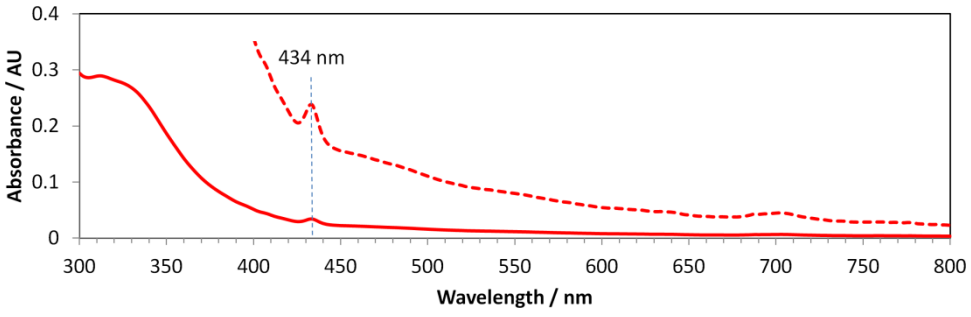


Figure 5.5 (Solid) UV-Vis spectrum of C_{60}(py) recorded in toluene. (Dashed) 7x zoom in y axis. The presence of a 434 nm peak is characteristic of a functionalised fullerene.

Mass spectra were recorded using both MALDI-ToF and an Atmospheric Solids Analysis Probe for accurate mass determination (see Figure 5.6). The MALDI-ToF spectrum provided a principal peak at

1106.2 corresponding to the molecular ion of $[C_{60}(py)]^-$ with formula $C_{86}H_{30}N_2O$ (1106.24 exact mass). The accurate mass ASAP spectrum yielded a mass of 1107.2406. This is only a 2.2 ppm deviation from the expected mass for $[C_{60}(py) + H]^+$ of 1107.2431, supporting the correct molecular formula assignment.

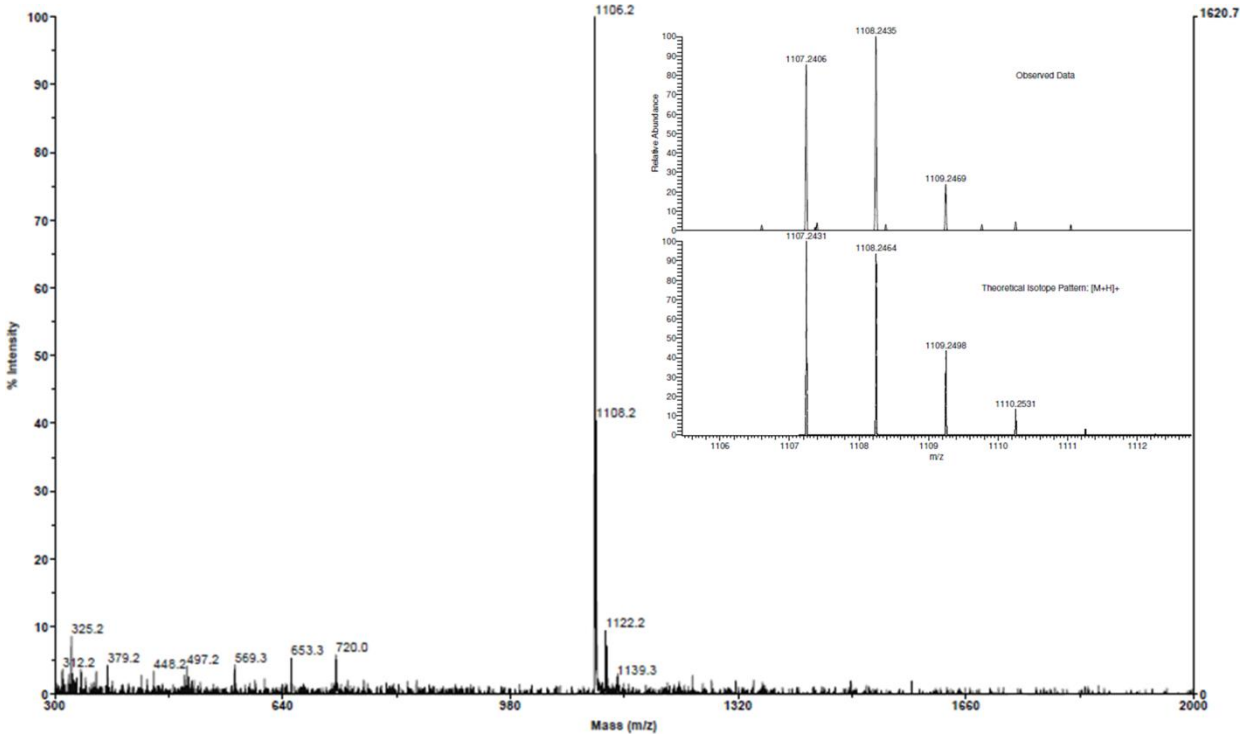


Figure 5.6 MALDI-ToF mass spectrum of C_{60}(py) recorded in negative ionisation mode using a DTCB matrix. Insert: corresponding accurate mass spectrum recorded using an Atmospheric Solids Analysis Probe (ASAP) ionisation technique. Top: observed data, bottom: theoretical [M+H]+ isotope distribution.

5.2.2 Characterisation of C_{60}(py)-Cr_7Co

The structure of the complex C_{60}(py)-Cr_7Co is expected to have a similar geometry to that of previously reported Cr_7M complexes.[138] That is, the pyridine group is expected to displace the axial H_2O ligand of the cobalt(III) centre, placing the C_{60}(py) group normal to the plane of the molecular magnet ring. A pictorial representation of this structure is shown in Figure 5.7.

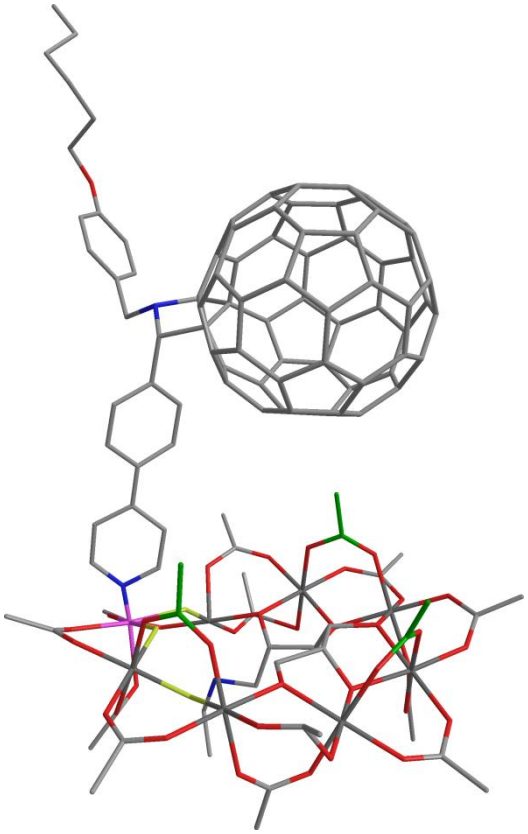


Figure 5.7 Structural cartoon of C_{60}(py)-Cr_7Co based on geometry of previously characterised Cr_7M compounds.[138] (Grey) carbon, (red) oxygen, (yellow) fluorine, (blue) nitrogen, (pink) Cobalt, (green) axial carbons of pivlate ligands on same face of molecular magnet as fullerene. All hydrogen atoms and terminal methyl groups of pivalate ligands are hidden for clarity.

To support the correct structural assignment, the complex C_{60}(py)-Cr_7Co was characterised using 300 MHz ^{1}H NMR and ESI mass spectrometry. Unfortunately, the ESI mass spectrum (see Figure 5.8) fails to show the expected molecular ion peak at 3307 m/z corresponding to the fullerene-molecular magnet complex. The absence of this peak is not thought to be unusual for non-covalent complexes, especially when both complex units are large and self-contained as the complexes have a high propensity to fragment across the coupling bond,[194-195] in this case the Co-N bond. The presence of both the C_{60}(py) fragment at 1107 m/z and Cr_7Co molecular magnet fragment at 2223 m/z supports that both molecular species are present in the sample.

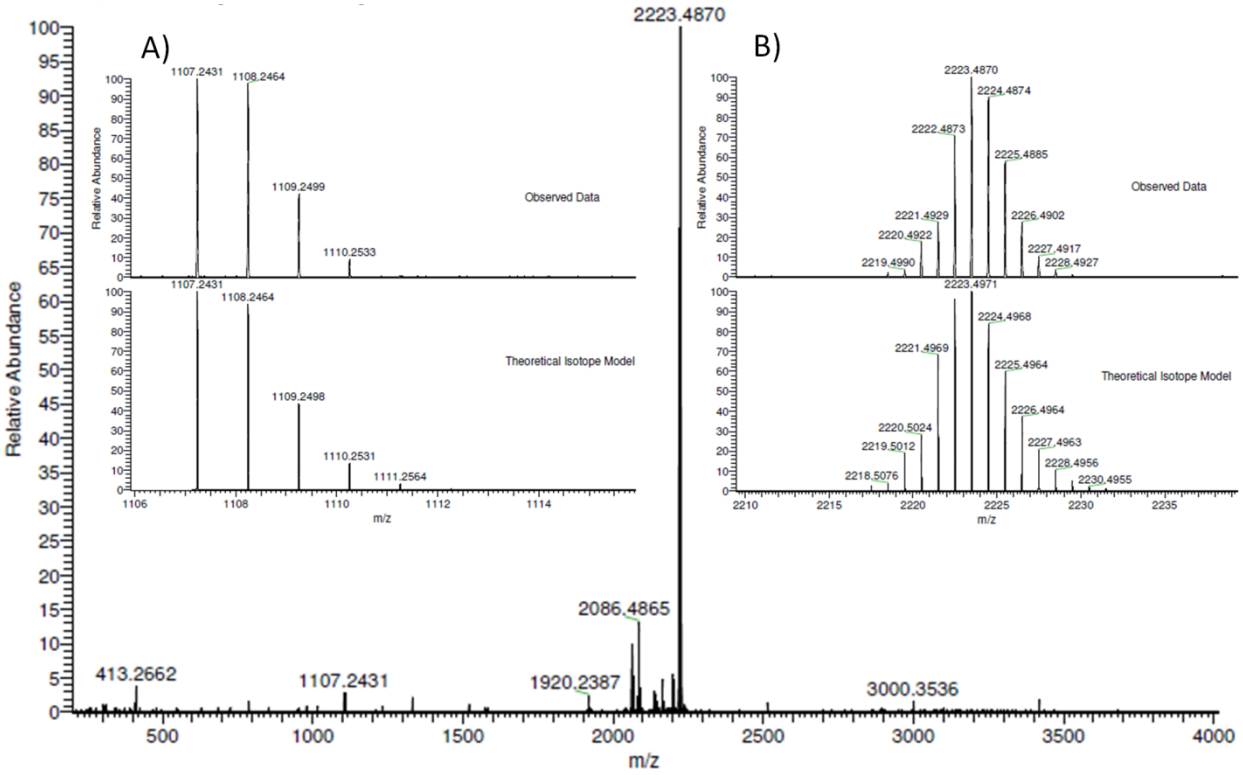


Figure 5.8 HESI mass spectrum recorded from C_{60}(py)-Cr_7Co. Inset A) observed vs theoretical isotope distribution for [C_{60}(py)+H], molecular formula ($C_{68}H_{30}N_2OH$). Inset B) observed vs theoretical isotope distribution for [Cr_7Co+Na], molecular formula ($C_{83}H_{149}Cr_7F_3CoN_1O_{35}Na$).

The ^{1}H NMR of both the uncomplexed Cr_7Co:H_2O and the C_{60}(py)-Cr_7Co complex were recorded using an acquisition window of 50 ppm to -50 ppm in line with previous NMR studies[192] (see Figure 5.9). In the Cr_7Co:H_2O spectrum, there are 15 resonances with equal integrated peak height between 24.69 ppm and -22.11 ppm. These are assigned to the 15 pivalate ligands each of which have three magnetically identical methyl substituents. The magnetic distinguishability of each of the pivalate environments is attributed to the use of an asymmetric templating molecule *N*-ethyl-D-glucamine. The peak at -25.89 ppm is assigned to the terminal methyl group of the ethyl substituent of the template. This assignment is based largely on the relative peak area, corresponding to three protons, and the chemical shift of alkyl chain protons of amines used as templating agents for similar Cr_7Co molecular magnets.[191-192] The C_{60}(py)-Cr_7Co spectrum is rather more complex. To aid the partial separation of the molecular magnet and C_{60}(py) peaks, I have assumed that all fullerene moiety proton environments are shifted up field compared to their uncomplexed spectra, commensurate with previous NMR studies of Cr_7Co rotaxane complexes,[191-192] leading to all observed resonances downfield of 7 ppm to be

attributed to pivalate environments. Additionally, the five narrower peaks (labeled in green) are indicative of a longer proton T_1 lifetime arising from an increased distance from the paramagnetic ring compared to that of the pivalate ligands and are therefore assigned to resonances of the C_{60}(py) unit. The shift of the pivalate peak positions, many by over 0.5 ppm, in C_{60}(py)-Cr_7Co compared to the Cr_7Co:H_2O spectrum confirms the absence of Cr_7Co:H_2O in the sample. Furthermore, the deviation of the narrow resonances 1-5 from the uncomplexed C_{60}(py) spectrum also suggests that the majority of the C_{60}(py) present must be bound. By taking the relative area of the 25.33 ppm peak to correspond to three methyl groups of one pivalate ligand, it can be seen that three of the pivalate ligands downfield of 7 ppm have been split into two peaks with areas corresponding to one and two methyl groups I propose that this splitting originates from the steric hindrance of the fullerene cage with the three axial pivalate groups. Evidence for this could be found using a variable temperature ^{1}H NMR experiment.

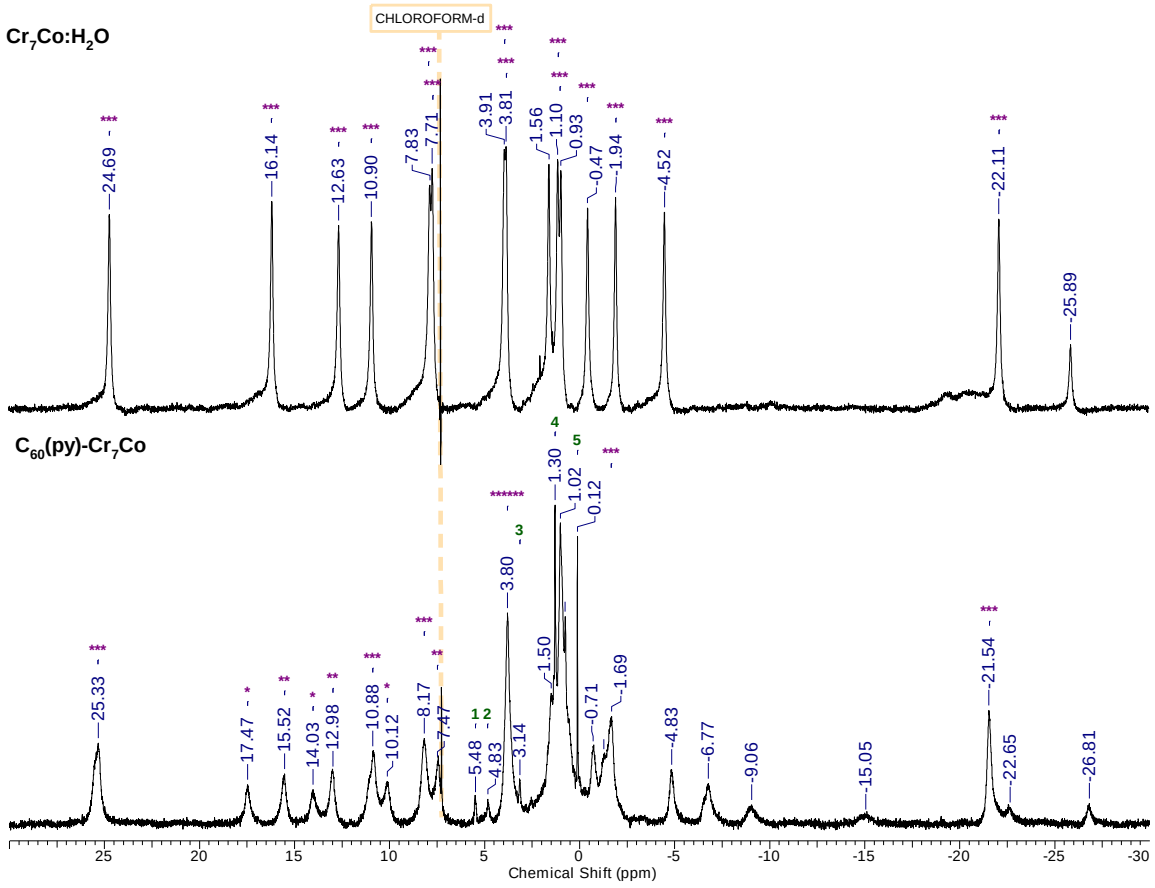


Figure 5.9 300 MHz ^{1}H NMR recorded from the molecular magnet Cr_7Co:H_2O and C_{60}(py)-Cr_7Co both using *N*-ethyl-D-glucamine as templating agent . +50 ppm to -50 ppm acquisition range used. purple* represents peak area corresponding to one methyl group of pivalate in Cr_7Co. Green numbered peaks assigned to C_{60}(py) substituent based on significantly reduced peak width.

5.3 N@C_{60}(py)-Cr_7Ni

The same scheme used to synthesise C_{60}(py)-Cr_7Co was applied to synthesise the target N@C_{60}(py)-Cr_7Ni complex. Initially, N@C_{60} was synthesised via the ion implantation method outlined in Section 2.1. This was then repeatedly enriched via the method detailed in Section 2.2 to yield N@C_{60} in C_{60} with a purity of 8 x 10^{-2} %. The N@C_{60}(py) component was purified using first a basified silica plug followed by HPLC using a semi-preparative Buckyprep column with toluene. To minimise sample loss, the final complexation step was carried out *in situ* in an ESR sample tube prior to CW and pulsed ESR characterisation. A 5 % excess of Cr_7Ni:H_2O was also used to promote complexation of the N@C_{60} spin centres (see Figure 5.10). As with C_{60}(py)-Cr_7Co, the resulting solution was brown in colour.

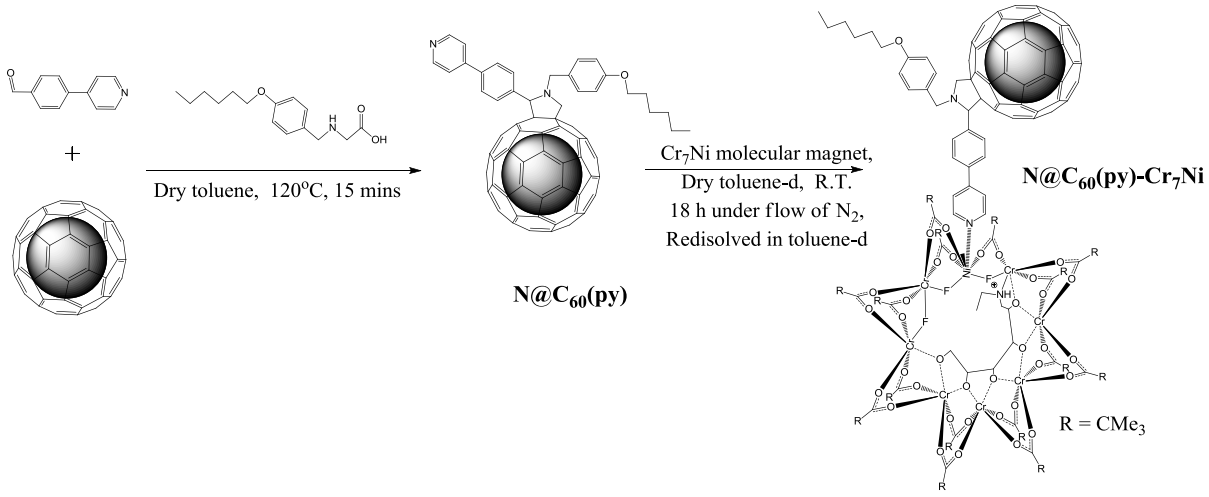


Figure 5.10 Reaction scheme used to synthesise N@C_{60}(py)-Cr_7Ni complex using 0.08 % N@C_{60} in C_{60} starting material.

5.3.1 Characterisation of N@C_{60}(py)

The HPLC peak collected as the N@C_{60}(py)/C_{60}(py) was found to have very similar retention time and peak shape to that of the pure sample of C_{60}(py) characterised in Section 5.2 (see Figure 5.11), supporting that the correct product had be isolated from the reaction.

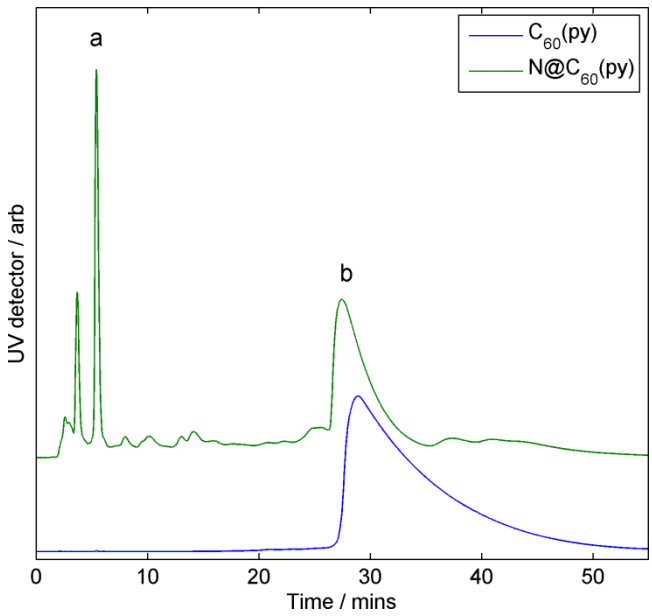


Figure 5.11 HPLC traces of N@C_{60}(py) purification (green) and pure C_{60}(py) (blue). Peak (a) was taken to be unreacted N@C_{60}/C_{60} based on peak retention time and the characteristic purple colour. Peak (b) was collected retained as the N@C_{60}(py)/C_{60}(py) peak The reaction mixture was passed through a short silica plug using 1 % T.E.A. and toluene as eluent mixture prior to HPLC analysis. Column: Buckyprep 10 x 250 mm. Eluent: Toluene. Flow rate: 7 mL^{-1}.

Comparison of the UV-Vis absorption profiles of the collected N@C_{60}(py) fraction and that of C_{60}(py) are almost identical (see Figure 5.12), supporting the purity of the isolated N@C_{60}(py) compound.

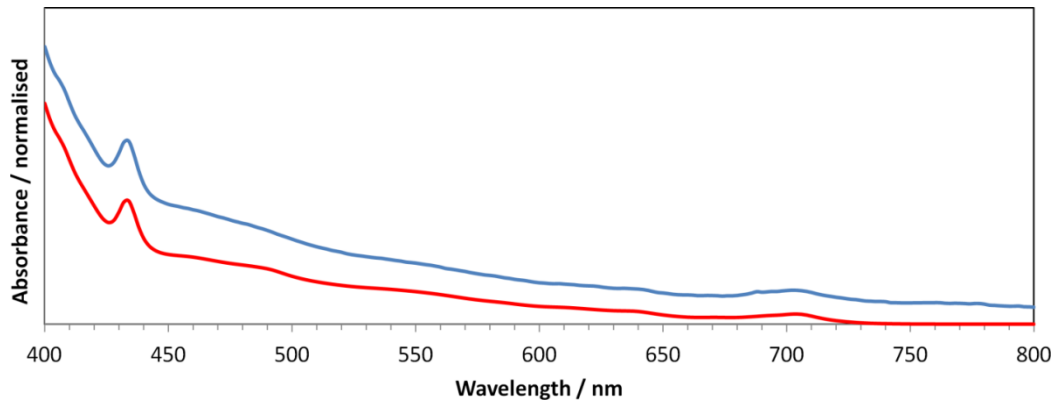


Figure 5.12 UV-Vis spectrum of N@C_{60}(py) recorded in toluene (red) overlaid with C_{60}(py) spectrum (blue). Both spectra are identical.

Both solution and frozen solution CW ESR spectra were recorded in toluene from N@C_{60}(py). The solution spectra showed the characteristic three hyperfine peaks of ^{14}N@C_{60} with the peak widths of around 0.15 mT, limited by the resolution of the spectrometer. The low temperature spectra however displayed the additional zero field peaks indicative of exohedral functionalisation of N@C_{60}. A model spin Hamiltonian of the form shown in Equation 5.1 was fitted to the recorded spectra using the EasySpin software package[147] (see Figure 5.13).

$$\widehat{\boldsymbol{H}} = \widehat{H}_{EZ}(g_{iso}) + \widehat{H}_{ZF}(D,E) + \widehat{H}_{HF}(A_{iso}) \quad (5.1)$$

This model includes terms for the Electron Zeeman Interaction ($\widehat{H}_{EZ}$), Zero Field Splitting ($\widehat{H}_{ZF}$) and Hyperfine Interaction of the electron spin with the ^{14}N nuclear spin ($\widehat{H}_{HF}$). The fitting variable used for each of the terms is shown in brackets in Equation 5.1. The use of an isotropic g-factor (g_{iso}) and isotropic hyperfine interaction (A_{iso}) parameters was found to be sufficient to model the experimental spectra. The ZFS interaction however required both axial (D) and rhombohedral(E) terms to accurately simulate the spectrum, constant with monofunctionalised N@C_{60} derivatives characterised in this thesis and elsewhere. [52-53, 55, 57-58, 60, 166] The only additional fitting parameter that was used in the model was the Gaussian linewidth of each transition (lwpp). The fitted model Hamiltonian gave the following parameters, $g_{iso} = 2.0022$, $A_{iso} = 15.95\,MHz$, $D = 14.54\,MHz$, $E = 0.33\,MHz$ and $lwpp = 0.109\,mT$.

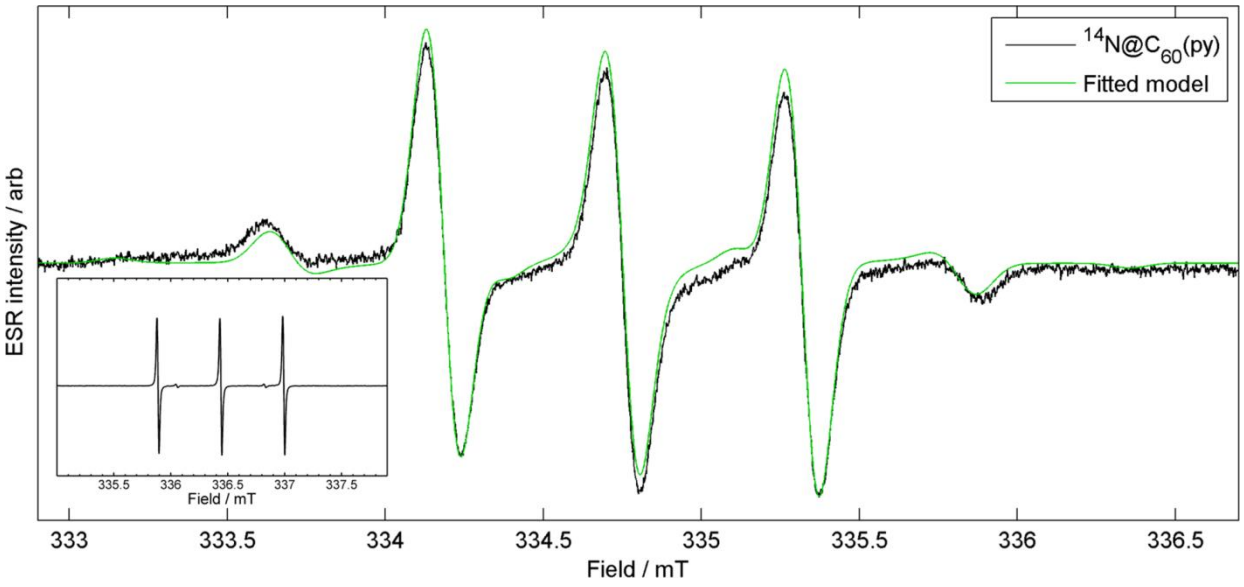


Figure 5.13 Frozen solution CW ESR spectra of N@C_{60}(py) (black) recorded at 77 K in toluene using a Miniscope ms200 spectrometer collected using a mw attenuation of 35 dB (16 µT mw power) and a modulation amplitude of 0.6 G. A model (green) was then fitted to this spectrum, resulting in the following fitted parameters: A_{iso}= 15.95 MHz, D=14.54 MHz, E=0.33MHz, linewidth 0.109 mT and g_{iso}=2.0022 with a RMS fit error of 0.04. Insert RT spectrum of same sample.

5.3.2 ESR study of N@C_{60}(py)-Cr_7Ni

To study the variable temperature T_1 and T_m behaviour of the N@C_{60}(py)-Cr_7Ni complex, two samples were prepared in 3.8 mm quartz ESR tubes, one with only the uncomplexed N@C_{60}(py) molecules and

the other containing the N@C_{60}(py)-Cr_7Ni complex in a 1:1.05 ratio. Each sample contained 9 x 10^{-8} mol of N@C_{60}(py) (calculated from the UV-Vis absorption coefficient of C_{60}(py)) with 5.6 x 10^{13} N@C_{60} spin centres (calculated using the inbuilt EMX software spin quantification tool based on the double integral of the N@C_{60}(py) spectrum) and was dissolved in 150 µl of toluene-d_8 and sealed after three freeze pump-thaw cycles. The final concentration of spin centres in each of the samples was 6.2 x 10^{-7} M for the N@C_{60}(py) sample and 6.1 x 10^{-4} M for the N@C_{60}(py)-Cr_7Ni sample calculated from the sum of the N@C_{60}(py) and Cr_7Ni concentrations. This concentration of spin centres in the N@C_{60}(py)-Cr_7Ni sample was deemed to be a reasonable compromise between maximising the signal of the N@C_{60}(py) resonances whilst maintaining magnetic isolation of the complex molecules.

A 10 K spectrum of the N@C_{60}(py)-Cr_7Ni sample shows the presence and separation of both the N@C_{60} and Cr_7Ni resonances at $g = 2$ and $g = 1.8$, respectively (see Figure 5.14). Due to the extremely long relaxation lifetime of N@C_{60} at low temperatures, CW measurements on the N@C_{60} moiety were carried out at an elevated temperature of 90 K to avoid saturation of the signal. At this temperature rapid fluctuations of the magnetic structure of the molecular magnet are expected.[130] The spectrum can be modelled fairly well using Equation 5.1 yielding fitted parameters almost identical to those found for N@C_{60}(py) in Figure 5.13 (see insert in Figure 5.14). The dipolar coupling magnitude (J_{dip}) between the $S_{3/2}$, g=2 N@C_{60}, and $S_{1/2}$, g=1.8 ground state of the molecular magnet is calculated to lie in the range of 8-20 MHz, corresponding to the separation of the centre of the Cr_7Ni ring and fullerene in either an anti (1.8 nm) or eclipsed (1.4 nm) conformation, respectively. A J_{dip} term within this range would be expected to significantly perturb the distribution of transitional energies, changing the appearance of the CW ESR spectrum. To illustrate this, a Hamiltonian of the form of Equation 3.2 was used to simulate the 1st derivative ESR spectrum of N@C_{60}(py), which included a dipolar coupled interaction J_{dip} of 17MHz with a g= 1.8 $S_{1/2}$ centre is shown in Figure B.2 in the Appendix.

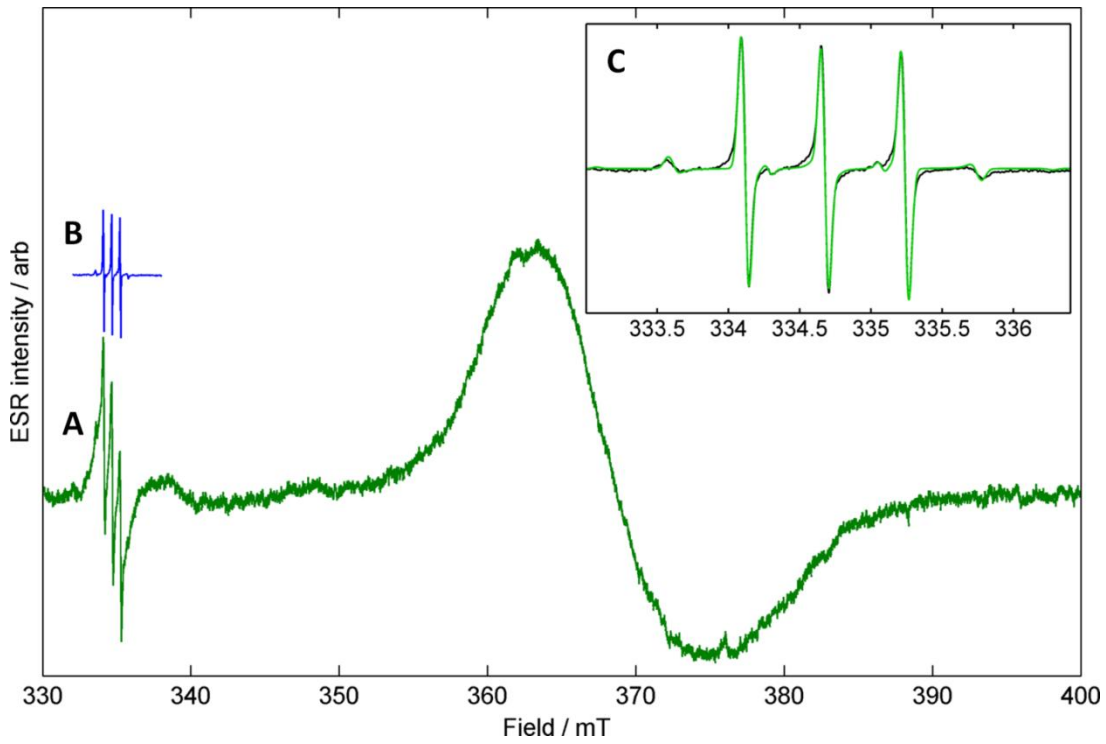


Figure 5.14 CW ESR spectrum collected from N@C_{60}(py)-Cr_7Ni sample in toluene-d_8 using an EMX spectrometer (A) 70 mT sweep using 0.3 G modulation amplitude and a mw attenuation of 30 dB (0.2mW), collected at 10 K. (B) 6 mT Sweep of g=2 region using 0.3 G modulation amplitude and a mw attenuation of 52 dB (0.00126 mW) collected at 90 K. (C) Model spin Hamiltonian of Equation 5.1 fitted to (B) with a 1 % impurity of ^{14}N@C_{60} included as secondary component of the model. Fitted parameters, A_{iso}= 15.74 MHz, D=14.58 MHz, E=0.21 MHz, line-width 0.057 mT and g_{iso}=2.0023 with a RMS fit error of 0.02.

The absence of any additional spectral features originating from the N@C_{60}(py)-Cr_7Ni complex is suggested to be due to rapid fluctuations of the molecular magnet's magnetic moment, causing the N@C_{60} centre to appear magnetically 'disconnected' from the ring, producing an CW spectrum almost identical to that of the uncomplexed N@C_{60}(py) molecule. To check that the observed spectrum was not simply due to a small fraction of the sample that was not complexed, a quantitative spin count was performed using the double integral of each of the three 'hyperfine lines' and compared to the total number prior to complexation. This yielded a total number of 6.0 x 10^{13} spin centres, within experimental error, the same as the 5.6 x 10^{13} spin centres added to the reaction mixture.

To measure the absorption spectrum of the N@C_{60}(py)-Cr_7Ni complex in its ground state, the sample was cooled below 5 K to form the coherent $S_{1/2}$ ground state of the ring.[130, 136-137] The absorption spectrum was measured using an echo detected field sweep experiment of the form $\frac{\pi}{2} - \tau - \pi - \tau - echo$, with $\pi = 160ns, \tau = 2000\,ns$ and field steps of 0.27G. Figure 5.15 illustrates the effect of

temperature on the appearance of the spectrum. Above 5 K, the spectrum resembles uncoupled N@C_{60}(py) as relaxation of N@C_{60}(py)-Cr_7Ni is too fast to be detected. Upon cooling the sample towards 2.75 K, the emergence of a new feature in the spectrum attributed to the N@C_{60}(py)-Cr_7Ni complex is seen.

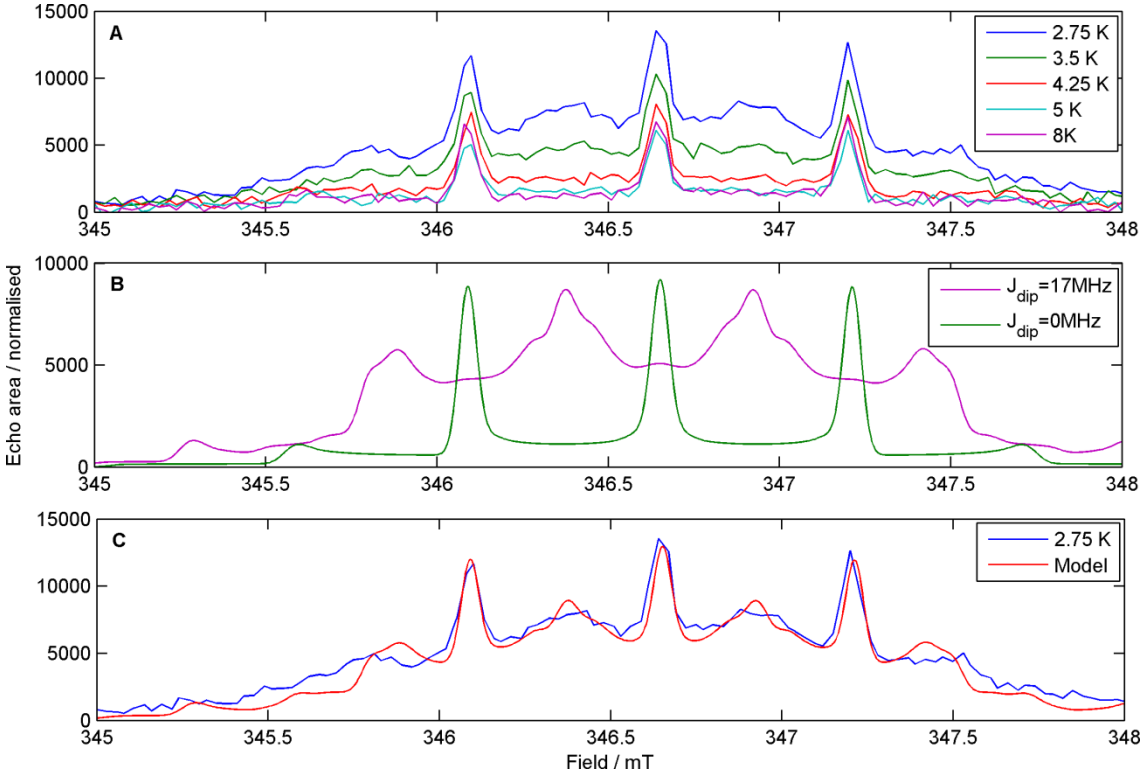


Figure 5.15 (A) Echo detected field sweep measurements of N@C_{60}(py)-Cr_7Ni carried out at 8-2.75 K using the following parameters: pulse sequence $\frac{\pi}{2} - \tau - \pi - \tau - echo$, with $\pi = 160ns, \tau = 2000\ ns$ and field steps of 0.27G. (B) Simulated absorption ESR field sweep of N@C_{60}(py) which included a J_{dip} interaction with a simple electron spin ½ centre (g_{iso}=1.8) using Equation 3.2. and the following parameters for the N@C_{60} centre: A_{iso}= 15.74 MHz, D=14.58 MHz, E=0.21 MHz, linewidth 0.057 mT and g_{iso}=2.0023 with J_{dip}=0 MHz (green) and J_{dip}=17 MHz (purple). (C) Composite model consisting of 74 % J_{dip}=17Mhz and 26 % J_{dip}=0 MHz (red) overlaid with the experimental echo detected field sweep collected at 2.75 K (blue), RMS fit error of 0.058.

The 2.75 K spectrum can be simulated using a linear combination of two components (Figure 5.15.C). The first uses the fitted model parameters obtained from the 90 K spectrum in Figure 5.14, describing the single spin centre molecule N@C_{60}(py). The second component uses the Hamiltonian of Equation 3.2 to include an additional dipolar coupling to a second $S_{1/2}$ spin centre with a g_{iso}=1.8 via a 17 MHz J_{dip} interaction term, with the remainder of the parameters common to both models. If one assumes that the point dipole approximation is valid, then using Equation 2.12 a coupling magnitude of 17 MHz would correspond to a separation of the two-spin centres of 1.4nm if a g_{iso} value of 1.8[138] is used for

the Cr_7Ni ring. This is the separation expected if the fullerene sits directly above the centre of the Cr_7Ni ring in an eclipsed conformation as depicted in Figure 5.7. This model corresponds to 74 % of the signal arising from the N@C_{60}(py)-Cr_7Ni complex, providing a lower bounds for the fraction of the N@C_{60}(py) that is bound. A further decrease in temperature is expected to extend the T_2 lifetime of the complex and increase its relative contribution to an echo detected field sweep.

The temperature dependence of T_1 and T_m was measured using inversion-recovery and Hahn echo pulse sequences, respectively (see Section 2.3). Both experiments were set up using soft pulses ($= 160\ ns$) with the centre of the field corresponding to the low field hyper fine line of the N@C_{60}(py) component (346.1 mT in Figure 5.15). In its uncomplexed state, the T_m of the pyridine functionalised N@C_{60}(py) molecule shows a weakly negative temperature dependence typical of endohedral fullerenes,[196] decreasing from 24 μs at 60 K to 9 μs at 2.5 K (see Figure 5.16). Upon complexation with the Cr_7Ni molecular magnet, the N@C_{60} T_m relaxation becomes dominated by local magnetic field fluctuations associated with population of excited magnetisation states of the antiferromagnetic ring. The T_m temperature dependence of the N@C_{60} moiety reveals three distinct dynamic regimes in the Cr_7Ni ring. Firstly, at high temperatures $\geq 10\ K$ a fast fluctuating "liquid" is observed with a T_m temperature dependence that is dominated by the small fraction of free N@C_{60}(py) in the sample, with the N@C_{60}(py)-Cr_7Ni complex component not contributing to the echo due to a much reduced transverse relaxation lifetime caused by the fluctuating magnetic state of the Cr_7Ni ring.[17, 187] Secondly, at intermediate temperatures thermal excitations of the $S_{1/2}$ ground state of the ring begin to slow, reducing the transverse relaxation rate of the N@C_{60}(py)-Cr_7Ni complex. This causes the complex to contribute to the echo decay , which can be seen as a significant dip in T_m centred around 1.75 μs at 5 K. Finally at the lowest temperature of 2.5 K, the T_m recovers to that of the uncomplexed N@C_{60}(py) signifying the onset of a long lived coherent ground state of the Cr_7Ni ring.

Comparison of the T_1 temperature dependence of N@C_{60}(py)-Cr_7Ni and N@C_{60}(py) reveals a maximum T_1(N@C_{60}(py))/ T_1(N@C_{60}(py)-Cr_7Ni) ratio of 7 at around 20 K, which reduces to 1.4 at low temperature

(2.5 K) and 1.8 at high temperature (100 K) (see Figure 5.17). It is also observed that the T_1 of the complex system displays a different exponential temperature dependence below 20 K.

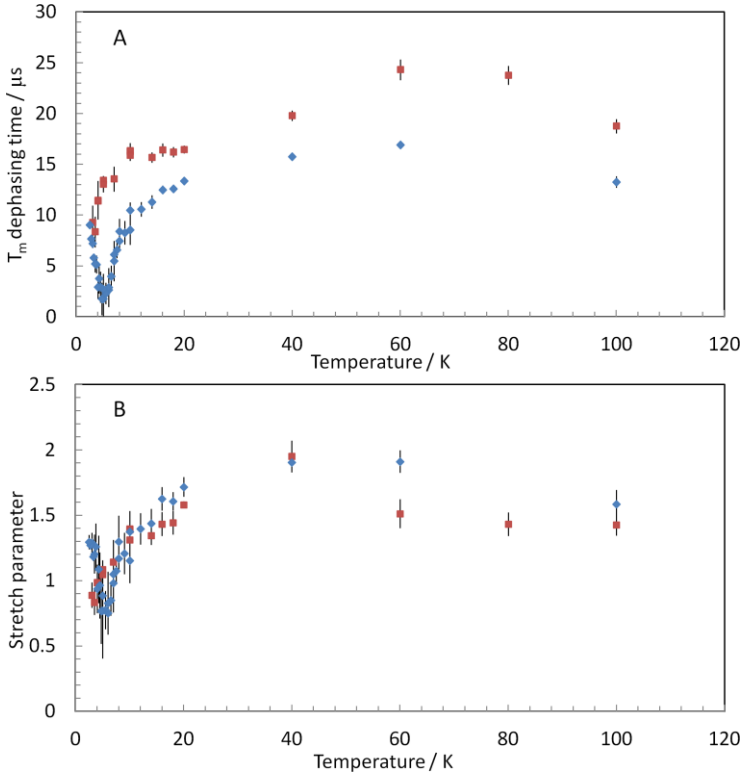


Figure 5.16 (A) Phase coherence lifetime T_m of N@C_{60}(py)-Cr_7Ni (blue) and N@C_{60}(py) (red) as a function of temperature.(B) corresponding fitted stretch parameter (n) for each T_m value Measured using a Hahn echo sequence $\frac{\pi}{2} - \tau - \pi - \tau - echo$, with $\pi = 160ns, \tau = 2000\ ns$. Errors shown indicate 95 % confidence level using a stretched exponential function of the form shown in Equation 5.4.

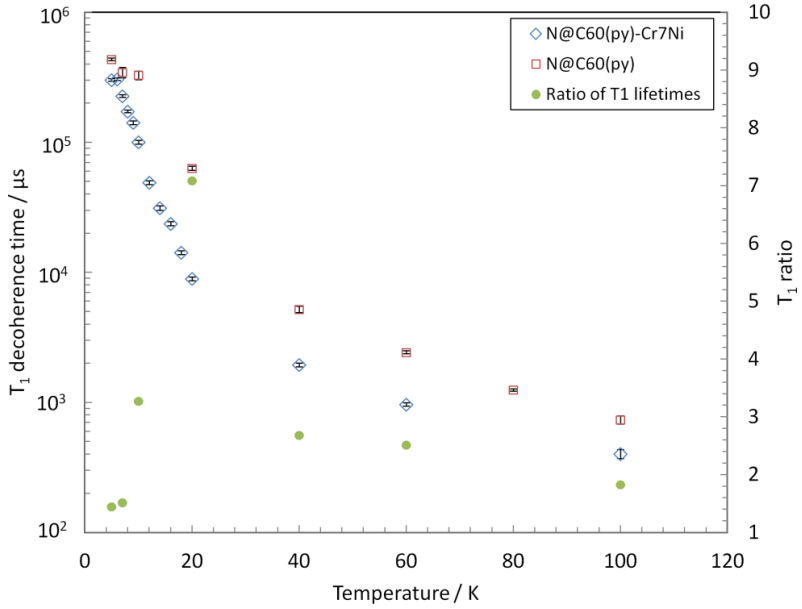


Figure 5.17 T_1 lifetime of N@C_{60}(py)-Cr_7Ni (blue) and N@C_{60}(py) (red) as a function of temperature. Measured using an inversion recovery sequence, with $\pi = 160ns, \tau = 2000\ ns$. Errors shown indicate 95 %. The ratios of the two T_1 values at each temperature point are overlaid as the secondary axis (green).

5.4 Discussion

In this chapter, I have used a 2,3 cycloaddition reaction to introduce Lewis base functionality to both C_{60} and N@C_{60}. The fitting of a model spin Hamiltonian to the CW ESR spectrum of N@C_{60}(py) indicated that the spin environment was similar to the pyrrolidine dimers N@C_{60}-3bz and N@C_{60}-5bz characterised in Chapter 3, yielding parameters of $g_{iso} = 2.0022$, $A_{iso} = 15.95\,MHz$, $D = 14.54\,MHz$, $E = 0.33\,MHz$ and $lwpp = 0.109\,mT$. Characterisation of weakly paramagnetic complex C_{60}(py)-Cr_7Co proved incompatible with mass spectroscopy with only the C_{60}(py) and Cr_7Co fragments identifiable, presumably due to the large mass of both the fullerene and metallic ring units coupled with the relatively weak dative covalent bond holding the complex together. ^{1}H NMR proved more instructive, showing a shift of the pivalate resonances of the Cr_7Co ring supporting that complexation has occurred. The splitting of three of the pivalate resonances could suggest that the fullerene cage is predominantly situated over the centre of the ring, causing the restricted rotation of the three axial pivalate *t*-Bu groups. To provide further evidence for the complex, I suggested that synthesising a Cr_7Co molecular ring using deuterated pivalic acid would permit the fullerene resonances to be separated from the molecular magnet and assigned.[191]

The CW ESR study of the N@C_{60}(py)-Cr_7Ni complex yielded many interesting features. At temperatures significantly above 5 K, when the molecular magnet undergoes rapid fluctuations, the N@C_{60} centre appears magnetically 'disconnected' from the ring, producing an CW spectrum almost identical to that of the uncomplexed N@C_{60}(py) molecule. When the system is cooled to below 5 K, the onset of a coherent $S_{1/2}$ ground state in the Cr_7Ni ring occurs and the emergence of another spectrum takes place. This spectrum can be accounted for by the addition of a dipolar coupling interaction (J_{dip}) of 17 MHz with an $S_{1/2}$ spin centre to the spin Hamiltonian of N@C_{60}(py). If we assume that using the point dipole approximation is the valid approach, then an interaction of this magnitude corresponds to a separation of the two radical centres of 1.4 nm. This distance is as would be expected if the fullerene sits directly above the ring and supports the suggestion that a steric interaction between the fullerene cage and the

axial pivalate group causes the splitting pattern seen in the ^1H NMR of C_{60}(py)-Cr_7Co. This result is exactly as hoped for demonstrating the ability to measure and accurately model the effect of a dipolar coupling interaction on an N@C_{60} electron spin transition spectrum of a two spin centre hetero dimer. This capability is a prerequisite to initialise and measure the state of a qubit in an array and supports that an N@C_{60} qubit element in a multi spin centre array will satisfy the DiVincenzo criteria 1, 2 and 5. Using the N@C_{60}(py)-Cr_7Ni system to fully test criteria 1,2 and 5 may prove challenging owing to the width of the Cr_7Ni ring spectrum. While it's ESR transitional spectrum is narrow for a transition metal complex at ≈400 G it remains 40 times wider than that of N@C_{60} causing the effect of the 17MHz dipolar coupling interaction to be difficult to resolve in the Cr_7Ni spectral region. The Resolution could be improved using a bridging unit with a shorter length to increase the dipolar interaction between the two spin centres to around 50 MHz. The significantly broader spectral features of Cr_7Ni magnet also causes the required concentration of spin centres to be higher than for a purely N@C_{60} based system to achieve the threshold number of spins per Gauss for detection, causing the required quantity of highly enriched N@C_{60} to be between 1-2 orders of magnitude larger than for an all N@C_{60}-N@C_{60} array system as shown in chapter 3 corresponding to ≈10 μg of 100 % enriched N@C_{60}(py).

In its uncomplexed state, the T_m of the pyridine functionalised N@C_{60}(py) molecule shows a weakly negative temperature dependence typical of endohedral fullerenes,[196] decreasing from 24 μs at 60 K to 9 μs at 2.5 K. Upon complexation with the Cr_7Ni molecular magnet, the N@C_{60} T_m relaxation becomes dominated by local magnetic field fluctuations associated with the population of excited magnetisation states of the antiferromagnetic ring. The T_m temperature dependence of the N@C_{60} moiety reveals three distinct dynamic regimes in the Cr_7Ni ring. Firstly, at high temperatures $\geq 10\ K$ a fast fluctuating "liquid" is observed with a T_m temperature dependence that is dominated by the small fraction of free N@C_{60}(py) in the sample, with the N@C_{60}(py)-Cr_7Ni complex component not contributing to the echo due to a much reduced transverse relaxation lifetime caused by the fluctuating magnetic state of the Cr_7Ni ring.[17, 187] Secondly, at intermediate temperatures between 10 K and 5 K thermal excitations of

the $S_{1/2}$ ground state of the ring begin to slow, reducing transverse relaxation rate of the N@C_{60}(py)-Cr_7Ni complex. This permits the complex to contribute to the echo decay and is seen as a significant dip in T_m centred around 1.75 μs at 5 K. Below 5 K, the onset of a coherent ground state takes place and the T_m rapidly increases to 9 μs at 2.5 K, in line with that of the uncomplexed N@C_{60}(py) sample. This is the first experiment that measures the effect of a dipolar coupled electron spin centre on the phase memory time of N@C_{60}. The recovery of a T_m of 9 μs at 2.5K lead two conclusions to be drawn with respect to the potential use of N@C_{60} in an extended qubit array. Firstly, that it is possible for an spin centre to be close proximity to an N@C_{60} centre without a significant reduction in T_m . This is a key requirement in any future scalable quantum computer based on N@C_{60}. Secondly a T_m of 9 μs is lower than desired for the successful implementation of an entanglement forming CNOT gate[27] of 11 μs in an N@C_{60} based array/ this suggests that the use of an N@C_{60}(py)-Cr_7Ni based quantum computational element will not satisfy the DiVincenzo criterion 3 which states the requirement that T_m is long compared to the gate operation time. One potential use of this system is to use the nitrogen nuclear spin of the N@C_{60} unit to act as a quantum memory for the Cr_7Ni, using the electron dipolar coupling to transfer the state from the Cr_7Ni unit to the nitrogen nuclear spin. This approach has been performed on pristine N@C_{60} to extend the quantum memory time of a single qubit to over 100 ms.

Chapter 6 Photostability of N@C_{60}

Owing to the difficulty in purifying N@C_{60}, it is important to minimise its degradation after synthesis. N@C_{60} has been shown to be photosensitive. Consequently, understanding the mechanism(s) of the photodecomposition process will help to identify compatible spectroscopic techniques, reaction schemes and processing methods without needing to put high purity N@C_{60} at risk. This chapter looks at two features of the photostability of N@C_{60}. Firstly, demonstrate a significant solvent dependence on the photostability of N@C_{60} when subject to ≥254nm UV irradiation, identifying decalin as the best solvent for use in UV-initiated photoexperiments in both deoxygenated and ambient environments. I then go on to quantitatively measure the dependence of the photostability of N@C_{60} on the concentration of oxygen using a 637nm He:Ne laser. With these findings, I discuss the limitations of creating a hybrid N@C_{60} Nitrogen-vacancy (NV^-) centre Optically Detected Magnetic Resonance (ODMR) experiment to interrogate the magnetic spin state of single N@C_{60} centres.

6.1 Introduction

The exact decay mechanism(s) of photodecomposition of N@C_{60} is yet to be pinned down, however it has been shown that pulsing a low purity N@C_{60} and N@C_{70} toluene solution with a 355 nm Nd:YAG laser results in the deterioration of the ESR signal.[51] The observed relative decay rates of N@C_{60} and N@C_{70} suggest that the decay is caused by vibrational excitation initiated by non-radiative relaxation of the excited triplet molecular species to the electronic ground state. This triplet mediated mechanism would also explain the observation that when oxygen (known to efficiently quench the triplet excited state of fullerenes) is present in the solvent of the endohedral fullerene solution, the photostability under ambient light is significantly enhanced.[52]

The photostability of exohedrally modified N@C_{60} is highly dependent on the geometry that the adduct forms with the carbon cage.[52] This is best illustrated by comparison of the photostability of three-

membered ring cyclopropane derivatives and five-membered ring pyrrolidine adducts. Pyrrolidine derivatives accelerate the photodecomposition of N@C_{60} by more than an order of magnitude compared to pristine N@C_{60}, while cyclopropane derivative show comparable stability to N@C_{60}. This dependence in photostability can be understood by considering the σ* orbital geometry of the carbon atoms of the fullerene cage that are involved in bonding with the exohedral substituent. In the case of the pyrrolidine substituent, the five-membered ring forces the fullerene carbon atoms into an almost sp^3 configuration causing the σ* orbital to project towards the centre of the cage, providing greater overlap with the endohedral nitrogen radical than is found in the sp^2 hybridised pristine N@C_{60} system. The cyclopropane derivative, however, distorts the carbon cage far less from its sp^2 configuration causing little change in photoreactivity.

6.2 254 nm UV stability of N@C_{60} in common solvents

This section examines the UV photosensitivity of N@C_{60} in a range of common solvents, to better understand the mechanism of N@C_{60} photosensitivity and identify the best solvent system to use for future photo-physical experiments.

6.2.1 Experimental set-up

2 mg of partially enriched N@C_{60}/C_{60} was added to each of four glass vials followed by 2 mL of one of the four solvents to be studied (*cis/trans*-decalin, benzene, toluene, o-xylene). This mixture was then sonicated for 1 hour to completely dissolve the solid endohedral fullerene sample. A 200 µl aliquot from each solution was added to two 4 mm diameter quartz ESR tubes. One tube of each set of two was then degassed using three pump-thaw cycles and flame sealed. The remaining tube was left under atmospheric conditions.

To irradiate the samples, one set of ESR tubes with each of the four N@C_{60}/C_{60} solutions was placed in a test tube rack. Ambient light was then excluded by placing a black box over the samples and UV irradiation from a commercial thin layer chromatography (TLC) (≥254nm) lamp was introduced to the

samples through a wide slit in the top of the box. At regular time intervals, a first derivative CW ESR spectrum was recorded for each of the solutions using a Magnetech ms200 ESR spectrometer. The average magnitude of the three characteristic hyperfine peaks of N@C_{60} was then used as a measure of the fraction of N@C_{60} remaining in the sample relative to t_0.

6.2.2 Solvent dependency

Due to the low concentration of fullerenes that are endohedral (approximately 1/1000) a rate constant for the decay process was extracted using a first order reaction kinetics model of the form $lnA = -kt + lnA_0$ where A_0 is the initial signal magnitude, A is the signal magnitude after time t and k is the overall rate constant for the decay process. A $\ln(\frac{A}{A_0})$ vs time plot for each of the solvents in both ambient and degassed environments is shown in Figure 6.1.

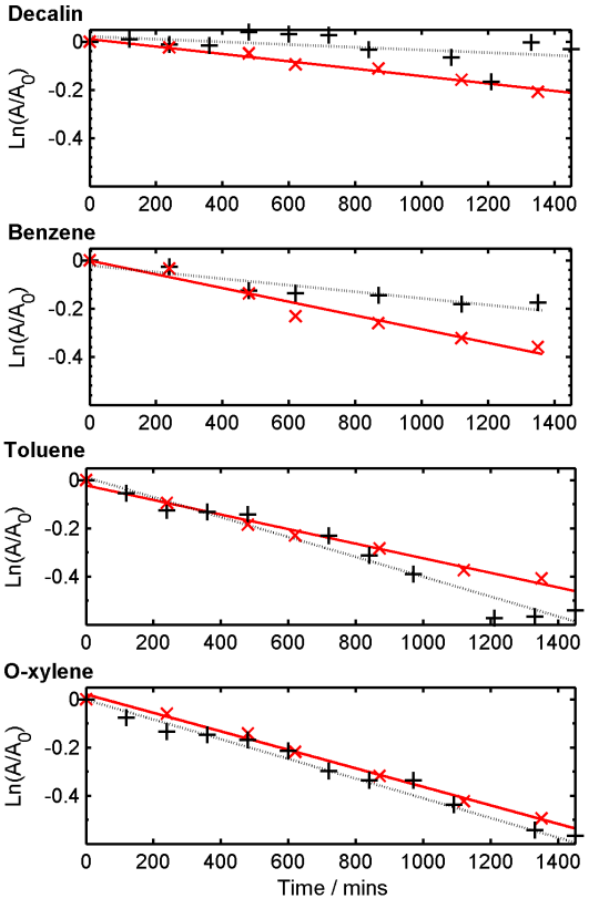


Figure 6.1 Natural log of first derivative ESR signal height of N@C_{60} plotted against 254 nm UV irradiation time. (red) degassed sample, (black) ambient sample, with linear fits.

All decay rates in Figure 6.1 were fitted to a linear equation, permitting a rate constant and half life for the decay ($t_{1/2}$) for each sample to be extracted using the gradient of the fitted equation (see Table 6.1 for a summary of the calculated parameters). The plot in Figure 6.2 highlights two trends in the data. . Firstly, the effect of the presence of oxygen on the decay rate is solvent dependent with the difference in decay rate between the degassed and ambient samples increasing along the series o-Xylene ≈ Toluene < Benzene < Decalin. Secondly, the decay rate of N@C_{60} is affected by solvent with the rate in both degassed and ambient conditions increasing along the series Decalin < Benzene < Toluene ≈ o-Xylene, despite the oxygen solubility in each solvent being similar (see Table 6.1).

Solvent	Dissolved [O_2] @ 294 K, 1atm (mol L^{-1}) x 10^3 values taken from[197]	Ambient		Degassed	
		k x 10^4 (min^{-1})	$t_{1/2}$ (min)	k x 10^4 (min^{-1})	$t_{1/2}$ (min)
Decalin	1.67	0.559	12399	1.54	4515
Benzene	1.92	1.37	5062	2.84	2437
Toluene	1.99	4.31	1680	3.03	2289
o-Xylene	1.95	4.09	1694	3.84	1804

Table 6.1 Rate constant k and half-life $t_{1/2}$ for the photo-induced decay of N@C_{60} in different solvents with and without oxygen present.

Both of these trends could be explained by the presence of two competing mechanisms available to induce the photodecomposition of N@C_{60} upon UV photo irradiation. Mechanism 1 takes place through the non-radiative relaxation of ^{3}{N@C_{60}} generated by direct absorption of a photon, with the rate expected to be very sensitive to the concentration of $^3O_2$ [51] Mechanism 2 proceeds through the formation of radical adduct of N@C_{60} with photo-generated radicals from the solvent, increasing the decomposition rate by reducing the activation energy required to form a covalent bond between the nitrogen and fullerene radicals.[55] The rate of mechanism 2 would be expected to be determined by the propensity for the solvent to form a radical adduct with N@C_{60} rather than the concentration of $^3O_2$. Using these two mechanisms the two trends can be explained by the switching of the dominant decay mechanism from mechanism 1 in decalin to mechanism 2 in toluene and o-xylene initiated by radicals formed from the methylated benzene solvents. As the rate of mechanism 2 increases, the overall rate of N@C_{60} decomposition would be expected to increase and the effect of the presence of $^3O_2$ decrease.

The presence of the radical adducts required to initiate mechanism 2 in the methylated benzene solvents is supported by previous studies that show that resonantly stabilised benzyl radical can form during UV irradiation[198] and the ability for these radicals to form adducts with C_{60}.[199] Work by F. Cataldo *et al.* has also reported that solvent radical initiated nano-clustering of C_{60} occurs in UV photo-cleavable solvents such as chloroform.[200] This process also has the insensitivity to the presence of oxygen that is expected in mechanism 2.[200]

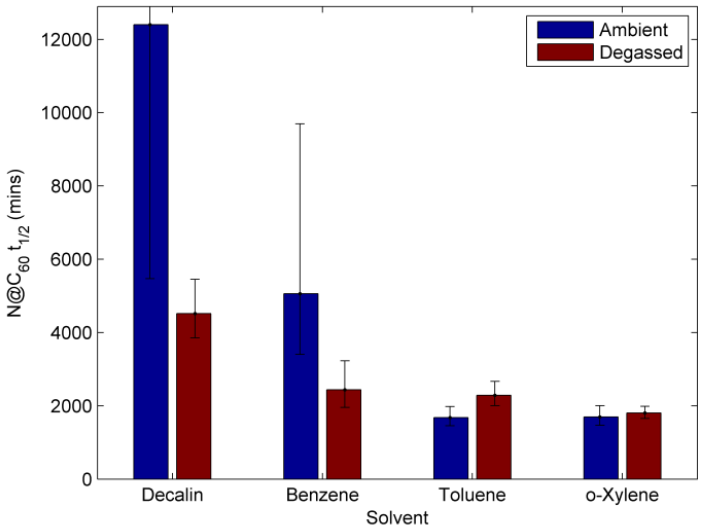


Figure 6.2 Comparison of different decay rates of N@C_{60} in different solvents with and without oxygen present, labelled as ambient and degassed, respectively. Error bars for 95 % confidence level of the fitted decay rate function. Upper bounds for ambient decalin sample is not shown since rate constant k approaches 0.

To probe for the formation of the photochemical adducts expected in the aromatic solvents if mechanism 2 is indeed present, the UV-Vis spectra of each of the four samples irradiated under ambient conditions were recorded before and after the experiment (see Figure 6.3). Comparison of the UV-Vis spectra before and after irradiation shows that a broad absorption peak appears between 400-500 nm in the aromatic solvent samples while the decalin solution remains unchanged. Previous studies on C_{60} subjected to UV irradiation have shown that this absorption feature is due to a reduction in symmetry of the fullerene cage caused by photopolymerisation of fullerenes to form nano-clusters.[201] The observation that this photopolymerisation feature is present in the aromatic solvents but not decalin is in direct support of the hypothesis that photodecomposition of N@C_{60} is primarily

taking place via a radical initiated photochemical process in the aromatic solvents and a photo-physical process in decalin.

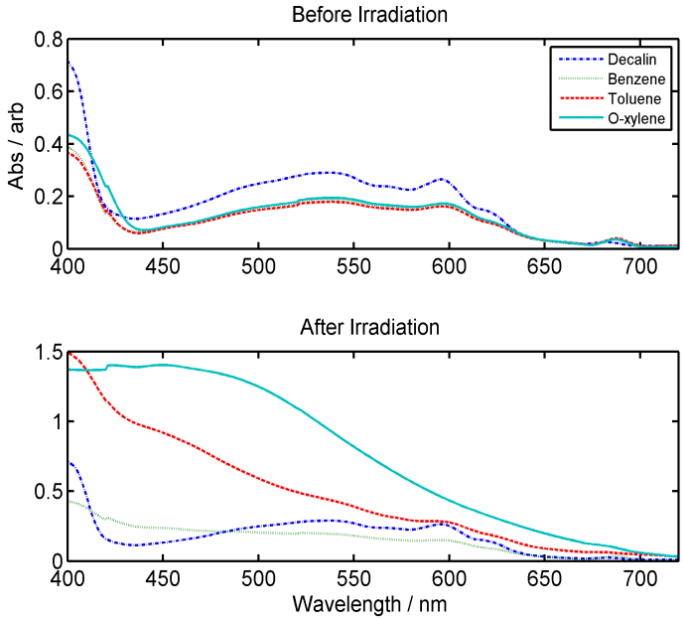


Figure 6.3 UV-Vis absorption spectra for the N@C_{60} / C_{60} mixture in each ambient solvent, both before and after irradiation.

6.3 637 nm laser stability of N@C_{60}

The only fixed wavelength study of the photostability of N@C_{60} has been carried out using a UV 355 nm laser source in toluene. By using a longer wavelength excitation source, the number of pathways that are available to degrade N@C_{60} is restricted. A 637 nm source was chosen for two reasons. Firstly, C_{60} absorption in the region of 627 to 648 nm corresponds to the orbitally-forbidden and spin-forbidden vibronic $1\ ^3T_{1g} + h_g \leftarrow 1\ ^1A_g$ transitions[202] and so directly excites the triplet ($T_1^{triplet}$) fullerene state whilst causing minimal vibrational excitation, making it an ideal wavelength to selectively probe the role of the fullerene triplet state on the stability of N@C_{60}. Additionally, one potential method for the detection of individual N@C_{60} centres is to deposit the N@C_{60} adjacent to a single Nitrogen-vacancy (NV^-) centre and use ODMR to probe the NV^- centre for additional spectral transitions due to dipolar coupling between the two radical centres.[203] So far, this technique has failed to show any additional splitting in the NV^- spectrum;[203] one possible cause for this is the decomposition of the N@C_{60} centre upon optically exciting the NV centre. 637 nm corresponds to the wavelength of the zero phonon

excitation of the NV^- centre from the ground state to first excited state and so corresponds to the minimum excitation energy required to perform ODMR on the NV^- centre.[204]

6.3.1 Experimental set-up

The N@C_{60} used in this study was synthesised using an ion implantation method[33] (see Section 2.1) and enriched using High Pressure Liquid Chromatography (HPLC)[42-43] as discussed in Section 2.2. The N@C_{60} used had a purity of approximately 200 ppm in C_{60}. 1.2 mg of N@C_{60}/C_{60} was added to a 10 mL glass vial followed by 2 mL *cis-trans*-decalin. This mixture was then sonicated for 1 hour to completely dissolve the solid endohedral fullerene sample. A 50 µl aliquot of the solution was added to two 4 mm diameter quartz ESR tubes. One of the tubes was then degassed using three pump-thaw cycles and flame sealed. The remaining tube was left under atmospheric conditions.

The 5 mW, 637 nm He:Ne laser was mounted to a laser table and aligned to the centre of the optical access hole of a Magnetech ms200 ESR spectrometer. Using a 4 mm quartz ESR tube filled with 50 µl of luminescent quantum dots, the correct sample height was taken to be that which corresponded to the maximum observed luminescence of the quantum dots, found to be 9 cm from the top of the ESR tube Collet. A schematic of the experimental set-up is shown in Figure 6.4.

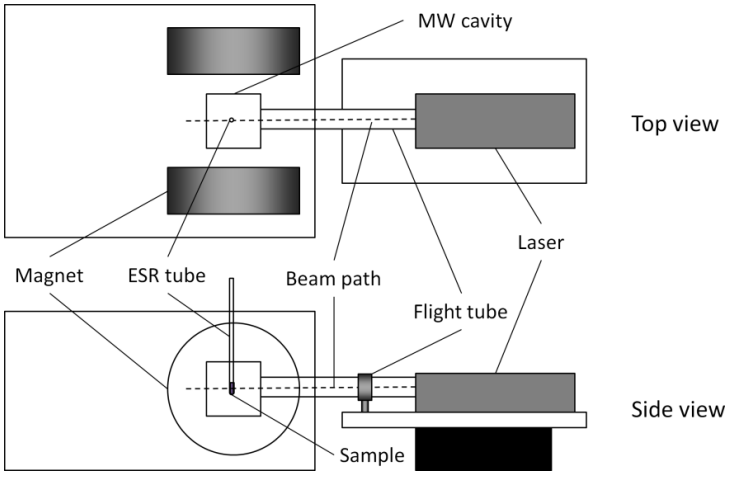


Figure 6.4 Schematic of the experimental set-up used to measure the *in situ* decomposition of N@C_{60} when subject to 637 nm laser illumination.

Once the ESR tube was inserted into the ESR spectrometer, an initial CW measurement of the spectrum was recorded. Following this the laser source was turned on and a new spectrum was recorded at 15 minute time intervals over the course of 24 hours. Since the width of the N@C_{60} hyperfine lines was found to remain constant for the duration of the experiment, the number of N@C_{60} molecules was taken to be proportional to the measured signal magnitude of the hyperfine lines relative to t = 0, before irradiation.

To check that the beam was not optically saturating the sample, the fraction of the fullerene molecules that were excited at any given time in the beam path was estimated using the following parameters:

$$\boldsymbol{Beam\ \emptyset = 1\ mm},\ \boldsymbol{ESR\ tube\ ID\ \emptyset\ = 3mm},\qquad \boldsymbol{Laser\ power = 5\ mW}$$

$$Beam\ area\ = \pi \times 0.5^2 = 0.78\ mm^2$$

$$Volume\ of\ laser\ path \approx 0.78\ \times 3 = 2.35\ mm^3$$

$$[\boldsymbol{N@C_{60}/C_{60}}] = \boldsymbol{0.6\ gL^{-1}} \equiv 5.07 \times 10^{14}\ molecules\ mm^3$$

$$\#\ molecules\ in\ beam\ path = 5.07\ \times 10^{\ 14} \times 2.35 = 1.8\ \times 10^{15}\ molecules$$

$$\boldsymbol{Power(W)} = \frac{n\ \cdot h \cdot c}{\lambda \cdot t}$$

$$\#\ photons\ pased\ \ through\ sample\ (n) = \frac{5 \cdot 10^3 \cdot \lambda}{h \cdot c} \cdot t = 1.6 \times 10^{16} \cdot t$$

The typical excitation lifetime that has been measured for C_{60} in the degassed solutions used in this study is around 20 μs. Therefore the number of excitations (taken to be equal to the number of photons absorbed)[205] that each molecule can undergo per second is estimated to be $\frac{1}{20\times10^{-6}} \approx 50000$. Using the measured sample absorbance at 637 nm of 0.066, and an estimation that 50 % of the photons are scattered by the curvature of the quartz ESR tube, the percentage of the incident photon flux that is absorbed by the sample is equal to $10^{-0.066} \cdot 0.5 = 7\ \%$. Consequently, the percentage of fullerene molecules in the beam path that are excited at any given time is $\frac{0.07\cdot1.6\times10^{16}}{50000\cdot1.8\times10^{15}} = 1.2\ \times 10^{-3}\ \%$, indicating that the laser power is sufficiently low to not optically saturate the sample during the irradiation.

After recording the photodecomposition rate of N@C_{60} under 637 nm laser illumination, the concentration of oxygen within each of the samples was measured with a flash photolysis experimental set-up by Dr Kiminori Maeda at the Centre for Advanced Electron Spin Resonance (CAESR) in Oxford University Inorganic Chemistry Department. The experiment used a pulsed 532 nm laser as the pump source to excite C_{60} to the singlet state S_1 and a white light mercury lamp at the probe source to excite the formed triplet fullerene species T_1 to higher T_n states (see Figure 6.5). A 750 nm monochromator attached to a photomultiplier tube was then used to measure the transient-absorbance (A_{750nm}) of the $T_1^{(triplet)} \longrightarrow T_n^{(triplet)}$ transitons. Since the Internal Conversion rate constant (k_{IC}) for $T_n^{(triplet)} \longrightarrow T_1^{(triplet)}$ is very fast compared to the time scale of the experiment, A_{750nm} is proportional to the concentration of the $T_1^{(triplet)}$ state $\left(\left[T_1^{(triplet)}\right]\right)$ (see equation 2.25).

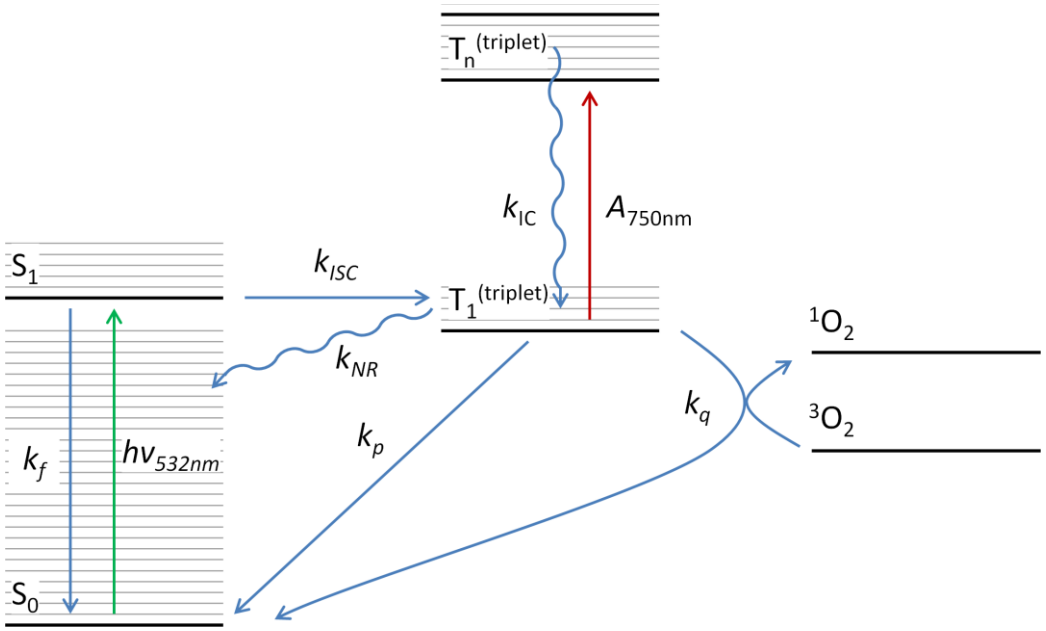


Figure 6.5 A simplified Jablonski diagram depicting the energy transfer pathways present in both of the ambient and degassed fullerene solutions. k_{ISC} is the rate constant for intersystem crossing, k_{IC} *is* the rate constant for internal conversion, k_{NR} is the rate constant for non-radiative relaxation, k_p is the rate constant for phosphorescence, k_q is the rate constant for triplet quenching by $^3O_2$, A_{750nm} is the transient-absorbance measured at 750nm.

6.3.2 Results

To calculate the concentration of oxygen present in the samples, values for the rate constants for the relaxation processes from the $T_1^{(triplet)}$ state in Figure 6.5 are needed. The rate constant for Intersystem crossing k_{ISC} was taken to be equal to the reciprocal of the measured $S_1 \longrightarrow T_1^{(triplet)}$ time of approximately 1 ns.[205] The rate constant for phosphorescence k_p has not been reliably measured due to it being negligibly small,[206] as such I have approximated k_p to be equal to 0. Relaxation of $T_1^{(triplet)} \longrightarrow S_0$ in the absence of a quencher leads to almost unitary conversion of the energy difference between the two states into thermal excitation of the molecule.[207] Owing to this, the rate constant for non-radiative relaxation can be taken to be equal to the reciprocal of the intrinsic lifetime[208] of $T_1^{(triplet)}$ measured in solution to be 142 μs.[209] The rate constant of quenching by $^3O_2$ k_q is taken from the average of two reported values[210-211] 1.9 x 10^9 M s^{-1} and 1.4 x 10^9 M s^{-1}.

$S_1 \longrightarrow T_1^{(triplet)}$ $ISC, quantum\ yield\ (\phi) \approx 1, \qquad k_{ISC} \cong 1 \times 10^9 s^{-1}$

$T_1^{(triplet)} \longrightarrow S_0$ $nonradiative\ relaxation,\ k_{NR} = 7000\ s^{-1}$

$T_1^{(triplet)} \longrightarrow S_0$ $phosphorescence,\ k_p \cong 1\ s^{-1}$

$T_1^{(triplet)} \longrightarrow S_0$ $quenched\ by\ {}^3O_2,\ k_q = 1.6 \times 10^9\ M\ s^{-1}$

These previously reported parameters together with the assumption that $[T_1^{(triplet)}] \propto A_{750nm}$ permit a first order rate equation to be constructed for the concentration of T_1 states and evaluated in terms of the measured A_{750nm} as a function of time:

$$\frac{d[T_1^{(triplet)}]}{dt} = -(\,k_p + k_{NR} + k_q[\,{}^3O_2]\,)[T_1^{(triplet)}]\,)$$

$$\therefore \int_0^t \frac{1}{[T_1^{(triplet)}]} d[T_1^{(triplet)}] = -\int_0^t (\,k_p + k_{NR} + k_q[\,{}^3O_2]\,)dt$$

$$\therefore\ ln\,[T_1^{(triplet)}]_t - ln\,[T_1^{(triplet)}]_0 = -(\,k_p + k_{NR} + k_q[\,{}^3O_2]\,) \cdot t$$

$$\therefore\ \frac{A_{750nm}^t}{A_{750nm}^0} = \frac{[T_1^{(triplet)}]_t}{[T_1^{(triplet)}]_0} = e^{-(\,k_p + k_{NR} + k_q[\,{}^3O_2]\,)\cdot t}$$

By fitting the decay profile of the A_{750nm} to a mono-exponential function of the form $A^{t}_{750nm} = A^{0}_{750nm} \cdot e^{(-\tau^{-1} \cdot t)} + C$, the $T_1^{(triplet)}$ lifetime together with the $[\,^3O_2]$ can be determined from the following equation:

$$\frac{A^{t}_{750nm}}{A^{0}_{750nm}} = e^{-1}, t = \tau \quad \therefore (\, k_p + k_{NR} + k_q[\,^3O_2]\,) = \tau^{-1}$$

$$\therefore\ [\,^3O_2] = \frac{\tau^{-1} - k_p - k_{NR}}{k_q}$$

Table 6.2 summarises the fitted parameters together with the $[\,^3O_2]$ for both the degassed and ambient samples. The effect of degassing the sample increases the $T_1^{(triplet)}$ lifetime by a factor of 50 from 0.37 µs to 18.6 µs, corresponding to a reduction in the $[\,^3O_2]$ from 1.69 x 10^{-3} M to 2.92 x 10^{-5} M. For comparison, the calculated $[\,^3O_2]$ in decalin at 294 K under ambient conditions[197] is 1.66 x 10^{-3} M, very similar to the value derived from the flash photolysis experiment.

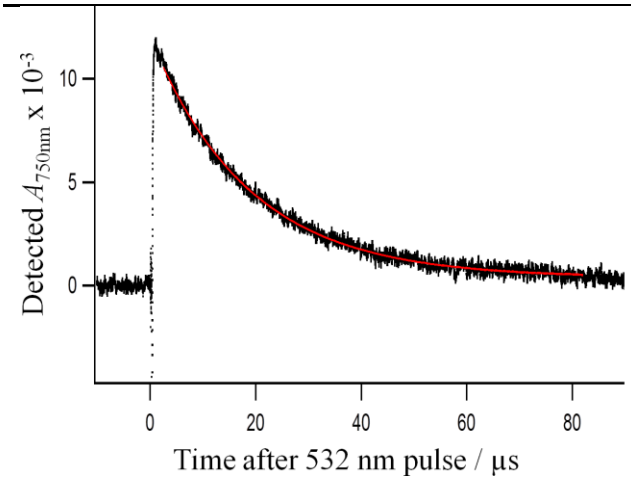
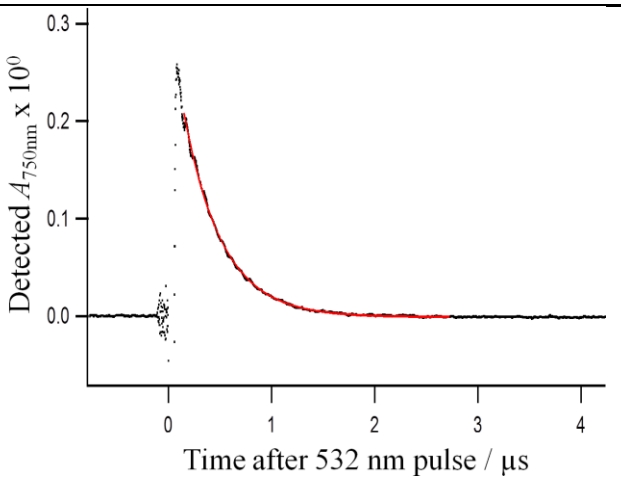
	Degassed sample	**Ambient sample**
		
C	$0.000389 \pm 3.27 \times 10^{-6}$	$-0.000961 \pm 7.11 \times 10^{-5}$
$\mathbf{A^0_{750nm}}$	$0.0117 \pm 7.77 \times 10^{-6}$	$0.315 \pm 5.68 \times 10^{-4}$
$\boldsymbol{\tau^{-1}}$	$0.0538\ \mathrm{ns}^{-1} \pm 7.52 \times 10^{-5}$	$2.712\ \mathrm{ns}^{-1} \pm 5.8 \times 10^{-3}$
$\boldsymbol{\tau}$	$\mathbf{18.6}$ µs	$\mathbf{0.37}$ µs
$[\,^3\mathbf{O_2}]$	$\mathbf{2.92 \times 10^{-5}}$ M	$\mathbf{1.69 \times 10^{-3}}$ M

Table 6.2 Parameters extracted from the equation $A^{t}_{750nm} = A^{0}_{750nm} \cdot e^{(-\tau^{-1} \cdot t)} + C$ fitted to the flash photolysis experiment designed to measure the lifetime (τ) of $T_1^{(triplet)}$ in both ambient and degassed samples. Coefficient values ± one standard deviation.

The N@C_{60} decomposition rates in both ambient and degassed samples fit well to a mono-exponential decay profile (see Figure 6.6), in agreement with previous reports.[52] Since the decay measurements were made *in situ*, the measurement error associated with the position of the sample inside of the mw cavity was removed, permitting a quantitative comparison between the decay rates of the two samples to be made (see Table 6.3).

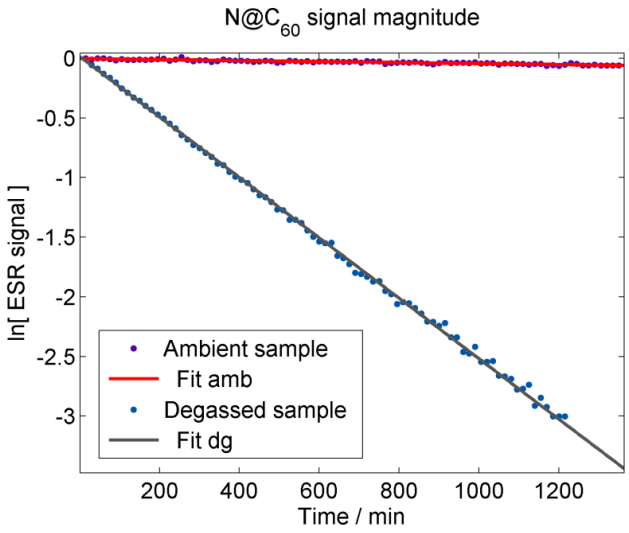


Figure 6.6 Plot of the natural log of the peak to peak ESR signal height of N@C_{60} hyperfine line while irradiated with 637 nm laser light. The fitted function for used was $f(t) = a \cdot t$.

The effect of degassing the solution increases the photosensitivity of N@C_{60} by a factor of 57 from a mean lifetime of 16 days in the ambient sample to only 6.6 hours when degassed. I will assume that the rate of exchange of N@C_{60} molecules in the laser beam path is short compared to the time required for a molecule to be excited a sufficient number of times to decay. Hence the following expression can be used to calculate the average number of excitations (N) that are required to induce the decay of an N@C_{60} molecule and (τ_d) is the mean lifetime of an N@C_{60} molecule taken from Table 6.3:

$$N = \frac{\#photons\ absorbed\ per\ second(\pm 20\ \%)\ \times 60 \times \tau_d}{total\ \#\ molecules\ in\ sample}$$

This equation calculates that in the ambient sample each N@C_{60} molecule must be on average excited 6.1 ± 1.3 x 10^4 times to induce decay. However, when the sample is degassed only 1.1 ± 0.27 x 10^3 excitations are required. Comparisons of the UV-Vis profiles of both samples are identical to pristine C_{60}

commensurate with photo-physical decay mechanism rather than photochemical mechanisms (see Figure 6.7).

f(t) = a*t	Degassed sample	Ambient sample
Coefficient (a)	-0.002509	$-4.4e^{-5}$
95 % confidence bounds	-0.002518, -0.0025	$-4.57e^{-5}$, $-4.23e^{-5}$
τ_d (min)	398±2	22727±920
SSE	0.06882	0.003667
R-square	0.9989	0.8579
Adjusted R-square	0.9989	0.8579
RMSE	0.02933	0.006419

Table 6.2 Fitting parameters for the decay profile of N@C_{60} signal while illuminated by 637 nm laser light. τ_d is the mean lifetime of an N@C_{60} molecule.

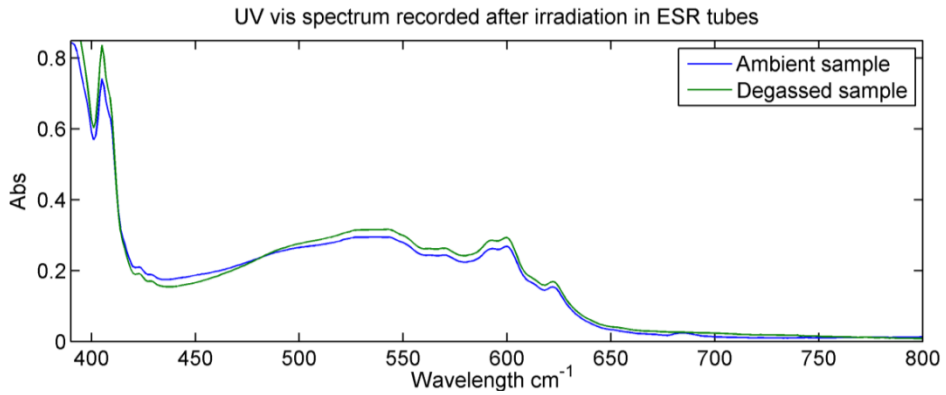


Figure 6.7 UV-Vis spectrum recorded from both the ambient and degassed samples after irradiation. Both spectra are identical to that of pristine C_{60}, suggesting that no photochemical reactions have taken place.

The favoured photo-physical process to cause the decay is via thermal excitation of the molecule resulting from relaxation of $T_1^{(triplet)} \longrightarrow S_0$ via a radiationless relaxation mechanism.[51] By using the calculated $[\,^3O_2]$ for each of the samples together with an assumption of the rate constant for non-radiative relaxation of N@C_{60} ($k_{NR}^{N@C_{60}}$) it is possible to estimate the quantum yield of non-radiative relaxation (ϕ_{NR}) for N@C_{60}. It has recently been reported that the intrinsic lifetime of the $T_1^{(triplet)}$ excited state of N@C_{60} is significantly shorter than that of C_{60} at 2.3 µs[15] compared to 142 µs.[44, 209] The cause of this is ascribed to an enhancement of non-radiative relaxation, mediated by an interaction between the nitrogen and fullerene cage.[15] I have therefore calculated ϕ_{NR} using two different assumptions: firstly, that N@C_{60} has the same k_{NR} as C_{60} and therefore assume that the nitrogen atom

does not significantly enhance the rate of non-radiative relaxation and secondly, that N@C_{60} has an intrinsic $T_1^{(triplet)}$ lifetime that is dominated by k_{NR}.

1) $\boldsymbol{k_{NR}^{N@C_{60}} = k_{NR}^{C_{60}} = 7000\ s^{-1}}$

For degassed sample: $\phi_{NR}^{N@C_{60}} = \frac{k_{NR}^{N@C_{60}}}{k_{NR}^{N@C_{60}} + k_p + k_q[\,^3O_2])} = \frac{7000}{7000+0+1.6\times10^9\cdot2.92\times10^{-5}} = 0.13 \pm 0.025$

For ambient sample: $\phi_{NR}^{N@C_{60}} = \frac{k_{NR}^{N@C_{60}}}{k_{NR}^{N@C_{60}} + k_p + k_q[\,^3O_2])} = \frac{7000}{7000+0+1.6\times10^9\cdot1.69\times10^{-3}} = 0.0026 \pm 0.0006$

By assuming that $k_{NR}^{N@C_{60}} = k_{NR}^{C_{60}}$ the ratio of the quantum yield for non-radiative relaxation between the degassed and ambient samples becomes identical to the ratio of T_1 lifetimes measured in the flash photolysis experiment. This leads to a 50-fold reduction of $\phi_{NR}^{N@C_{60}}$ from 0.13 ± 0.025 in the degassed sample to 0.0026 ± 0.0006 in the ambient sample. By taking the product of each $\phi_{NR}^{N@C_{60}}$ value with the average number of excitation that an N@C_{60} molecule must undergo to decompose *N*, the mean number of times a molecule must relax via a non-radiative mechanism to decompose is 139 ± 73 and 158 ± 79 for the degassed and ambient samples, respectively. There is less than a 14 % difference between the two values, with both values lying well within each of the other's calculated error bounds. This is consistent with the number of non-radiative de-excitations required cause a decay of N@C_{60} to be a constant and independent of $[\,^3O_2]$ and is what would be expected if the decomposition mechanism occurs via the thermal excitation of N@C_{60} resulting from non-radiative relaxation of the $T_1^{(triplet)}$ state.

2) $\boldsymbol{k_{NR}^{N@C_{60}} \neq k_{NR}^{C_{60}}, k_{NR}^{N@C_{60}} = 4.4 \pm 0.44 \times 10^5 s^{-1}}$

For degassed sample: $\phi_{NR}^{N@C_{60}} = \frac{k_{NR}^{N@C_{60}}}{k_{NR}^{N@C_{60}} + k_p + k_q[\,^3O_2])} = \frac{4.4\times10^5}{4.4\times10^5+0+1.6\times10^9\cdot2.92\times10^{-5}} = 0.90 \pm 0.02$

For ambient sample: $\phi_{NR}^{N@C_{60}} = \frac{k_{NR}^{N@C_{60}}}{k_{NR}^{N@C_{60}} + k_p + k_q[\,^3O_2])} = \frac{4.4\times10^5}{4.4\times10^5+0+1.6\times10^9\cdot1.69\times10^{-3}} = 0.14 \pm 0.026$

If $k_{NR}^{N@C_{60}} \neq k_{NR}^{C_{60}}$ and instead is approximated as the inverse of the reported $T_1^{(triplet)}$ lifetime of 2.3 µs then $k_{NR}^{N@C_{60}} = 4.4 \times 10^5 s^{-1}$. This leads to only a 6.4-fold reduction of $\phi_{NR}^{N@C_{60}}$ from 0.9 ± 0.02 in the degassed sample to 0.14 ± 0.026 in the ambient sample. This gives rise to the average number of times a molecule must relax via a non-radiative mechanism to decompose to be 960 ± 300 and 8500 ± 3800 for the degassed and ambient samples, respectively. The difference between these values falls well outside of the calculated error bounds for each of the values, with a minimum ratio of 7.3:1 for degassed to ambient conditions. It is difficult to see how this difference could be reconciled by a decay mechanism that occurs via the thermal excitation caused by non-radiative relaxation of $T_1^{(triplet)}$.

6.4 Discussion

The UV (≥254nm) photostability of N@C_{60} does indeed depend on the solvent used. It is suggested that this dependence is due to a change in the dominant decay mechanism of N@C_{60} from a photo-physical ^{3}{N@C_{60}} relaxation process to a photochemical radical polymerisation process initiated by photoexcitation of the solvent molecules. The radical mechanism appears significant in aromatic solvents that such as toluene and o-xylene where rapid decomposition of N@C_{60} is observed along with minimal rate dependence on [O_2]. In decalin however, the ^{3}{N@C_{60}} process appears dominant giving rise to an increased photostability of N@C_{60} and a significant [O_2] dependence. The conclusion of this study is that the most suitable solvent to use in future UV photo-physical experiments is Decalin as it provides N@C_{60} with the highest resistance to photodecomposition in both degassed and ambient environments.

The irradiation of a solution of N@C_{60} in decalin with 637 nm laser light is shown to cause the decay of the CW ESR signal. The effect of oxygen on this process is marked, with a retardation of 57-fold when an ambient oxygen concentration is present. If one assumes that the intrinsic $T_1^{(triplet)}$ lifetime is similar for both N@C_{60} and C_{60}, then the change in the decay rate of N@C_{60} correlates with the ratio of

the $\phi_{NR}^{N@C_{60}}$ between the degassed and ambient samples, suggesting that decomposition is occurring via local heating caused by $T_1^{(triplet)} \xrightarrow{NR} S_0$ as previously suggested.[51]

The instability of N@C_{60} to 637 nm lasers light adds significant complication to the design of any experimental set-up that would utilise an NV^- centre to optically probe the spin state of a single N@C_{60} molecule. This study shows that the average number of excitations for a single N@C_{60} molecule to decompose was only 1.1 ± 0.27 x 10^3 and 6.1 ± 1.3 x 10^4 excitations for the degassed and ambient samples, respectively. These numbers extrapolate to a life time of N@C_{60} of the order of 1 ms when subjected to the high photon fluxes used in NV^- ODMR experimental set-ups.[212] The requirement that N@C_{60} be only a few nanometres from the NV^- centre to observe any dipolar coupling makes selectively exciting the NV^- centre unfeasible. One possible approach would be to effectively remove the $T_1^{(triplet)} \xrightarrow{NR} S_0$ process from the decay pathway of N@C_{60} by using a solid state quencher of the $T_1^{(triplet)}$ state that is comparable to the efficiency of $^3O_2$ but permits a far higher concentration to dissolved $^3O_2$. Due to the large incident photon flux, the quencher would also need to be able to transport the energy of the excited state away from the N@C_{60} centre to avoid local heating. If the decomposition does indeed take place via the thermal excitation of the molecule then conducting the experiment at low temperature could also enhance the photostability of N@C_{60} by increasing the rate of thermal dissipation. The effect of temperature could be tested for by measuring the rate of photodecomposition as a function of temperature using a CW ESR spectrometer equipped with a cryostat.

Chapter 7 Conclusions and future outlook

7.1 Conclusions

In this thesis I have investigated both the chemical and physical properties of $N@C_{60}$ to further the assessment of $N@C_{60}$ as a qubit building block of an electron spin based quantum computing architecture.

In Chapter 3, I demonstrated that the frozen matrix electron spin environment in $N@C_{60}$-C_{60} Dimer-3bz and Dimer-5bz molecules are very similar, concluding that increasing the length of a rigid spacer or π system has negligible effect on the spin centre. The slightly smaller fitted axial ZFS parameter of between 14.19-14.25MHz could indicate that the geometry of the pyrrolidine group differs. This slightly smaller D parameter was also found in the $N@C_{60}$(py) compound of Chapter 5 and the recently reported $^{15}N@C_{60}$-C_{60} dimer[29] (Figure 1.9.g) making it unlikely that it is due to a measurement error.

The ESR spectrum arising from a two-spin centre $N@C_{60}$-$N@C_{60}$ molecule suggests that the presence of two $N@C_{60}$ functionalized molecules in close proximity to one another does not significantly affect the stability of the endohedral nitrogen species. This is a fundamental requirement for the successful implementation of $N@C_{60}$ as a quantum logic element. The ability for the spin Hamiltonian for the centre $N@C_{60}$-$N@C_{60}$ molecule to be approximated to a simple point dipole-dipole interaction will aid theorists when constructing models to describe larger arrays of coupled $N@C_{60}$ molecules. Since this reaction is compatible with microgram quantities, the way is open for further chemical functionalization of high purity $N@C_{60}$. This method can be used to create two-spin centre $N@C_{60}$ molecules with the required narrow coupling strength distribution to allow $N@C_{60}$ to be exploited for quantum information processing applications.

In Chapter 4, I have shown that polystyrene offers a suitable polymer host matrix for N@C_{60} and N@C_{60}-C_{60}, permitting both uniform dispersion of the magnetic molecules and, when the polystyrene is deuterated, long phase memory times of up to 21 μs. Previous experimental studies have shown that candidate two-qubit molecules exhibit a coupling of about 2.7 MHz.[137] Theoretical studies offer an estimate of the time needed to implement an entanglement-forming CNOT gate between the qubits of about 11 μs[27], which is substantially shorter than our measured phase memory time for ^{15}N@C_{60}-Dimer-3bzo in D-ps of 21 μs. I therefore conclude that using a polymer matrix should preserve a sufficiently long phase coherence lifetime in covalently linked N@C_{60} arrays to perform simple entanglement operations.

The alignment of the rigid molecule Ald-5bz using a silicone liquid crystal elastomer proved successful, producing a Herman's orientation parameter of 0.55, close to that measured in the host Si-LCE of 0.65. The alignment of fullerene dimer molecules however is much poorer. The resulting P_2 and P_4 order parameters for the 'pentagon pinch' mode at 1465 cm^{-1} of 0.01 and 0.28 are difficult to interpret due to the rotational freedom of the fullerene cage about the OPV bridging unit and the unknown axis of the principal polarisability component. The qualitative conclusion that can be drawn is that the degree of alignment of the Dimer-3bzo molecules is most likely significantly lower than found for Ald-5bz. The results of the instantaneous diffusion experiment using a Si-LCE composite containing N@C_{60} Dimer-3bzo suggest that a clustering of the fullerene component is occurring. This clustering is likely to represent the cause of the suppression of T_2 to a maximum of 1.4 μs at 40 K. This poor dispersion would also reduce any ordering effect of the Si-LCE matrix of the fullerene dimer molecules. The conclusion of this study is that Si-LCE is not a suitable matrix to impart alignment on fullerene dimer molecules such as Dimer-3bzo.

In Chapter 5, the characterisation of weakly paramagnetic complex C_{60}(py)-Cr_7Co was found to be incompatible with mass spectroscopy. ^{1}H NMR proved more instructive, showing a shift of the pivalate resonances of the Cr_7Co ring supporting that complexation has occurred. The splitting of three of the

pivalate resonances could suggest that the fullerene cage is predominantly situated over the centre of the ring, causing the restricted rotation of the three axial pivalate *t*-Bu groups. To provide further evidence for the complex, I suggest that using a deuterated Cr_7Co molecular ring could permit the fullerene resonances to be separated from the molecular magnet and assigned.[191]

At 90 K the N@C_{60} ESR transitions in the N@C_{60}(py)-Cr_7Ni appear magnetically 'disconnected' from the ring, producing an CW ESR spectrum almost identical to that of the uncomplexed N@C_{60}(py) molecule. At 2.75 K however, when the Cr_7Ni ring is almost entirely in its $S_{1/2}$ ground state, the addition of a 17 MHz J_{dip} dipolar coupling interaction can be inferred by modelling the observed perturbation to the N@C_{60} ESR spectral distribution. In its uncomplexed state, the T_m of the pyridine functionalised N@C_{60}(py) molecule shows a weakly negative temperature dependence typical of endohedral fullerenes,[196] decreasing from 24 μs at 60 K to 9 μs at 2.5 K. In the N@C_{60}(py)-Cr_7Ni complex however at temperatures above 10 K only the small fraction of free N@C_{60}(py) in the sample contributes to the Hahn echo decay profile in the g = 2 region, resulting in T_m values approximately 2/3 of that measured for the uncomplexed N@C_{60}(py) sample. On further cooling the T_m reduces with temperature to a minimum of 1.75 μs at 5 K. Below 5 K, the onset of a coherent ground state takes place and T_m rapidly increases to around 9 μs at 2.5 K, in line with that of the uncomplexed N@C_{60}(py) sample. This proves that it is possible form a two spin centre array containing N@C_{60} without adversely affecting the phase memory time of N@C_{60}. This is a key requirement of any future QIP architecture that relies on creating entangled arrays using the dipolar coupling interactions between N@C_{60} and other hetero electron spin based qubits.

Chapter 6, I show that irradiation of N@C_{60} with 637 nm laser light causes decay of the ESR signal. The effect of oxygen on this process is marked, with a retardation of 57-fold when an ambient oxygen concentration is present. The change in decay rate of N@C_{60} correlates well to the ratio of the quantum yield of radiationless relaxation ($\phi_{NR}^{N@C_{60}}$) between the degassed and ambient samples if the intrinsic $T_1^{(triplet)}$ lifetime is similar for both N@C_{60} and C_{60}, suggesting that decomposition is occurring via local

heating caused by $T_1^{(triplet)} \xrightarrow{NR} S_0$. This result leads me to conclude that it is unlikely that a scheme that optically detects the spin state of a N@C_{60} molecule by coupling it to an NV^- centre will be achievable owing to the propensity for N@C_{60} to photodegrade.

The UV (≥254nm) photostability of N@C_{60} is found to depend on the solvent used. It is proposed that this dependence is due to a change in the dominant decay mechanism of N@C_{60} from a ^{3}{N@C_{60}} relaxation process to a radical polymerisation process initiated by photoexcitation of the solvent molecules. The radical mechanism is dominant in aromatic solvents such as Toluene and o-Xylene where rapid decomposition of N@C_{60} is observed along with minimal rate dependence on [O_2]. In Decalin however, the ^{3}{N@C_{60}} process is dominant giving rise to an increased photostability of N@C_{60} and a significant [O_2] dependence. The conclusion of this study is that the most suitable solvent to use in future UV photo-physical experiments is Decalin as it provides N@C_{60} with the highest resistance to photodecomposition in both degassed and ambient environments.

7.2 Future focus

The ability to form two-spin centre arrays containing N@C_{60} has now been shown with isotropic distribution of coupling parameters measured. The next goal is to control the coupling distribution by aligning the inter electron spin axis with the applied magnetic field. The holy grail would be to synthesise a single crystal containing these two-spin centre molecules. This however is non-trivial as the inclusion of solubilising groups such as aliphatic chains into the molecule reduced the propensity for crystallisation to occur. This apparent mismatch could be tackled by careful selection of solubilising groups that have controlled degrees of freedom such as *t*-Bu groups. Another approach could be to use a co-crystallising agent such as a porphyrin or Phthalocyanine. Co-crystallisation with macromolecules has been shown to work well for single N@C_{60} molecules, with the single channels formed within the crystal suggested as a potential intercalation site for N@C_{60}-N@C_{60} molecules.[22] The use of a uniaxial strained polymer can theoretically provide sufficiently long phase coherence lifetime required to

perform entanglement operations between N@C_{60} spin centres. The challenge now stands to identify a suitably orientable polymer system that permits the homogenous dispersion of N@C_{60} molecules. This could also be accomplished by incorporating liquid crystalline groups into the dimer molecule, promoting both alignment and dispersion within a polymer matrix.

The ability to link N@C_{60} to an antiferromagnetic metallic ring opens up the exciting possibility to create multi-spin centre arrays containing hetero spin centres. Experiments that might be envisioned are the transfer of coherence from the ring to N@C_{60} and probing the effect of the magnetic field on the relaxation of N@C_{60} to interrogate the magnetic dynamics of the molecular magnet ring. The fact that in the complexed state the phase coherence lifetime of N@C_{60} is around an order of magnitude larger than that of the molecular magnetic (measured to be 600ns) at 2.75 K suggests that there is potential of using either the electron or nuclear spin of an N@C_{60} centre as a quantum memory for an antiferromagnetic magnet qubit array.

References

1. A. M. Turing, *Proc. Lond. Math. Soc.*, 1937, **s2-42**, 230-265.
2. C. Pettey and R. v. d. Meulen, *Gartner's 2012 Hype Cycle for Emerging Technologies Identifies "Tipping Point" Technologies That Will Unlock Long-Awaited Technology Scenarios*, http://www.gartner.com/newsroom/id/2124315, Accessed 29/05/2013, 2013.
3. D. Deutsch, *Proc. R. Soc. London. A*, 1985, **400**, 97-117.
4. P. W. Shor, Foundations of Computer Science, 1994 Proceedings., 35th Annual Symposium on, 1994.
5. L. M. K. Vandersypen, M. Steffen, G. Breyta, C. S. Yannoni, M. H. Sherwood and I. L. Chuang, *Nature*, 2001, **414**, 883-887.
6. C. Lu, Yang, D. E. Browne, T. Yang and J.-W. Pan, *Phys. Rev. Lett.*, 2007, **99**, 250504.
7. E. Lucero, R. Barends, Y. Chen, J. Kelly, M. Mariantoni, A. Megrant, P. O'Malley, D. Sank, A. Vainsencher, J. Wenner, T. White, Y. Yin, A. N. Cleland and J. M. Martinis, *Nat. Phys.*, 2012, **8**, 719-723.
8. E. Martin-Lopez, A. Laing, T. Lawson, R. Alvarez, X. Zhou, Qi and J. L. O'Brien, *Nat. Photon*, 2012, **6**, 773-776.
9. N. Xu, J. Zhu, D. Lu, X. Zhou, X. Peng and J. Du, *Phys. Rev. Lett.*, 2012, **108**, 130501.
10. S. Jordan, *Quantum Algorithm Zoo*, http://math.nist.gov/quantum/zoo/, Accessed 29/05/2013, 2013.
11. L. K. Grover, *Proceedings, 28th Annual ACM Symposium on the Theory of Computing* 1996, 212.
12. T. Van der Sar, Z. H. Wang, M. S. Blok, H. Bernien, T. H. Taminiau, D. M. Toyli, D. A. Lidar, D. D. Awschalom, R. Hanson and V. V. Dobrovitski, *Nature*, 2012, **484**, 82-86.
13. R. P. Feynman, *Int. J. Theor. Phys.*, 1982, **21**, 467-488.
14. A. Aspuru-Guzik, A. D. Dutoi, P. J. Love and M. Head-Gordon, *Science*, 2005, **309**, 1704-1707.
15. D. P. DiVincenzo, *arXiv*, 2000, arXiv:quant-ph/0002077.
16. W. Harneit, *Phys. Rev. A*, 2002, **65**, 032322.
17. A. Schweiger and G. Jeschke, *Principles of Pulsed Electron Paramagnetic Resonance* Oxford University Press, Oxford, 2001.
18. J. J. L. Morton, A. M. Tyryshkin, A. Ardavan, K. Porfyrakis, S. A. Lyon and G. A. D. Briggs, *Phys. Rev. Lett.*, 2005, **95**, 200501.
19. R. M. Brown, A. M. Tyryshkin, K. Porfyrakis, E. M. Gauger, B. W. Lovett, A. Ardavan, S. A. Lyon, G. A. D. Briggs and J. J. L. Morton, *Phys. Rev. Lett.*, 2011, **106**, 110504.
20. W. Scherer and M. Mehring, *J. Chem. Phys.*, 2008, **128**, 052305-052311.
21. F. Simon, H. Kuzmany, H. Rauf, T. Pichler, J. Bernardi, H. Peterlik, L. Korecz, F. Fülöp and A. Jánossy, *Chem. Phys. Lett.*, 2004, **383**, 362-367.
22. B. Naydenov, C. Spudat, W. Harneit, H. I. Süss, J. Hulliger, J. Nuss and M. Jansen, *Chem. Phys. Lett.*, 2006, **424**, 327-332.
23. J. Yang, P. Feng, A. Sygula, W. Harneit, J.-H. Su and J. Du, *Phys. Lett. A*, 2012, **376**, 1748-1751.
24. C. B. Simon, A. Ardavan, G. A. D. Briggs, D. A. Britz, D. Gunlycke, J. Jefferson, M. A. G. Jones, D. F. Leigh, B. W. Lovett, A. N. Khlobystov, S. A. Lyon, J. J. L. Morton, K. Porfyrakis, M. R. Sambrook and A. M. Tyryshkin, *J. Phys.*, 2006, **18**, S867.
25. E. Suhovoy and A. Blank, *Isr. J. Chem.*, 2008, **48**, 45-51.
26. J. E. Grose, E. S. Tam, C. Timm, M. Scheloske, B. Ulgut, J. J. Parks, H. D. Abruna, W. Harneit and D. C. Ralph, *Nat. Mater.*, 2008, **7**, 884-889.
27. C. Ju, D. Suter and J. Du, *Phys. Rev. A*, 2007, **75**, 012318.
28. W. Harneit, M. Waiblinger, K. Lips, S. Makarov and A. Weidinger, *AIP Conf. Proc.*, 2000, **544**, 207-210.

29. S. Plant, M. Jevric, J. Morton, A. Ardavan, A. N. Khlobystov, G. A. D. Briggs and K. Porfyrakis, *Chem. Sci.*, 2013, **4**, 2971-2975.
30. M. Saunders, H. A. Jiménez-Vázquez, R. J. Cross and R. J. Poreda, *Science*, 1993, **259**, 1428-1430.
31. M. Saunders, R. J. Cross, H. A. Jiménez-Vázquez, R. Shimshi and A. Khong, *Science*, 1996, **271**, 1693-1697.
32. T. Almeida Murphy, T. Pawlik, A. Weidinger, M. Hohne, R. Alcala and J. M. Spaeth, *Phys. Rev. Letts.*, 1996, **77**, 1075.
33. A. Weidinger, M. Waiblinger, B. Pietzak and M. T. Almeida, *Appl. Phys. A: Mater. Sci. Process.*, 1998, **66**, 287-292.
34. B. Pietzak, M. Waiblinger, T. A. Murphy, A. Weidinger, M. Höhne, E. Dietel and A. Hirsch, *Chem. Phys. Lett.*, 1997, **279**, 259-263.
35. S. Ito, H. Shimotani, H. Takagi and N. Dragoe, *Fullerenes, Nanotubes, Carbon Nanostruct.*, 2008, **16**, 206-213.
36. H. Huang, M. Ata and M. Ramm, *Chem. Commun.*, 2002, 2076-2077.
37. M. Ata, H. Huang and T. Akasaka, *J. Phys. Chem. B*, 2004, **108**, 4640-4646.
38. N. Takahashi, H. Dock, N. Matsuzawa and M. Ata, *J. Appl. Phys.*, 1993, **74**, 5790-5798.
39. S. Abe, G. Sato, T. Kaneko, T. Hirata, R. Hatakeyama, K. Yokoo, S. Ono, K. Omote and Y. Kasama, *Jpn. J. Appl. Phys., Part 1*, 2006, **45**, 8340-8343.
40. T. Kaneko, S. Abe, H. Ishida and R. Hatakeyama, *Phys. Plasmas*, 2007, **14**, 1107051-1107053.
41. T. Suetsuna, N. Dragoe, W. Harneit, A. Weidinger, H. Shimotani, S. Ito, H. Takagi and K. Kitazawa, *Chem. Eur. J*, 2003, **9**, 598.
42. M. Kanai, K. Porfyrakis, G. A. D. Briggs and T. J. S. Dennis, *Chem. Commun.*, 2004, 210-211.
43. P. Jakes, K.-P. Dinse, C. Meyer, W. Harneit and A. Weidinger, *Phys. Chem. Chem. Phys.*, 2003, **5**, 4080-4083.
44. H. Nikawa, Y. Araki, Z. Slanina, T. Tsuchiya, T. Akasaka, T. Wada, O. Ito, K.-P. Dinse, M. Ata, T. Kato and S. Nagase, *Chem. Commun.*, 2010, **46**, 631-633.
45. A. Weidinger, M. Waiblinger, B. Pietzak and T. Murphy, Almeida., *Applied Physics A*, 1998, **66**, 287-292.
46. T. A. Murphy, T. Pawlik, A. Weidinger, M. Hohne, R. Alcala and J. M. Spaeth, *Phys. Rev. Lett.*, 1996, **77**, 1075.
47. J. J. L. Morton, A. M. Tyryshkin, A. Ardavan, K. Porfyrakis, S. A. Lyon and G. A. D. Briggs, *J. Chem. Phys.*, 2006, **124**, 014508/014501-014508/014505.
48. M. Waiblinger, B. Pietzak, K. Lips and A. Weidinger, *AIP Conf. Proc*, 1998, **442**, 388-391.
49. A. Iwasiewicz-Wabnig, K. Porfyrakis, G. A. D. Briggs and B. Sundqvist, *Phys. Status Solidi B*, 2009, **246**, 2767-2770.
50. M. Waiblinger, K. Lips, W. Harneit, A. Weidinger, E. Dietel and A. Hirsch, *Phys. Rev. B*, 2001, **63**, 045421/045421.
51. B. Goedde, N. Weiden and K. P. Dinse, *AIP Conference Proceedings*, 1999, **486**, 144-147.
52. G. Liu, A. N. Khlobystov, A. Ardavan, G. A. D. Briggs and K. Porfyrakis, *Chem. Phys. Lett.*, 2011, **508**, 187-190.
53. E. Dietel, A. Hirsch, B. Pietzak, M. Waiblinger, K. Lips, A. Weidinger, A. Gruss and K.-P. Dinse, *J. Am. Chem. Soc.*, 1999, **121**, 2432-2437.
54. F. Hörmann, A. Hirsch, K. Porfyrakis and G. A. D. Briggs, *Eur. J. Org. Chem.*, 2011, **2011**, 117-121.
55. M. A. G. Jones, D. A. Britz, J. J. L. Morton, A. N. Khlobystov, K. Porfyrakis, A. Ardavan and G. A. D. Briggs, *Phys. Chem. Chem. Phys.*, 2006, **8**, 2083-2088.
56. M. Maggini, G. Scorrano and M. Prato, *J. Am. Chem. Soc.*, 1993, **115 (21)**, 9798-9799.
57. L. Franco, S. Ceola, C. Corvaja, S. Bolzonella, W. Harneit and M. Maggini, *Chem. Phys. Lett.*, 2006, **422**, 100-105.
58. J. Zhang, J. J. L. Morton, M. R. Sambrook, K. Porfyrakis, A. Ardavan and G. A. D. Briggs, *Chem. Phys. Lett.*, 2006, **432**, 523-527.

59. J. Zhang, K. Porfyrakis, J. J. L. Morton, M. R. Sambrook, J. Harmer, L. Xiao, A. Ardavan and G. A. D. Briggs, *J. Phys. Chem. C*, 2008, **112**, 2802-2804.
60. G. Liu, A. N. Khlobystov, G. Charalambidis, A. G. Coutsolelos, G. A. D. Briggs and K. Porfyrakis, *J. Am. Chem. Soc.*, 2012, **134**, 1938-1941.
61. B. Pietzak, M. Waiblinger, T. A. Murphy, A. Weidinger, M. Hohne, E. Dietel and A. Hirsch, *Carbon*, 1998, **36**, 613-615.
62. B. Goedde, M. Waiblinger, P. Jakes, N. Weiden, K. P. Dinse and A. Weidinger, *Chem. Phys. Lett.*, 2001, **334**, 12-17.
63. M. Waiblinger, K. Lips, W. Harneit, A. Weidinger, E. Dietel and A. Hirsch, *Phys. Rev. B*, 2001, **63**, 045421.
64. G. Liu, A. N. Khlobystov, G. A. D. Briggs and K. Porfyrakis, *Chem. Commun.*, 2012, **48**, 5148-5150.
65. K. Komatsu, G.-W. Wang, Y. Murata, T. Tanaka, K. Fujiwara, K. Yamamoto and M. Saunders, *J. Org. Chem.*, 1998, **63**, 9358-9366.
66. G. W. Wang, K. Komatsu, Y. Murata and M. Shiro, *Nature*, 1997, **387**, 583-586.
67. R. Taylor, M. P. Barrow and T. Drewello, *Chem. Commun.*, 1998, 2497-2498.
68. S. Lebedkin, S. Ballenweg, J. Gross, R. Taylor and W. Krätschmer, *Tetrahedron Lett.*, 1995, **36**, 4971-4974.
69. A. B. Smith, H. Tokuyama, R. M. Strongin, G. T. Furst, W. J. Romanow, B. T. Chait, U. A. Mirza and I. Haller, *J. Am. Chem. Soc.*, 1995, **117**, 9359-9360.
70. J. R. Morton, K. F. Preston, P. J. Krusic, S. A. Hill and E. Wasserman, *J. Am. Chem. Soc.*, 1992, **114**, 5454-5455.
71. J. C. Hummelen, C. Bellavia-Lund and F. Wudl, in *Fullerenes and Related Structures* ed. A. Hirsch, Springer Berlin Heidelberg, Berlin, Editon edn., 1999, pp. 93-134.
72. S. Ōsawa, E. Ōsawa and M. Harada, *J. Org. Chem.*, 1996, **61**, 257-265.
73. K. Komatsu, N. Takimoto, Y. Murata, T. S. M. Wan and T. Wong, *Tetrahedron Lett.*, 1996, **37**, 6153-6156.
74. P. Timmerman, H. L. Anderson, R. Faust, J. Nierengarten, T. Habicher, P. Seiler and F. Diederich, *Tetrahedron*, 1996, **52**, 4925-4947.
75. A. Sarkar, S. Okada, K. Komatsu, H. Nakanishi and H. Matsuda, *Macromolecules*, 1998, **31**, 5624-5630.
76. Y. Shirai, Y. Zhao, L. Cheng and J. M. Tour, *Organic Letts.*, 2004, **6**, 2129-2132.
77. Y. Zhao, Y. Shirai, A. D. Slepkov, L. Cheng, L. B. Alemany, T. Sasaki, F. A. Hegmann and J. M. Tour, *Chemistry - A European Journal*, 2005, **11**, 3643-3658.
78. K. Komatsu, Y. Murata, N. Takimoto, S. Mori, N. Sugita and T. S. M. Wan, *J. Org. Chem.*, 1994, **59**, 6101-6102.
79. N. Zhou, E. F. Merschrod S and Y. Zhao, *J. Am. Chem. Soc.*, 2005, **127**, 14154-14155.
80. N. Zhou and Y. Zhao, *J. Org. Chem.*, 2010, **75**, 1498-1516.
81. N. Dragoe, S. Tanibayashi, K. Nakahara, S. Nakao, H. Shimotani, L. Xiao, K. Kitazawa, Y. Achiba, K. Kikuchi and K. Nojima, *Chem. Commun.*, 1999, 85-86.
82. T. S. Fabre, W. D. Treleaven, T. D. McCarley, C. L. Newton, R. M. Landry, M. C. Saraiva and R. M. Strongin, *J. Org. Chem*, 1998, **63**, 3522-3523.
83. F. Diederich, L. Isaacs and D. Philp, *Chem. Soc. Rev.*, 1994, **23**, 243-255.
84. T. Suzuki, Q. Li, K. C. Khemani, F. Wudl and O. Almarsson, *J. Am. Chem. Soc.*, 1992, **114**, 7300-7301.
85. J. Knol and J. C. Hummelen, *J. Am. Chem. Soc.*, 2000, **122**, 3226-3227.
86. F. Djojo, A. Herzog, I. Lamparth, F. Hampel and A. Hirsch, *Chem. Euro. J*, 1996, **2**, 1537-1547.
87. T. Habicher, J. F. Nierengarten, V. Gramlich and F. Diederich, *Ang. Chem. Int. Ed.*, 1998, **37**, 1916-1919.
88. Y. Z. An, Y. Rubin, C. Schaller and S. W. McElvany, *J. Org. Chem.*, 1994, **59**, 2927-2929.
89. H. L. Anderson, R. Faust, Y. Rubin and F. Diederich, *Ang. Chem. Int. Ed.*, 1994, **33**, 1366-1368.

90. F. Giacalone, J. L. Segura and N. Martín, *J. Org. Chem.*, 2002, **67**, 3529-3532.
91. R. Gomez, J. L. Segura and N. Martin, *Chem. Commun.*, 1999, 619-620.
92. A. I. De Lucas, N. Martín, L. Sánchez and C. Seoane, *Tetrahedron Lett.*, 1996, **37**, 9391-9394.
93. Y. Sun, T. Drovetskaya, R. D. Bolskar, R. Bau, P. D. W. Boyd and C. A. Reed, *The Journal of Organic Chemistry*, 1997, **62**, 3642-3649.
94. P. D. W. Boyd, P. Bhyrappa, P. Paul, J. Stinchcombe, R. Bolskar, Y. Sun and C. A. Reed, *J. Am. Chem. Soc.*, 1995, **117**, 2907-2914.
95. S. Higashida, H. Imahori, T. Kaneda and Y. Sakata, *Chem. Lett.*, 1998, **27**, 605-606.
96. J. L. Segura, N. Martín and M. Hanack, *Eur. J. Org. Chem*, 1999, **1999**, 643-651.
97. L. Echegoyen and L. E. Echegoyen, *Acc. Chem. Res.*, 1998, **31**, 593-601.
98. P. A. van Hal, J. Knol, B. M. W. Langeveld-Voss, S. C. J. Meskers, J. C. Hummelen and R. A. J. Janssen, *J. Phys. Chem. A*, 2000, **104**, 5974-5988.
99. A. Dhanabalan, J. Knol, J. C. Hummelen and R. A. J. Janssen, *Synth. Mets.*, 2001, **119**, 519-522.
100. E. H. A. Beckers, P. A. van Hal, A. Dhanabalan, S. C. J. Meskers, J. Knol, J. C. Hummelen and R. A. J. Janssen, *J. Phys. Chem. A*, 2003, **107**, 6218-6224.
101. D. M. Guldi, C. Luo, A. Swartz, R. Gómez, J. L. Segura and N. Martín, *J. Phys. Chem. A*, 2003, **108**, 455-467.
102. W. Ten Hoeve, H. Wynberg, E. E. Havinga and E. W. Meijer, *J. Am. Chem. Soc.*, 1991, **113**, 5887-5889.
103. J. Segura and N. Martín, *Tetrahedron Lett.*, 1999, **40**, 3239-3242.
104. C. Atienza, B. Insuasty, C. Seoane, N. Martin, J. Ramey, G. M. A. Rahman and D. M. Guldi, *J. Mat. Chem.*, 2005, **15**, 124-132.
105. J. Delgado, E. Espíldora, M. Liedtke, A. Sperlich, D. Rauh, A. Baumann, C. Deibel, V. Dyakonov and N. Martín, *Chem. Eur. J*, 2009, **15**, 13474-13482.
106. J. L. Delgado, F. o. Cardinali, E. Espíldora, M. R. Torres, F. Langa and N. Martín, *Organic Lett.*, 2008, **10**, 3705-3708.
107. J. L. Delgado, S. l. Osuna, P.-A. Bouit, R. Martínez-Alvarez, E. Espíldora, M. Solà and N. Martín, *J. Org. Chem*, 2009, **74**, 8174-8180.
108. H. Detert, D. Schollmeyer and E. Sugiono, *Eur. J. Org. Chem*, 2001, **2001**, 2927-2938.
109. M. J. Gómez-Escalonilla, F. Langa, J.-M. Rueff, L. Oswald and J.-F. Nierengarten, *Tetrahedron Lett.*, 2002, **43**, 7507-7511.
110. F. Langa, M. J. Gomez-Escalonilla, J. M. Rueff, T. M. F. Duarte, J. F. Nierengarten, V. Palermo, P. Samorì, Y. Rio, G. Accorsi and N. Armaroli, *Chem. Eur. J*, 2005, **11**, 4405-4415.
111. H. Irngatinger and A. Weber, *Tetrahedron Lett.*, 1996, **37**, 4137-4140.
112. H. Irngartinger, A. Weber, T. Escher, P. W. Fettel and F. Gassner, *Eur. J. Org. Chem.*, 1999, 2087-2092.
113. P. Belik, A. Gügel, J. Spickermann and K. Müllen, *Ang. Chem. Int. Ed.*, 1993, **32**, 78-80.
114. M. P. Cava and D. R. Napier, *J. Am. Chem. Soc.*, 1957, **79**, 1701-1705.
115. A. Gügel, P. Belik, M. Walter, A. Kraus, E. Harth, M. Wagner, J. Spickermann and K. Müllen, *Tetrahedron*, 1996, **52**, 5007-5014.
116. L. A. Paquette and R. J. Graham, *J. Org. Chem.*, 1995, **60**, 2958-2959.
117. T. J. Hingston, M. R. Sambrook, K. Porfyrakis and G. A. D. Briggs, *Tetrahedron Lett.*, 2006, **47**, 7413-7415.
118. J. M. Lawson, A. M. Oliver, D. F. Rothenfluh, Y.-Z. An, G. A. Ellis, M. G. Ranasinghe, S. I. Khan, A. G. Franz, P. S. Ganapathi, M. J. Shephard, M. N. Paddon-Row and Y. Rubin, *J. Org. Chem.*, 1996, **61**, 5032-5054.
119. S. G. Liu, D. Kreher, P. Hudhomme, E. Levillain, M. Cariou, J. Delaunay, A. Gorgues, J. Vidal-Gancedo, J. Veciana and C. Rovira, *Tetrahedron Lett.*, 2001, **42**, 3717-3720.
120. Y. Murata, N. Kato, K. Fujiwara and K. Komatsu, *J. Org. Chem.*, 1999, **64**, 3483-3488.
121. K. Lee, H. Song, B. Kim, J. T. Park, S. Park and M.-G. Choi, *J. Am. Chem. Soc.*, 2002, **124**, 2872-2873.

122. B. K. Park, G. Lee, K. H. Kim, H. Kang, C. Y. Lee, M. A. Miah, J. Jung, Y.-K. Han and J. T. Park, *J. Am. Chem. Soc.*, 2006, **128**, 11160-11172.
123. P. Zanello, F. Fabrizi de Biani, A. Cinquantini and E. Grigiotti, *Comptes Rendus Chimie*, 2005, **8**, 1655-1659.
124. S. R. Plant, University of Oxford, 2010.
125. A. Werner, *Berichte der deutschen chemischen Gesellschaft*, 1908, **41**, 3447-3465.
126. R. D. Cannon and R. P. White, *Prog. Inorganic Chem.*, 1988, **36**, 195-298.
127. K. L. Taft and S. J. Lippard, *J. Am. Chem. Soc.*, 1990, **112**, 9629-9630.
128. Y. T. S. N. V. Gerbeleu, G. A. Timco and K. M. I. a. G. A. P. A. S. Batsanov, *Dokl. Akad. Nauk SSSR*, 1990, **313**, 1459.
129. F. K. Larsen, E. J. L. McInnes, H. El Mkami, J. Overgaard, S. Piligkos, G. Rajaraman, E. Rentschler, A. A. Smith, G. M. Smith, V. Boote, M. Jennings, G. A. Timco and R. E. P. Winpenny, *Ang. Chem. Int. Ed.*, 2003, **42**, 101-105.
130. G. A. Timco, E. J. L. McInnes and R. E. P. Winpenny, *Chem. Soc. Rev.*, 2013, **42**, 1796-1806.
131. F. Troiani, V. Bellini and M. Affronte, *Phys. Rev. B*, 2008, **77**, 054428.
132. G. A. Timco, T. B. Faust, F. Tuna and R. E. P. Winpenny, *Chem. Soc. Rev.*, 2011, **40**, 3067-3075.
133. G. A. Timco, S. Carretta, F. Troiani, F. Tuna, R. J. Pritchard, C. A. Muryn, E. J. L. McInnes, A. Ghirri, A. Candini, P. Santini, G. Amoretti, M. Affronte and R. E. P. Winpenny, *Nat. Nano.*, 2009, **4**, 173-178.
134. M. N. Leuenberger and D. Loss, *Nature*, 2001, **410**, 789-793.
135. R. Caciuffo, T. Guidi, G. Amoretti, S. Carretta, E. Liviotti, P. Santini, C. Mondelli, G. Timco, C. A. Muryn and R. E. P. Winpenny, *Phys. Rev. B*, 2005, **71**, 174407.
136. C. J. Wedge, G. A. Timco, E. T. Spielberg, R. E. George, F. Tuna, S. Rigby, E. J. L. McInnes, R. E. P. Winpenny, S. J. Blundell and A. Ardavan, *Phys. Rev. Lett.*, 2012, **108**, 107204.
137. A. Ardavan, O. Rival, J. J. L. Morton, S. J. Blundell, A. M. Tyryshkin, G. A. Timco and R. E. P. Winpenny, *Phys. Rev. Lett.*, 2007, **98**, 057201.
138. G. A. Timco, E. J. L. McInnes, R. G. Pritchard, F. Tuna and R. E. P. Winpenny, *Ang. Chem. Int. Ed.*, 2008, **47**, 9681-9684.
139. S. Piligkos, H. Weihe, E. Bill, F. Neese, H. El Mkami, G. M. Smith, D. Collison, G. Rajaraman, G. A. Timco, R. E. P. Winpenny and E. J. L. McInnes, *Chem. Eur. J*, 2009, **15**, 3152-3167.
140. C. M. Casadei, L. Bordonali, Y. Furukawa, F. Borsa, E. Garlatti, A. Lascialfari, S. Carretta, S. Sanna, G. Timco and R. Winpenny, *J. Phys.*, 2012, **24**, 406002.
141. M. H. Levitt, *Spin Dynamics: Basics of Nuclear Magnetic Resonance*, Wiley, 2008.
142. C. Meyer, W. Harneit, K. Lips, A. Weidinger, P. Jakes and K. P. Dinse, *Phys. Rev. A*, 2002, **65**, 0612011-0612014.
143. G. Liu, M. d. C. Gimenez-Lopez, M. Jevric, A. N. Khlobystov, G. A. D. Briggs and K. Porfyrakis, *J. Phys. Chem. B*, 2013, **117**, 5925-5931.
144. N. J. Stone, *Atomic Data and Nuclear Data Tables*, 2005, **90**, 75-176.
145. G. Jeschke, *Macromolecular Rapid Communications*, 2002, **23**, 227-246.
146. A. G. Maryasov, M. K. Bowman and Y. D. Tsvetkov, *Applied Magnetic Resonance*, 2006, **30**, 683-702.
147. S. Stoll and A. Schweiger, *J. Mag. Res.*, 2006, **178**, 42-55.
148. A. Ardavan, J. J. L. Morton, S. C. Benjamin, K. Porfyrakis, G. A. D. Briggs, A. M. Tyryshkin and S. A. Lyon, *Phys. Stat. Soli. b*, 2007, **244**, 3874-3878.
149. W. L. Yang, Z. Y. Xu, H. Wei, M. Feng and D. Suter, *Phys. Rev. A*, 2010, **81**, 032303.
150. J. J. L. Morton, A. M. Tyryshkin, A. Ardavan, S. C. Benjamin, K. Porfyrakis, S. A. Lyon and G. A. D. Briggs, *Nat. Phys.*, 2006, **2**, 40-43.
151. S. Simmons, R. M. Brown, H. Riemann, N. V. Abrosimov, P. Becker, H.-J. Pohl, M. L. W. Thewalt, K. M. Itoh and J. J. L. Morton, *Nature*, 2011, **470**, 69-72.
152. C. L. Stephenson and T. Vo-Dinh, in *Mordern Techniques in Raman Spectroscopy*, ed. J. J. Laserna, John Wiley and Sons Ltd, Chichester, Editon edn., 1996, p. 15.

153. W. Jeremy Jones, D. K. Thomas, D. W. Thomas and G. Williams, *J. Mol. Struc.*, 2004, **708**, 145-163.
154. D. A. Long, *Raman Spectroscopy*, McGraw-Hill International Book Company, c1977, London, 1977.
155. M. S. Park, Y. S. Wong, J. O. Park, S. S. Venkatraman and M. Srinivasarao, *Macromolecules*, 2011, **44**, 2120-2131.
156. G. Socrates, *Infrared and Raman Characteristic Group Frequency Tables and Charts*, 3rd edn., John Wiley & sons, 2001.
157. S. Kotsiris, Y. Vasil'ev, A. Streletskii, M. Han, L. Mark, O. Boltalina, N. Chronakis, M. Orfanopoulos, H. Hungerbühler and T. Drewello, *Eur. J. Mass. Spec.*, 2006, **12**, 397-408.
158. T. Parella, *2D COSY*, http://triton.iqfr.csic.es/guide/eNMR/eNMR2D/cosy.html, Accessed 14/05/2013, 2013.
159. T. Parella, *2D HSQC*, http://triton.iqfr.csic.es/guide/nmr/manual/18a_gehmqc.html#geHSQC, Accessed 14/05/2013, 2013.
160. T. Parella, *2D me-HSQC*, http://triton.iqfr.csic.es/guide/tutorials/2Dhet/inviedetgp.html, Accessed 14/05/2013, 2013.
161. J. Zhang, K. Porfyrakis, J. J. L. Morton, M. R. Sambrook, J. Harmer, L. Xiao, A. Ardavan and G. A. D. Briggs, *J. Phys. Chem. C*, 2008, **112**, 2802-2804.
162. J. L. Segura and N. Martin, *Chem. Soc. Rev.*, 2000, **29**, 13-25.
163. G. Socrates, in *Infrared and Raman Characteristic Group Frequency Tables and Charts*, ed. G. Soctrates, John Wiley & sons, Editon edn., 2001, p. 366.
164. D. W. Mayo, in *Course Notes on the Interpretation of Infrared and Raman Spectra*, ed. F. A. M. Dana W. Mayo, Robert W. Hannah John wiley & sons, Editon edn., 2004, pp. 107-130.
165. J. Menéndez and J. Page, in *Light Scattering in Solids VIII*, eds. M. Cardona and G. Güntherodt, Springer Berlin Heidelberg, Editon edn., 2000, vol. 76, pp. 27-95.
166. K. P. Dinse, *Phys. Chem. Chem. Phys.*, 2002, **4**, 5442-5447.
167. C. Ménard-Moyon, N. Izard, E. Doris and C. Mioskowski, *J. Am. Chem. Soc.*, 2006, **128**, 6552-6553.
168. B. J. Farrington, M. Jevric, G. A. Rance, A. Ardavan, A. N. Khlobystov, G. A. D. Briggs and K. Porfyrakis, *Ang. Chem. Int. Ed.*, 2012, **51**, 3587-3590.
169. P. Jakes, N. Weiden, R. A. Eichel, A. Gembus, K. P. Dinse, C. Meyer, W. Harneit and A. Weidinger, *J. Magn. Reson.*, 2002, **156**, 303-308.
170. B. Naydenov, C. Spudat, M. Scheloske, H. I. Suess, J. Hulliger and W. Harneit, *Phys. Stat. Soli. b*, 2006, **243**, 2995-2998.
171. J. Yang, P. Feng, A. Sygula, W. Harneit, J.-H. Su and J. Du, *Physics Letters A*, 2012, **376**, 1748-1751.
172. E. W. Thulstrup and J. Michl, *J. Am. Chem. Soc.*, 1982, **104**, 5594-5604.
173. H. L. Anderson, *Adv. Mater.*, 1994, **6**, 834-836.
174. W. Ren, P. J. McMullan and A. C. Griffin, *Macro. Chem. Phys.*, 2008, **209**, 1896-1899.
175. B. Luy, K. Kobzar and H. Kessler, *Ang. Chem. Int. Ed.*, 2004, **43**, 1092-1094.
176. J. C. Freudenberger, S. Knör, K. Kobzar, D. Heckmann, T. Paululat, H. Kessler and B. Luy, *Ang. Chem. Int. Ed.*, 2005, **44**, 423-426.
177. L. Jin, C. Bower and O. Zhou, *App. Phys. Lett.*, 1998, **73**, 1197-1199.
178. Z. Zheng, K.-H. Yim, M. S. M. Saifullah, M. E. Welland, R. H. Friend, J.-S. Kim and W. T. S. Huck, *Nano Letters*, 2007, **7**, 987-992.
179. A. Arbor, in *PhAT Sytems Operations Manual* Kaiser Optical Systems, Editon edn., 2004, p. 296.
180. S. Nomura, N. Nakamura and H. Kawai, *J. Pol. Sci. A*, 1971, **9**, 407-420.
181. H. Kuzmany, R. Pfeiffer, M. Hulman and C. Kramberger, *Phil. Trans. R. Soc. Lond. A*, 2004, **362**, 2375-2406.
182. W. Hoogsteen, A. R. Postema, A. J. Pennings, G. Ten Brinke and P. Zugenmaier, *Macromolecules*, 1990, **23**, 634-642.

183. J. R. Klauder and P. W. Anderson, *Phys. Rev.*, 1962, **125**, 912-932.
184. A. Schweiger and G. Jeschke, in *Principles of Pulsed Electron Paramagnetic Resonance* Oxford University Press, Oxford, Editon edn., 2001, p. 216.
185. R. Brown, DPhil, University of Oxford, 2011.
186. J. J. L. Morton, A. M. Tyryshkin, A. Ardavan, K. Porfyrakis, S. A. Lyon and G. A. D. Briggs, *Phys. Rev. B*, 2007, **76**, 085418/085411-085418/085416.
187. S. S. Eaton and G. R. Eaton, *Relaxation Times of Organic Radicals and Transition Metal Ions*, Springer-Verlag, Berlin, 2001.
188. I. M. Brown, in *Time Domain Electron Spin Resonance*, eds. L. Kevan and R. N. Schwartz, Wiley Interscience, New York, Editon edn., 1980.
189. B. Ma and Y.-P. Sun, *Journal of the Chemical Society, Perkin Transactions 2*, 1996, 2157-2162.
190. B. Shih, *Temperature-dependent Raman Spectroscopy of Fullerene and Carborane Nano Wheels*, https://docs.google.com/viewer?a=v&q=cache:RgTus0JzvlAJ:nanojapan.rice.edu/Downloads/2011%2520RQI/2011_Shih,Ben_TEMPERATURE-DEPENDENT%2520RAMAN%2520SPECTROSCOPY%2520OF%2520FULLERENE%2520AND%2520CARBORANE%2520NANOCAR%2520WHEELS.pdf+fullerene+raman&hl=en&gl=uk&pid=bl&srcid=ADGEESjQ_gEwC8tqtJWdQU6XtMm8vpzSVQLKmCLBYd3XgfCKuibbWgN-kqDCrjb4ZwvrycN7nOdn3DdMkjA4j3uA6hmP30Z_40KLRkaOpvo6NBnv3kI7wNM0QvWG1uj6j7d5O8S9APz6&sig=AHIEtbQyXgt9bcNWR6kcaHQtBe5Ui74VPw, Accessed 08/04/2013, 2013.
191. B. Ballesteros, T. B. Faust, C.-F. Lee, D. A. Leigh, C. A. Muryn, R. G. Pritchard, D. Schultz, S. J. Teat, G. A. Timco and R. E. P. Winpenny, *J. Am. Chem. Soc.*, 2010, **132**, 15435-15444.
192. E. C. Sañudo, T. B. Faust, C. A. Muryn, R. G. Pritchard, G. A. Timco and R. E. P. Winpenny, *Inorg. Chem.*, 2009, **48**, 9811-9818.
193. H. Esaki, N. Ito, S. Sakai, T. Maegawa, Y. Monguchi and H. Sajiki, *Tetrahedron*, 2006, **62**, 10954-10961.
194. M. F. Wyatt, *J. Mass Spec.*, 2011, **46**, 712-719.
195. C. A. Schalley and A. Springer, *Mass Spectrometry of Non-Covalent Complexes: Supramolecular Chemistry in the Gas Phase*, Wiley, 2009.
196. R. M. Brown, Y. Ito, J. H. Warner, A. Ardavan, H. Shinohara, G. A. D. Briggs and J. J. L. Morton, *Phys. Rev. B*, 2010, **82**, 033410.
197. P. Luehring and A. Schumpe, *J. Chem. Eng. Dat.*, 1989, **34**, 250-252.
198. M. Koyanagi and K. Uejoh, *J. Luminescence*, 1997, **72–74**, 511-512.
199. P. J. Krusic, E. Wasserman, P. N. Keizer, J. R. Morton and K. F. Preston, *Science*, 1991, **254**, 1183-1185.
200. F. Cataldo, *Pol. In.*, 1999, **48**, 143-149.
201. Y. P. Sun, B. Ma, C. E. Bunker and B. Liu, *J. Am. Chem. Soc.*, 1995, **117**, 12705-12711.
202. S. Leach, M. Vervloet, A. Desprès, E. Bréheret, J. P. Hare, T. John Dennis, H. W. Kroto, R. Taylor and D. R. M. Walton, *Chem. Phys.*, 1992, **160**, 451-466.
203. K. Huebener, R. S. Schoenfeld, J. Kniepert, C. Oelmueller and W. Harneit, *Phys. Stat. Soli. b*, 2008, **245**, 2013-2017.
204. B. B. Buckley, G. D. Fuchs, L. C. Bassett and D. D. Awschalom, *Science*, 2010, **330**, 1212-1215.
205. V. A. Nadtochenko, I. V. Vasil'ev, N. N. Denisov, I. V. Rubtsov, A. S. Lobach, A. P. Moravskii and A. F. Shestakov, *J. Photochem. Photobio. A*, 1993, **70**, 153-156.
206. A. Klieneweishede; and J. Mattey;, in *CRC Handbookof Organic Photochemistry and Photobiology, Volumes 1 & 2, Second Edition*, ed. H. W. F. Lenci;, CRC Press, Editon edn., 2010, pp. 28-23.
207. Y. Kajii, T. Nakagawa, S. Suzuki, Y. Achiba, K. Obi and K. Shibuya, *Chem. Phys. Lett.*, 1991, **181**, 100-104.
208. M. R. Fraelich and R. B. Weisman, *J. Phys. Chem.*, 1993, **97**, 11145-11147.

209. r. Etheridge, H. T., M. R. Fraelich and R. B. Weisman, in *Advances in the Chemistry and Physics of Fullerenes and Related Materials*, eds. K. M. Kadish and R. S. Ruoff, The Electrochemical Society, Pennington, NJ, Editon edn., 1994, p. 803.
210. J. W. Arbogast, A. P. Darmanyan, C. S. Foote, F. N. Diederich, R. L. Whetten, Y. Rubin, M. M. Alvarez and S. J. Anz, *J. Phys. Chem.*, 1991, **95**, 11-12.
211. D. K. Palit, A. V. Sapre, J. P. Mittal and C. N. R. Rao, *Chem. Phys. Lett.*, 1992, **195**, 1-6.
212. A. Gruber, A. Dräbenstedt, C. Tietz, L. Fleury, J. Wrachtrup and C. V. Borczyskowski, *Science*, 1997, **276**, 2012-2014.

Appendix A

A.1 Mass spectrum of Dimer-5bz.....198

A.2 Mass spectrum of Dimer-3bzo.....199

A.3 Mass spectrum of Dimer-3bz (1).....200

A.4 Mass spectrum of Dimer-3bz (2).....200

A.5 Scan of the empty Miniscope ms200 cavity.....201

A.6 $^{15}N@C_{60}$-c_{60} Dimer-3bz impurity model EasySpin code.....201

A.7 $^{14}N@C_{60}$ -$^{14}N@C_{60}$ Dimer-3bz model EasySpin code.....202

A.1 Mass spectrum of Dimer-5bz

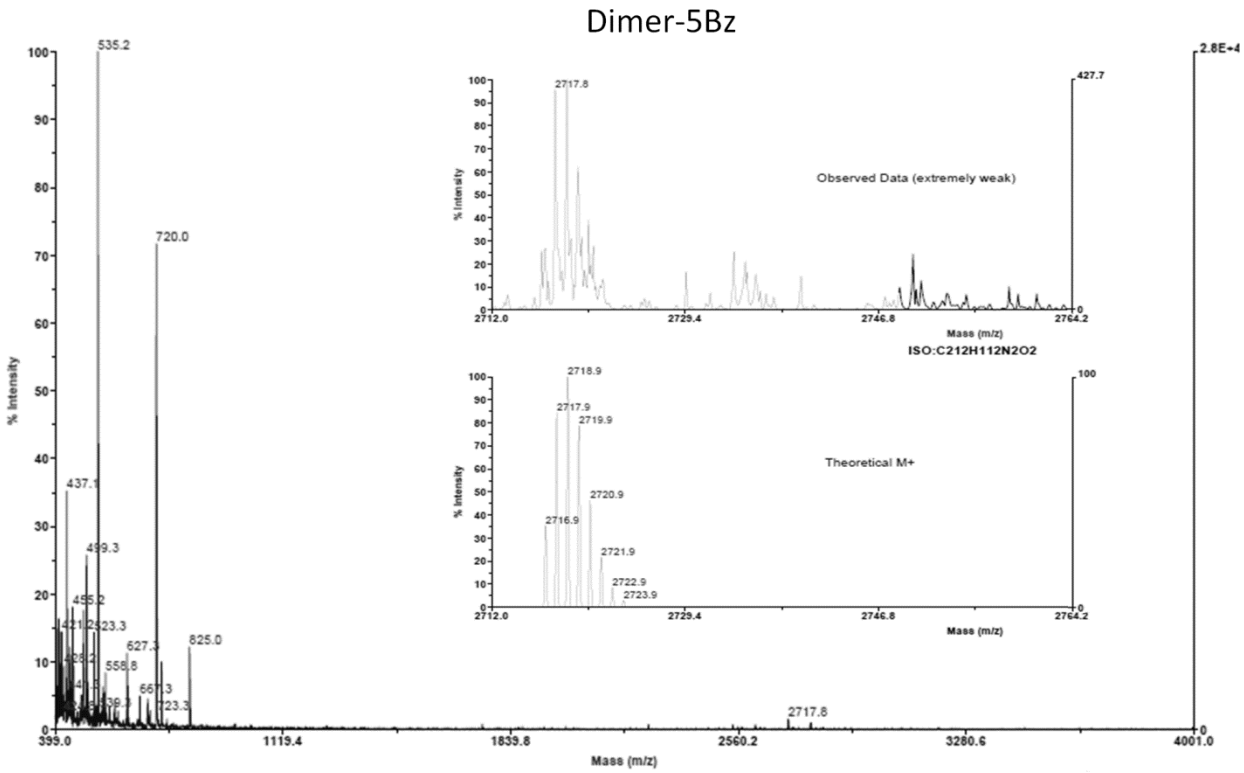


Figure A.1 MALDI ToF mass spectrum of Dimer-5bz, recorded in negative mode using a Voyager DE-STR instrument.

A.2 Mass spectrum of Dimer-3bzo

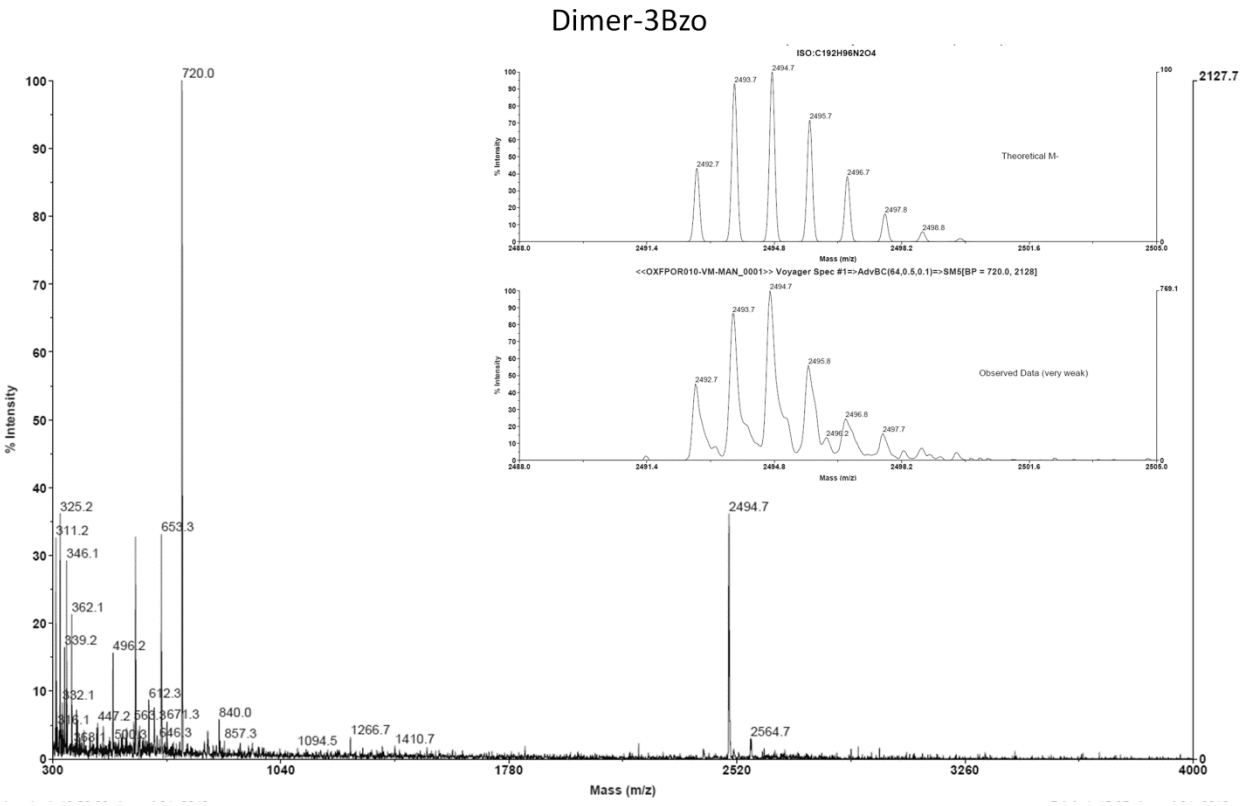


Figure A.2 MALDI ToF mass spectrum of Dimer-3bzo, recorded in negative mode using a Voyager DE-STR instrument.

A.3 Mass spectrum of Dimer-3bz (1)

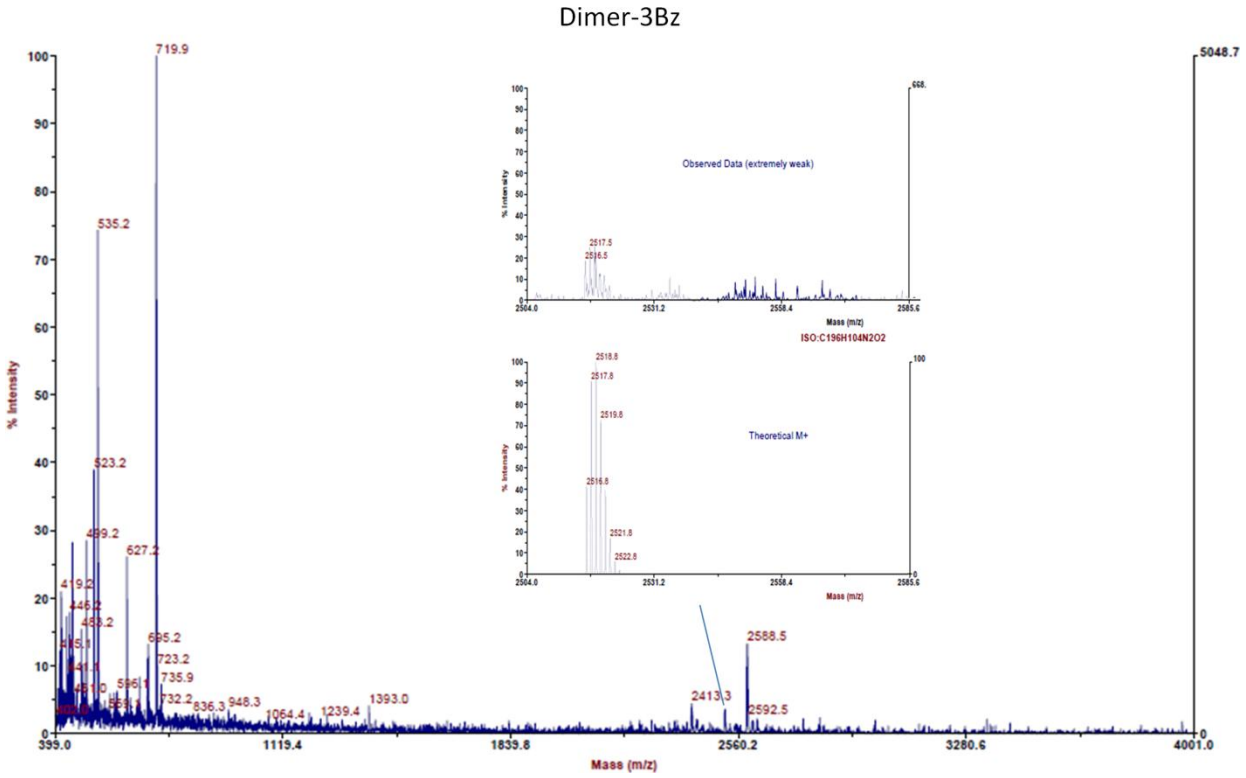


Figure A.3 MALDI ToF mass spectrum of Dimer-3bz recorded in negative mode using a Voyager DE-STR instrument (recorded after column purification, prior to final HPLC purification step).

A.4 Mass spectrum of Dimer-3bz (2)

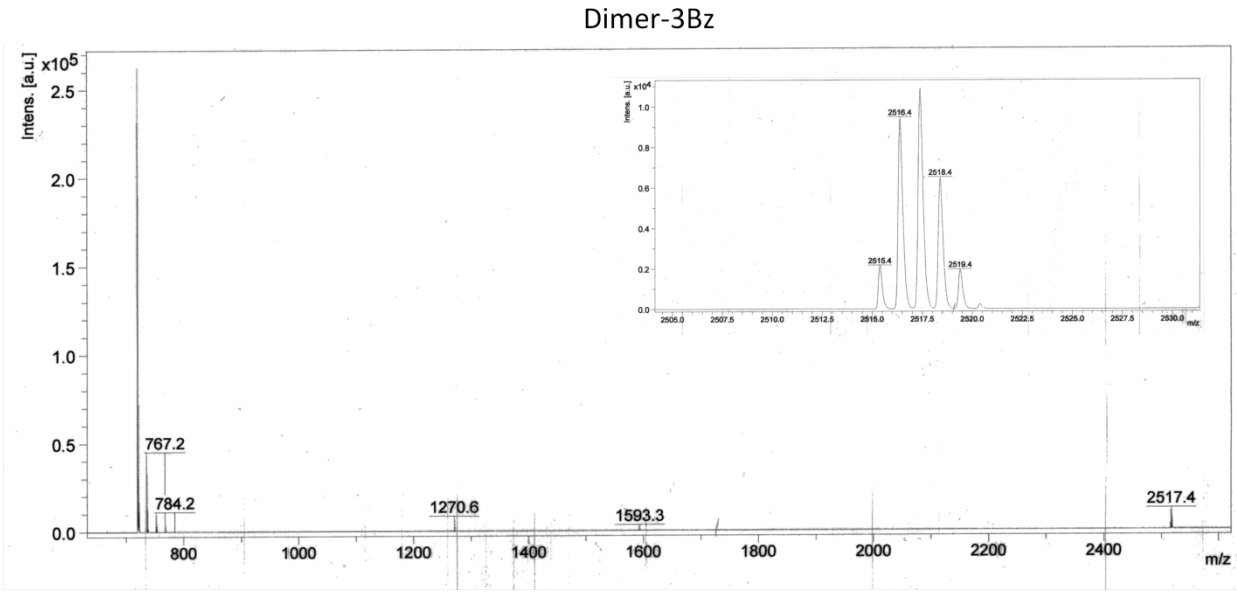


Figure A.4 MALDI ToF mass spectrum of Dimer-3bz recorded in negative mode using a Bruker Ultraflex III instrument (recorded after final HPLC purification step).

A.5 Scan of the empty Miniscope ms200 cavity

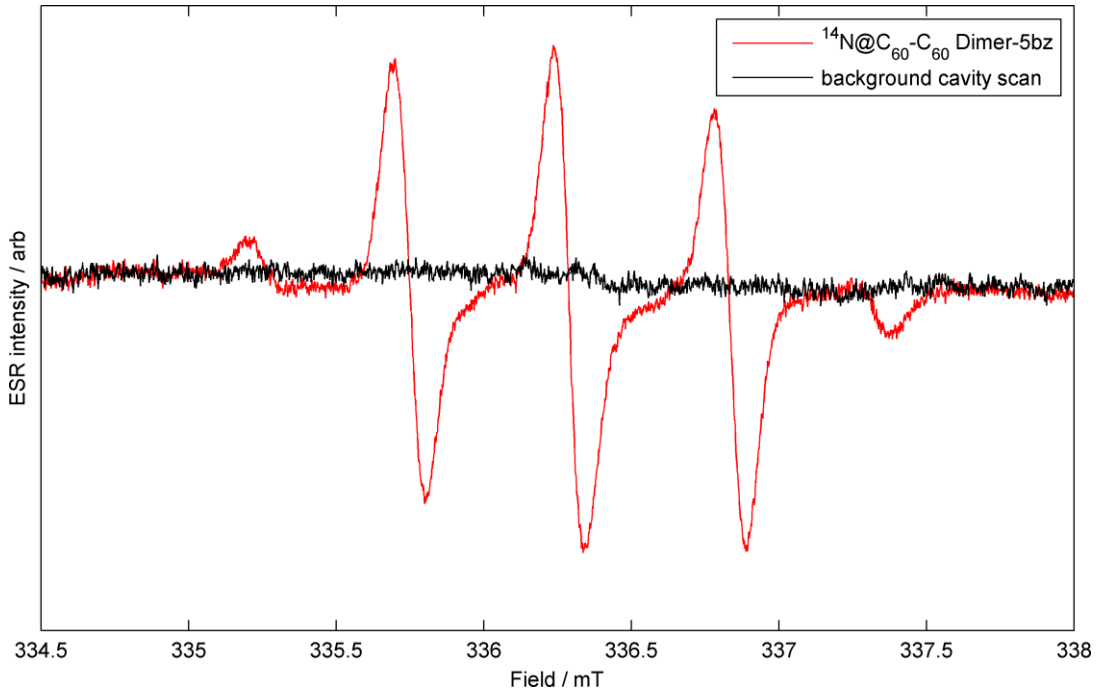


Figure A.5 Overlay of 77K Miniscope ms200 spectra of $^{14}N@C_{60}$-C_{60} Dimer-5bz with a background scan of the empty cavity to illustrate the effect sinusoidal oscillation of the background to the collected spectra.

A.6 $^{15}N@C_{60}$-c_{60} Dimer-3bz impurity model EasySpin code

```
% 15N@C60-C60 dimer simulation

Sys0.Nucs = '15N';
Sys0.S = 3/2;
Sys0.n = 1;
Sys0.g = 2.00271;
Sys0.A = 21.24; % Hyperfine interaction in MHz, taken from Zhang DPhil pp71
Sys0.D = [14.19 0.74]; % ZFS [D E] in MHz
Sys0.lw = 0.121; % Peak to peak line width in mT

Exp.mwFreq = 9.391148; % Microwave frequency in GHz
Exp.CenterSweep=[335 5];% Applied magnetic field sweep width in mT
Exp.nPoints = 2000;

[x2,y2]=pepper(Sys0, Exp );

plot( x2, y2,'c');
```

Figure A.6 EasySpin code used to simulate $^{15}N@C_{60}$-c_{60} Dimer-3bz impurity.

A.7 $^{14}N@C_{60}$ -$^{14}N@C_{60}$ Dimer-3bz model EasySpin code

```
% 14N@C60-14N@C60 dimer simulation

jdip=[2.675]; % Jdip dipolar coupling term in MHz
Sys1.Nucs = ['14N , 14N'];
Sys1.S = [1.5 , 1.5];
Sys1.g = [2.0027  , 2.0027];
Sys1.A = [15.7360,0; 0, 15.7360]; % Hyperfine [14N(1),14N(2); 14N(1),14N(2)]
Sys1.D = [14.19, 0.74; 14.19, 0.74]; % ZFS [D(1), E(1);D(2), E(2)] in MHz
Sys1.lw = 0.121; % Peak to peak line width in mT

Exp.mwFreq = 9.391148; % Microwave frequency in GHz
Exp.CenterSweep=[335 5];% Applied magnetic field sweep width in mT
Exp.nPoints = 2000;

for k=1:1

Sys1.ee=jdip(k)*[1 1 -2];% Dipolar interaction tensor [xx yy zz] in MHz
[Fitx{k}Fity{k}]=pepper(Sys1, Exp);

end

 for k=1:1

 subplot(1,1,k);

 h=plot(Fitx{k},Fity{k});

 end

 xlabel('Magnetic field (mT)');
 ylabel('EPR intensity (a.u.)');
```

Figure A.7 EasySpin code used to simulate $^{14}N@C_{60}$ -$^{14}N@C_{60}$ Dimer-3bz spectrum

Appendix B

B.1 HPLC Trace of C_{60}(py).....204

B.2 Simulated derivative ESR spectrum of N@C_{60}(py)-Cr_7Ni.....204

B.3 ^{14}N@C_{60} (py)-Cr_7Ni Model EasySpin Code.....200

B.1 HPLC Trace of C_{60}(py)

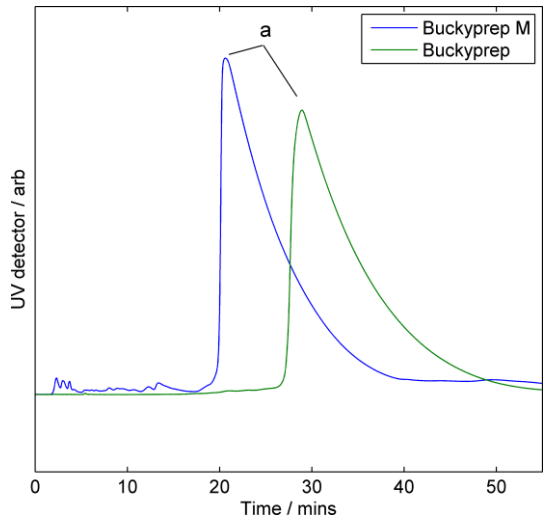


Figure B.1 HPLC trace of C_{60}(py) retention time using two different columns. Peak (a) was collected retained as the C_{60}(py) peak The reaction mixtures were passed through a short silica plug using a 1% T.E.A / toluene eluent mixture prior to HPLC analysis. Columns: (blue) Buckyprep-M 20 x 250 mm. Eluent: Toluene, flow rate: 18 mL min^{-1}. (green) Buckyprep 10 x 250 mm. Eluent Toluene, flow rate: 7 mL min^{-1}.

B.2 Simulated derivative ESR spectrum of N@C_{60}(py)-Cr_7Ni

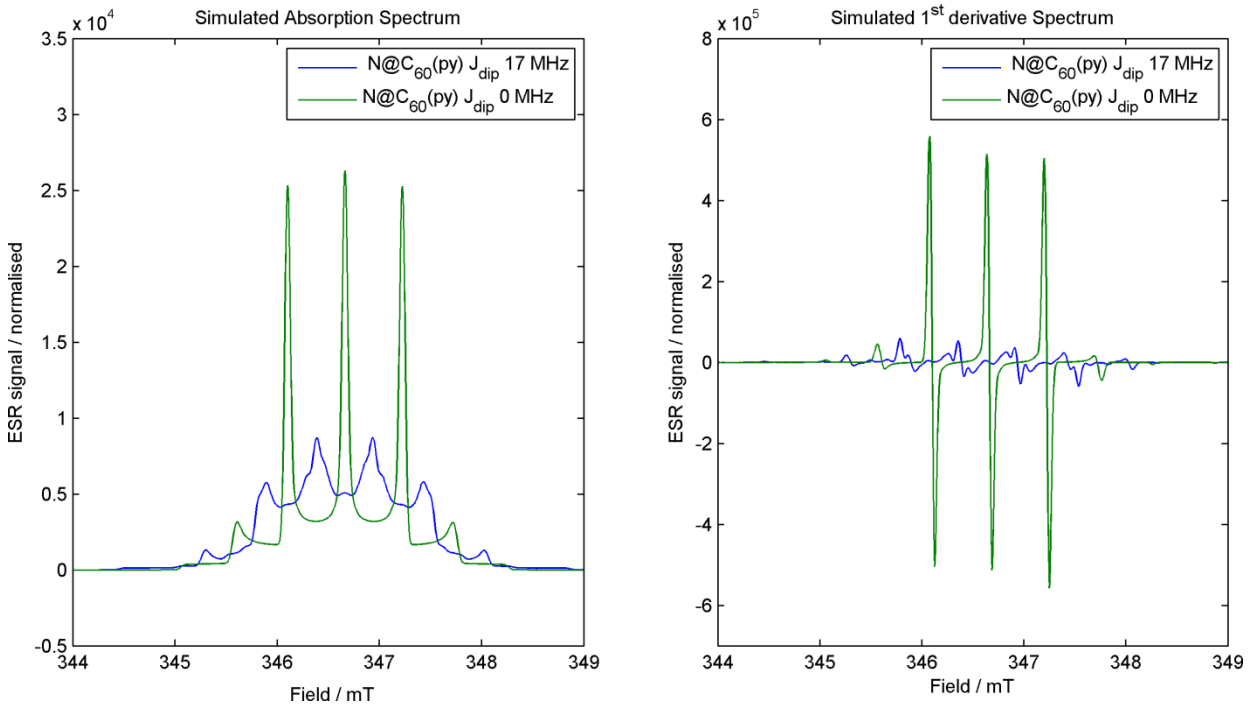


Figure B.2 Simulated absorption and derivative ESR spectrums of N@C_{60}(py)-Cr_7Ni that includes a dipolar interaction of J_{dip} between an S=3/2 g=2 N@C_{60} centre and an S= ½ g=1.8 electron spin centre using Equation 2.24 and the following parameters: hyperfine splitting term (A_{iso}= 15.74 MHz), Axial zero field term (D=14.58 MHz, E=0.21 MHz), line-width 0.057 mT and g_{iso}=2.0023 with J_{dip}=0 MHz (green) and J_{dip}=17 MHz (blue).

B.3 $^{14}N@C_{60}$ (py)-Cr_7Ni Model EasySpin Code

```
% 17 MHz coupling
jdip0=17;
Sys0=struct('S',[3/2,1/2], 'g',[2.00271, 1.8]);
Sys0.Nucs='14N,58Ni';
Sys0.A=  [15.74, 0; 0, 0];
Sys0.D= [14.6,0.21; 0 0];
Sys0.lw= 0.06; %mT
Sys0.ee=jdip0*[1 1 -2];
Sys0.weight=1;

% 0 MHz coupling
jdip=0;
Sys1=struct('S',[3/2,1/2], 'g',[2.00271, 1.8]);
Sys1.Nucs='14N,58Ni';
Sys1.A=  [15.74, 0; 0, 0];
Sys1.D= [14.6,0.21; 0 0];
Sys1.lw= 0.06; %mT
Sys1.ee=jdip*[1 1 -2];
Sys1.weight=1;


Exp = struct('mwFreq',9.7172,'Range',[344 349]);
Opt.nKnots = [91 0];
Opt.Output ='summed';

% Simulations

% Absorption spectra
Exp.Harmonic = 0;
[B0a,Spc0a]=pepper(Sys0,Exp,Opt);
[B0b,Spc0b]=pepper(Sys1,Exp,Opt);
% First derivative spectra
Exp.Harmonic = 1;
[B1a,Spc1a]=pepper(Sys0,Exp,Opt);
[B1b,Spc1b]=pepper(Sys1,Exp,Opt);

% Plot data figure
subplot(1,2,1);
plot(B0a,Spc0a,B0b,Spc0b,B0c,Spc0c);
title('Simulated Absorption Spectrum');
ylabel('ESR signal / normalised');xlabel('Field / mT');
legend(' N@C_{60}(py) J_{dip} 17 MHz','N@C_{60}(py) J_{dip} 0 MHz')
subplot(1,2,2);
plot(B1a,Spc1a,B1b,Spc1b,B1c,Spc1c);
title('Simulated 1^{st} derivative Spectrum');
ylabel('ESR signal / normalised');xlabel('Field / mT');
legend(' N@C_{60}(py) J_{dip} 17 MHz','N@C_{60}(py) J_{dip} 0 MHz')
```

Figure B.3 EasySpin code used to simulate absorption and 1st derivative spectrum of $^{14}N@C_{60}$ (py)-Cr_7Ni with both J_{dip}=0Mhz and J_{dip}=17Mhz (shown in figure B.2)